

ISSN 2071-4726
2071-0305

Magazine of Civil Engineering

96(4), 2020





ПОЛИТЕХ
Санкт-Петербургский
политехнический университет
Петра Великого

Инженерно-строительный институт
Центр дополнительных профессиональных программ
195251, г. Санкт-Петербург, Политехническая ул., 29,
тел/факс: 552-94-60, www.stroikursi.spbstu.ru,
stroikursi@mail.ru

**Приглашает специалистов организаций, вступающих в СРО,
на курсы повышения квалификации (72 часа)**

Код	Наименование программы	Виды работ*
Курсы по строительству		
БС-01-04	«Безопасность и качество выполнения общестроительных работ»	п.1,2, 3, 5, 6, 7, 9, 10, 11, 12, 13, 14
БС-01	«Безопасность и качество выполнения геодезических, подготовительных и земляных работ, устройства оснований и фундаментов»	1,2,3,5
БС-02	«Безопасность и качество возведения бетонных и железобетонных конструкций»	6,7
БС-03	«Безопасность и качество возведения металлических, каменных и деревянных конструкций»	9,10,11
БС-04	«Безопасность и качество выполнения фасадных работ, устройства кровель, защиты строительных конструкций, трубопроводов и оборудования»	12,13,14
БС-05	«Безопасность и качество устройства инженерных сетей и систем»	15,16,17,18,19
БС-06	«Безопасность и качество устройства электрических сетей и линий связи»	20,21
БС-08	«Безопасность и качество выполнения монтажных и пусконаладочных работ»	23,24
БС-12	«Безопасность и качество устройства мостов, эстакад и путепроводов»	29
БС-13	«Безопасность и качество выполнения гидротехнических, водолазных работ»	30
БС-14	«Безопасность и качество устройства промышленных печей и дымовых труб»	31
БС-15	«Осуществление строительного контроля»	32
БС-16	«Организация строительства, реконструкции и капитального ремонта. Выполнение функций технического заказчика и генерального подрядчика»	33
Курсы по проектированию		
БП-01	«Разработка схемы планировочной организации земельного участка, архитектурных решений, мероприятий по обеспечению доступа маломобильных групп населения»	1,2,11
БП-02	«Разработка конструктивных и объемно-планировочных решений зданий и сооружений»	3
БП-03	«Проектирование внутренних сетей инженерно-технического обеспечения»	4
БП-04	«Проектирование наружных сетей инженерно-технического обеспечения»	5
БП-05	«Разработка технологических решений при проектировании зданий и сооружений»	6
БП-06	«Разработка специальных разделов проектной документации»	7
БП-07	«Разработка проектов организации строительства»	8
БП-08	«Проектные решения по охране окружающей среды»	9
БП-09	«Проектные решения по обеспечению пожарной безопасности»	10
БП-10	«Обследование строительных конструкций и грунтов основания зданий и сооружений»	12
БП-11	«Организация проектных работ. Выполнение функций генерального проектировщика»	13
Э-01	«Проведение энергетических обследований с целью повышения энергетической эффективности и энергосбережения»	
Курсы по инженерным изысканиям		
И-01	«Инженерно-геодезические изыскания в строительстве»	1
И-02	«Инженерно-геологические изыскания в строительстве»	2,5
И-03	«Инженерно-гидрометеорологические изыскания в строительстве»	3
И-04	«Инженерно-экологические изыскания в строительстве»	4
И-05	«Организация работ по инженерным изысканиям»	7

*(согласно приказам Минрегионразвития РФ N 624 от 30 декабря 2009 г.)

**По окончании курса слушателю выдается удостоверение о краткосрочном повышении
квалификации установленного образца (72 ак. часа)**

Для регистрации на курс необходимо выслать заявку на участие, и копию диплома об образовании по телефону/факсу: 8(812) 552-94-60, 535-79-92, , e-mail: stroikursi@mail.ru.

Magazine of Civil Engineering

SCHOLAR JOURNAL

ISSN 2071-0305

Свидетельство о государственной регистрации:
Эл № ФС77-77906 от 19.02.2020,
выдано Роскомнадзором

Специализированный научный журнал. Выходит с
09.2008.

Включен в Перечень ВАК РФ

Индексируется в БД Scopus

Периодичность: 8 раз в год

Учредитель и издатель:

Санкт-Петербургский политехнический университет
Петра Великого

Адрес редакции:

195251, СПб, ул. Политехническая, д. 29

Главный редактор:

Екатерина Александровна Линник

Научный редактор:

Виталий Владимирович Сергеев

Заместитель главного научного редактора:

Галина Леонидовна Козинец

Редакционная коллегия:

PhD, проф. Т. Аввад;
д.т.н., проф. М.И. Бальзанников
д.т.н., проф. А.И. Белостоцкий;
к.т.н., проф. А.И. Боровков;
д.т.н., проф. А. Бородинец;
PhD, проф. М. Велькович;
PhD, проф. Р.Д. Гарг;
PhD, М.Р. Гарифуллин;
Dr.-Ing, проф. Т. Грис;
д.т.н., проф. Т.А. Дацюк;
д.т.н., проф. В.В. Елистратов;
Dr.-Ing., проф. Т. Кэрки;
д.т.н., проф. Д.В. Козлов;
д.т.н., доцент С.В. Корниенко;
д.т.н., проф. Ю.Г. Лазарев;
д.т.н., проф. М.М. Мухаммадиев;
Dr.-Ing. Habil., проф. Х. Пастернак;
Dr.-Ing., проф. Ф. Рёгинер;
д.т.н., проф. Т.З. Султанов;
д.т.н., проф. М.Г. Тягунов;
акад. РАН, д.т.н., проф. М.П. Федоров;
Dr.-Ing., проф. Д. Хецк;
д.г.-м.н. А.Г. Шашкин;
д.т.н. В.Б. Штильман

Дата выхода: 29.06.2020

© ФГАОУ ВО СПбПУ, 2020
© Иллюстрация на обложке: Илья Смагин

Magazine of Civil Engineering

SCHOLAR JOURNAL

ISSN 2071-0305

Peer-reviewed scientific journal

Start date: 2008/09

8 issues per year

Publisher:

Peter the Great St. Petersburg Polytechnic University

Indexing:

Scopus, Russian Science Citation Index (WoS),
Compendex, EBSCO, Google Academia, Index
Copernicus, ProQuest, Ulrich's Serials Analysis System,
CNKI

Corresponding address:

29 Polytechnicheskaya st., Saint-Petersburg, 195251,
Russia

Editor-in-chief:

Ekaterina A. Linnik

Science editor:

Vitaly V. Sergeev

Deputy chief science editor:

Galina L. Kozinetc

Editorial board:

T. Awwad, PhD, professor
M.I. Balzannikov, D.Sc., professor
A.I. Belostotsky, D.Sc., professor
A.I. Borovkov, PhD, professor
A. Borodinets, Dr.Sc.Ing., professor
M. Veljkovic, PhD, professor
R.D. Garg, PhD, professor
M. Garifullin, PhD, postdoctorant
T. Gries, Dr.-Ing., professor
T.A. Datsyuk, D.Sc., professor
V.V. Elistratov, D.Sc., professor
T. Kärki, Dr.-Ing., professor
D.V. Kozlov, D.Sc., professor
S.V. Korniyenko, D.Sc., professor
Yu.G. Lazarev, D.Sc., professor
M.M. Muhammadiev, D.Sc., professor
H. Pasternak, Dr.-Ing.habil., professor
F. Rögener, Dr.-Ing., professor
T.Z. Sultanov, D.Sc., professor
M.G. Tyagunov, D.Sc., professor
M.P. Fedorov, D.Sc., professor
D. Heck, Dr.-Ing., professor
A.G. Shashkin, D.Sc.
V.B. Shtilman, D.Sc.

Date of issue: 29.06.2020

© Peter the Great St. Petersburg Polytechnic University.
All rights reserved.
© Coverpicture – Ilya Smagin

Contacts:

E-mail: mce@spbstu.ru

Web: <http://www.engstroy.spbstu.ru>

Contents

Salakhutdinov, M.A., Gimranov, L.R., Kuznetsov, I.L., Fakhrutdinov, A.E., Nurgaleeva, L.M. PFRP structures under the predominately short term load	3
Liseikin, A.V., Seleznev, V.S., Adilov, Z.A. Monitoring of the natural frequencies of Chirkey arch dam	15
Bilous, I.Yu., Deshko, V.I., Sukhodub, I.O. Building energy modeling using hourly infiltration rate	27
Kosichenko, Yu.M., Baev, O.A. Efficiency and durability of the linings channels of geosynthetics	42
Ayoob, N.S., Abid, S.R., Hilo, A.N., Daek, Y.H. Water-impact abrasion of self-compacting concrete	60
Solovyev, S.A. A probabilistic approach to estimation of the ultimate load of end-bearing piles on settlement criterion	70
Al-Rousan, R., Abo-Msamh, I. Impact of anchored CFRP on the torsional and bending behaviour of RC beams	79
Denisov, A.V. Radiation changes of concrete aggregates under the influence of gamma radiation	94
Kirsanov, M.N. Analytical dependence of the deflection of the spatial truss on the number of panels	110
Mirsaidov, M.M., Khudainazarov, Sh.O. Spatial natural vibrations of viscoelastic axisymmetric structures	118
Vatin, N., Korniyenko, S.V., Gorshkov, A.S., Pestryakov, I.I., Olshevskiy, V. Actual thermophysical characteristics of autoclaved aerated concrete	129
Wedatalla, A.M.O., Yanmin, Y.J. The effect of simulated ambient conditions on durability of concrete	138



DOI: 10.18720/MCE.96.1

PFRP structures under the predominately short term load

M.A. Salakhutdinov^a, L.R. Gimranov^a, I.L. Kuznetsov^a, A.E. Fakhрутdinov^b, L.M. Nurgaleeva^c

^a Kazan State University of Architecture and Engineering, Kazan, Russia

^b Joint-stock company "Special Economic Zone "Innopolis", Innopolis, Russia

^c LLC "Tatneft-Presscomposite", Elabuga, Russia

* E-mail: lider-kazann@yandex.ru

Keywords: pultruded FRP profiles, bolted joints, experimental studies

Abstract. The subject of the study is a load bearing capacity of building structures from fiber reinforced polymer (FRP) shapes under the short term load, such as snow load and occupancy load, which significantly exceed values of dead load. Experimentally determined actual strength and stiffness under the short term load of following structural members and connections: of I-beams; bolted connections under the bearing load with different directions of material's pultrusion relatively to applied force; connections transferring load via contact surfaces, at the ends of structural members, oriented normally to the direction of pultrusion; webs of the I-beams under locally applied load perpendicularly to the direction of pultrusion. Experimental studies deemed following results. Minimal flexural strength of beams obtained experimentally is on average 1.25 times higher than values of flexural strength determined theoretically. Strength of different types of connections obtained after testing procedures is on average 1.35–2.5 times higher of its theoretical values. Conducted studies allow widening of the field of an applicability of FRP profiles as structural members of small scale structures subjected to predominantly atmospheric or live loads, for instance, tiered and covered seating pavilion. Such types of structures subjected to short term load allow to utilize strength and stiffness of their structural members more deeply.

1. Introduction

Structures made from fiber reinforced polymers have become more common in building construction practice. Some structural members from fiber reinforced polymers are being casted right in the construction site using infusion methods with mechanical properties such as strength from 65-90MPa and elasticity modulus from 3100 MPa up to 4000 MPa [1]. However, practice of production certain nomenclature of profiles of different shapes found its place in a new emerging manufacturing method based on pultrusion process. Pultruded fiber reinforced polymers (PFRP) are made of strand rovings inside of matrix from polymer. PFRP have mechanical properties similar to that of the wood in its orthotropic behavior and with strength in longitudinal direction up to 250MPa and elasticity module in the same direction up to 26000MPa.

The strength to density ratio, commonly used as criterion of the material effectiveness in load bearing structures, for PFRP in longitudinal direction can reach up to $250/1.85 = 135$ that is higher than for the steel $250/7.85 = 31.8$ and wood $130/0.5 = 26$.

Today more than 300 firms worldwide are involved in production of fiberglass profiles made by pultrusion process. Significant share of production volume in those companies is accommodated for lattice flooring, windows and doors profiles, handrails and fence, stairs, manholes, noise barriers, outdoor lighting poles, cable channels and antennas (Figure 1).





Figure 1. Examples of products made from fiberglass profiles.

In addition to already mentioned nomenclature of various products fiberglass profiles for building construction industry in different shapes (hollow sections, angles, channels, I-beams, T-beams etc.) are produced. Structures of suspended galleries, footbridges and crossings etc. are known to be made of fiberglass-reinforced profiles produced by pultrusion process [2–4].

Structural analysis of load bearing members of structures made from pultruded fiberglass reinforced profiles (PFRP) is performed predominately on the basis of industry standards and design manuals of individual manufacturers [5] which are not obligatory for every participant [6]. Main types of joints being used in the field are bolted joints [7–9] and bolted joints with different shapes of steel cleats [10–12].

Despite of the existing results of research and normative codes (mostly US and Europe based) versatile service conditions render it difficult to apply codes mentioned above to the all structural shapes, loading cases, local standards of production and regions of location. Regarding to the examples of structures from PFRP and the tendencies in applicability of PFRP, apparent tilt to the structures of pedestrian crossings [13], bridges [14] and special engineering structures [15, 16] has become obvious. This study addresses issues related to the load conditions of structural members and joints those ratio of values of short-term load to the values of dead load is equal 4 and higher (for instance design snow load at most parts of Russia exceeds 1 kPa and in some regions can be up to 5.6kPa). Also structural forms, structures and joints of members of the structures meant to be subjected mostly to short-term load were reviewed. Design of joints of the structural members with steel plates acting as load transferring members extensively studied in following papers [10–12]. Various types of beam to column connections are also extensively studied [17, 18]. Bolted connections play pivotal role in designing structures made of PFRP [19–21]. Different local effects in bolted connections were meticulously scrutinized in [22, 23]. PFRP members such as built up columns under the compression load were subject of research in [24]. The point of interest of a current study was design solutions of connections without additional steel force transferring plates. End use conditions of structures in current studies supposed to be such that short-term load applied either to the roof system or to the other members of the structures cause stresses significantly higher than that caused by dead load. Short term load duration also reduces influence of a load duration factors on the strength of structural members allowing higher stress levels. Nevertheless, required strength of a structural member was significantly lower than actual strength obtained from tests experiments. Structural shape designed during current study covered seating pavilion with tiered rows, assumed short term loads from occupancy during events at summertime period and snow load up to 3.5 kPa during winter periods with almost excluded load from occupancy. Both types of mentioned loads significantly exceed dead load and have short term nature. Also supposed function and location of a mention seating pavilions also widens the field of applicability of PFRP allowing usage during events at summer camps which service during winter period is extremely constrained. Design of joints with absent of steel plates provides uniformity of inside connection displacements during temperature changes ranging from -35 °C to 60 °C.

PFRP have some competitive advantages:

- strength (normative tensile strength up to 380MPa);
- resistance to corrosion and to the chemically aggressive environment;
- light weight(material density 1850 kg/m³);
- dielectric properties;
- reduced service cost of the surface area.

Mechanical properties of PFRP which are the subject of this studies are shown in table1.

Table 1. Mechanical properties of PFRP

Mechanical properties of material	Description	Unit	Value
1	2	3	4
Longitudinal ultimate tensile strength(min)	$R_{t,L}^H$	MPa	380
Longitudinal elasticity modulus in tension(min)	$E_{t,L}^H$	GPa	28
Longitudinal ultimate compressive strength(min)	$R_{c,L}^H$	MPa	270
Longitudinal elasticity modulus in compression (min)	$E_{c,L}^H$	GPa	20
Shear modulus , (min)	G_{LT}^H	GPa	3
Transverse elasticity modulus in compression (min)	$E_{c,T}^H$	GPa	7
Poisson Ratio (min)	ν_{TL}		0.1

Nevertheless more wide usage of PFRP as structural members of the structures is constrained by the lack of regulating codes and required experience. Actually only first steps in direction of proliferation of structural PFRP into building industry had been made.

Therefore the substantiation of possibility of more wide usage of the PFRP as structural members of the different load bearing structures is very important.

The objectives of this study are:

- establishing peculiarities in working under the predominantly short-term load of PFRP structures and joints of structural members;
- explore the possibility of widening field of applicability of PFRP in structures of seating pavilions.

To reach mentioned objectives following tasks should be accomplished:

- structural shape of interest should be introduced as an example which widens field of applicability of PFRP structures;
- experimental data should be gathered concerning of load bearing capacity of joints of the PFRP structures under the short-term load;
- joints of structural members of PFRP structures without web cleats should be studied and assessed as main types of connections in mentioned structures.

First steps in pushing envelope further in the field of PFRP applicability are being made in the form of design projects and already erected structures. Vivid example of this is the covered seating pavilion on 200 seats with 5 tiered rows for sports venues. At least 11 of such pavilions were erected in different locations.

The structural shape of this covered 5x22.3 m seating pavilion (Figure 2) includes following structural members and systems. Columns installed with grid 2.375x4.75 m, in aisle area – 1.1 m, roof system include primary and secondary roof beams, purlins, brace members (Figure 3). Seating part of pavilion includes stringers, seating beams, lattice flooring for seats. All mentioned structures are made of PFRP. Columns, primary and secondary beams have I-beam cross section with dimensions 200x200x15x15 mm, purlins – channels of 150x70x8x8 mm, stringers have paired channels cross section of 200x100x10x10 mm, braces and beams for seats made of 75x75x6x6 mm and 105x105x13x13 mm angles, lattice flooring has spacing of 38x38 mm. Joint gusset for stringers and roof beams were supposed to be made by splitting channels and I-beams cross sections in half resulted in T-beams cross sections and angles of required geometry.



Figure 2. Spatial view of covered 5x22.3m seating pavilion on 200 tiered seats.

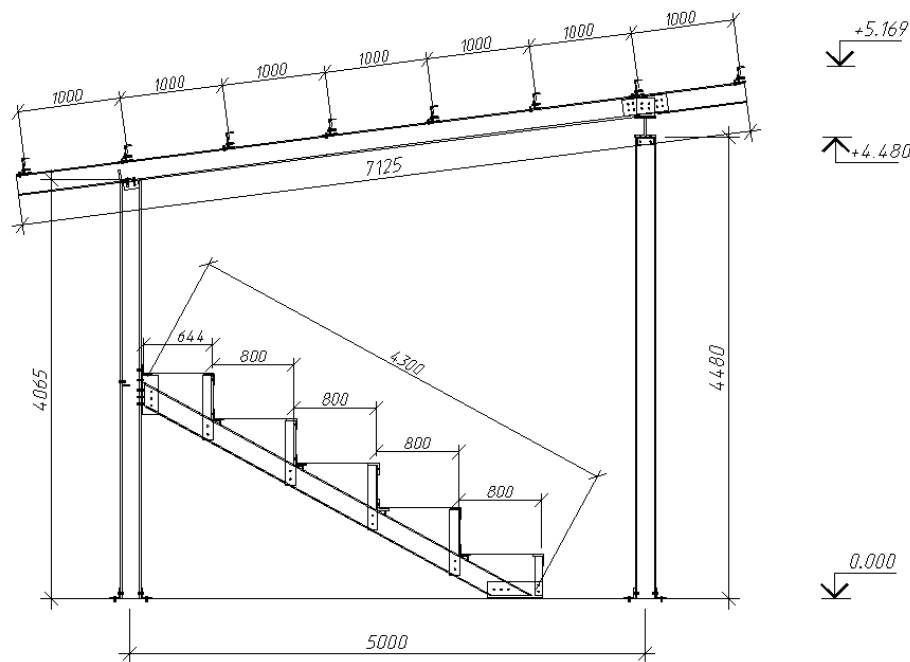


Figure 3. Side view of the seating pavilion.

Roof of the seating pavilion covered with steel deck connected to the purlins with bolts. Bolted connections of seating pavilion have galvanized coatings bolts M12 or M16 with strength grade of 8.8. During designing of the seating pavilion calculations of load bearing capacity of PFRP members considered snow load of 3.2 kPa, wind load of 0.3 kPa and live load at 4 kPa.

2. Methods

Some compositions of structural members of the pavilion have very innovative fulfillment and structural form that can be tested by only experimental approach. For example, some structural members transfer load via bolted connections in longitudinal and perpendicular directions to the grains and some via direct contact of surfaces in members ends.

In order to confirm the results of structural analysis made during designing of a pavilion and also to obtain actual data on load bearing capacity of structural members and joint solutions experimental tests were conducted. Those test included flexural bending of I-beams (Figure 4), compressing test of joints parallel to the direction of pultrusion and also in the lateral direction (Figure 5, Figure 6), compressing tests of end faces of profiles and the web of the I-beams in perpendicular to the direction of pultrusion (Figure 7, Figure 8). In structural analysis of columns of the covered seating pavilion results of experimental studies [24] were taken in consideration.

Experiments were conducted with 2000 kN hydraulic press (Figure 4), 500 kN electromechanical press (Figure 6). Mentioned presses were equipped with force measuring devices and were connected to the PC and operated by it displaying results of the test in real time.

In order to determine experimental values of load bearing capacity of the PFRP as flexural elements, I-beam with cross section dimensions 200 mm – height, 15 mm – web and flanges thickness, 200 mm – width was simply supported (1550 mm span) and loaded by local force at the middle of the span. Test is shown in Figure 11.



Figure 4. Flexural bending test of I-beam from PFRP: a –hydraulic press; b – scheme of a loading.

To determine load bearing capacity of bolted joints two types of connections were made. First one has two bolts and meant to be tested for compression load perpendicular to the direction of pultrusion (Figure 5a). Second type of joint was also a connection with two bolts only with compressing load applied parallel to the direction of pultrusion (Figure 5b). Test is shown in Figure 6.

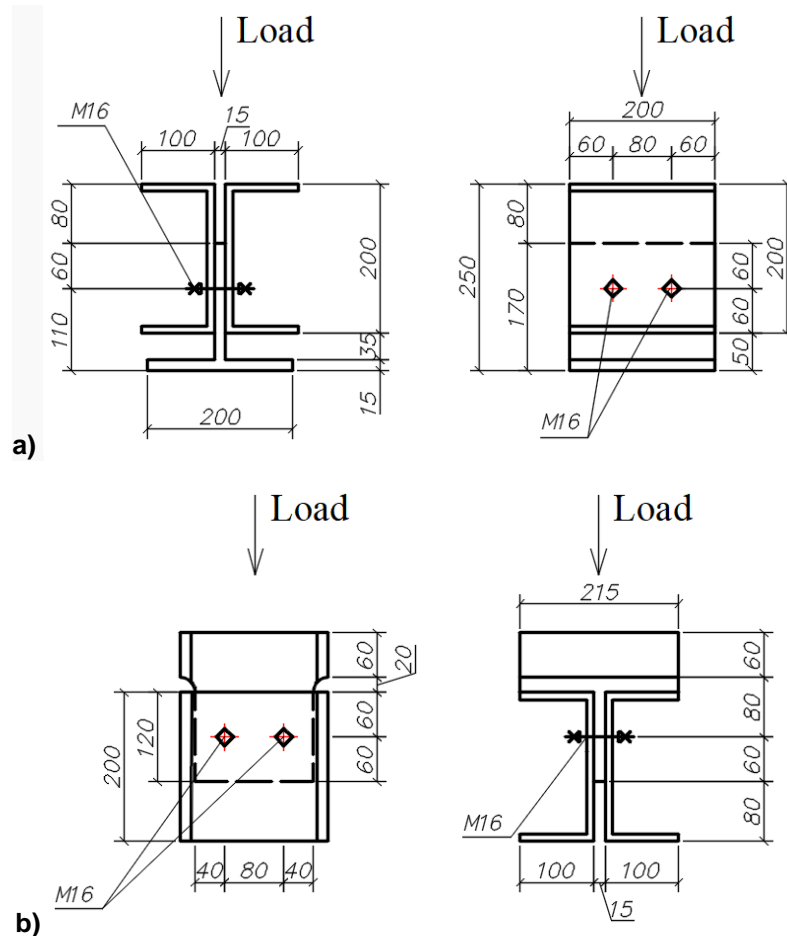


Figure 5. Bolted connection of the PFRP with two bolts: a) test with load perpendicular to the direction of pultrusion; b) test with load parallel to the direction of pultrusion.

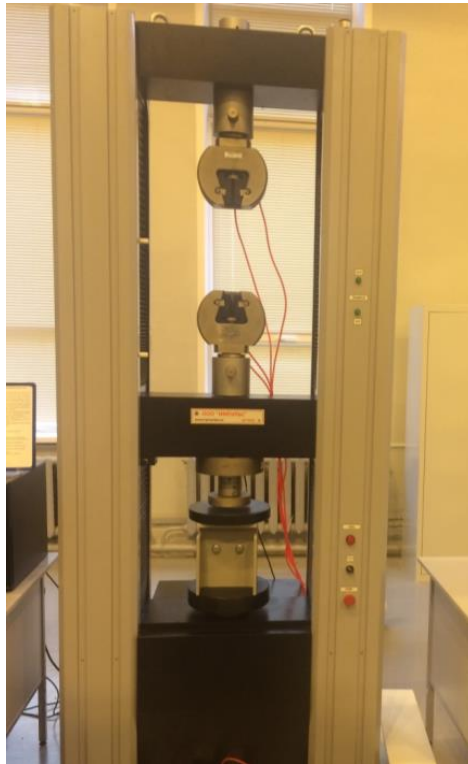


Figure 6. Test of the connection with two bolts with load applied perpendicular to the direction of pultrusion.

In the main frame of the study tests of the web of the I-beam during action of local load parallel and perpendicular to the direction of pultrusion were conducted. Load was acting on the span of a web of the I-beam with length of 200 mm. Thickness of the web and flanges of the I-beam was 15 mm, with width of the I-beam 200 mm. The process of test is shown on the Figure 7.



Figure 7. Test of the web of the I-beam under the local compressive load.

During final stage of the experimental study face ends of the I-beam profile was tested for crumpling under compressing load. Tested samples were 200 long pieces of I-beam profile with height of 200 mm, thickness of the web and flanges 15 mm and width of 200 mm.

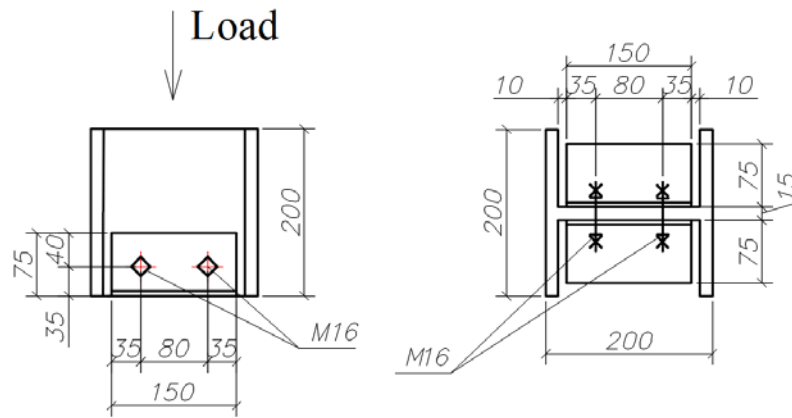


Figure 8. Sample of the I-beam profile during test on crumbling of the face ends under the compressing load.

As a result of experimental study actual values of load bearing capacity of the possible structural members and joints were obtained. Comparison of the experimental and theoretical values calculated earlier was conducted.

3. Results and Discussion

Accordingly, to established plan of the study a range of experimental tests were held. Full sized test of I-beam profile with span 1.5 m in case of flexural bending was conducted. Diagram showing dependence between maximum vertical deformation of the beam and gradually ramped load is depicted in Figure 9.

Actual and theoretical ultimate loads were $P_{ult} = 143.14$ kN and $P_{theor} = 114.14$ kN respectively. Hence safety factor could be assessed at 1.25 that is experimental load values is 1.25 times bigger that theoretical as also shown in [25].

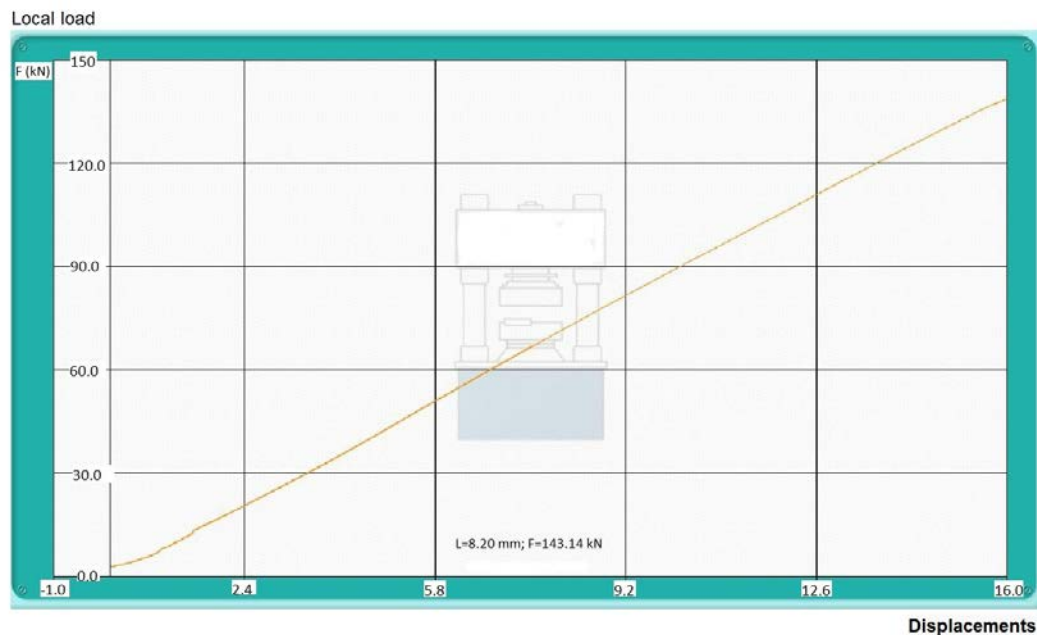


Figure 9. Diagram of vertical displacements under the local load applied at the middle of the span.

Most of the studies concerning of load bearing capacity of PFRP structures [10] focus on ultimate load that joints are able to transfer. This study nevertheless also includes test of a beam in loading case scenario close to its service period. Tested solutions of joints also were explicitly linked to certain structural shape which excluded steel web cleats in case of predominately short term load. Tested connections were also more structurally similar to those with cleats from FRP material. FRP cleats were fabricated from I-beams utilizing longitudinal cut alongside of the web. The main difference was that cleats were produced as a single piece whereas stringers were built up members. Described web cleats presumably have different stress distribution such that results of [11] study couldn't have been directly utilized. The effects of action on column flanges presumed to be similar to those described in [11]. The differences in stress distribution inside of web cleats from PFRP angles comparatively to the one described above supposedly are all due to gap between angles.

Displacements of the angles in gap area are presumably more tangible than those in the area of connection between flanges and web of T-shape cleats. Failure mode of web cleats in the heel area also apparently depends on this gap as shown in [12]. Mentioned above peculiarities were taken into account during development of connections for the experimental studies. Also one of the important aspects of experimental studies were tests of specimens of girders from I-shapes subjected to local force acting on the top flanges of the girders (Figure 7) and compressing tests of short specimens of I shapes acting as column members (Figure 17). Short length of the column specimens was due to the goal of avoiding of possible buckling effects. Main purpose was to focus on the bearing strength of the ends of specimens. Bearing strength of specimens around hole area was also a subject of interest. Connections in tested specimens were developed in such a way that probability of lamination failure or cracks in areas of connections between flanges and webs was reduced to the minimum.

The following results were obtained after the experimental tests of joints with two bolts. For joints with load applied perpendicular to the direction of pultrusion actual ultimate compressing force is amounted for $S_{b,90} = 57$ kN, in case of parallel applied compressive load is $S_{b,0} = 83$ kN. Theoretical values of load bearing capacity for joints mentioned above for the perpendicular and parallel cases of applied load relatively to the direction of pultrusion are $S_{b,90} = 22.4$ kN, $S_{b,0} = 48$ kN respectively. Thus conducted experimental studies has shown that an actual experimental ultimate compressive load for joints exceed one that calculated theoretically for the perpendicular case of applied load up to 2.5 times, for the parallel case – 1.7 times. Considering duration of applied load methods used to calculate theoretical values can be utilized in engineering calculations. Results of the tests are depicted in diagrams shown in Figures 10–11. Diagrams show ultimate values of the compressive load P_u and summarized displacements in the joint Δ . Failure of the joint under the ultimate load is shown in Figures 12–13.

Theoretical values of ultimate load were devised from expressions in the related codes. The values of design strength take into consideration several aspects ranging from duration of the load, load-stress state and specific material properties to the stress level during service period. Tangible difference between experimental values of ultimate load and theoretical values of critical load expressed from design strength for each load case, thus comprised of safety factors, and material resistance factor. Latter factor depends on mechanical properties of material of specific PFRP producer whereas safety factor usually additionally increased to accommodate stresses near design material resistance during service period. Therefore the case of stresses reaching near limit of design material resistance during only very limited amount of service time is ought to be argued. All tested specimens of bolted connections showed failure mode related to the failure of material around hole area. Failure of material in connection of flanges and webs occurred only during tests of local force acting on flanges of I-shape girders.

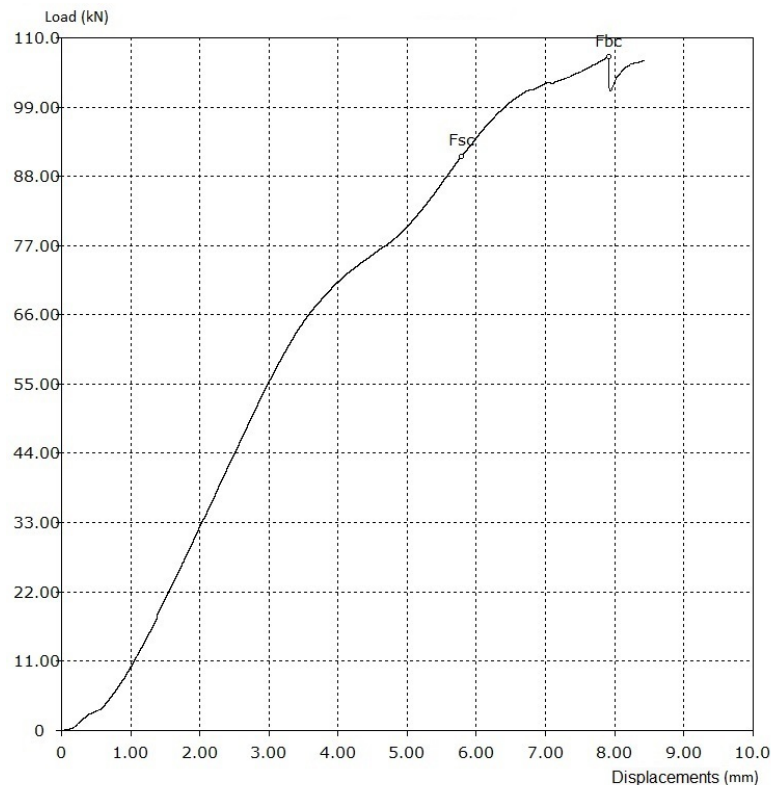


Figure 10. Diagram of displacements Δ (mm) in joints with two bolts under the compressing load P_u (kN) applied perpendicular to the direction of pultrusion.

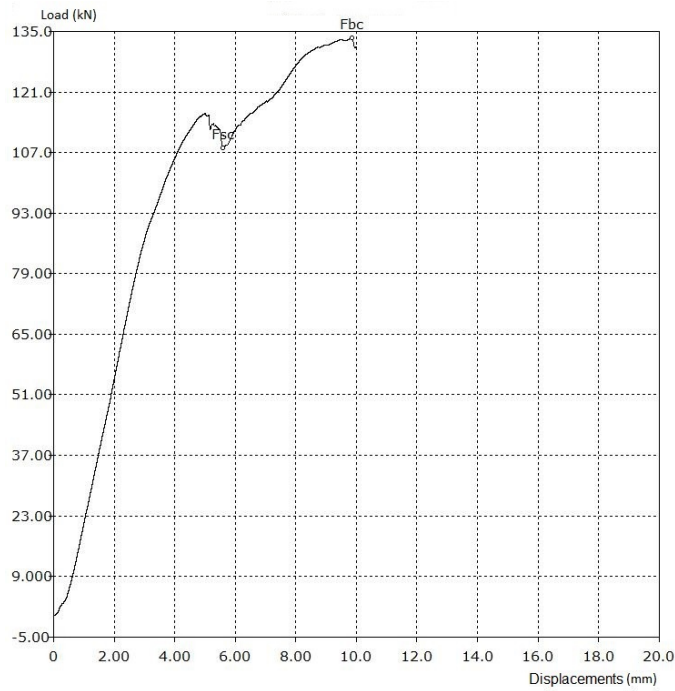


Figure 11. Diagram of displacements Δ (mm) in joints with two bolts under the compressing load P_u (kN) applied parallel to the direction of pultrusion.



Figure 12. Failure of joints under the compressing load in case of load applied perpendicular to the direction of pultrusion.



Figure 13. Failure of joints under the compressing load in case of load applied parallel to the direction of pultrusion.

Test results of the web of the I-beam under the local compressing load are shown as a diagram in Figure 14. Failure of the web under the compressing load is shown in Figure 15. Test has shown that load bearing capacity of the web fragment of the I-beam (Figure 7) under the locally applied load is 130 kN. That fact makes possible design solutions of the joints where secondary beam is installed onto primary beam above causing local stresses in the web of the primary beam.

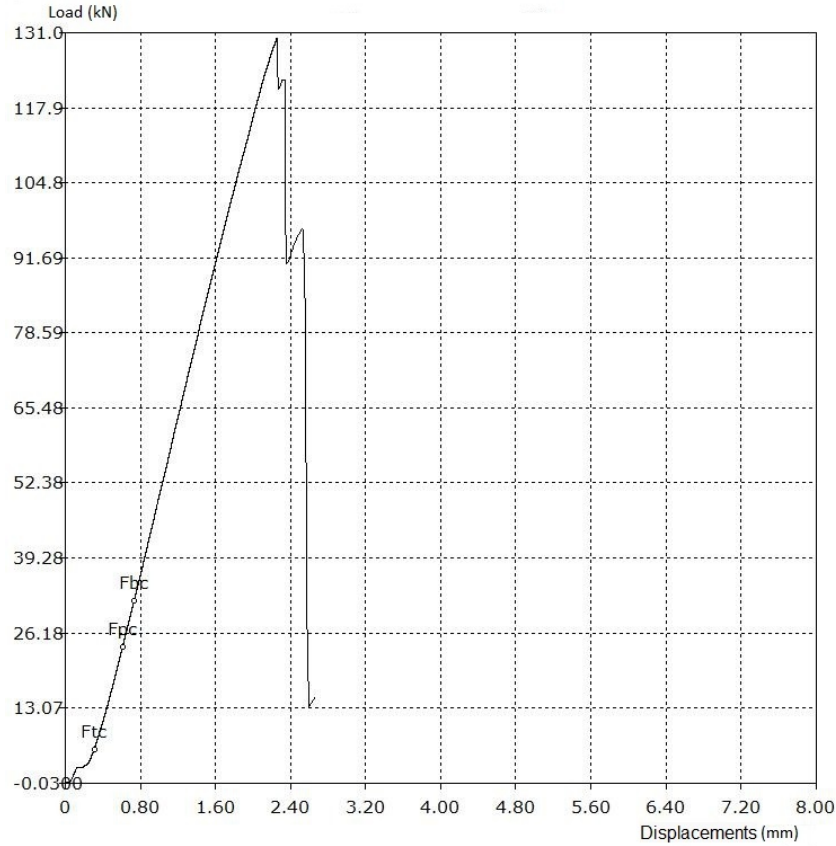


Figure 14. Diagram of local displacements Δ (mm) of the web of the I-beam under the local compressive load P_u (kN).



Figure 15. Failure of the web of the I-beam under the ultimate local compressive load.

Tests of the face ends of the PFRP are shown as a diagram in Figure 16. Failure mode of the I-beam is shown in Figure 17.

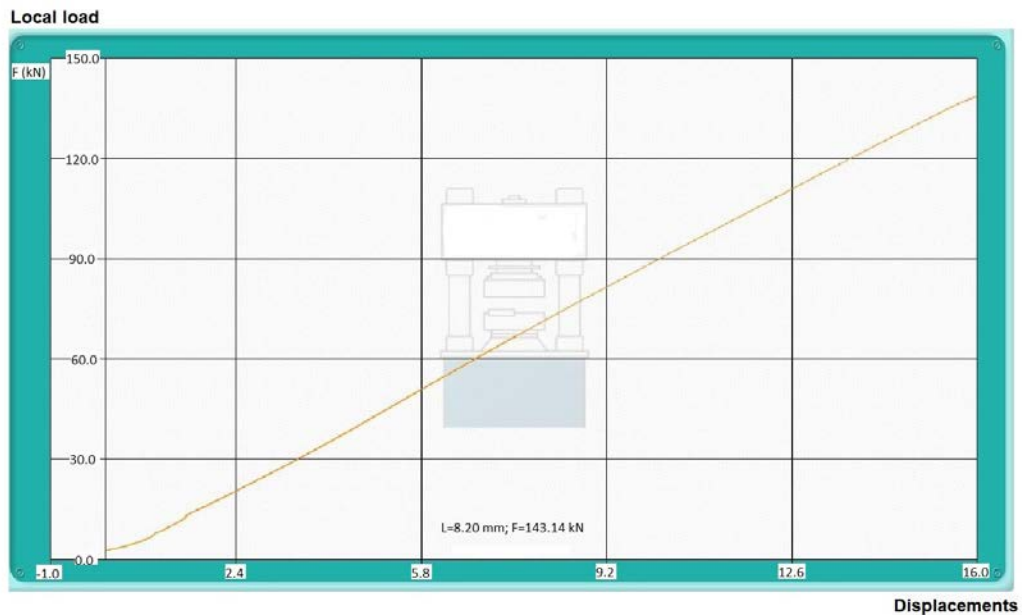


Figure 16. Diagram of displacements Δ (mm) under the crumbling load P_u (kN).



Figure 17. Failure mode of the I-beam under the crumbling load.

Tests have shown that ultimate compressing load was $P_{ult} = 692$ kN. Theoretical values of ultimate compressive load is $P_{ult} = 513$ kN. Thus actual experimental values of load bearing capacity of the I-beam under the crumbling load are higher than theoretical values on 35 %.

Experimental test of structural members in flexural bending have shown that limit state for the girder with mentioned span to dept ratio is determined by failure of material due to flexural stress and not by torsional buckling of the girder, which also confirmed by test data presented in [23].

Material failure mode around holes for the bolts in longitudinal and transverse directions, is consisted with 1st and 2nd types of failure described in [2], and confirms that patterns of bolts had been chosen correctly.

4. Conclusions

Conducted experimental studies confirms safety of the designing decisions and possibility of widening of the field of an applicability of PFRP as structural members of different structures. Although tested samples were subjected only to a short term load obtained during the tests safety factors allows to assume acceptable safety margin of the whole structure during its exploitation term.

After conducted studies following conclusions can be made:

- - experimental test confirmed designing decisions and sufficient load bearing capacity of the structural members made from PFRP and joint solutions connecting these structural members;

- - obtained values of yield strength to the ultimate strength ratios were:
 - a) in case of members in bending – 0.89
 - b) in case of compression (buckling excluded) – 0.74
 - c) in case of bending of flanges of the I-beam in lateral direction – 0.52
 - d) in case of bolted connection with force transfer in longitudinal direction – 0.6
 - e) in case of bolted connection with force transfer in longitudinal direction – 0.59
- - studies make case for more wide application of PFRP as structural members of different structures.

References

1. Nekliudova, E.A., Semenov, A.S., Melnikov, B.E., Semenov, S.G. Experimental research and finite element analysis of elastic and strength properties of fiberglass composite material. Magazine of Civil Engineering. 2014. 47(3). Pp. 25–39. DOI: 10.5862/MCE.47.3
2. Bank L.C. Composites for construction: structural design with FRP materials. New Jersey, 2006. 567p. URL: <https://ru.scribd.com/doc/144235738/Composites-for-Construction-Structural-Design-With-FRP-Materials-Malestrom> (date of reference 07.11.2018).
3. Van Den Einde, L., Zhao, L., Seible, F. Use of FRP composites in civil structural applications. Construction and Building Materials. Vol. 17. No. 6-7. 2003. Pp. 389–403.
4. Dubinchik, E.V., Pastushkov, V.G., Yankovskiy, L.V. Osobennosti primeneniya kompozitnykh materialov v stroitelstve [Some application aspects of composite polymer materials in the bulding construction]. Modernizatsiya i nauchnyye issledovaniya v transportnom komplekse. 2013. Vol. 3. Pp. 175–181.
5. Kayumov, R.A., Sharafutdinova, A.A. Ob otsenke dolgovechnosti stroitelnykh konstruksiy iz stekloplastika [About an estimation of operational durability of building designs from fiberglass]. Izvestiya kazanskogo gosudarstvennogo arkhitekturno-stroitel'nogo universiteta. 2017. No. 2(40). Pp. 114–123.
6. Ascione, L., Caron, J., Godonou, P., and etc. Prospect for new guidance in the design of FRP. Joint Research Centre. Institute for the Protection and the Security of the Citizen. Italy, 2016. 176p. URL: <https://ec.europa.eu/jrc/en/publication/eur-scientific-and-technical-research-reports/prospect-new-guidance-design-frp> (date of reference 07.11.2018).
7. Qureshi, J., Mottram, J.T. Moment-rotation response of nominally pinned beam-to-column joints for frames of pultruded fibre reinforced polymer. Construction and Building Materials. 2015. No. 77. Pp. 396–403.
8. Cooper, C., Turvey, G.J. Effects of joint geometry and bolt torque on the structural performance of single bolt tension joints in pultruded GFRP sheet material. Composite structures. 1995. Vol. 32. No. 1-4. Pp. 217–226.
9. Camanho, P.P., Matthews, F.L. Stress analysis and strength prediction of mechanically fastened joints in FRP: a review. Composites Part A: Applied Science and Manufacturing. 1997. Vol. 28. No. 6. Pp. 529–547.
10. Qureshi, J., Mottram, J.T. Behavior of pultruded beam-to-column joints using steel web cleats. Thin-Walled Structures. 2013. Vol. 73. Pp. 48–56.
11. Qureshi, J., Mottram, J.T. Response of beam-of-column web cleated joints for pultruded frames. Journal of Composites for Construction. 2014. Vol. 18. No. 2. Pp.11. URL: [http://ascelibrary.org/doi/abs/10.1061/\(ASCE\)CC.1943-5614.0000392](http://ascelibrary.org/doi/abs/10.1061/(ASCE)CC.1943-5614.0000392)
12. Qureshi, J., Mottram, J.T., Zafari, B. Robustness of simple joints in pultruded FRP frames. Structures. 2015. Vol. 3. Pp. 120–129.
13. Zinoviyev, V.S., Ovchinnikov, I.G. Vozmozhnost primeneniya kompozitnykh materialov pri izgotovlenii i montazhe peshekhodnykh mostov [The possible application of composite materials for manufacturing and installation of pedestrian bridges]. Novyye idei novogo veka: materialy mezhdunarodnoy nauchnoy konferentsii FAD TOGU. Khabarovsk: Izd-vo TGU, 2013. Vol. 2. Pp. 278–284.
14. Sorina, T.G., Safonov, A.A., Khayretdinov, A.Kh. Osobennosti primeneniya uglestekloplastika v pultruzionnykh kompozitnykh profilyakh dlya mostostroyeniya [Peculiarities of using carbon glass-reinforced plastic in pultrusion composite profiles for bridge engineering]. Problemy mashinostroyeniya i nadezhnosti mashin. 2010. No. 1. Pp. 58–62.
15. Fedorov, Yu.Yu., Vasilyev, S.V. Traversa dlya P-obraznykh opor liniy elektroperedach iz pultruzionnogo stekloplastika [Traverse for n-shaped poles power lines from pultruded fiberglass]. Innovatsii v nauke. 2017. No. 4(65). Pp. 42–45.
16. Kochunov, Yu.A. Primeneniye kompozitnykh materialov dlya izgotovleniya podderzhivayushchikh konstruksiy liniy prodolnogo elektrosnabzheniya [Application of composite materials for manufacturing of supporting structures of longitudinal power supply lines]. Transport Urala. 2014. No. 1(40). Pp. 76–80.
17. Mottram, J.T., Zheng, Y. State-of-the-art review on the design of beam-to-column for pultruded frames. Composite Structure. 1996. Vol. 35. No. 4. Pp. 387–401.
18. Coelho, A., Mottram, J.T. A review of the behavior and analysis of bolted connections and joints in pultruded fibre reinforced polymers. Materials and Design. 2015. Vol. 74. Pp. 86–107.
19. Smith, S.J., Parsons, I.D., Hjelmstad, K.D. An experimental study of the behavior of connections for pultruded GFRP I-beams and rectangular tubes. Composite structures. 1998. Vol. 42. No. 3. Pp. 281–290.
20. Nerilli, F., Marino, M., Vairo, G. A numerical failure analysis of multi-bolted joints in FRP laminates based on basalt fibers. XXIII Italian Group of Fracture Meeting, IGFXXIII. Procedia Engineering. 2015. Vol. 109. Pp. 492–506.
21. Lee, Y., Kim, S., Won, Y. Strength evaluation of bolt arrangement in PFRP bolted connection with 2 bolts. J. Korean Soc. Adv. Comp. Struc. 2014. Vol. 5. Pp. 17–22.
22. Chen, C., Hu, D., Liu, Q., Han, X. Evaluation on the interval values of tolerance fit for the composite bolted joint. Composite structures. 2018. Vol. 206. Pp. 628–636.
23. Rosales-Iriarte, F., Fellows, N.A., Durodola, J.F. Experimental evaluation of the effect of clamping force and hole clearance on carbon composites subjected to bearing versus bypass loading. Composite structures. 2011. Vol. 93. No. 3. Pp. 1096–1102.
24. Boscato, G., Casalegno, C., Russo, S., Mottram, J.T. Buckling of built-up columns of FRP C-sections. Journal of Composites for Construction. 2014. Vol. 18. No. 4. Pp. 11–23.
25. Liu, T. Stability behavior of pultruded glass-fiber reinforced polymer I-sections subject to flexure. Pittsburgh, 2017. 270 p.

Contacts:

Marat Salakhutdinov, lider-kazann@yandex.ru

Linur Gimranov, leenur@mail.ru

Ivan Kuznetsov, kuz377@mail.ru

Adel Fakhrutdinov, faxrutdinoff@yandex.ru

Lilia Nurgaleeva, nurgaleevalm@fiberpull.ru



DOI: 10.18720/MCE.96.2

Monitoring of the natural frequencies of Chirkey arch dam

A.V. Liseikin^{a*}, V.S. Seleznev^a, Z.A. Adilov^b

^a Seismological Division of Geophysical Survey of Russian Academy of Sciences, Novosibirsk, Russia

^b Dagestan Division of Geophysical Survey of Russian Academy of Sciences, Makhachkala, Russia

* E-mail: lexik1979@mail.ru

Keywords: arch dam, structural health monitoring, natural frequencies, normal modes, standing waves

Abstract. The article presents a method for monitoring the natural frequencies of HPP dams according to continuous seismic observations. The object of the research is the largest arched dam in Russia, the Chirkey HPP located in the Caucasus. If damaged, it could cause great loss of property and human life, but disasters can be minimized by using effective dam structural health monitoring. The study for changes in the natural frequencies of engineering structures is one of the most common methods of remote control over their structural health. However, the determination of values of natural frequencies of huge concrete dams is a very difficult procedure due to their have complex construction. Moreover, interpretation of changes in the natural frequencies values is difficult due to the significant influence of the water level in the reservoir. Consequently, at the initial stage, we performed a detailed study of the natural oscillations of the dam using the method of coherent restoration of the standing wave fields with the definition of both the natural frequencies of the structure and their modes. They were conducted twice at the minimum and maximum upstream level and for the first time highlighted the features of seasonal changes in the full field of standing waves. The normal modes were determined that are present in oscillations at different upstream levels and which frequencies can be detected continuously from the records of seismic equipment. The series of frequency changes during the year are calculated. For the first time we established that, frequency changes are by 5 to 11 days behind reservoir level changes and assumed that relaxation processes of the dam body and / or its base cause the delay after the upstream level changes. We calculated dependencies for predicting the frequency values from the reservoir level, taking into account the delay time. As a result, we proposed an approach for monitoring of the dam structural health based on a comparison of the observed natural frequencies with the predicted ones. The developed method can be applied to monitor the structural health of concrete dams of other HPPs.

1. Introduction

For control of the health of engineering structures, monitoring methods based on the analysis of changes in time of various parameters of the field of standing waves (primarily, natural frequencies) are widely used [1–10]. At the same time, variations of the field of standing waves can be related not only with the appearance of any defects in the structure, but also with other factors. For example, this may be a time-varying external load, without causing defects. In the case of hydroelectric dams, such a load, which is usually seasonally varying, is the water pressure from the reservoir [7–8, 11–13]. In heavy and complex structures, which include hydroelectric dams, the standing wave field has a complex structure, to determine which, it is necessary to perform measurements with high detail [14]. Therefore, to avoid misinterpretation, before conducting research on the monitoring of the state of structures based on changes in their natural frequencies, it is necessary, firstly, to determine reliably these frequencies and, secondly, to study thoroughly all the factors affecting them. As the occasion requires making immediate decisions a method for determining, the current values of the frequencies (near real time) should be developed.

Thus, the main objective of the study is to develop a method for continuous real-time monitoring of the natural frequencies of the Chirkey arched dam.

There are various ways to study the natural frequencies of structures. For example, based on the registration of oscillation under the influence of artificial sources of vibration type or explosions [11, 15–16], or under the influence of earthquakes [9].

Liseikin, A.V., Seleznev, V.S., Adilov, Z.A. Monitoring of the natural frequencies of Chirkey arch dam. Magazine of Civil Engineering. 2020. 96(4). Pp. 15–26. DOI: 10.18720/MCE.96.2



This work is licensed under a CC BY-NC 4.0

Methods with artificial sources, especially in the study of large structures, such as hydroelectric dams, are quite labor-intensive and high-cost, and therefore not common for solving problems of operational monitoring of the structural health.

Methods based on the registration of earthquakes, due to the inability to predict the time and place of their occurrence, are also unacceptable. Nevertheless, these methods are implemented and give some information about the health of the structures, albeit with low accuracy [9].

There are also ways to study the natural frequencies of structures, based on the registration of background microseismic vibrations. Their main advantage is that many sources of microseismic vibrations are used. These methods are based on the well-known fact that practically in any engineering structure, due to its limited volume, forms a set of standing waves when oscillations propagate [14]. It does not matter where the sources of these oscillations are. A number of authors, using this property of standing waves, determine the natural frequencies from the maxima of the spectra of microseismic vibrations recorded at several points of the structure [7, 8, 13, 17]. This method is quite simple to implement. But due to difficulties in constructing natural oscillation modes possible errors in the identification of each of the natural frequencies could occur. In addition, various noises from operating hydroelectric equipment can be superimposed on the valid signal. The situation is complicated by the fact that in the case of an unsuccessful arrangement of sensors in the field of standing wave nodes, their frequencies are almost impossible to determine [18].

There is a way to determine the current values of the natural frequencies of a structure using continuous recordings of seismic stations located in its vicinity. In work [19], it is shown that standing waves forming in the dam of the Sayano-Shushenskaya HPP are a source of waves that, propagating in the earth, are recorded by highly sensitive stations of the seismological network at distances of several kilometers. A technique has been developed to isolate such oscillations by averaging the amplitude spectra of seismic records with duration from several hours to several days. This method assumes that the natural frequencies of the object have already been identified.

In work [14], a method of coherent recovery of standing-wave fields was proposed, which makes it possible to isolate coherent in time and space oscillations – standing waves from the data of the registration of microseismic oscillations. Through the use of registration at the reference point, the implementation of measurements is carried out by a limited number of sensors on an arbitrarily dense network of observations. This makes it possible to construct detailed modes for each of the natural frequencies and eliminates the error in their identification.

The object of the research is the Chirkey dam. It is located in the Caucasus, in an area with increased seismic activity (9 points on the general seismic zoning map); it has the largest arch type dam in Russia, 232 m high and 338 m long. The designed head of the generators is 170 m, and seasons fluctuations of the reservoir level are almost 40 m. In accordance with the standards, the hydroelectric station is equipped with a system of continuous seismometrical and seismological observations, the characteristics of which are given in work [20]. In the literature, there are no data on studies of changes in the parameters of the natural oscillations of the dam.

This paper proposes a method for monitoring the natural frequencies of a HPP dam using continuous seismic observations at stations installed inside the dam and / or at a distance from it. This problem was solved as follows. At the initial stage, a detailed study of the natural oscillations of the dam was carried out by the method of coherent restoration of the standing wave fields with the definition of the natural frequencies and modes of the structure. These studies were carried out at different levels of reservoir filling in order to determine the features of seasonal changes in standing wave fields. Later, using continuous recordings from seismic stations, averaged amplitude spectra were calculated, which were used to determine the current values of the natural frequencies of the dam and to analyze their changes over time. Changes in frequency values that were not related to the appearance of structural defects were established. Further, in case of detection of anomalous deviations of the values of natural frequencies, it is possible to draw conclusions about the appearance of defects in the structure.

2. Methods

To study the natural oscillations of the dam, we used the method of coherent restoration of standing wave fields, which allows us to construct a detailed field of standing waves from microseismic oscillations recorded at various points of a building or structure and to determine the natural frequencies and modes of object oscillations. The study can be divided into two stages: the first is the measurement of oscillations on a detailed grid using the reference point and the second is the signal processing of the received data in order to obtain a one-time field of standing waves and determine of natural frequencies and modes.

The measurement of microseismic oscillations was performed using autonomous three-component seismic stations “Baikal-ASN” (own development of GS RAS). GS-20DX velocimeters were used as seismic receivers. The frequency range of recorded oscillations is 1–60 Hz, the sampling frequency is 200 Hz.

To equalize the amplitude-frequency response of seismic receivers in the low-frequency domain (1–10 Hz), the method of low-frequency deconvolution of digital recording of a short-period seismometer, well-proven in seismological studies, was used [21]. Registration was carried out by a series of consecutive measurements of oscillations by 5 units of equipment. The recording time of each measurement is 10 minutes. Data were obtained at 287 different points located on 10 profiles at different levels, passing either through the galleries inside the dam or the balconies (Fig. 1). At the level of 290 m, the profile is forced to be broken due to the impossibility of installing seismic sensors (penstocks pass in this place). Additionally, three sets of equipment were used at reference points. They did not change their position in the course of measuring oscillations in moving points. Points number 1 and number 2 were set due to the fact that it was obviously not known where in the dam the nodal lines would pass, and as it is known, if the point falls close to the natural oscillation node, then the coherence value will be lowered [14]. During the analysis of the coherence functions, it was found that the position of point number 2 is more suitable for subsequent use (the coherence values for the set of selected modes are higher and, accordingly, the conversion accuracy is higher). Point number 3 was established for the purpose of the subsequent implementation of the assessment of the seismic stability of the dam. The orientation of the devices was carried out in the following way: the X-channel is directed in the radial direction relative to the dam, Y in the tangential direction, Z in the vertical direction. The measurements were carried out twice - with close to the minimum and maximum filling levels of the reservoir in order to determine the features of seasonal changes in the parameters of the fields of standing waves in the body of the dam.

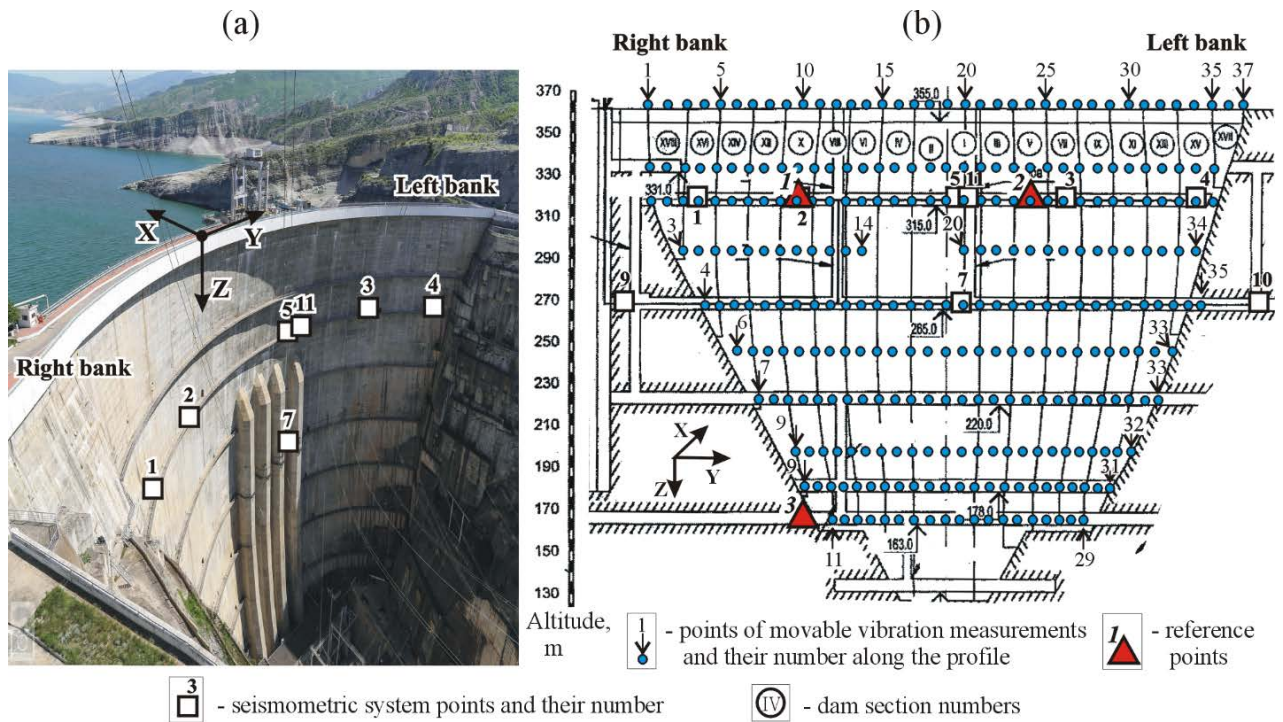


Figure 1. The appearance of the dam of the Chirkey HPP (a) and the scheme of seismic observations (b).

After registering according to the method described above, a set of continuous (10-minutes) multi-time records was obtained at $N = 287$ observation points. The task of digital processing was to bring time-varying seismic records to a single time, followed by the allocation of standing waves formed in the structure. For this, the method of calculating Wiener filters was used to recalculate the oscillations from the reference point to each of the N observation points, described in detail in work [14]. After receiving the filter set, at the final stage of processing, the oscillations recorded at the reference point were recalculated at each point on the structure. Below there are the basic formulas used for digital data processing.

The formula for calculating the Wiener filter, which provides the recalculation of oscillations from the reference point to the i -th, taking into account the splitting of the original record into disjoint time fragments, has the form:

$$h_i(\omega) = \frac{\sum_{j=1}^n \overline{F_{ij}}(\omega) \overline{F_{0j}}^*(\omega)}{\sum_{j=1}^n |\overline{F_{0j}}(\omega)|^2}, \tag{1}$$

where $h_i(\omega)$ is the frequency characteristic of the Wiener filter for recalculating the oscillations between the reference and i -th points, $i=1, \dots, N$; $\overline{F_{ij}}(\omega)$ and $\overline{F_{0j}}(\omega)$ - Fourier transforms of j -th fragments of simultaneous records in the i -th and reference points, respectively, and the superscript * means complex conjugation, n is the number of such fragments.

Formula (1) allows the calculation of the filter characteristics with an error that depends on the parameters of the registered implementation of the oscillations of the object being examined. Such parameters are: the sampling interval of the recorded oscillations with respect to time – Δt , the length of a single fragment, into which the recording of vibrations is divided – T , the number of fragments in the recording – n . The choice of the first two parameters is not difficult. The sampling interval is linked to the frequency range in which the oscillations of the object of research are studied – was chosen equal to 0.005 s. The length of a single fragment is related to the required resolution of the spectral analysis – $\Delta f = 1/T$. To survey complex objects that have a whole range of degrees of freedom and, accordingly, a whole series of resonant bandwidths in the frequency response, resolution is required, linked to the width of these resonant bandwidths and the frequency distances between them. Taking into account the experience of conducting such studies, the length of a single fragment was chosen to be 10 s, which corresponds to a resolution of 0.1 Hz. More difficult is the question of the number of fragments. The calculation by formula (1) is only a certain estimate of the filter characteristic, the error of which depends on the number of fragments n and the ratio of noise energy and useful signals, i.e., in fact, to what extent the change of oscillations from point to point is described by a linear system.

The expression for calculating the relative error of the amplitude characteristic of the filter (1) is:

$$\varepsilon(|h_{0i}(\omega)|) = \frac{\sqrt{1 - \gamma_{0i}^2(\omega)}}{|\gamma_{0i}(\omega)|\sqrt{2n}}, \quad (2)$$

where $\gamma^2(\omega)$ is the coherence function calculated by the formula:

$$\gamma^2(\omega) = \frac{\left| \sum_{j=1}^n \overline{F_i}(\omega) \overline{F_0}^*(\omega) \right|^2}{\sum_{j=1}^n |\overline{F_0}(\omega)|^2 \sum_{j=1}^n |\overline{F_i}(\omega)|^2} \quad (3)$$

In accordance with (2), with an increase in the number of fragments for calculating the characteristic of a filter that recalculates oscillations from the reference point of the object being inspected to i -th, any given error in constructing the filter can be achieved. In order to improve the performance of measurements, it is necessary to choose the optimal value of n (or record length) so that the results are accurate enough, but the measurements would be performed as quickly as possible. With a small number of fragments, even a small increase in their number provides a significant decrease in error. For large values of n , the decrease in error with an increase in the number of fragments slows down. High accuracy of oscillation recalculation is quickly achieved with large values of $\gamma^2(\omega)$. For cases with small values of the coherence function, a large number of fragments in simultaneous recording is required. In our case, the values of $\gamma^2(\omega)$ were 0.64–0.81, and $n = 60$ (for 10-minute records, a single fragment with a length of 10 s), the relative error of the amplitude characteristic was 0.02–0.04.

At the final stage, after the construction of a set of filters using formula (1), the oscillations recorded at the reference point were recalculated at each point on the structure. As a result, a full field of coherent oscillations is obtained, analyzing which standing waves are distinguished – by the characteristic space-stable arrangements of alternating maxima (antinodes) and minima (nodes) of amplitude. For each of the standing waves, the natural frequencies of the structure are determined.

In order to further monitor the natural frequencies of the structure, averaged amplitude spectra are constructed from the records of microseismic oscillations. The values of the frequencies corresponding to the previously defined natural frequencies are determined by the local maxima of the amplitudes. Nevertheless, the frequencies are determined at points located in the antinodes of standing waves, in accordance with the method¹⁸. Further, the factors affecting changes in frequencies, but not related to changes in the structural health of the dam, are examined. For example, the changing level of the reservoir. Exclusion of such factors will increase the degree of reliability of the results of health monitoring of the structure.

3. Results and Discussion

The data in Fig. 2, show changes in the sets of amplitude spectra of coherent oscillations, according to the results of two experimental works – with maximum and minimum upstream level. It can be seen from the figure that in both cases the overwhelming part of the oscillation energy is concentrated on the X-component, which is directed radially (across the dam). It is noticeable that the X-component of the oscillations has both a general and a difference. For example, oscillations of the 1st, 2nd, and 4th modes (the mode number corresponds to the number of observed antinodes along the profile), although with different frequencies and intensities, are repeated at the maximum and minimum filling levels of the reservoir. At frequencies between the 2nd and 4th modes, another stable oscillation is observed, having one antinode, which can be classified as the secondary first mode. That is, in this case, the two first modes are observed with different oscillation frequencies. This phenomenon is due to the fact that the first and secondary standing waves are formed in objects that combine different sections of the dam. The same happens with the higher modes of oscillations, creating a very complex picture, which can only be understood when carrying out more detailed work. With these observations, the remaining oscillations are much less pronounced and do not repeat in shape with different modes of filling the reservoir. It can be said that the fields of standing waves at frequencies not equivalent to the two 1st, 2nd and 4th modes are completely different. Such a difference, in our opinion, can be caused by a significant change in the stress-strain state of the dam with a change in upstream level.

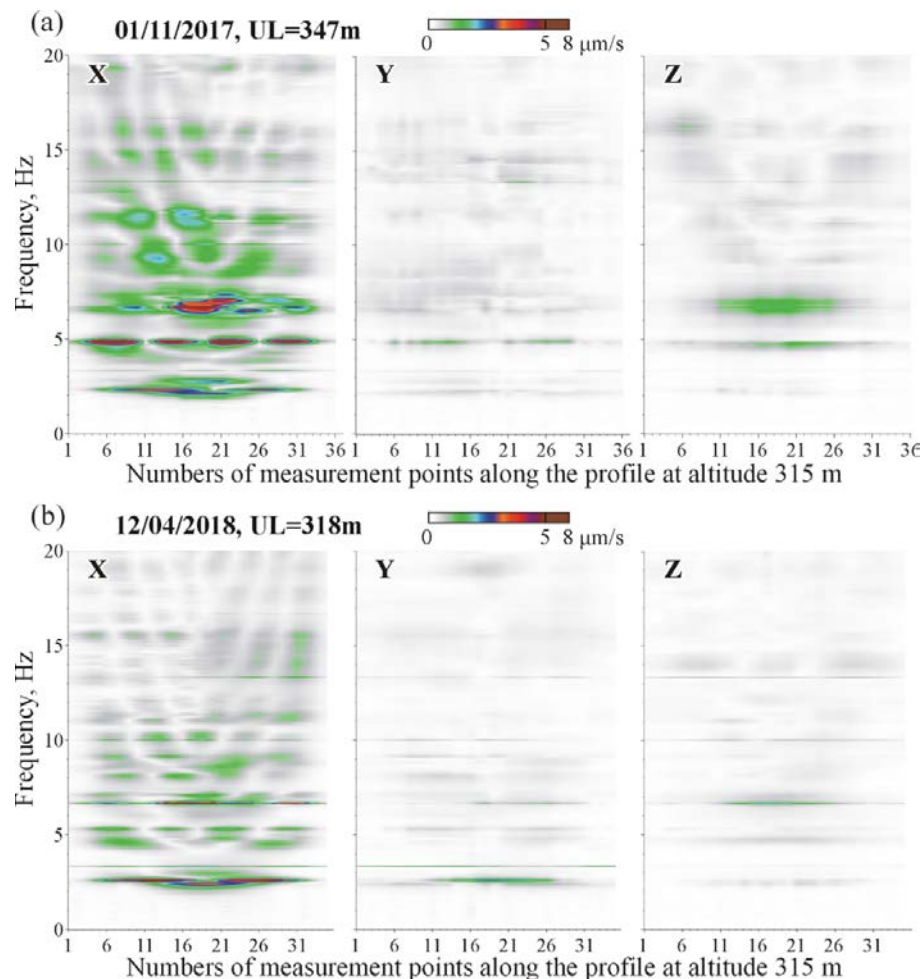
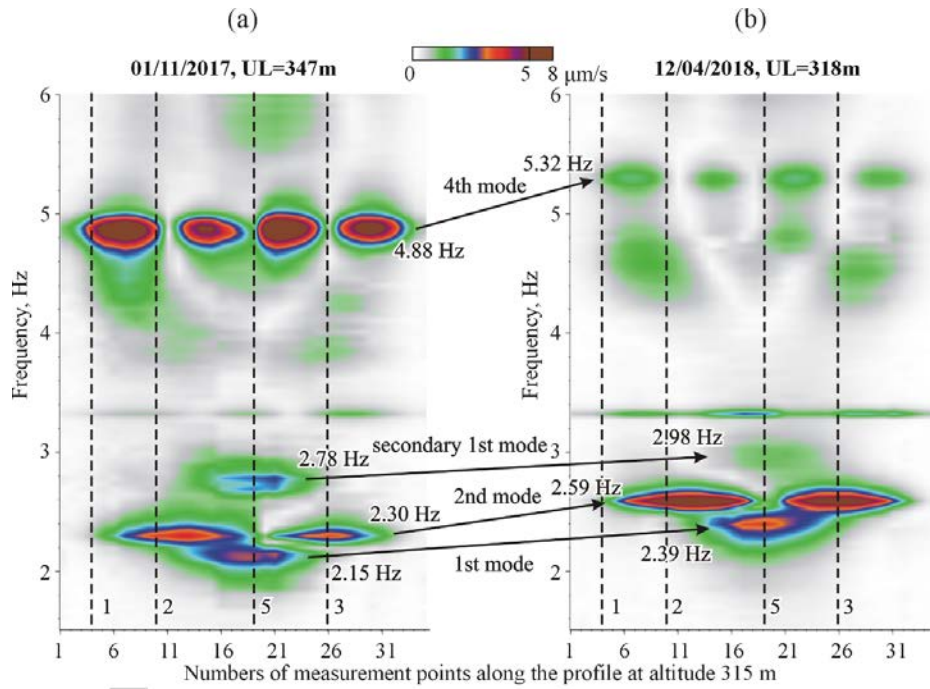


Figure 2. Sets of amplitude spectra of coherent oscillations of the dam along the profile at altitude 315 m at the maximum (a) and minimum (b) upstream level (UL).

Fig. 3 shows a more detailed image of changes in the low-frequency part of the spectra of transverse oscillations of the dam. It is seen that with the reduction of the upstream level (from 347 m to 318 m), the frequencies of the two 1st, 2nd and 4th modes increased by 0.20-0.45 Hz from the values of 2.15 Hz, 2.78 Hz, 2.30 Hz and 4.88 Hz to 2.39 Hz, 2.98 Hz, 2.59 Hz and 5.32 Hz, respectively. Fig. 4 shows the schematic images of the two 1st, 2nd, and 4th modes of natural oscillations of the dam of the Chirkey HPP, it is clear that at the maximum and minimum upstream level, they practically do not change, but only the frequencies change. Only some distortions of the form of the 1st mode are noticeable, which, in our opinion, are associated with a superposition of the oscillations of the 2nd mode, in frequency close to the 1st. This is possible due to the low quality factor of the oscillations.



 - the position of the seismic system points with respect to the profile

Figure 3. Changes in the amplitude spectra of transverse oscillations of the dam at the maximum (a) and minimum (b) levels of the reservoir (UL).

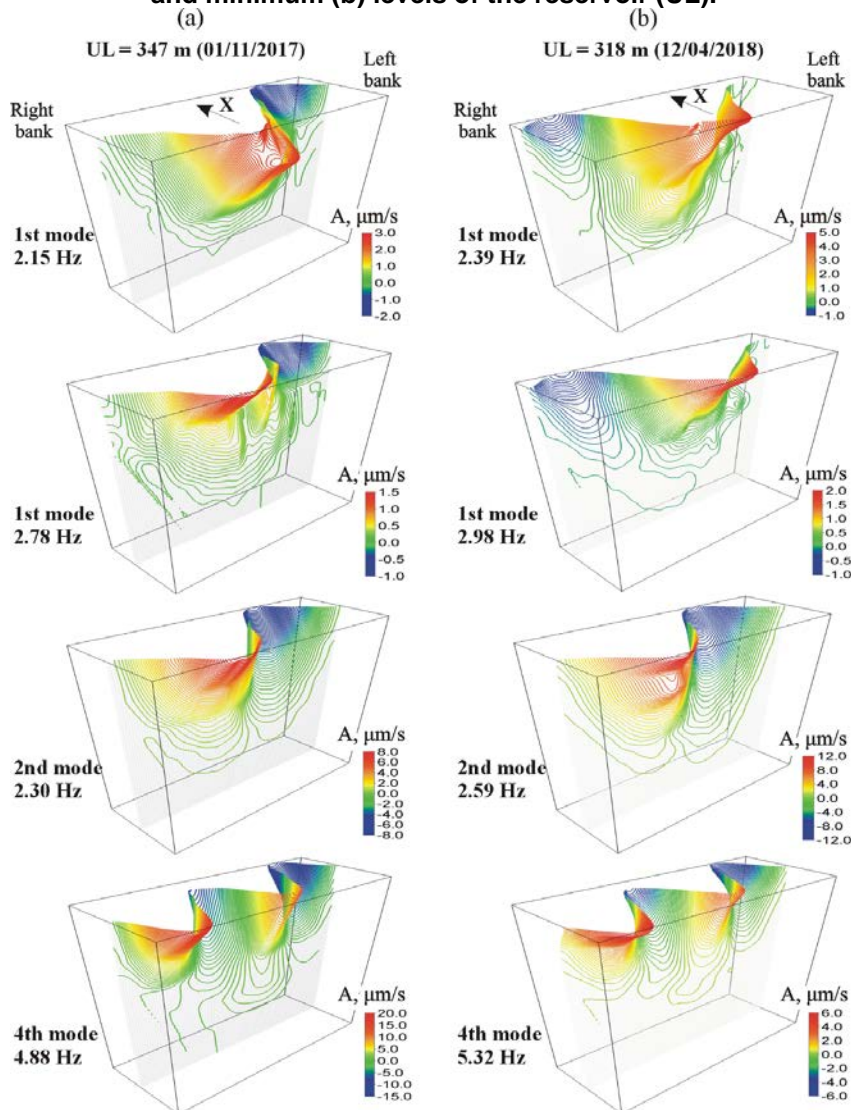


Figure 4. Schematic images of two 1st, 2nd and 4th modes of radial oscillations of the dam of the Chirkey HPP at high (a) and low (b) levels of the reservoir.

Due to the fact that the oscillations of only four modes (two 1st, 2nd and 4th) repeat with a high degree of reliability both at the minimum and at the maximum upstream level, these modes can be used for continuous monitoring of the structural health of the Chirkey dam. The remaining natural oscillations, of course, also carry information about the state of the dam. But, due to changes in the field of standing waves when changing the upstream level, it is expected that these oscillations will be observed only in limited time intervals.

The foregoing method of studying the natural oscillations of a dam compares favorably with methods using artificial sources. However, it should be understood that this method is not suitable for solving problems of continuous and operational monitoring of dam condition due to time spent on research. For example, it takes 2 days to field experiment and 1-2 days to perform digital data processing and analysis of the results, without taking into account the delivery of equipment and personnel. Therefore, for the purposes of further research, data of continuous recording of oscillations of the existing seismometric system in the dam body was used. The current frequency values were determined from the maxima of the amplitude spectra of seismic noise recordings at points located near the antinodes of each of the modes.

Consider the features of the recorded oscillations on a seismometric system, the location of the points of which was shown in Fig. 1. Fig. 5 shows the averaged amplitude spectra of the records of oscillations on the X-component, obtained in points 3 and 5 for the period of observations from 10/01/2015 to 12/28/2016. The method of their construction consists in calculating for each day of observations of sets of amplitude spectra for the fragments, each 100 s long, followed by averaging. Despite the fact that in this example, heterogeneous data is presented (registered values of accelerations and velocities), it is seen from the figure that the fields of oscillations at two different points are fundamentally different. This is caused by the different position of the points relative to the nodes and antinodes of the standing waves. For example, observation point No. 5 is located in the antinodes of the two first modes (Fig. 3) and simultaneously at the node of the second mode, therefore, only two vibration maxima are traced in the low-frequency (2–3 Hz) part of the spectrum. Observation point No. 3 is located in the antinodes of the second mode, therefore only one maximum of oscillations is traced. More clearly it can be seen from Fig. 6, which shows the averaged spectra with amplitudes normalized in a narrow frequency range. It can be seen that in point No. 5 for the entire observation period, oscillation maxima are observed with frequencies corresponding to the two first modes, and in point No. 3 – corresponding to the second mode. It is noticeable that there is a close correlation between changes in the level of the reservoir (upstream level) and frequencies - with increasing upstream level frequency decreases. It is more difficult to interpret changes in the frequency of the 4th mode. The design of the position of the points of the seismometric system of the Chirkey dam was carried out without taking into account the spatial position of the nodes and antinodes. Unfortunately, all available observation points were concentrated near the nodes of the 4th mode (see Fig. 3). This made it impossible to trace continuously changes in the frequencies of this mode (Fig. 6). In 2019, it is planned to upgrade the seismometric system in the dam of the Chirkey HPP with the addition of observation points and, if we take into account the spatial position of the 4th mode antinodes, it will be possible to investigate frequency changes of it.

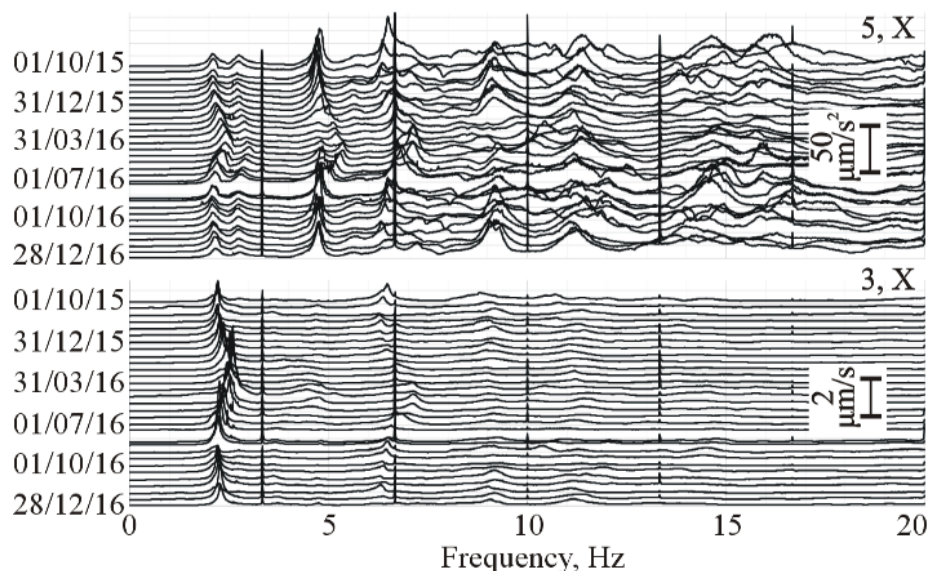


Figure 5. Averaged amplitude spectra of daily records of radial oscillations of the dam at two observation points.

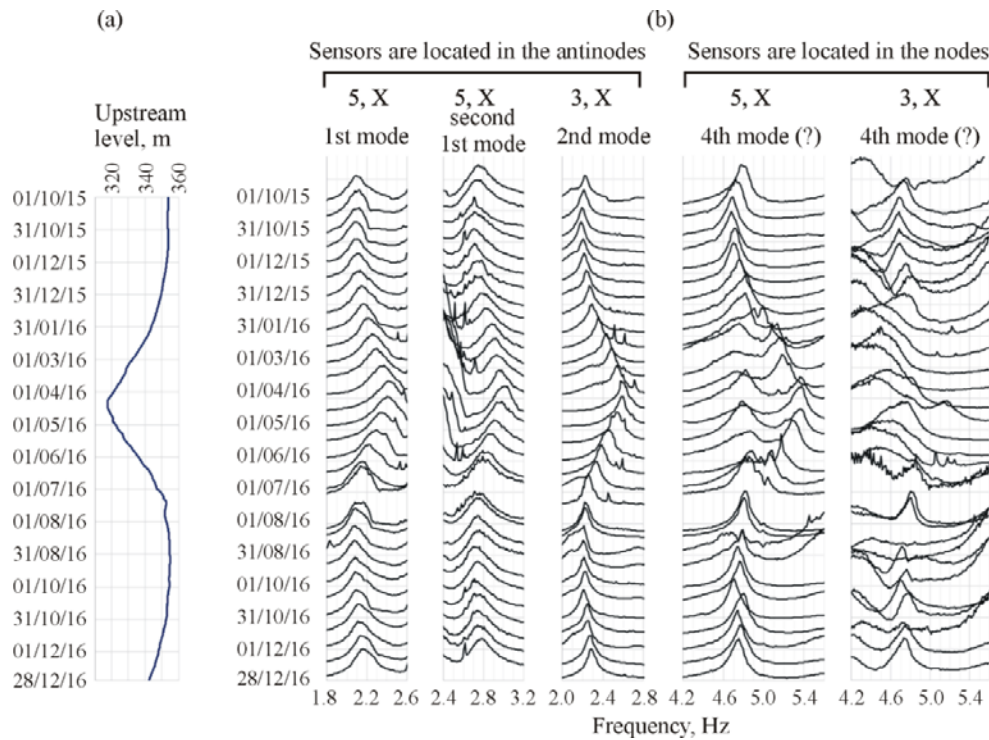


Figure 6. Changes of the upstream level of the Chirkey reservoir (a) and the normalized average amplitude spectra of daily records of the radial oscillations of the dam at two observation points (b).

Thus, the existing system of seismometric observations in the dam of the Chirkey HPP allows tracking continuous changes in the frequencies of the two first and second modes. Let us consider in more detail how these frequencies change over time and depending on the upstream level. Fig. 7 shows the graphs of these parameters for 2016. Given the variation in frequency values relative to the trend, it is possible to determine the error of their determination – it is about 0.01–0.02 Hz. In general, with the growth of the upstream level, the frequencies decrease. Such a dependence is characteristic of hydroelectric dams [7–8, 11–13] and is explained by researchers as the change in the added mass of water (the larger the mass, the lower the natural frequency). We then considered what other factors, in addition to the added mass, can affect the values of frequencies. To check this, we constructed dependencies between the values of frequencies and the upstream level (Fig. 8).

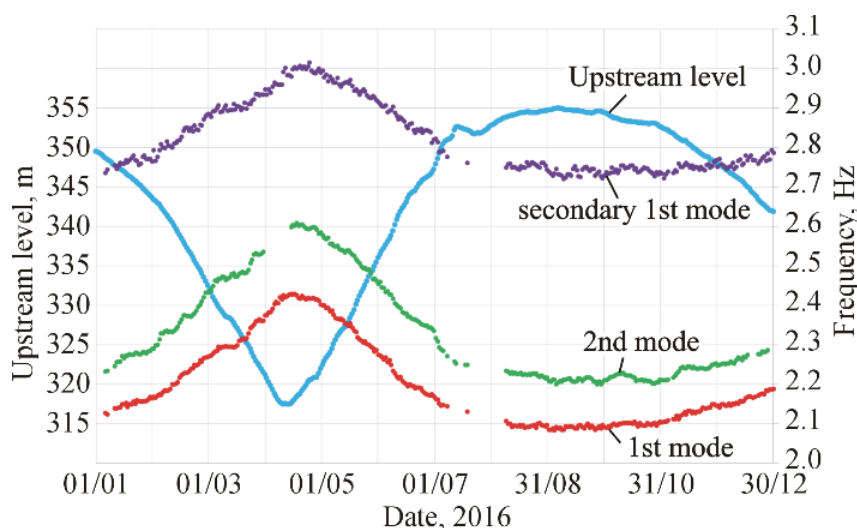


Figure 7. The changes of the upstream level of the Chirkey reservoir and of the values of natural frequencies of the dam.

Fig. 8a shows that the dependence between the values of frequencies and the upstream level is ambiguous. Graphs have differences depending on the mode of the reservoir – its filling or drawdown. In general, there is a lag in frequency changes from the course of changes in the upstream level. This leads to the formation of loops on graphs similar to hysteresis loops. It can be assumed that such a delay is due to the fact that the dam does not instantly react to changes in the level of the reservoir, but gradually relaxes. If this is not taken into account, then when monitoring the natural frequencies of the dam, an incorrect conclusion can be made about its condition.

The following study [22] can be an additional confirmation of the relaxation hypothesis. The results of studies of the relationship between seasonal changes in the water level in the reservoir and variations in the apparent electrical resistance of a rock mass inside a well located on the right bank near the dam are presented. The fact of the delay of the apparent resistance from the water level in the reservoir, which is 12 days, is established. One of the reasons for this delay, according to the authors of the study, is associated with a lag in the deformation of rocks from changes in the upstream level.

To estimate the relaxation time, we introduced a time shift between the series of changes in the upstream level and frequency values (Fig. 8b). It can be seen that after a shift of 5, 7 and 11 days for each of the three natural frequencies, the dependencies become more simple and unambiguous. They can be approximately approached by linear functions. Thus, by introducing a time shift, we took into account the relaxation time of the dam.

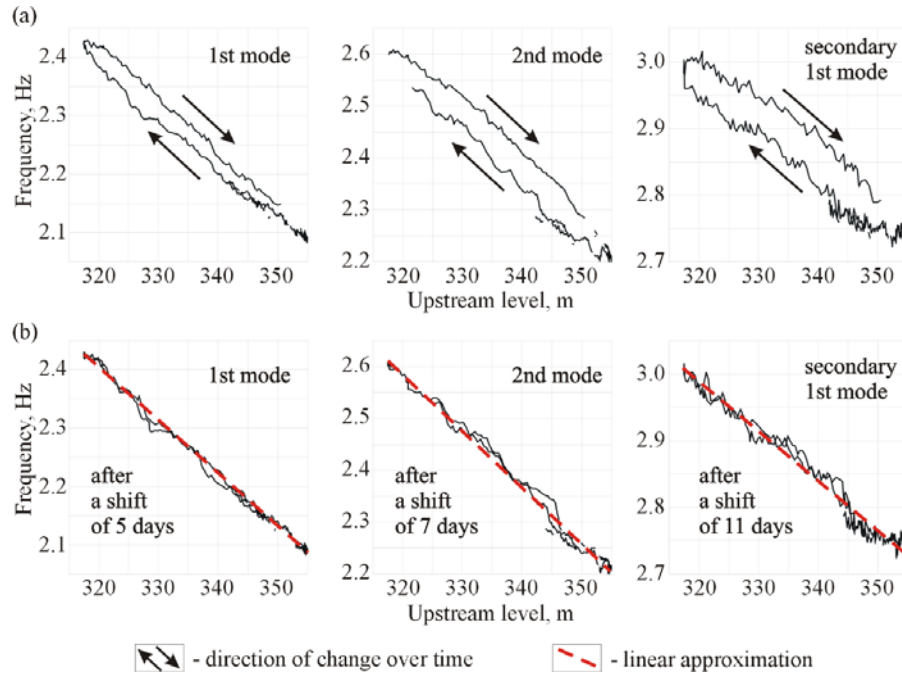


Figure 8. The dependencies of the natural frequencies of the dam on the upstream level for 2016: (a) one-time dependencies and (b) dependencies after the time shift.

As noted above, the natural frequencies of large structures can be determined from records of seismic stations located at some distance from them. At a distance of 5.5 km from the Chirkey dam, the Dubki seismic station (DBKG, Fig. 9a) is located. We tried to determine what information can be gained from the continuous records of this seismic station. For this purpose, a technique for determining the natural frequencies of structures from records of remote seismic stations was used. The analysis of the seismograms showed that from the records of microseismic vibrations on the seismic station, with a length of about 1 day, using the method of accumulation of spectra, it is possible to determine the frequencies of the first mode. To assess the reliability of such determinations, the obtained values were compared with the values determined from the vibration spectra recorded by the seismic system located in the dam body. As can be seen from fig. 9b, where the half-year series of changes in upstream level and frequency values of the 1st mode, defined in different ways, are presented, the latter is set with an accuracy of 0.03 Hz. Thus, if data on the vibrations of the body of the dam are absent then records of the Dubki seismic station can be used for monitoring purposes. However, it should be noted that this seismic station is located on the territory of the village of the same name, and at a distance of 5.5 km from the hydroelectric power station. Therefore, all sorts of interference complicate the records of the useful signal. Because of this, it is possible to determine the frequency of only the 1st mode with an error approximately twice as large. Therefore, records of the Dubki seismic station should be used only in exceptional cases. For example, in case of failure of the recording equipment located in the dam.

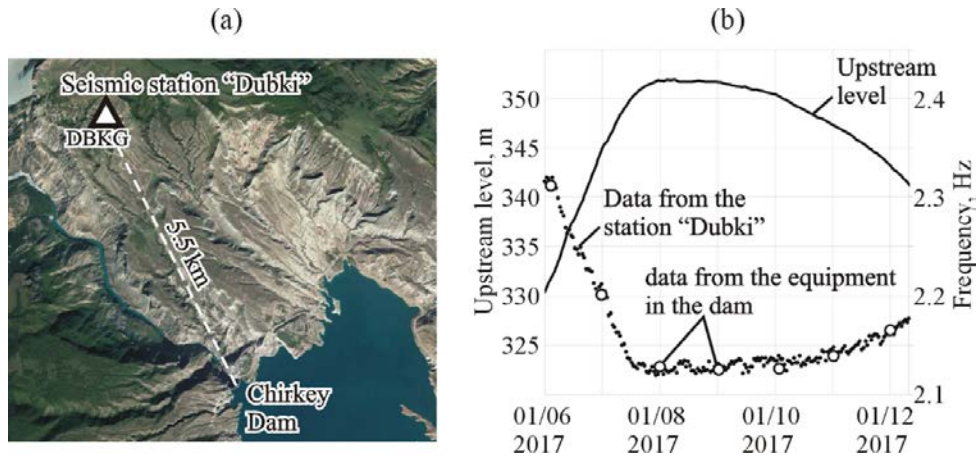


Fig. 9. Position of the Dubki seismic station (a) and changes in the frequencies of the 1st mode and the upstream level (b).

In order to develop a method for monitoring the natural frequencies of the dam, we approximated their dependence on the current values of the upstream level. For this, simple dependencies of the form were used:

$$f(t) = aH(t - \tau) + b, \quad (4)$$

where $f(t)$ is the approximated value of the natural frequency at time t , a and b are the coefficients of the approximation by a linear function, τ is the time shift that compensates for the delay in frequency changes relative to the changes in upstream level – $H(t)$. The approximation coefficients were determined by the least squares method according to the data presented in Fig. 8b. In addition, we calculated the value of the standard deviation σ of the experimental data with respect to linear regression. The results of determining these parameters are given in Table 1.

Table 1. The parameters of the approximation of the dependences of the natural frequencies from the upstream level according to the data for 2016.

Mode	a (Hz/m*10 ³)	b (Hz)	τ (days)	σ (Hz)
1st	-8.996	5.279	5	0.008
2nd	-10.962	6.094	7	0.014
Secondary 1st	-7.285	5.317	11	0.014

It is proposed to monitor the natural frequencies of the dam as follows. First of all, the current frequency values of the two first and second modes are determined from the averaged spectra of seismic records at points located near the antinodes. Taking into account the data on the level of the reservoir, according to the formula (4) and with the parameters given in Table. 1, the predicted values of the natural frequencies are calculated. The experimental and predicted values of frequencies are compared. If the observed frequencies exceed the predicted ones by more than 3σ (a “three-sigma” rule is used), it is concluded that the technical condition of the dam has changed and there is need to establish the reasons for these changes.

An example implementation of the method is shown in Fig. 10, which presents the predicted values of the natural frequencies from the upstream level and the data of their experimental determination. The figure shows that the observed values are located within the confidence intervals. This means that in 2017 the technical condition of the dam remained stable (the same as in 2016).

The approaches presented in the article can be used on other arched and concrete dams of hydroelectric power stations. Other researchers are also developing approaches to monitoring the natural frequencies of dams for structural health monitoring of dam and damage detection. However, this technique is still new and not widely used. The main reason, in our opinion, is associated with large errors in determining the frequencies and difficulties in interpreting their changes, which are more dependent on changes in the reservoir water level. All this leads to a low degree of reliability in the research results.

Most of the errors can be eliminated by studying the natural oscillations of dams using very dense observation systems. The method of coherent reconstruction of standing wave fields, used in the work, allows

such studies to be performed with high accuracy. Due to the possibility of implementing observations with a small amount of recording equipment, the technique is quite technologically advanced.

Some researchers took into account the effect of the reservoir water level by introducing a corrective function that depends only of the upstream level. In our study, we found that the natural frequency values are affected not only by seasonal fluctuations in the water level, but also by additional factors associated with relaxation processes in the dam or its foundation. These processes lead to the fact that the dependences between the reservoir water level and frequencies take the form of loops similar to hysteresis loops. Therefore, to consider this effect, we propose introducing an additional parameter into the correction function that describes the delay in frequency changes relative to changes in water level. Perhaps this effect also exists for other large hydroelectric dams. However, as far as we know, other researchers have not yet studied it.

It should be noted that changes in the structural health, for example, associated with the aging of concrete or with changes in the properties of the dam foundation, are quite long in time. Therefore, to identify such changes may take years or even decades of experimental observations.

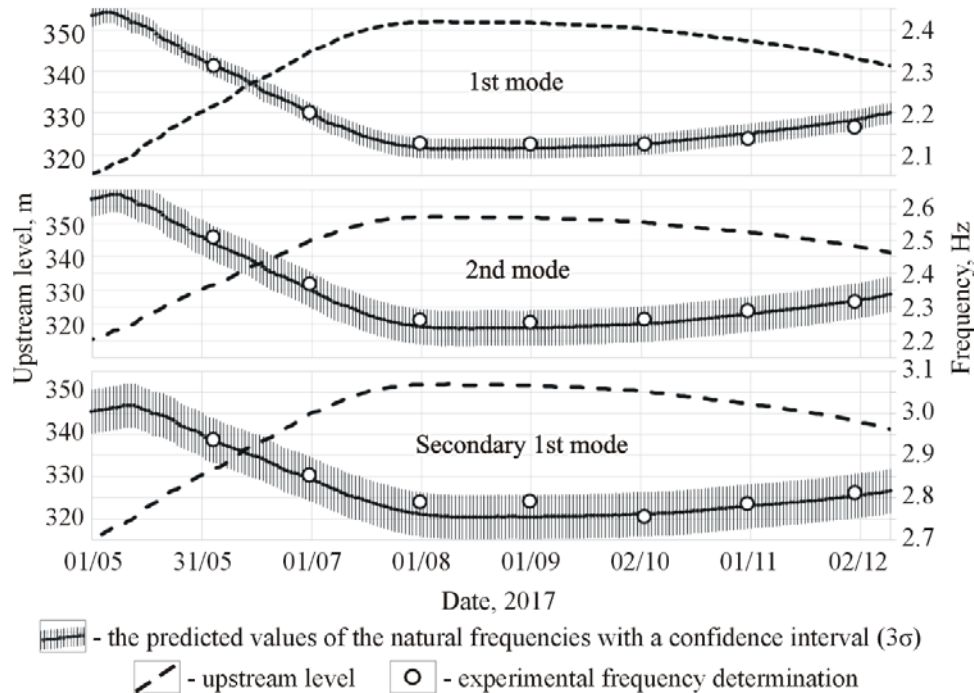


Figure 10. An example of the implementation of the method of monitoring the natural frequencies of the dam of the Chirkey hydroelectric power station.

4. Conclusions

1. Detailed studies of the Chirkey HPP dam were performed using the method of coherent restoration of standing wave fields at the maximum and minimum filling levels of the reservoir with the definition of natural frequencies and modes.

2. Our research has determined that the total field of standing waves changes when the upstream level changes, and two 1st, 2nd and 4th modes remain unchanged, the frequencies of which, in general, decrease with increasing reservoir level. These modes can be used for continuous monitoring of the structural health of the dam by periodically determine the frequency values from the records of seismic equipment. The points of the existing seismometric system are located near the 4-mode nodes, which do not allow to reliably determining the values of its frequencies.

3. It was determined that there are additional factors leading to the hysteresis effect in the dependence between the upstream level and natural frequencies, presumably related to relaxation processes in the dam body and / or in the dam-base system after changing the reservoir level. The time of such relaxation is from 5 to 11 days.

4. A method has been developed for monitoring the structural health of the dam, based on a comparison of the observed frequencies with the predicted ones. The latter are determined by linear dependencies on the upstream level taking into account the time shift associated with relaxation processes.

5. Acknowledgments

The authors would like to thank the staff of RusHydro and personally A. M. Kurahmaev for assistance in conducting experiments and for providing records from the seismometric system in the dam.

References

1. Yang, Z., Le, Wang. Structural Damage Detection by Changes in Natural Frequencies. *Journal of intelligent material systems and structures*. 2010. 21(3). Pp. 309–319. DOI: 10.1177/1045389X09350332
2. Belostotsky, A.M., Akimov, P.A., Negrozov, O.A., Petryashev, N.O., Petryashev, S.O. Sherbina, S.V., Kalichava, D.K., Kaytukov, T.B. Adaptive finite-element models in structural health monitoring systems. *Magazine of Civil Engineering*. 2018. 78(2). Pp. 169–178. DOI: 10.18720/MCE.78.14
3. Devriendt, S., Weijtjens, W., El-Kafafy, M., De Sitter, G. Monitoring resonant frequencies and damping values of an offshore wind turbine in parked conditions. *IET Renewable Power Generation*. 2014. 8(4). Pp. 433–441. DOI: 10.1049/iet-rpg.2013.0229
4. Ercolani, G.D., Felix, D.H., Ortega, N.F. Crack detection in prestressed concrete structures by measuring their natural frequencies. *Journal of Civil Structural Health Monitoring*. 2018. 8(4). Pp. 661–671. DOI: 10.1007/s13349-018-0295-2
5. Jin, S.-S., Jung, H.-J. Vibration-based damage detection using online learning algorithm for output-only structural health monitoring. *Structural Health Monitoring*. 2018. 17(4). Pp. 727–746. DOI: 10.1177/1475921717717310
6. Pan, J., Zhang, Z., Wu, J., Ramakrishnan, K.R., Singh, H.K. A novel method of vibration modes selection for improving accuracy of frequency-based damage detection. *Composites Part B: Engineering*. 2019. 159(15). Pp. 437–446. DOI: 10.1016/j.compositesb.2018.08.134
7. Bukenya P., Moyo P., Oosthuizen C. Long Term Ambient Vibration Monitoring of Roode Elsberg Dam – Initial Results. *International symposium on “Dams in global environmental challenges”*. Bali, Indonesia, 2014. No. 500.
8. Darbre, G.R., De Smet, C.A.M., Kraemer, C. Natural frequencies measured from ambient vibration response of the arch dam of Mauvoisin. *Earthquake Engineering and Structural Dynamics*. 2000. 29(5). Pp. 577–586. DOI: 10.1002/(SICI)1096-9845(200005)29:5<577::AID-EQE924>3.0.CO;2-P
9. Weng, J.H., Loh, C.H. Structural health monitoring of arch dam from dynamic measurements. *12th Biennial International Conference on Engineering, Construction, and Operations in Challenging Environments; and Fourth NASA/ARO/ASCE Workshop on Granular Materials in Lunar and Martian Exploration*. 2010. Pp. 2518–2534. DOI: 10.1061/41096(366)235
10. Loh, C.H. Sensing solutions for assessing and monitoring dams. *Sensor Technologies for Civil Infrastructures*. 2014. 1. Pp. 275–308. DOI: 10.1533/9781782422433.2.275
11. Proulx J., Paultre P., Rheault J., and Robert Y. An experimental investigation of water level effects on the dynamic behaviour of a large arch dam. *Earthquake Engineering and Structural Dynamics*. 2001. 30(8). Pp. 1147–1166. DOI: 10.1002/eqe.55
12. Pereira, S., Magalhães, F., Gomes, J.P., Cunha, Á., Lemos, J.V. Dynamic monitoring of a concrete arch dam during the first filling of the reservoir. *Engineering Structures*. 2018. 174(1). Pp. 548–560. DOI: 10.1016/j.engstruct.2018.07.076
13. Egorov A.Y., Kostylev V.S., Sarantsev M.I. Determining the natural frequencies of the dam at the Sayano-Shushenskaya hydroelectric power plant based on data from a seismometer system and computations. *Power Technology and Engineering*. 2017. 50(5). Pp. 506–510. DOI: 10.1007/s10749-017-0740-0
14. Emanov, A.F., Seleznev, V.S., Bakh, A.A., Gritsenko, S.A., Danilov, I.A., Kuz'menko, A.P., Saburov, V.S., Tat'kov, G.I. Standing waves in engineering seismology. *Geologiya i Geofizika*. 2002. 43(2). Pp. 192–207.
15. Loh, C.-H., Wu, T.-C. System identification of Fei-Tsui arch dam from forced vibration and seismic response data. *Journal of Earthquake Engineering*. 2000. 4(4). Pp. 511–537. DOI: 10.1080/13632460009350381
16. Mendes, P., Oliveira Costa, C., Almeida Garrett, J., Oliveira, S. Development of monitoring system to Cabril dam with operational modal analysis. *The Proceedings of the 2nd Experimental Vibration Analysis for Civil Engineering Structures (EVACES)*. Porto, 2007.
17. Sevim, B., Bayraktar, A., Altunisk, A.C. Finite element model calibration of Berke arch dam using operational modal testing. *Journal of Vibration and Control*. 2011. 17(7). Pp. 1065–1079 (2011). DOI: 10.1177/1077546310377912
18. Seleznev V.S., Liseikin A.V., Alzhanov R.Sh., Gromyko P.V. Sposob organizatsii nepreryvnogo seysmometricheskogo monitoringa inzhenernykh sooruzheniy i ustroystvo dlya yego osushchestvleniya [The method of organizing continuous seismometric monitoring of engineering structures and device for its implementation]. Patent Russia. No. 2546056, 2013. (rus)
19. Seleznev, V.S., Liseikin, A.V., Bryksin, A.A., Gromyko, P.V. What caused the accident at the Sayano-Shushenskaya hydroelectric power plant (SSHP): A seismologist's point of view. *Seismological Research Letters*. 2014. 85(4). Pp. 817–824. DOI: 10.1785/0220130163
20. Antonovskaya, G.N., Kapustian, N.K., Moshkunov, A.I., Danilov, A.V., Moshkunov, K.A. New seismic array solution for earthquake observations and hydropower plant health monitoring. *Journal of Seismology*. 2017. 21(5). Pp. 1039–1053. DOI: 10.1007/s10950-017-9650-8
21. Dergach, P.A., Tubanov, Ts.A., Yushin, V.I., Duchkov, A.A. Features in software implementation of low-frequency deconvolution algorithms. *Seismic Instruments*. 2019. 55(3). Pp. 345–352. DOI: 10.3103/S0747923919030046
22. Idarmachev I.Sh., Deshcherevskiy A.V., Idarmachev Sh.G. Otsenka svyazi mezhdru izmeneniyami urovnya vody v Chirkeyskom vodokhranilishche i elektricheskim soprotivleniyem porod v oblasti pravoberezhya plotiny GES [Assessment of the connection between changes in the level of water in the Chirkei water reservoir and electric resistance of rocks in the right-course of the weather plant]. *Gidrotekhnicheskoye stroitelstvo*. 2019. No. 3. Pp. 25–31. (rus)

Contacts:

Aleksei Liseikin, lexik1979@mail.ru

Victor Seleznev, svs0428@mail.ru

Zarahman Adilov, adilov79@mail.ru



DOI: 10.18720/MCE.96.3

Building energy modeling using hourly infiltration rate

I.Yu. Bilous*, V.I. Deshko, I.O. Sukhodub

National Technical University of Ukraine “Igor Sikorsky Kyiv Polytechnic Institute”, Kyiv, Ukraine

* E-mail: bilouys_inna@ukr.net

Keywords: buildings, energy efficiency, ventilation, air exchange rate, temperature, heating

Abstract. In Eastern Europe countries, including Ukraine, a significant part of the buildings belongs to the mass development of the 80s, which are characterized by a low level of energy efficiency. For such countries with sharply continental climates, heating costs prevail to a large extent. Improved thermal protection forces more attention to be paid to heat losses with ventilation. The distribution of air exchange between individual rooms is difficult to determine, especially due to natural ventilation. The work is devoted to considering the conditions of natural convection and determining the effect on the energy consumption of a building. The article considers the advanced ASHRAE technique for calculating natural air exchange. The influence of the temperature and wind characteristics of the outdoor air on the natural component of the air exchange rate at the different locations of the representative rooms of an 8-story building is analyzed. The value of the air exchange rate for typical conditions of Kiev does not exceed 0.25 h⁻¹, 0.65 h⁻¹ and 0.4 h⁻¹ for two-chamber and single-chamber double-glazed windows, triple glazing in wooden double binders, respectively. On the first floors, air exchange is associated with air infiltration, and on the last floors there is exfiltration, which must be taken into account when dynamically modeling the energy characteristics of a building. The example is with additional mechanical ventilation to maintain a comfortable environment. 5R1C dynamic grid models were created to study the energy performance of the building. The estimate of additional heating costs due to infiltration is 23 % for the North and 43 % for the South orientation of rooms with two-chamber energy-saving windows. It has been established that in dynamics, the energy consumption of a building with normative air exchange and the calculated value of the *natural component differs by 50–75 %*, which is a possible level of savings under actual air exchange conditions in comparison with standard ones. This savings can be reduced by increasing air exchange during busy hours, for example, due to additional aeration.

1. Introduction

HVAC systems are designed to maintain the thermal comfort and quality of the indoor climate. The HVAC systems usually have a large percentage of the total energy cost in the building. In developed countries this figure can be about 40%, for post-Soviet countries this figure is over 40 %. [1] Considering global trends aimed at reducing energy consumption and greenhouse gas emissions, software for modeling energy processes in a building is used to deepen the analysis of energy consumption, allowing to consider different design and operation options [2, 3].

In the European area of the post-Soviet countries, including Ukraine, a large part of buildings belongs to the typical construction of the 80-ies, which is characterized by low energy efficiency. The energy performance of these buildings is influenced by the thermophysical properties of the envelope, geometry, solar heat gains and additional internal heat gains, air exchange rate and operating conditions. Effect of innovative energy-saving measures on building envelope and heat sources is investigated in detail in papers [4, 5]. One of the most influential parameters is the air exchange rate [6, 7]. Energy need calculations based on dynamic modeling are carried out using such software products as EnergyPlus (37 %), TRNSYS (35 %), DOE-2 (16 %) and others [8].

For buildings of 70–80's typical development in the post-Soviet countries the low level of thermal insulation properties of building enclosures is typical. For the proper functioning of such buildings, the significant part of energy costs is used for heating (for Eastern European countries heating period lasts for about six months). The trends of the last decades are aimed at improving the thermal insulation properties of



building enclosures. For instance, according to the standard of Ukraine [9], with regard to the recommendations of the energy saving measures implementation priority, the main attention is paid to the measures for thermal renovation of the building envelope and heating system regulation. After the introduction of energy saving measures (the first stage), the ventilation component of heat loads in residential and commercial buildings can range from 25 to 50% [9]. In order to ensure proper working environment from the air exchange point of view, the specified air exchange rate is regulated in the standards. In buildings, the air exchange rate is provided in two ways: naturally and mechanically. In most of the old Soviet buildings of typical construction mechanical ventilation is not provided or is not working.

For buildings in Eastern Europe after thermo-modernization the component of ventilation losses significantly increases in the overall energy balance of building losses. At the same time, improving the thermal performance of windows results in a reduction in air exchange through natural ventilation. Features of energy-saving measures implementation in Ukraine follow the general trends in Central and Western Europe, where after the implementation of measures associated with improvement of building envelope thermophysical properties, the CO₂ concentration in premises with natural ventilation has increased significantly [10]. Reducing this component is the second step in implementing energy-saving measures in Ukraine. Therefore, in the context of widespread implementation of programs aimed at increasing the thermal protective properties of the building envelope, greater attention should be paid to factors influencing natural ventilation (free convection).

Recent studies have confirmed this need and paid considerable attention to air exchange research [11, 12]. Studies [13] have shown that the most influential parameter on the energy balance of a building is the air exchange rate. For example, infiltration share in France can be 15%. In the USA researchers conclude that this component reaches 33 %. [14]

It is difficult to determine the real value of air exchange rate in spaces. A number of scientific studies are devoted to the determination of this parameter using experimental approach based on measuring the CO₂ concentrations [10, 15–18] but it requires a large number of representative spaces and experimental studies.

Accurate consideration of the infiltration component is the key to the reliability and quality of the calculations to determine the feasibility of implementing energy-saving measures. The calculation of natural ventilation is based on the use of physical and empirical models [19]. Physical models for determining natural air exchange are quite complex and require a large number of output parameters, which significantly complicates the calculation for buildings with many zones. These approaches use algebraic equations that relate characteristics of the building, such as height, orientation, air permeability of building envelope, and weather conditions. One of the first approaches was developed by Shaw and Tamura [20], which was based on a single equation that combined the stack and wind effect to calculate the natural air exchange rate.

Empirical approaches have been reflected in software for calculating the energy performance of buildings. Among the most widely used software complexes for energy modeling of buildings are: eQuest (17 %), EnergyPlus (12 %), TRNSYS (8 %), DOE2 (8 %), DesignBuilder (6 %), and Ecotect Analysis (5 %) [19]. It should be noted that the general capabilities of airflow modeling in the above software systems are based on empirical equations to determine infiltration designed for residential buildings based on ASHRAE approaches and cannot be applied to taller buildings or buildings with natural or mechanical ventilation systems. Therefore, a number of empirical methods for determining air exchange that are reflected in software can be used for low-rise residential buildings [21–23].

More recently proposed method of estimating infiltration in commercial buildings using EnergyPlus [24] considers wind, not just temperature effects [20, 25]. This approach is based on the use of constant coefficients *A*, *B*, *C*, *D* for DOE-2 and BLAST methodology (formula 1) [24].

$$\text{Infiltration} = I_{\text{design}} \cdot F_{\text{shedule}} [A + B \cdot \Delta T + C \cdot W + D \cdot W^2], \quad (1)$$

where I_{design} is defined by EnergyPlus as the "design infiltration rate", which is the airflow through the building envelope under design conditions; F_{shedule} is a factor between 0.0 and 1.0 that can be scheduled, typically to account for the impacts of fan operation on infiltration [24]; ΔT is the indoor-outdoor temperature difference, °C; W is the wind speed in m/s. It should be noted that EnergyPlus varies the outdoor temperature and wind speed by zone height for use in Equation (1) and for other calculations. How this was handled in this study is detailed in Ng et al. [26]. *A*, *B*, *C*, and *D* are constants, for which values are suggested in the EnergyPlus user manual [24]. Two sets of values are presented: DOE-2 and BLAST.

However, as mentioned above, this approach (the considered coefficients) describes with sufficient accuracy the processes of air exchange only in low-rise buildings. In addition, the method provides a simplified picture of the impact of building envelope air permeability, weather and HVAC system operation on infiltration rate [26]. The method [24] does not allow to consider the wind direction and height, which is especially important for the leeward and windward facades of the building.

One of the software used for the analysis of air flows in buildings is CONTAM [26]. CONTAM is a multi-zone computer program for air quality and ventilation analysis that allows determining infiltration, exfiltration and airflows into rooms from controlled mechanical ventilation systems, wind pressures acting on the exterior surfaces of a building, the stack effect caused by the difference in indoor and outdoor air temperatures, concentrations of pollutants and their effects on humans. It should be noted that this software product is used at the design stage and has not found its application in the energy management of existing buildings.

The software complexes discussed above allow for an hourly change in weather data based on typical meteorological year (TMY) data [26, 27].

For Ukraine and other post-Soviet countries, with a respect to improving the energy efficiency of typical development buildings, the assessment of the baseline level of energy consumption when implementing a set of energy-saving measures is one of the key issues. In calculations of the baseline level of energy consumption, air exchange rate is taken in accordance with the normative values [28], and its actual value is difficult to determine experimentally, given that the natural component of this parameter has a dynamic nature.

When calculating the buildings energy performance in Ukraine using stationary and quasi-stationary methods, the climatic characteristics for the respective regional center are used, namely, the monthly average outside temperature, solar heat gains on the horizontal and vertical surfaces for the quasi-stationary method, the average values for the heating period are used for heating degree-day method [1]. The impact of the wind in the models for the monthly and seasonal averaging intervals is considered by the normative value of the air exchange rate.

In terms of efficient energy use (heating system regulation) the energy need for heating should be calculated on the basis of hourly changing climatic characteristics [1]. In Ukraine, dynamic models for determining the buildings energy performance [1], which require the use of hourly climate data, such as International Weather for Energy Calculations (IWEC) file, are becoming increasingly widely used [27]. Similar approaches are relevant both for the design and in-depth analysis of the energy performance of existing buildings, and the climatic conditions of Ukraine are similar for the countries of Central and Eastern Europe (Ukraine, Baltic States, Belarus, Hungary, Poland, Czech Republic, Slovakia, Western Russia).

The analysis shows that the empirical methods for calculating the natural air exchange rate are quite simple, but usually can be used only for low-rise buildings or partially account for influential parameters on the air exchange rate in buildings. Software-based mathematical models for determining the natural air exchange rate allow the calculation of air exchange rate by zone and are commonly used at the design stage, and have not been widely used in energy consumption regulation. There is a need to develop empirical methods that can be easily used and accurately describe the actual natural air exchange for existing housing stock of buildings.

With the described problems, there is a need for improved empirical methods for determining the air exchange in buildings, which are simpler than models based on physical modeling, but at the same time allow to calculate for multi-story buildings in conditions of operation, considering the time variability of weather conditions, which will allow for a more detailed calculation of the baseline level of energy consumption.

The aim of the paper is to develop approaches to the in-depth analysis and specification of air exchange rates in the context of dynamic change of environmental characteristics for the existing building stock of post-Soviet countries, based on the climate characteristics of Kyiv, Ukraine. Objectives of the study are to:

1. provide a generalized methodology for determining the calculated value of the air exchange rate;
2. develop a mathematical model of local determination of the air exchange rate in multi-story buildings;
3. carry out a comparative analysis of the air exchange rate for different values of air permeability for climatic data of a typical year meteorological file IWEC [27];
4. show the importance of influential parameters with the help of air exchange rate modelling and to evaluate its influence on the change of energy need local characteristics.

2. Methods

Usually, mathematical models for determining buildings energy consumption use the value of the air exchange rate for ventilation component (air exchange). Air exchange is difficult to determine experimentally. Even with the same window designs in terms of air permeability, different amounts of air enter the room. Room air exchange depends on a number of factors, both external and internal ones. The generalization of the methods for air exchange rate determination based on the calculation of pressure differences given in the studies of Berge A. and others [30, 31] and according to the ASHRAE approaches [21] is used in the paper, which allows to use the given technique for multi-story buildings. The pressure difference that determines the air exchange rate in a building is created by three different mechanisms: stack effect, wind pressure effect, forced ventilation effect (Fig. 1) and is calculated as their sum (formula 2):

$$\Delta P_{tot} = \Delta P_s + \Delta P_w + \Delta P_v = \Delta P_{inf} + \Delta P_v, \quad (2)$$

ΔP_{tot} is total pressure difference, Pa;

ΔP_s is pressure difference from stack effect, Pa;

ΔP_w is the wind pressure difference, Pa;

ΔP_v is pressure difference from forced ventilation, Pa;

ΔP_{inf} is infiltration pressure difference, Pa.

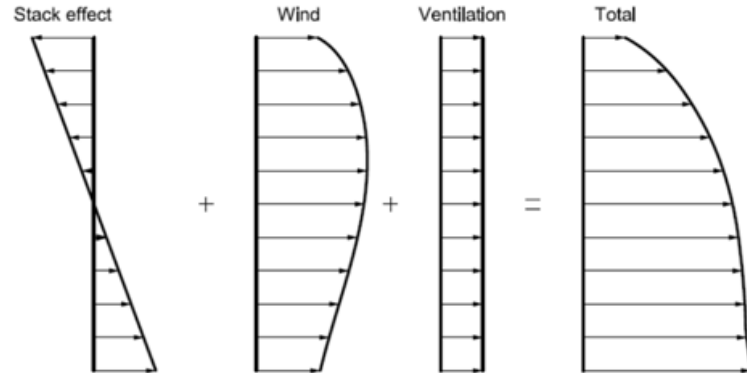


Figure 1. Example of building height distribution and sum of pressure difference profiles [31].

The stack effect is also called the buoyancy effect created by the difference in density between warm and cold air. Reduction of air pressure with the height determined by the formula (3):

$$\Delta P_s = P_e(z) - P_i(z) = z(\rho_e - \rho_i)g, \quad (3)$$

z is height from the reference point, m;

ρ_e, ρ_i are density of exterior and interior air, kg/m³;

g is acceleration of gravity, m/s².

From the neutral pressure level towards the first floor, the pressure difference is positive, towards the last floor it is negative. Assuming that air is the ideal gas, formula (3) looks like:

$$\Delta P_s = 3456 \cdot z \left(\frac{1}{T_e} - \frac{1}{T_i} \right), \quad (4)$$

T_e, T_i are exterior and interior air temperature, respectively, K.

Wind pressure is created when airflow hits an obstacle. The magnitude of the wind pressure depends on the wind speed and direction (windward, leeward side, etc.).

Most software products for modeling wind pressure, use the following formula [30, 31, 7]:

$$\Delta P_w = \frac{\rho U_{met}^2}{2} C_h C_p(\theta), \quad (5)$$

ρ is density of the environment air, kg/m³;

U_{met} is wind speed according to the nearest weather station, m/s;

$C_p(\theta)$ is wind pressure factor considering wind direction through the angle of incidence θ ;

θ is the magnitude of the wind angle relative to the normal drawn to the considered surface, °;

C_h is wind pressure factor that considers the height.

$$C_h = \frac{U_H^2}{U_{met}^2} = A_0^2 \left(\frac{H}{H_{ref}} \right)^{2a}, \quad (6)$$

U_H is wind speed at the highest point of the object, m/s;

A_0 is the wind shelter coefficient; [20]

H is height of the considered floor of the building from the ground level, m;

H_{ref} is height at which the weather station measures wind speed, m;

a is an exponential coefficient that considers wind shelter for a given area [30].

The amount of air entering the room due to leakage under the specified conditions (without mechanical ventilation) is determined by the following formula:

$$G_{inf} = C(\Delta P_{inf})^p \text{ or } G_{inf} = \frac{\Delta P_{inf}^p}{R_b} F_w \quad (7)$$

G_{inf} is the amount of air entering the room due to leakage, kg/h;

C, p are coefficient and the degree index depend on the purpose of the building;

R_b is window air permeability resistance, $(m^2 \cdot h \cdot Pa^{2/3})/kg$ [32];

F_w is window area, m^2 .

The space air exchange rate as a characteristic of the ventilation node in mathematical models is determined by the following formula [32]:

$$n = \frac{G_{inf}}{\rho V}, \quad (8)$$

V is volume of the space, m^3 ;

n is air exchange rate, h^{-1} .

The above method allows to consider the infiltration and exfiltration flows into the space, which significantly affects the energy performance characteristics.

Model description. For the purpose of building energy performance study, a group of representative premises having southern and northern orientation was considered with the thermophysical properties of building envelope for typical construction: 1) triple glazed windows in PVC profiles; 2) triple glazing in wooden twin sashes; 3) double glazing in wooden twin sashes (old translucent structures). The building has 8 floors, where the constant indoor air temperature of 18°C is maintained during the heating period. Based on the selected representative premises (on the 1st, 3rd, 6th floor with southern and northern orientation), a study of the change in the air exchange rate in a multi-story building with different types of windows permeability was carried out according to the above described method. The hourly values from the IWEK file for the climatic conditions of Kyiv (Ukraine) [27] were used: dry bulb temperature, wind speed and direction, barometric pressure.

3. Results and Discussion

3.1. Calculation of hourly natural air exchange in accordance with IWEK climate data of a typical year

The climate file IWEK [27] shows hourly values for wind speed and direction. Wind direction is given in degrees clockwise starting from north (0°).

From the analysis of the IWEK file for Kyiv city (Ukraine) of [27], it follows that the most typical wind direction for the cold season is northern and northwestern, and the average speed is 2.7 m/s, which is similar to the data of building climatology of Ukraine for the given region. [29]. The range of fluctuations of hourly values of wind speed is from 0 m/s to 18 m/s (rarely). The wind direction changes every two hours on average.

According to IWEK, the average outdoor air temperature for the heating season is 1.7 °C, which is slightly different from the current climatology [29] value of -0.1 °C. The minimum external temperature in the IWEK file occurs in February and is -15.8 °C. Regular changes in average daily outside air temperature can be up to 4 °C, and fluctuations within the day can be up to 5 °C. The behavioral trends of daily, between-day and seasonal temperature fluctuations are similar for those of Central and Eastern Europe.

Given that the hourly data for a typical year gives 8760 points, for each point there is a complex effect of a number of factors. Therefore, the impact has been explored alternately to separation the impact of change in outside temperature, wind speed and direction on the value of in pressure difference from wind and stack

effect. The considered range of change in outside temperature, wind speed and direction may be relevant for other climatic zones.

Fig. 2 presents the height profiles of pressure difference caused by the stack effect, depending on the change in ambient temperature. This phenomenon is related to the difference in density between warm and cold air and does not depend on the orientation of the premise.

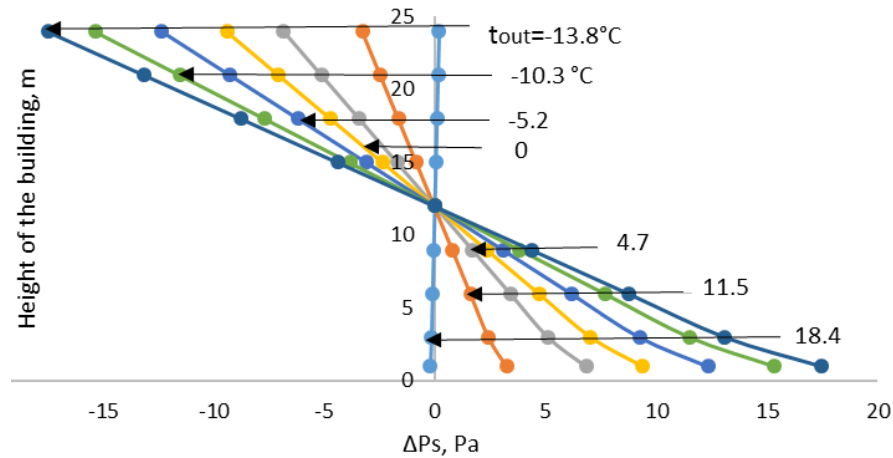


Figure 2. The change in pressure caused by the effect stack depending on the change in ambient air temperature.

Provided that the exterior air temperature is close to the interior one (peak solar activity during off-season) the pressure difference from the stack effect can be offset.

The study investigates changes in pressure difference height profile for different wind speed and direction at different ambient air temperatures and their effect on windward and leeward enclosures. Figure 3 presents the corresponding graphs of wind pressure profiles on the southern side of the building, depending on the building floor and wind direction. Representative days are used, for which the wind speed is 3 m/s (typical wind speed for the conditions of Ukraine [29]) and exterior air temperature is 3 °C (average typical exterior air temperature for December in the city of Kyiv (Ukraine) [28]). The graph shows that the magnitude of the pressure change caused by wind effect increases with height.

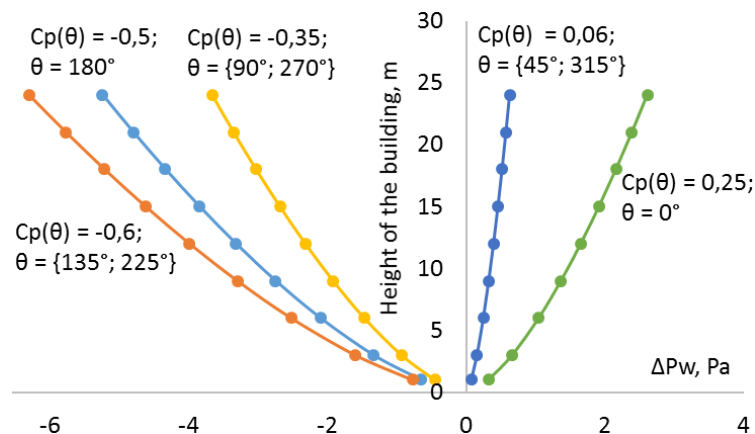


Figure 3. Changes in wind pressure depending on the incidence angle of the wind direction θ .

The wind vector directed to the surface (windward side) causes positive values of wind pressure difference, for leeward sides it is negative.

As mentioned above, northern and northwestern wind direction is typical for Kyiv (Ukraine). The average wind speed is 2.7 m/s, the wind speed greater than 8 m/s typically has northwestern direction. The change in wind pressure effect for different wind speed profiles and wind incidence angle $\theta = 0^\circ$ is shown in Fig. 4. Similar calculations are performed for incidence angles $\theta = 180^\circ$ (profiles are similar with a negative value of change in wind pressure). The analysis shows that the pressure difference increases with wind velocity increase.

Figs. 2-4 shows that the pressure difference caused by the stack effect has a greater effect on the natural the air exchange rate as opposed to the wind effect.

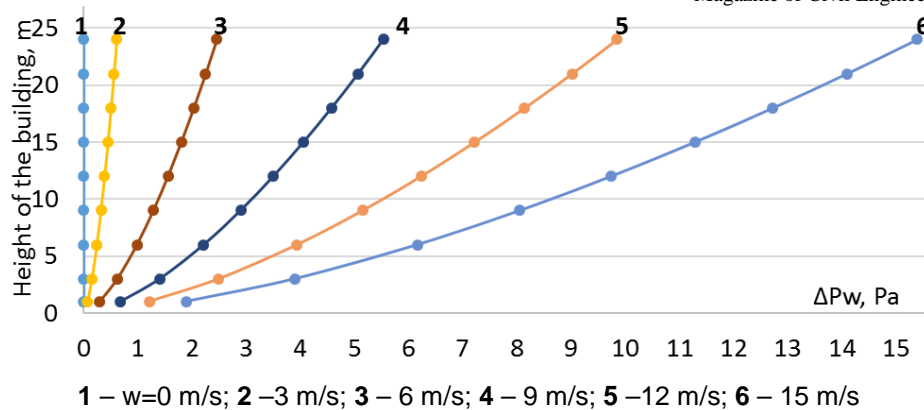


Figure 4. Change of wind pressure difference depending on change of wind speed at northern wind direction on the northern side of building ($\theta = 0^\circ$).

This paper investigates the natural component of air exchange, which is determined by the sum of the pressure difference from the stack and the wind effect. Fig. 5 shows the average resulting infiltration pressure difference depending on building height in January and March for the southern (S) and northern (N) orientations. Fig. 5 shows that for the first floors (1-3 floors) the typical effect is infiltration of the exterior air, where, accordingly, the heat consumption will be the highest. The profile of change in the average monthly values of infiltration pressure difference depending on the height in January is more low-angle that is stronger than in March for the similar premises. This feature is caused by a number of factors: the ambient air temperature decreases (the pressure difference from the effect stack increases); different wind speeds and directions specific for a particular period of the year.

Also, Figure 5 shows the profile of changes in the mean monthly values of the infiltration pressure difference depending on height for southern (S) and northern (N) orientations for March, the orientation difference is caused by wind effect (wind direction). A similar analysis was carried out for January data, the difference of profiles is less, which is caused by a combination of factors and their influence on the magnitude of the stack and wind effect of the pressure difference profiles.

Thus, the above method allows to determine the quantitative dependence of the distribution of infiltration pressure difference and air exchange on a specific set of characteristics of the terrain and building.

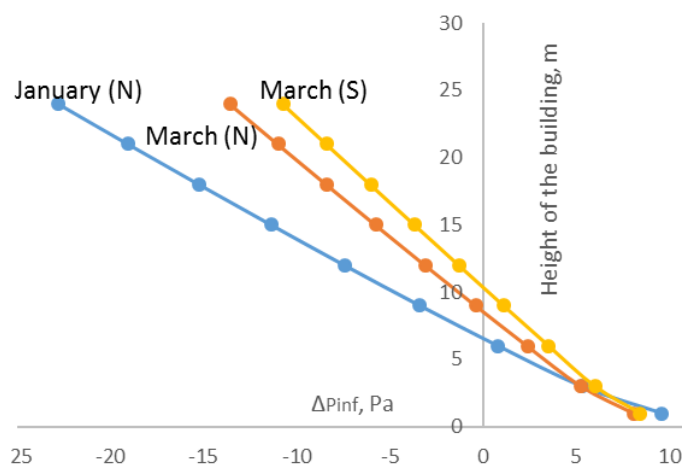
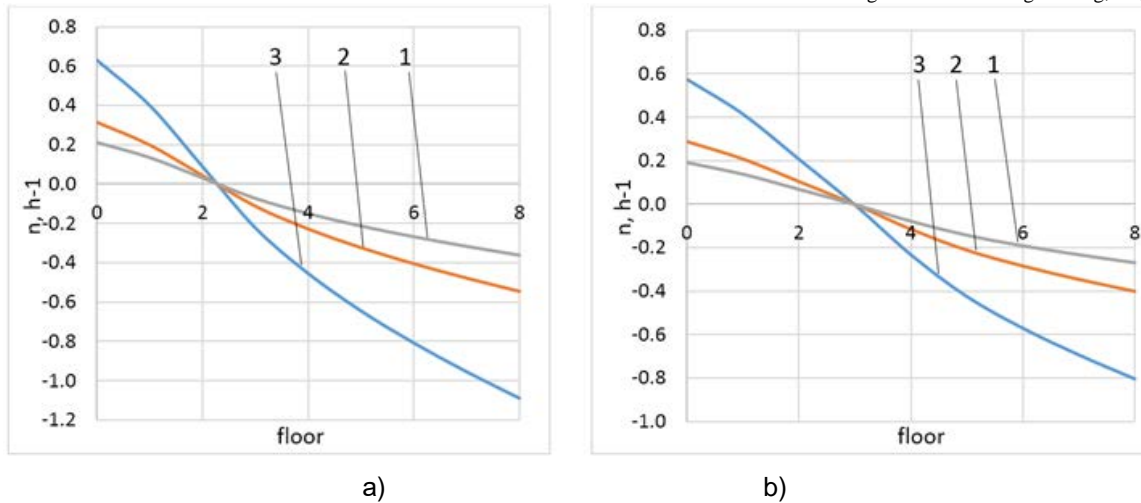


Figure 5. Change in average monthly pressure difference depending on height for January and March of typical year data for rooms with N and S orientation.

As mentioned above, the considered technique takes into account both infiltration and exfiltration natural air flows in the building. Fig. 6 shows an example of changing the air exchange rate for rooms of the northern (N) orientation of the building under consideration for different values of the air permeability coefficients. For the off-season, the air exchange rate decreases somewhat compared to the cold period, which is explained by the decrease in the temperature difference between the indoor and outdoor environment.



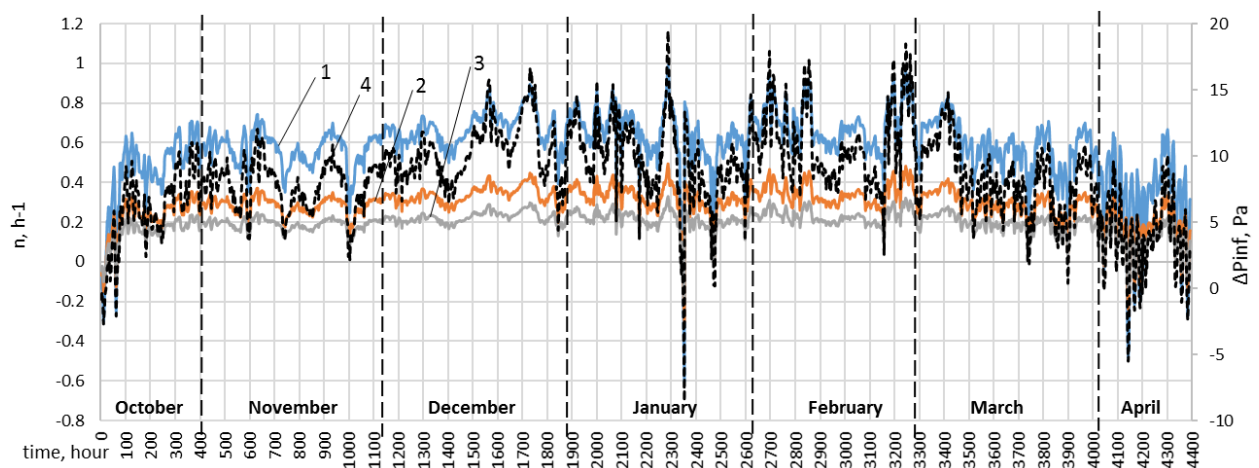
1 – for triple-glazed PVC windows; 2 – triple-glazed wooden windows; 3 – double-glazed wooden windows;

Figure 6. Average air exchange rate for representative premises (N orientation) for different types of window structures for January (a) and March (b).

An hourly calculation of air exchange rate was carried out for representative premises of different orientation and floor location. The natural air exchange rate for premises with north-eastern orientation is slightly smaller than for other orientations, which is related to the wind direction, the difference is more noticeable for windows with less air permeability resistance. The average annual calculated natural air exchange rate is about $0.25 h^{-1}$ – for triple-glazed PVC windows, $0.4 h^{-1}$ – triple-glazed wooden windows, $0.65 h^{-1}$ – double glazed wooden window. This value may actually be greater for older windows with wooden frames as airtightness has decreased during operation. During the year, the maximum value of the air exchange rate is greatest for double glazed windows and can range from -2 to $1.2 h^{-1}$, which is typical for periods with gusty winds of more than 15 m/s.

During the off-season, the air exchange rate decreases somewhat compared to the cold period, which is explained by the decrease in the temperature difference between the indoor and outdoor environments.

On the ground floor there is a phenomenon of infiltration (fresh air inflow naturally due to leakage in window structures), in the above floors there is an area where it is on average close to zero, which is related to the NPL of the building (stack effect), on the upper floors there is an exfiltration which corresponds to negative air exchange rate values. Fig. 7 shows the variation of hourly values of air exchange rate during the season for premises on the ground floor with N orientation.



1 – double-glazed wooden windows; 2 – triple-glazed wooden windows; 3 – for triple-glazed PVC windows; 4 – pressure difference for natural ventilation

Figure 7. Hourly values of air exchange rate for premises on the ground floor with N orientation.

Fig. 7 shows that windows with improved thermophysical characteristics are less sensitive to fluctuations in environmental parameters. In general, on the ground floor the range of infiltration air exchange rate change is $-0.2 \dots 0.25 h^{-1}$ – for double-glazed windows with PVC profile, $-0.4 \dots 0.5 h^{-1}$ – for triple-glazed wooden windows, $-0.5 \dots 1 h^{-1}$ – for double glazed windows. The negative values of air

exchange rate on the ground floor are explained by a short gusty wind with a velocity of more than 10 m/s and a frontal direction to the considered enclosure.

The results of simulation of the average air exchange rate 0.25 h^{-1} was obtained for the heating season for triple-glazed windows with PVC profile. The similar results show that the annual average infiltration rates in Beijing range from 0.02 to 0.82 h^{-1} with a median value of 0.16 h^{-1} [15]. For upper floors (not shown in Fig. 6) the range of variation is $-1.5 \dots 0.25 \text{ h}^{-1}$ – for double-glazed windows with PVC profile, $-2 \dots 0.5 \text{ h}^{-1}$ – for triple-glazed wooden windows, $-4 \dots 1 \text{ h}^{-1}$ – for double glazed ones.

The obtained results show that for the ground floors there is a positive variation range of the hourly air exchange rate values, for the upper floors it is negative. For double-glazed windows, the air exchange rate of -4 h^{-1} is characterized by a wind speed of 18 m/s at the level of 10 m (meteorological measurements).

It should be noted that for the conditions of Ukraine this type of research was not conducted, similar trends are obtained for Chinese conditions [15], but quantitatively the differences in results are due to the different nature of buildings and climatic data.

The use of more efficient windows leads to less sensitivity depending of the air rate exchange on the considered factors, due to the fact that modern windows have greater air permeability resistance value. The obtained results show the dynamics of air exchange due to natural infiltration and how much it is necessary to supplement the air exchange mechanically to ensure comfort under certain modes / operating conditions [30].

3.2. Calculation of energy consumption and analysis of energy need for heating with change of actual natural air exchange rate

Input data. A group of representative rooms is in the buildings of typical development of the 1970s. Room dimensions are $5.5 \times 6.1 \text{ m}$, room height is 3 m. The room has one outside wall ($5.5 \times 3.0 \text{ m}$) with a window ($5 \times 2 \text{ m}$). The outer wall has a thermal resistance of $0.8 \text{ m}^2 \cdot \text{K/W}$ (the main layer is brickwork in one brick). Ceiling over the heated premises is reinforced concrete (20 cm). The building is located in Kyiv, Ukraine. The design indoor air temperature is 18°C . Solar heat gain coefficient for window is 0.56. Climate hourly data from the IWEK file for the city of Kyiv were used [27]. Solar heat gains are calculated using IWEK file data and EnergyPlus "Full interior and exterior with reflection" technique. The low level of thermal insulation properties is relevant for a large volume of buildings in countries such as Ukraine, Baltic States, Belarus, Hungary, Poland, Czech Republic, Slovakia, Russia.

Figure 7 shows the hourly variations of the outside temperature and solar heat gains for premises with N and S orientation during heating period.

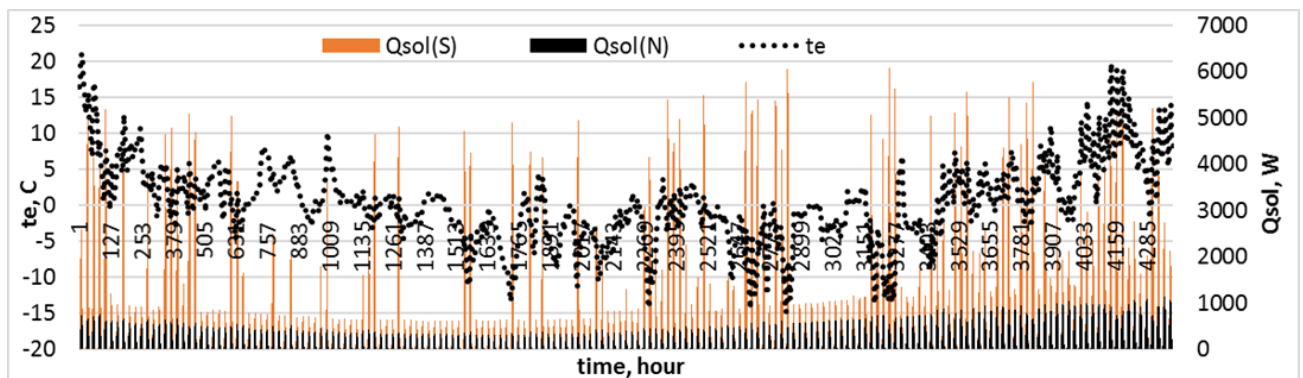


Figure 7. Variations of exterior air temperature t_{out} , solar heat gains Q_{sol} for premises with N and S orientation.

Model description. According to 5R1C model (dynamic grid room model, five resistances, one capacity), energy need for heating Φ_{HC} is calculated as the heating power value for each hour to be supplied to the indoor air temperature node (θ_{air}) to maintain a given temperature setpoint [6]. The dynamic method scheme is implemented on the basis of EN ISO 13790 [33] and EN ISO 13786 [34] and shown in Fig. 8.

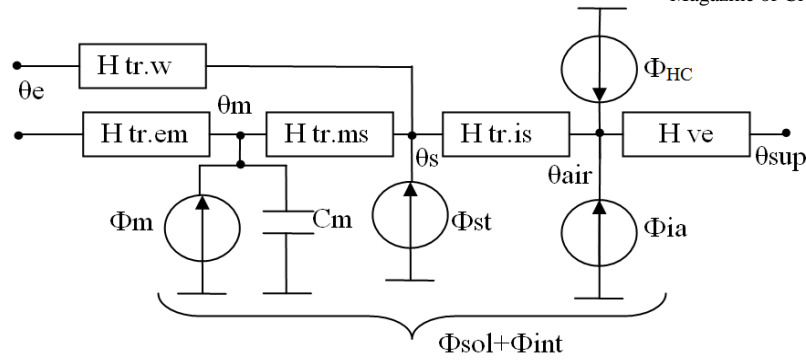


Figure 8 - Dynamic grid room model, five resistances, one capacity (5R1C) [2]: θ_{air} , θ_s , θ_e , θ_m , θ_{sup} are temperature of air, internal surfaces, external environment, opaque enclosures, supply air, respectively, °C; Φ_m , Φ_{st} , Φ_{ia} are additional solar (Φ_{sol}) and internal heat gains (Φ_{int}), distributed between the air node, the surface of the inner enclosure and walls, W; Φ_{HC} is heat flow from the heating system, W; C_m is internal heat capacity of opaque building enclosures, J/K; $H_{tr.w}$, $H_{tr.em}$, $H_{tr.ms}$, $H_{tr.is}$, H_{ve} are coupled conductivity between temperature nodes characterizing transmission losses through building envelope and ventilation, W/K.

The energy need for heating is based on the calculation of the heating level, $\Phi_{HC.nds}$, for each hour to be delivered to the internal air temperature node, θ_{air} , to maintain a certain set-point temperature. The set-point temperature is an average weighted value of internal air temperature and radiant temperature.

Heat transfer by ventilation, H_{ve} , is directly connected to internal air temperature node, θ_{air} , and the node that corresponds to supply air temperature, θ_{sup} . Heat transfer by transmission is divided into two parts: the first one is through fenestration surfaces, like windows, $H_{tr.w}$, that do not have thermal mass, the second one is through opaque surfaces H_{op} , that have thermal mass, and, in its turn, is divided into two parts: $H_{tr.em}$ and $H_{tr.ms}$. Solar (Φ_{sol}) and internal heat gains (Φ_{int}) are distributed between the internal air temperature node, θ_{air} , the central node, θ_s (mixture of θ_{air} and mean radiant temperature θ_r) and the node representing the building mass, θ_m . The thermal mass is reflected by the specific heat, C_m , located between $H_{tr.ms}$ and $H_{tr.em}$. The coupling by conductivity is determined between the internal air temperature and the central node. The value of the heat flux due to internal sources, Φ_{int} , and the value of the heat flux in the zone of the room due to the sun, Φ_{sol} , are divided between the three nodes: internal air temperature, θ_{air} , and internal nodes, θ_s , θ_m .

$$H_{tr.is} = h_{is} A_{tot} \quad (9)$$

$$H_{tr.ms} = h_{ms} A_m \quad (10)$$

$$H_{tr.em} = \frac{1}{\frac{1}{H_{op}} - \frac{1}{H_{tr.ms}}} \quad (11)$$

$$H_{tr.1} = \frac{1}{\frac{1}{H_{ve}} + \frac{1}{H_{tr.is}}} \quad (12)$$

$$H_{tr.2} = H_{tr.1} + H_{tr.w} \quad (13)$$

$$H_{tr.3} = \frac{1}{\frac{1}{H_{tr.2}} + \frac{1}{H_{tr.ms}}} \quad (14)$$

$$C_m = \sum k_j A_j \quad (15)$$

$$\Phi_{m.tot} = \Phi_m + H_{tr.em}\theta_e + \frac{H_{tr.3}(\Phi_{st} + H_{tr.w}\theta_e + H_{tr.1}(\frac{\Phi_{ia} + \Phi_{HC.nd}}{H_{ve}} + \theta_{sup}))}{H_{tr.2}} \quad (16)$$

$$\theta_m = \frac{\theta_{m,t} + \theta_{m,t-1}}{2} \quad (17)$$

$$\theta_{m,t} = \frac{\theta_{m,t-1}(\frac{C_m}{3600} - 0.5(H_{tr.3} + H_{tr.em})) + \Phi_{m.tot}}{\frac{C_m}{3600} + 0.5(H_{tr.3} + H_{tr.em})} \quad (18)$$

$$\theta_s = \frac{H_{tr.ms}\theta_m + \Phi_{st} + H_{tr.w}\theta_e + H_{tr.1}(\frac{\Phi_{ia} + \Phi_{HC.nd}}{H_{ve}} + \theta_{sup})}{H_{tr.ms} + H_{tr.w} + H_{tr.1}} \quad (19)$$

$$\theta_s = \frac{H_{tr.ms}\theta_m + \Phi_{st} + H_{tr.w}\theta_e + H_{tr.1}(\frac{\Phi_{ia} + \Phi_{HC.nd}}{H_{ve}} + \theta_{sup})}{H_{tr.ms} + H_{tr.w} + H_{tr.1}} \quad (20)$$

$$\theta_{air} = \frac{H_{tr.is}\theta_s + H_{ve}\theta_{sup} + \Phi_{ia} + \Phi_{HC.nd}}{H_{tr.is} + H_{ve}} \quad (21)$$

$\Phi_{ia}, \Phi_m, \Phi_{st}$ internal and solar radiation heat gains are distributed between the 3 nodes, $\theta_{air}, \theta_s, \theta_m$;

$\Phi_{m.tot}$ is total heat flow, W;

h_{is} is heat transfer coefficient between the internal air temperature node, θ_{air} , and central node, θ_s ,

has a fixed value $h_{is} = 3.45 \frac{W}{m^2 K}$;

h_{ms} is heat transfer coefficient between the nodes m and s, has a fixed value $h_{ms} = 9.1 \frac{W}{m^2 K}$;

A_m is effective mass area, m²;

A_j is area of the j-element, m²;

A_{tot} is the area of all external enclosures of the building, m²;

C_m is internal heat capacity, J/K;

k_j is internal heat capacity per unit area of the j-element of the building, J/(m²·K);

$H_{tr.is}$ is coupling by conductivity between node s and inside air temperature, W/K

$H_{tr.1}, H_{tr.2}, H_{tr.3}$ are conductivity of conditional nodes 1, 2, 3, W/K

Model validation. Based on the considered series of models and results of studies [35–37], a model built on the basis of the EnergyPlus software can serve as a reference model for verification. The verification of the simplified hourly calculation method of EN 13790 [23], implemented on the basis of the grid model 5R1C, was carried out with the model based on the EnergyPlus software product. The difference between the results of grid calculation models is less than 5 % and slightly higher value of load in 5R1C model is explained by the common node for internal and external envelope inertia protections, this feature can produce more model's discrepancy results in the summer. The models considered performed an hourly calculation. During the

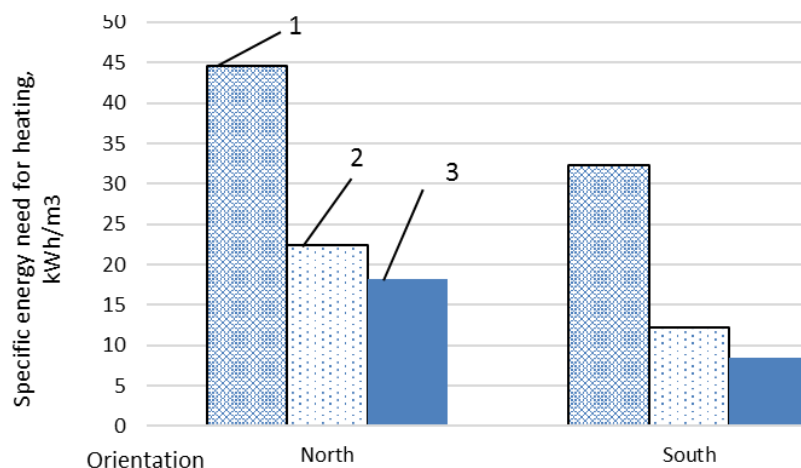
heating period for the facility the located in Kyiv (Ukraine), the discrepancy between the results of the two models was estimated on the basis of an adjusted coefficient of determination of $R^2 = 0.968$.

Simulation results. When using the calculated values of the natural component of air exchange rate, due to infiltration (leaks in window construction), the supply of fresh air into the room area and heat loss significantly change under the influence of natural factors, and accordingly the energy consumption of the building also changes.

Mathematical modeling of specific energy need for heating of representative rooms of northern (N) and southern (S) orientation is carried out with the condition of only transmission losses ($n = 0$), for normative values of air exchange multiplicity ($n = 1 \text{ h}^{-1}$) and for the calculated value of natural component ($n = \text{var.}$) air exchange.

Fig. 9 shows the annual specific energy need for heating for northern (N) and southern (S) orientation on the example of representative rooms with triple-glazed energy-saving windows with PVC profile located on the ground floor. The maximum estimate of additional energy costs due to natural ventilation (infiltration) compared to energy consumption with only transmission losses ($n = 0$) differs by 23% for northern and 43 % for southern orientations.

The obtained value for the natural component of air exchange does not allow to provide a normative level of air exchange for comfortable working conditions. Comparison of the specific energy need for heating calculated for the normative values ($n = 1 \text{ h}^{-1}$) and the obtained level of natural air exchange establishes that the difference of energy need for the entire heating period can be more than 50 %, compared with $n = 1 \text{ h}^{-1}$. For example, for the premises on the ground floor with N orientation it can be 50 %, for S orientation it can be 65 %. This difference can be reduced by increasing air exchange rate during occupied hours, for example, by airing.



1 – normative values of air exchange rate $n = 1 \text{ h}^{-1}$; 2 – calculated (natural component) air exchange rate; 3 – no air exchange

Figure 9. Annual specific building energy need for heating under different conditions of air exchange

Fig. 10 shows the change in hourly values of specific energy for heating using normative (1) and calculated (2) values of natural air exchange rate and for premises with only transmission heat losses component (3) oriented to the North (a) and South (b) located on the ground floor.

The results of mathematical modeling show that at a certain level of natural air exchange for the considered type of windows (air permeability resistance), the heating system of the rooms oriented to the south can be switched off during the off-season (October, April), i.e. solar heat gains work as a passive heating system. The heating season can be reduced by more than 30 days.

During the cold period of the year, the energy need for heating calculated for the values of normative air exchange rate, and according to the variable natural conditions (natural exchange rate), line 2, varies up to 50 %, and for the off-season period the difference can be up to 75 %. Addition to the energy need due to natural air exchange (the difference between 2 and 3) is about 20 %, the value of fluctuations in the heating load increases by one and a half - two times.

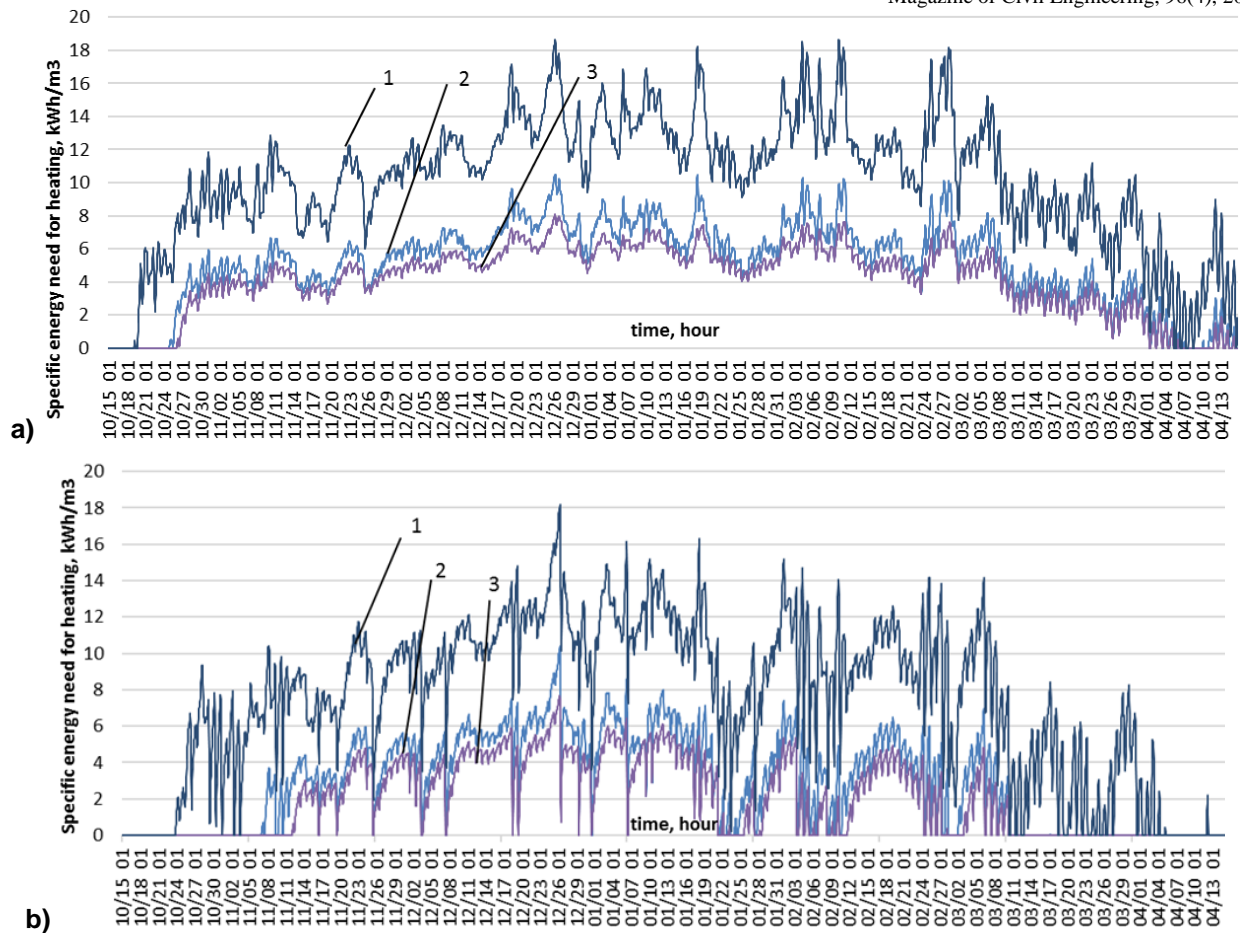


Figure 10. Load on the heating system for the heating period of the premises oriented to the north (a) and south (b): 1 – at the normative values of air exchange rate $n = 1 \text{ h}^{-1}$; 2 – calculated (natural component); 3 – no air exchange

For premises oriented to the South, the fluctuations of the load on the heating system during the day are somewhat larger and the effect of natural air exchange on them is not so obvious, unlike for the northern orientation, which is explained by solar heat gains into the premises. Also, on some days there are short-term shutdowns of heating during peak hours of solar activity, the amount of which is reduced by the influence of air exchange.

4. Conclusions

1. The article reviews literature sources and approaches to the assessment of natural air exchange in a building, taking into account the cumulative variability of a number of external and internal factors. A generalized technique for determining the natural air exchange rate for multi-story buildings is proposed, the considered methodology is based on ASHRAE approaches and allows to calculate natural air exchange for medium-sized buildings. The calculation was made for climatic conditions typical in Central and Eastern Europe. The calculations used the data of the international climate file IWEC (typical year), e.g. for the city of Kyiv, Ukraine. The natural component of the air exchange rate is calculated for air permeability coefficients of the most typical characteristics of window construction, namely: triple-glazed PVC window, triple and double-glazed wooden window. The calculation was carried out for representative premises of 8-story building that have one window of different orientation.

2. For energy efficient triple-glazed PVC windows an hourly calculation of the natural component of air exchange rate at different locations of representative premises showed that the infiltration value does not exceed 0.25 h^{-1} , for triple-glazed wooden windows it can be 0.4 h^{-1} , for double-glazed wooden windows it can be 0.65 h^{-1} . It should be noted that on the first floors, in general, the natural component of air exchange has a positive value (air infiltration), while on the last floors, it has a negative value (air exfiltration), which must be taken into account in the dynamic modeling of building energy performance.

3. General trends show that as thermal resistance of building envelope structures increases, heat losses are reduced, while the share of heat losses with air exchange increases ensuring conditions of comfort. In addition, the improvement of window structures leads to a decrease in natural air exchange through them. The research shows to what extent mechanical ventilation should be additionally used to maintain the normative value of the air exchange rate during the people occupancy period. In further studies it is planned

to perform hourly calculation of air exchange rate taking into account building air flow conditions with regard to the landscape, mechanical ventilation and heat recovery.

4. Dynamic grid models have been developed to study buildings energy performance based on EN ISO 13790 [33] and EN ISO 13786 [34] standards. The model was validated with the model created in the EnergyPlus software package.

It is established that the maximum estimate of additional energy costs due to natural ventilation (infiltration) compared to the energy consumption of the building with only transmission losses ($n = 0$) differs by 23 % for northern and 43% southern orientations for premises with energy efficient triple-glazed PVC windows. It is also established that the energy consumption of the building at the normative value of the air exchange rate ($n = 1 \text{ h}^{-1}$) and the calculated value of the natural component of the air exchange rate differs by 50–75 %, which is a possible savings result under the actual conditions of air exchange compared with the normative. This savings can be reduced by increasing air exchange during occupation periods using premises airing to ensure proper ventilation in the room.

5. For residential and public buildings of typical development of the post-Soviet countries there is a general tendency to improve the thermal characteristics of the building enclosures. Replacing windows reduces air exchange through natural ventilation, so more attention should be paid to mechanical ventilation. In order to maintain the normative value of the air exchange rate during occupancy, natural or mechanical ventilation should be used additionally. The actual natural component of air exchange in the premises of variable occupancy rate consideration specifies the determination of the level of energy-saving measures efficiency for thermo-modernization, a component that must be provided by mechanical ventilation, and can also be utilized in heat recovery devices. The dynamics of the air exchange rate influence on energy consumption under these conditions needs further investigation.

6. The results of the paper provide a methodology, demonstrate the needs and boundaries for quantifying natural air exchange for the conditions of Central and Eastern Europe (temperate climate) for typical characteristics of buildings in post-Soviet countries before and after window replacement.

5. Acknowledgements

The research was supported by Ministry of Education and Science of Ukraine under the project "Engineering aspects of energy management system functioning in residential and public facilities".

References

1. Deshko, V.I., Bilous, I.Yu. Mathematical Models for Determination of Specific Energy Need for Heating and Cooling of the Administrative Building. *International Journal of Engineering & Technology*. 2018. No. 4.3(7). Pp. 325. DOI:10.14419/ijet.v7i4.3.19826
2. Borodinecs, A., Zemitis, J., Sorokins, J., Baranova, D.V., Sovetnikov, D.O. Renovation need for apartment buildings in Latvia. *Magazine of Civil Engineering*. 2016. 68. Pp. 58–64. DOI:10.5862/MCE.68.6
3. Kostenko, V.A., Gafiyatullina, N.M., Semchuk, A.A., Kukolev, M.I. Geothermal heat pump in the passive house concept. *Magazine of Civil Engineering*. 2016. 68. Pp. 18–25. DOI:10.5862/MCE.68.2
4. Borodinecs, A., Prozuments, A., Zajacs, A., Zemitis, J. Retrofitting of fire stations in cold climate regions. *Magazine of Civil Engineering*. 2019. 90. Pp. 85–92. DOI:10.18720/MCE.90.8
5. Bayramukov, S.H., Dolaeva, Z.N. Dynamic programming in optimization of comprehensive housing stock modernization. *Magazine of Civil Engineering*. 2017. 76. Pp. 3–19. DOI:10.18720/MCE.76.1
6. Bilous, I.Y., Deshko, V.I., Sukhodub, I.O. Building inside air temperature parametric study. *Magazine of Civil Engineering*. 2016. 68. DOI:10.5862/MCE.68.7
7. Bilous, I., Deshko, V., Sukhodub, I. Parametric analysis of external and internal factors influence on building energy performance using non-linear multivariate regression models. *Journal of Building Engineering*. 2018. 20. DOI:10.1016/j.jobee.2018.07.021
8. Mukhtar, A., Yusoff, M.Z., Ng, K.C. The potential influence of building optimization and passive design strategies on natural ventilation systems in underground buildings: The state of the art. *Tunnelling and Underground Space Technology*. 2019. April(92). DOI:10.1016/j.tust.2019.103065
9. DSTU-N B V.3.2-3:2014. Nastanova z vikonannya termomodernizatsii zhitlovikh budinkiv. Chinniy vid 2015-10-01. K.: Minregion Ukraïni, 2015. 40 p.
10. Földváry, V., Bekö, G., Langer, S., Arrhenius, K., Petráš, D. Effect of energy renovation on indoor air quality in multifamily residential buildings in Slovakia. *Building and Environment*. 2017. 122. Pp. 363–372. DOI:10.1016/j.buildenv.2017.06.009
11. Younes, C., Shdid, C.A., Bitsuamlak, G. Air infiltration through building envelopes: A review. *Journal of Building Physics*. 2012. No. 3(35). Pp. 267–302. DOI:10.1177/1744259111423085
12. Jokisalo, J., Kalamees, T., Kurnitski, J., Eskola, L., Jokiranta, K., Vinha, J. A comparison of measured and simulated air pressure conditions of a detached house in a cold climate. *Journal of Building Physics*. 2008. No. 1(32). Pp. 67–89. DOI:10.1177/1744259108091901
13. Ren, Z., Chen, D. Simulation of air infiltration of Australian housing and its impact on energy consumption. *Energy Procedia*. 2015. 78. Pp. 2717–2723. DOI:10.1016/j.egypro.2015.11.611
14. Kalamees, T. Air tightness and air leakages of new lightweight single-family detached houses in Estonia. *Building and Environment*. 2007. No. 6(42). Pp. 2369–2377. DOI:10.1016/j.buildenv.2006.06.001
15. Shi, S., Chen, C., Zhao, B. Air infiltration rate distributions of residences in Beijing. *Building and Environment*. 2015. 92. Pp. 528–537. DOI:10.1016/j.buildenv.2015.05.027

16. Leivo, V., Prasauskas, T., Du, L., Turunen, M., Kiviste, M., Aaltonen, A., Martuzevicius, D., Haverinen-Shaughnessy, U. Indoor thermal environment, air exchange rates, and carbon dioxide concentrations before and after energy retro fits in Finnish and Lithuanian multi-family buildings. *Science of the Total Environment*. 2018. 621. Pp. 398–406. DOI:10.1016/j.scitotenv.2017.11.227
17. Stabile, L., Dell'Isola, M., Russi, A., Massimo, A., Buonanno, G. The effect of natural ventilation strategy on indoor air quality in schools. *Science of the Total Environment*. 2017. 595. Pp. 894–902. DOI:10.1016/j.scitotenv.2017.03.048
18. Salthammer, T. Formaldehyde sources, formaldehyde concentrations and air exchange rates in European housings. *Building and Environment*. 2019. 150. Pp. 219–232. DOI:10.1016/j.buildenv.2018.12.042
19. Ng, L., Persily, A. Airflow and indoor air quality analyses capabilities of energy simulation software. *Proceedings from Indoor Air 2011*. Austin, TX, United States; 5 June 2011 do 10 June 2011; Kod 97918
20. Ng, L.C., Persily, A.K., Emmerich, S.J. Improving infiltration modeling in commercial building energy models. *Energy and Buildings*. 2015. 88. Pp. 316–323. DOI:10.1016/j.enbuild.2014.11.078
21. Jokisalo, J., Kurnitski, J., Korpi, M., Kalamees, T., Vinha, J. Building leakage, infiltration, and energy performance analyses for Finnish detached houses. *Building and Environment*. 2009. No. 2(44). Pp. 377–387. DOI:10.1016/j.buildenv.2008.03.014
22. Chen, S., Levine, M.D., Li, H., Yowargana, P., Xie, L. Measured air tightness performance of residential buildings in North China and its influence on district space heating energy use. *Energy and Buildings*. 2012. 51. Pp. 157–164. DOI:10.1016/j.enbuild.2012.05.004
23. Nielsen, T.R., Drivsholm, C. Energy efficient demand controlled ventilation in single family houses. *Energy and Buildings*. 2010. No. 11(42). Pp. 1995–1998. DOI:10.1016/j.enbuild.2010.06.006
24. EnergyPlus Energy Simulation Software. <http://apps1.eere.energy.gov/buil-dings/energyplus>
25. Ng, L.C., Musser, A., Persily, A.K., Emmerich, S.J. Multizone airflow models for calculating infiltration rates in commercial reference buildings. *Energy and Buildings*. 2013. 58. Pp. 11–18. DOI:10.1016/j.enbuild.2012.11.035
26. Ng, L.C., Persily, A.K., Emmerich, S.J. Consideration of envelope airtightness in modelling commercial building energy consumption. *International Journal of Ventilation*. 2014. No. 4(12). Pp. 369–377. DOI:10.1080/14733315.2014.11684030
27. International Weather for Energy Calculations: https://energyplus.net/weather-location/europe_wmo_region_6/UKR.
28. DSTU B A.2.2-12:2015. Yenergetichna yefektivnist budivel. Metod rozrakhunku yenergospozhyvannya pri opalenni, okholodzhenni, ventilyatsii, osviltleni ta garyachomu vodopostachanni. Uvedeniy vpershe; chinniy vid 2015.01.01. K.: Minregionbud Ukraïni, 2015. 140 s.
29. DSTU-N B V.1.1-27:2010. Budivelna klimatologiya. K.: Minregion Ukraïni, 2011. 127 s.
30. Biler, A., Tavil, A., Su, Y., Kha, N. A Review of Performance Specifications and Studies of Trickle. *Vent. Buildings*. 2018. No. 8. Pp. 152–183. DOI:10.3390/buildings8110152
31. BERGE, A. Analysis of Methods to Calculate Air Infiltration for Use in Energy Calculations. Sweden 2011. Pp.98.
32. DSTU B V.2.2-19:2007 Metod viznachennya povitroproniknosti ogorodzhvalnikh konstruksiy v naturnikh umovakh. – K.: Ukrarkhbudinform, 2008. – 20 s.
33. EN ISO 13790:2008. Energy performance of buildings – Calculation of energy use for space heating and cooling. – CEN. European Committee for Standardization, 2008. – 53 r.
34. EN ISO 13786:2007. Thermal performance of building component - Dynamic thermal characteristics - Calculation methods. — CEN. European Committee for Standardization, 2007 - 27 r.
35. Crawley, D.B., Lawrie, L.K., Winkelmann, F.C., Buhl, W.F., Huang, Y.J., Pedersen, C.O., Strand, R.K., Liesen, R.J., Fisher, D.E., Wittef, M.J., Glazer, J. EnergyPlus: Creating a new-generation building energy simulation program. *Energy and Buildings*. 2001. 33. Pp. 319–331. DOI: 10.1016/S0378-7788(00)00114-6
36. Krarti, M., Chuangchid, P., Ihm, P. Foundation heat transfer module for EnergyPlus program. Seventh International IBPSA Conference, Rio de Janeiro, Brazil August 13-15, 2001. P. 931–938.
37. Vivian, J., Zarrella, A., Emmi, G., Carli, M. An evaluation of the suitability of lumped-capacitance models in calculating energy needs and thermal behaviour of buildings. *Energy and Buildings*. 2017. 150. Pp. 447–465. DOI:10.1016/j.enbuild.2017.06.021

Contacts:

Inna Bilous, bilous_inna@ukr.net

Valerij Deshko, te@kpi.ua

Iryna Sukhodub, ira_krot@ukr.net

© Bilous, I.Yu., Deshko, V.I., Sukhodub, I.O.2020



DOI: 10.18720/MCE.96.4

Efficiency and durability of the linings channels of geosynthetics

Yu.M. Kosichenko*, **O.A. Baev**

Russian Scientific Research Institute of Land Improvement Problems, Novocherkassk, Russia

* E-mail: kosichenko-11@mail.ru

Keywords: anti-filter liner, geocomposite material, polymer geomembrane, geocomposite material, geosynthetic clay liner, filtration

Abstract. The investigation is concerned with seepage-control canal lining made of geosynthetic materials (GSM): polymer geomembranes and bentonitic mats (bentomats) with protective coatings. Efficiency and longevity criteria of lining made of geomembranes, bentomats and protective coatings (concrete, stone, gabion, and soil) have been stated. New lining designs with GSM of high reliability are proposed, including two or three layers of seepage-control lining made of bentomats and geomembranes, as well as protective layers made of geotextiles, rock filling, gabions. We have considered the effectiveness of already constructed sections of Bentofix bentomat linings at Donskoy principal canal (Rostov region, Russia) according to the following three criteria:

- - Filtration costs of the bentomat lining compared to the ground bed,
- - Efficiency degree due to the bentomat lining compared to the alternative options,
- - Filtering resistances of the bentomat lining compared to the alternative options.

We have developed a technique to assess the effectiveness of bentonite mats taking into account the regeneration (self-healing) of possible damage due to the regeneration of Ca-bentonite. It is based on the method of successive change of steady states, when the nonsteady process of filtering through damages of the bentomat is divided into a number of steady states. Studies of the aging coefficient of the geomembrane made of polyethylene (HDPE) by the modulus of elongation in the test basin during the period of 8–10 years have made it possible to extrapolate these data and determine the longevity (service life). There is also a calculation of the geomembrane longevity according to the Arrhenius equation. We have made a comparative analysis of the efficiency of various types of canal linings which showed that the most effective type is the bentomat liner, which also has the highest service life.

1. Introduction

Urgency of the research is caused by high losses of water during its transportation through canals in the Russian Federation [1], which amount is equal to 4.8 km³/year (more than 30 % of use). The main reasons are the low technical level and a significant wear factor of land reclamation systems and hydraulic structures.

According to the FSBSI “RosNIIPM”, the average value of the efficiency coefficient of the principal canals for today is 0.829, which is significantly less than the requirements of the standards [2]. In this case, the efficiency of the canals in the ground channel is 0.790, and the canals in the lining is 0.870.

Studies of the seepage-control efficiency of the canals were performed by A.G. Alimov [3], M.A. Bandurin [4], S.V. Solsky [5], Yu.M. Kosichenko and O.A. Baev [6–8].

Thus, the studies [3] made it possible to develop express methods for ultrasonic testing of water permeability of isolation joint and concrete of canal linings, which (with a sufficient density of ultrasonic sounding) provide acceptable accuracy (with an error of 5 %) for determining water losses through linings.

The issues of the evaluation of efficiency of drainage and concrete blankets of concrete dams on a rocky basis are considered in the work of S.V. Solsky et al. [5], where the authors used the method of numerical modeling and data of field observations.



The study of M.A. Bandurin [9] contains an original software and hardware complex for diagnosing the technical condition of water supply structures of irrigation systems which ensures the detection of defects in linings and ground beds using acoustic and geo-radar location-based methods of non-destructive testing. However, there are no specific examples of their use on existing canals with lining.

During the last 10–20 years, geosynthetic materials [10] in small hydraulic engineering have been increasingly used. They can be successfully used for the facilities intended for nature protection purposes – storage of industrial and household waste, ash dumps, as well as on canals and reservoirs of clean water.

The use of waterproof geosynthetic materials (geomembranes and bentomats) on the canals of irrigation systems (with losses up to 30 %, where 80–90 % of these losses occur due to filtration), is especially promising [11]. In modern conditions, the efficiency of most irrigation canals is 0.75–0.80, and when using a new generation seepage-control lining made of geosynthetics, the efficiency will reach 0.97–0.98 [11]. Thus, the seepage-control effect due to the use of geosynthetic materials for canals can be about 20–30 %.

The articles [6, 7, 11] consider new multilayer constructions of seepage-control coatings using bentonite materials. They differ by the fact that they provide increased reliability due to healing of possible damage to the bentomat and duplication of protective and waterproofing layers.

Despite the fact that the linings using geosynthetic materials (geomembranes and bentomats) are highly reliable, nevertheless, various damages can happen during construction and operation. Therefore, a significant amount of scientific works has been devoted to studying the water permeability of polymer screens and linings.

We would like to highlight the article of the authors [12] where various methods for calculating the water permeability of polymer screens are considered: experimental, theoretical and experimental-theoretical. When analyzing the filtration flow through the hole in the polymer geomembrane according to a number of calculated dependences, including J.P. Giroud [13], the results are consistent with each other. However, according to the formula of R.K. Rowe [14], the discrepancy reaches 75 %.

Another article of the authors [15] investigates the problem of water permeability of a polymer screen made of geomembrane through a system of slots. The solution to this issue was obtained by the method of conformal mappings and the motion hodograph.

Here, comparison with the formula of J.P. Giroud gives more discrepancy in the range of 67–128 % depending on the width of the slot, which is fundamentally different from other formulas because it uses the law of nonlinear filtering and empirical coefficients according to field studies.

Foreign authors [16, 17] obtained an empirical equation for calculating the flow rate of the liquid through a composite coating due to defects in the geomembrane. Three types of defects (circular defects, defects of infinite length and damage in the form of cracks) and three types of contact (excellent, good and bad) were considered.

Hydrated bentonite has a low shear resistance, which can have a negative affect to the stability of structures including bentonite clay inserts (GCL) [16, 17]. The GCL bentonite layer is encapsulated between two geomembranes which reduce the possibility of bentonite hydration. These articles present an analytical method for evaluating the degree of hydrated area of a bentonite layer depending on time, initial and hydrated moisture of bentonite, the hydraulic conductivity of bentonite, the width of the floor, the distance between the floors.

The potential assessment of the longevity of exposed geotextiles and geomembranes is considered in [18]. In case of the unexposed (or coated) high density polyethylene (HDPE) geomembrane with a thickness of 1.5 mm with a value of 50 % of the remain firm and elongation, the half-life under these conditions was approximately 450 years. Laboratory incubation would take 12 years. The data was then extrapolated to a temperature of 20 °C for laboratory values of the half-lives. For open geosynthetics, the situation is completely different. They are directly exposed to ultraviolet radiation at elevated temperatures, that reduces the service life. The ratio of unexposed and exposed samples for the HDPE geomembrane is approximately seven. Research results for geomembranes range from 47 to 97 years, which took 12 years of laboratory incubation to reach. These results are considered to be the most interesting and were first obtained by the authors.

However, the data on the durability of closed geomembranes in [18] are significantly overestimated. So, according to our calculations [11] (according to the obtained formula from the Rice equation), the predicted (calculated) service life of geomembranes with a protective coating of rockfill is 130 years. As for the open geomembranes without protective coatings, their service life, according to our on-site surveys, can be maximum of 25 years. Similarly, Techpolymer company guarantees the service life of geomembranes made of HDPE and LDPE polyethylene to be minimum of 25 years. On-site and laboratory studies of Carpi company [19] also have showed that the service life of permanently open geomembranes is more than 50 years, and for geomembranes under water - 200 years. The Federal Institute for Materials Research in Berlin (BAM) has performed severe tests of the service life of bentonite mats [20] during the period of 365 days. Then the test

results were extrapolated by the Arrhenius method, according to which the period of the possibility of using bentomats for 200 years was established, which confirms the previously considered data.

Considerable attention is also paid abroad to the use and research of geosynthetic materials (geomembranes) and bentonite mats (bentomats). The article [21] discusses laboratory studies of the flow efficiency of conventional and multicomponent geocomposites for five different bentonite clay inserts (GCL) and a number of different geomembranes (GM).

The canal lining is used to reduce the loss of water pressure during irrigation [22]. The use of geosynthetic materials that have been widely used in construction areas, in combination with concrete or as a separate material by replacing concrete with PVC, geosynthetic material is the most economical material for canal lining.

The influence of the defect in the geomembrane on the water filtration in soil dams and methods for filtration monitoring were considered in [23]. Defects in the geomembrane can lead to the potential danger of a dam with a geomembrane on its surface. Therefore, three-dimensional saturated and unsaturated seepage fields with various sizes of defects in the geomembrane were modeled by FEM method. The process of filtering through geomembrane defects was modeled using methods for removing defective elements and enhancing permeability. The results show that leakage, caused by defects, has a significant effect on the local seepage field near the defects and slightly affects other parts of the dam.

The overall scheme for calculating the flow rate of a liquid through a composite coating (geomembrane + ground base) with holes is presented in [14]. The solutions obtained for a circle hole and damaged ripples can be used to interpret field conditions and analyze leakage data under on-site conditions. Moreover, a number of existing solutions are obtained as special cases from the general solution.

The longevity of the open geomembrane coatings is considered in [24, 25]. It is noted that factors such as ultraviolet radiation, elevated temperature and exposure to oxygen reduce the geomembrane service life. For incubation purposes, ultraviolet fluorescent lamps were used, where five different geomembranes were evaluated. Each material was incubated at temperatures from 60 to 80 °C, up to 50 % of reduction in strength and elongation. The results received by the authors are similar [18].

M.P. Sainov and A. O. Zverev [26] have performed research of the stress-strain behavior of rockfill dam with a screen with the main waterproof element of a polymer geomembrane. Thin geomembrane modeling was carried out on the example of the Bovilla dam (Albania) built in 1996. The results of numerical calculations showed that the most vulnerable part of the dam is the interface node between the screen and the concrete structure.

Other authors consider the results of experimental studies of tensile polymer geomembranes (made of polyvinyl chloride and polyethylene). The test procedure differs from the standard and is similar to that adopted abroad. A geomembrane (fixed at the edges) experiences a normal state and is in a state of biaxial tension. As experiments have shown, the tensile strength of geomembranes made of polyethylene is about 2.5 times higher than that of geomembranes made of polyvinyl chloride.

Interesting studies on self-healing clay-cement diaphragm of ground dams are given in the article [27]. Using the dam of the Gotsatlinskaya HPP (Republic of Dagestan, Russian Federation) as an example, we can consider the process of colmation of slot-like damages of such a diaphragm. Mathematical models in two-dimensional and three-dimensional formulation were developed. By numerical simulation, a quantitative assessment of the dynamics of the pressure gradients for the following cases is obtained: fully operational seepage-control element with a through and washed crack.

Based on the review of both domestic and foreign publications, we can conclude the domestic literature has only few publications on the research issue that concern the efficiency and reliability of linings, but at the same time in the last 5–10 years a whole series of works appeared regarding the use of new geosynthetic materials for canals to create linings of increased efficiency and reliability, some of which are protected by patents of the Russian Federation. In foreign publications, many of the works are devoted to researchers of geosynthetic materials, in particular to polymer geomembranes and especially bentonite mats. Therefore, the main research questions relate to the water permeability of the geomembrane, there are only few works regarding the models of water permeability of bentomats taking into account self-healing of damages in view of their complexity, and a significant number of publications still raise the issues of longevity (service life) of geosynthetic materials. Meanwhile, there are no works regarding the screen constructions, coatings and linings in foreign publications. Studies of longevity give overestimated results because they are based on a very short test period. The calculation formulas for determining the water permeability of screens take into account many heterogeneous facts that have fractional degrees that violate the principles of dimensional theory, and, in the end, they are not confirmed by on-site data and laboratory tests with samples. No studies have been found in foreign publications on the comparative effectiveness of various canal linings, including the use of geosynthetics.

Taking into account the above conclusion on the review of publications, we the necessary study of the effectiveness and durability of concrete blankets made of geosynthetic materials (GM) in relation to the channels quite reasonable and appropriate. Moreover, the open irrigation network of channels in Russia (only in state ownership) is more than 50 thousand km, 43 % of which require reconstruction, and the total demand for fuel and lubricants for seepage-control lining is by 2030 will be 1.8 billion m². At the same time, the antifiltration effect of the use of GM on channels will be 20–30 %, which will save from losses up to 2 km³/year.

Thus, the purpose of the present study is to examine the efficiency and longevity of seepage-control linings made of geosynthetics materials.

The purposes of the study include as follows:

- analysis of domestic and foreign publications regarding the methods for assessing the efficiency and longevity of seepage-control linings;
- justification of criteria for the efficiency and longevity of seepage-control linings of canals made of geosynthetics materials;
- development of new and improved constructions of seepage-control linings made of geosynthetics materials;
- study of the efficiency and longevity of seepage-control linings made of geosynthetics materials;
- development of a technique for efficiency and longevity of linings made of bentomats taking into account their self-healing;
- a comparative analysis of the efficiency of various types of seepage-control linings of canals.

2. Methods

Consider the methodology for determining the effectiveness of anti-filtration lining of bentonite mats in the presence of possible damage, taking into account their healing.

Methodology for calculation of the efficiency (permeability) of a bentomat lining (taking into account self-healing of damages) was carried out by the method of successive replacement of stationary states, when the time-varying contour of healing of a circular shape damage is replaced by a number of its stationary states with an interval of time $\Delta\tau_i$. Such a replacement of the healing circuit makes it possible to consider the filtering process through damage in the bentomat as established over a time interval $\Delta\tau_1$. This is justified by the fact that the healing process is very slow, and therefore, filtering through screen damage is quite acceptable to consider stationary for a time interval $\Delta\tau_i$ – with the healing speed in the sample $v_s = 0.67$ mm/hour.

As a result, the filtering process through damage to the screen will differ from other types of cladding in that it is unsteady, since when hydrated, the damage is partially healed.

With complete hydration of the damage for the considered example, the healing time is [10]: $\tau = 37.5$ hour. With a diameter of damage of mm, the healing efficiency is 80–100 %.

The healing rate in the initial period for Ca-bentonite is determined by the formula:

$$v = \frac{r_0}{\tau}.$$

Healing of Na-bentonite lesions will be faster, and the healing rate will be greater. For this, it is necessary to conduct special studies in laboratory conditions.

To calculate the effectiveness (water permeability) of the anti-filtration cladding from bentates, the dependences of the flow rate through the hole in the bentonite mat with a protective layer of soil into the soil base were used.

To solve this problem, p-analytic functions of a complex variable and the conformal mapping method were used. An approximate solution to this problem consists first in considering a plane problem by the method of conformal mappings, followed by establishing a connection with the axisymmetric problem using p-analytic functions. As a result of the solution, the authors of [12] obtained approximate calculation formulas for the following particular cases:

when $k_2 / k_1 \geq 10$:

$$q_0 = \frac{2\pi^2 k_1 r_0 (h_0 + \delta_o)}{\ln(8\delta_0 / \pi r_0)}, \quad (1)$$

when $k_2 / k_1 < 10$:

$$q_0 = \frac{2\pi^2 k_1 r_0 (h_0 + \delta_0 - h_1)}{\ln(8\delta_0 / \pi r_0)}, \quad (2)$$

h_1 is piezometric pressure in the bentate screen hole, m:

$$q_0 = \frac{2\pi^2 k_1 r_0 (h_0 + \delta_0 - h_1)}{\ln(8\delta_0 / \pi r_0)}, \quad (3)$$

where σ is the ratio of the filtration coefficients of the protective and underlying layers of the screen, $\sigma = k_1 / k_2$;

k_1 is filtering coefficient of the protective coating, m³/day;

k_2 is coefficient of filtration of the underlying base, m³/day;

r_0 is hole radius in the bentomate screen, m;

h_0 is water depth in the channel, m;

δ_0 is the thickness of the protective layer of soil, m;

H_c is capillary vacuum of the base soil $H_c = (0.5-0.6)$;

h_c is the height of the capillary rise of water in the ground, m.

To determine the predicted service life of the linings, the on-site experiments of samples of polymer materials were used, which were carried out in a test basin with an area of 5x1.9 m along the bottom with slopes 1:2.5 with a water depth of 3.0 m under various conditions; under water at $t = -20+30$ °C, direct atmospheric exposure at $t = -20+30$ °C; with a protective coating of ground with a thickness of 0.5 m at $t = -15+20$ °C. The tests were performed on a polymer geomembrane of high density polyethylene (HDPE) 1.0 mm thick with tensile strength of $\sigma_{p0} = 27$ kN/m and elongation of $\varepsilon_0 = 700$ %. On-site tests of the samples have been carried out for 8–10 years, and later, the extrapolation method was used to evaluate the longevity. In addition, the longevity (service life) was determined by calculation using the Rice and Arrhenius equations. After sampling the geomembrane directly from the test basin, the tensile test (σ_p) and elongation tests (ε_p) were carried out at the tensile testing machine.

A comparative analysis of the efficiency of various types of seepage-control linings was carried out to compare the main technical indicators and reliability indicators, the longevity of traditional concrete linings, ground-film and concrete-film linings (from 0.2–0.4 mm thick polyethylene film) with new types of linings - concrete-film and ground-film linings from polymer geomembrane (thickness from 1.0 to 1.5 mm). As indicators, the averaged and admissible filtration coefficients of the lining were taken into account, reliability indicators - the probability of operation without failure and the probability of failure and longevity.

3. Results and Discussion

3.1. Criteria for the efficiency and longevity of linings made of geosynthetic materials

Modern seepage-control canal linings should have a sufficiently high efficiency and longevity. In accordance with these requirements, they should minimize filtering losses and exclude flooding of the canal territories with groundwater. In addition, they should exclude failures and damages, first of all, of the seepage-control element during operation and have a long service life corresponding to the canal class as a hydraulic structure in accordance with Russian Building Norms SP 58.13330.2012 [28].

Using the experience of designing, building and operating canals in Russia and abroad [11], the following criteria for the efficiency and longevity of seepage-control linings using geosynthetic and geocomposite materials are proposed:

- considering the permeability of the seepage-control element from the geomembrana (GM) or bentonite mats (GCL):

$$k'_{GM} \leq k'_{GM.PER.}; k'_{GCL} \leq k'_{GCL.PER.};$$

- considering the strength when breaking geomembrane or bentomats:

$$\sigma_{GM} \geq \sigma_{GM.PER.}; \sigma_{GCL} \geq \sigma_{GCL.PER.};$$

- considering the relative elongation of the geomembrane or bentomats at break:

$$\varepsilon_{GM} \leq \varepsilon_{GM.PER.}; \varepsilon_{GM} \leq \varepsilon_{GCL.PER.};$$

- considering the longevity (service life) of the geomembrane or bentonite mats:

$$\tau_{GM} \geq \tau_{GM.PER.} = \tau_{NOR.}; \tau_{GCL} \geq \tau_{GCL.PER.} = \tau_{NOR.}$$

For protective coatings (concrete, stone, gabion and ground), the criteria for efficiency and longevity are as follows:

- considering the efficiency of the protection of the seepage-control filter element ($k_{ef.}$) together with the geotextile gasket from through damage and punctures of the geomembrane or bentomat:

$$k_{ef.} = F_{dam.} / F_{total} \leq 0.01 \%;$$

- considering the hydraulic protective covering:

$$n_{prot.} \leq n_{per.} = 0.0175 \div 0.0225;$$

- considering to the degree of destruction of the protective coating ($\Pi_{pr.}$):

$$\Pi_{pr.} \leq \Pi_{pr.per.} = F_{pr.cov.} / F_{pr.total} \leq (1 \div 2) \%;$$

- considering the longevity (service life) of protective coatings:

$$t_{pr.} \geq t_{pr.per.} = t_{nor.}$$

The following designations are accepted here:

- k'_{GM}, k'_{GCL} are averaged (according to the study) coefficient of filtration of the lining made of geomembrane or bentomat, m/s;
- $k'_{GM.PER.}, k'_{GCL.PER.}$ are permissible coefficient of filtration of the lining made of geomembrane or bentomat, m/s;
- $\sigma_{GM}, \sigma_{GCL}$ are tensile strength of the geomembrane or bentomat according to tests, MPa, kN/m;
- $\sigma_{GM.PER.}, \sigma_{GCL.PER.}$ are permissible values of the strength of the geomembrane or bentonite, MPa, kN/m;
- $\varepsilon_{GM}, \varepsilon_{GCL}$ are elongation at break of the geomembrane or bentomat according to test results, %;
- $\varepsilon_{GM.PER.}, \varepsilon_{GCL.PER.}$ are permissible values of elongation according to tests of geomembrane or bentomat, %;
- τ_{GM}, τ_{GCL} are longevity (service life) according to geomembrane or bentomat research, years;
- $\tau_{GM.PER.}, \tau_{GCL.PER.}, \tau_{nor.}$ are permissible values of geomembrane or bentomat service life, as well as the rated value of the hydraulic structure according to SP 58.13330.2012 [28], years;
- $k_{ef.}$ is efficiency factor of the protection of the seepage-control element together with the geotextile gasket;
- $n_{prot.}, n_{per.}$ are coefficient of hydraulic roughness of the protective coating according to observations and allowed according to the reference data;
- $\Pi_{prot.}, \Pi_{prot.per.}$ are the degree of destruction of the protective coating according to study or the permissible value according to the reference data, %;
- $t_{prot.}, t_{prot.per.}$ are the longevity (service life) of the protective coating according to the study and the permissible value according to the standard.

3.2. New constructions of seepage-control linings made of geosynthetics materials

In order to ensure increased water impermeability, reliability, and longevity, it is recommended to use multilayer coating structures on the canals of irrigation and drainage systems and reservoirs, including waterproof, protective, and filtering elements made of geosynthetic materials (Figure 1) [6].

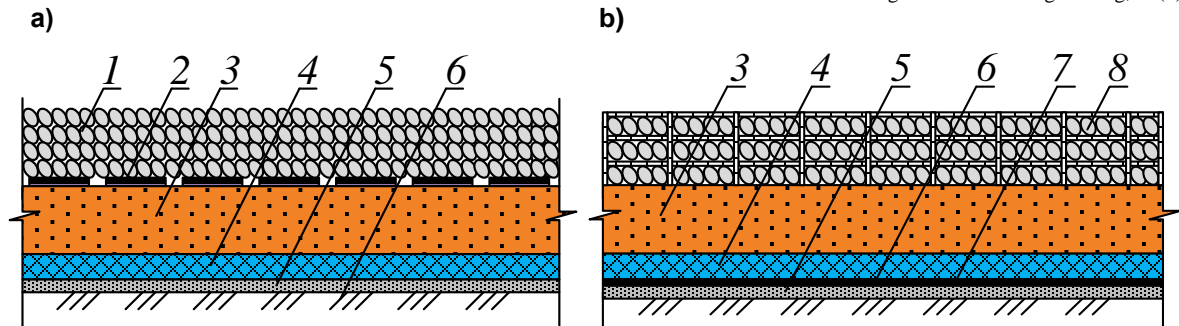


Figure 1. Multilayer constructions of seepage-control coatings with geosynthetics for canals and ponds: a, b – with a seepage-control element made of bentonite mats and a protective layer; 1 – a protective coating of rockfill; 2 – non-woven geotextile; 3 – a protective layer of ground; 4 – bentonite mat; 5 – the underlying layer of sand; 6 – compacted base; 7 – polymer geomembrane thermally bonded with a lower layer of bentonite mat; 8 – gabions filled with rocks.

The construction made of the bentonite mat coating (Figure 1, a) consists of three protective layers (rockfill, geotextiles, and a protective ground layer) and a seepage-control layer of bentonite mats. Moreover, in case of damage to the bentonite mat during the construction or operation of the structure, the damage will be regenerated (healed) during the hydration period of the material.

The coating structure (Figure 1, b) consists of two protective layers (gabions filled with rock material and a protective layer of ground), and the main working layer, including a bentonite mat, additionally thermally bonded with a polymer waterproof geomembrane. In case of damage to one of the seepage-control elements (bentonite mat or geomembrane), the structure will be watertight due to the second (duplicate) element.

Based on the analysis of the functions of each structural element of multilayer seepage-control coatings (Figure 1), the authors concluded that, in general, the first structure acquires an increased level of protection (from erosion and damage) - a triple level of reliability, and to provide a seepage-control function – a single level. For the second structure, the protective and seepage-control function correspond to a double level of reliability.

3.3. Study of the efficiency and longevity of canal linings made of geosynthetics materials

The calculations of the efficiency (water permeability) of linings with a geomembrane and protective coatings of ground and concrete were previously considered in the works of the authors [11, 15, 29].

Considering the fact that there are no methods for calculating of efficiency of bentonite mats linings (water permeability) taking into account self-healing of their damages, let us consider these features and, accordingly, the calculation method.

The main advantage of bentonite mats is the ability to regenerate (“heal”) damage due to swelling of the bentonite mat when it is moistened [20]. Bentonite mats withstand a large number of cycles of “freezing – defrosting” and “hydration – dehydration” with high waterproofing properties.

When using Na-bentonite due to its hydration, a 12–16 times increase in volume occurs, and when hydrating Ca-bentonite – only 2–4 times. For a tight fit of the bentomat to the base, loading with a protective coating is necessary with a pressure on the bentomat of at least 250 kg/m², for example, with a concrete thickness of at least 0.10 m and a rock material thickness of at least 0.20 m.

Currently, bentonite mats in Russia are manufactured by “Techpolymer”, “Bentisol”, “Isobent” (Russian Federation) and some other manufacturers, that usually use activated calcium bentonite. This results in a high filtration rate at the first contact with water. Another disadvantage of domestic production of bentonite mats is the uneven distribution of bentonite clay granules between geotextile layers. The use of calcium bentonite clay significantly affects the deterioration of the properties of bentomats, the producibility of their use and the longevity of the seepage-control screen.

The bentomats have been used abroad for several decades already. “NAUE” (Germany) developed and patented bentonite mats of the “Bentofix” brand back in 1937. “Bentofix” brand bentonite mats are made from natural sodium bentonite in the form of a powder, mainly with a fraction of ≤ 0.063 mm (85 %). Due to the use of bentonite powder, the best (uniform) seepage-control characteristics of bentomats (over the entire surface) are achieved, resulted in the instant hydration upon contact with water. Due to the absence of air cavities in the mats, a higher internal pressure is created inside, which provides higher seepage-control properties of the material [6].

Bearing and covering geotextile materials in such bentomats are needle-punched together with subsequent heat treatment, resulting in the formation of a so-called “thermal lock”, which contributes to higher shear strength of the lower and covering geotextiles, and due to high internal pressure, the period of the bentomat hydration and self-healing of possible damage is reduced [6].

Starting from 2012 the Donskoy Principal Canal (DPC) (Rostov region, Russian Federation) has been under reconstruction that provides for the expansion of the canal from 45th to 112th km, an increase in its flow efficiency from 80 m³/s to 110 m³/s and a lining with a seepage-control screen made of “Bentofix” bentomats in the most dangerous areas with a length of more than 2500 m with a protective coating of rockfill (thick at the bottom – 0.7 m, on the slopes – 0.3 m [6].

On-site investigation and calculations of the efficiency of DPC sections with bentomat linings carried out at the end of 2018 by the authors of [6] showed high efficiency, reliability, and working capacity of the lining.

Table 1 shows the results of comparing the efficiency of the canal lining made of bentomats with alternative options.

Table 1. Estimated efficiency of seepage-control lining made of bentomats at DPC and alternative option in the 1st section (PK 108 + 62 – PK 112 + 94).

Type of lining or screen	Lining (screen) filtration coefficient t, k , m/s	Filtration resistance of the lining (screen), F , m	Specific filtration losses from the canal with the lining (screen) $Q_{f.scr.}$ or $Q_{f.alt.}$, m ² /day	The efficiency of lining (screen) use $\mathcal{E}_{scr.}$ or $\mathcal{E}_{alt.}$	Efficiency criterion		
					$N_1 = \frac{Q_{f.land}}{Q_{f.scr.}}$	$N_2 = \frac{\mathcal{E}_{scr.}}{\mathcal{E}_{alt.}}$	$N_3 = \frac{\Phi_{scr.}}{\Phi_{alt.}}$
Bentofix lining	10^{-14}	$5.2 \cdot 10^8$	$1.3 \cdot 10^{-7}$	$5 \cdot 10^6$	$5 \cdot 10^6$	–	–
Alternative options							
Film screen	10^{-8}	520	0.109	6.0	6.0	$8.3 \cdot 10^5$	$1 \cdot 10^6$
Geomembrane screen	10^{-10}	51800	0.0013	506.0	$5 \cdot 10^2$	$1 \cdot 10^4$	$1 \cdot 10^4$
Clay compacted screen	$1.2 \cdot 10^{-9}$	4290	0.0015	427.0	$4.3 \cdot 10^2$	$1.2 \cdot 10^4$	$1.2 \cdot 10^4$

Note: Specific losses for filtering from a canal in the ground channel $Q_{f.land} = 0.658$ m²/day.

The criteria given in Table 1 correspond to the following: N_1 is efficiency criterion for filtration costs of lining made of bentomats in comparison with the ground bed; N_2 is efficiency criterion according to the effect degree of the lining from bentomats in comparison with alternative options (film screen, screen made of geomembrane, clay compacted screen); N_3 is efficiency criterion for filtration resistance of a bentomat lining compared to alternative options.

Analysis of the results of the calculated assessment of the criteria in Table 1 indicates that, according to the efficiency criterion, N_1 the lining made of bentomats far exceeds the ground channel by $5 \cdot 10^6$ times, and alternative options exceed the ground channel by 6 to 500 times. According to the criterion N_2 , the lining made of bentomats exceeds all alternatives from $1 \cdot 10^4$ to $8.3 \cdot 10^5$ times, and by the criterion N_3 is respectively, from $1 \cdot 10^4$ to $1 \cdot 10^6$ times. Thus, according to all the criteria, a very high assessment of the efficiency of bentomat lining was obtained, and this characterizes its high seepage-control properties.

Figures 2, 3 show the results of studies of the longevity (service life) of a lining with a polymeric geomembrane made of HDPE polyethylene with a thickness of 1.0 mm in a test basin where samples of materials were in different conditions.

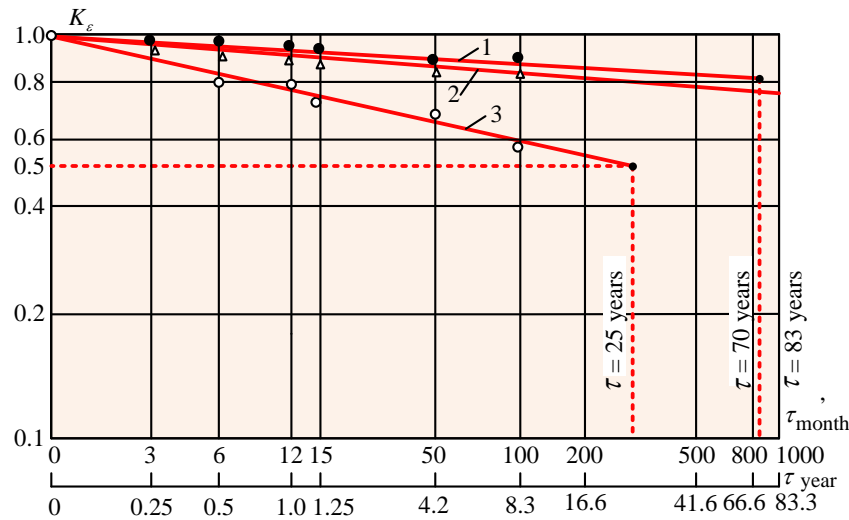


Figure 2. Change in the coefficient of aging of polymer membranes by breaking elongation in various conditions: 1 – under water at $t = -20+30\text{ }^{\circ}\text{C}$; 2 – direct atmospheric exposure at $t = -20+30\text{ }^{\circ}\text{C}$; 3 – a protective coating of ground with a thickness of 0.5 m at $t = -15+20\text{ }^{\circ}\text{C}$.

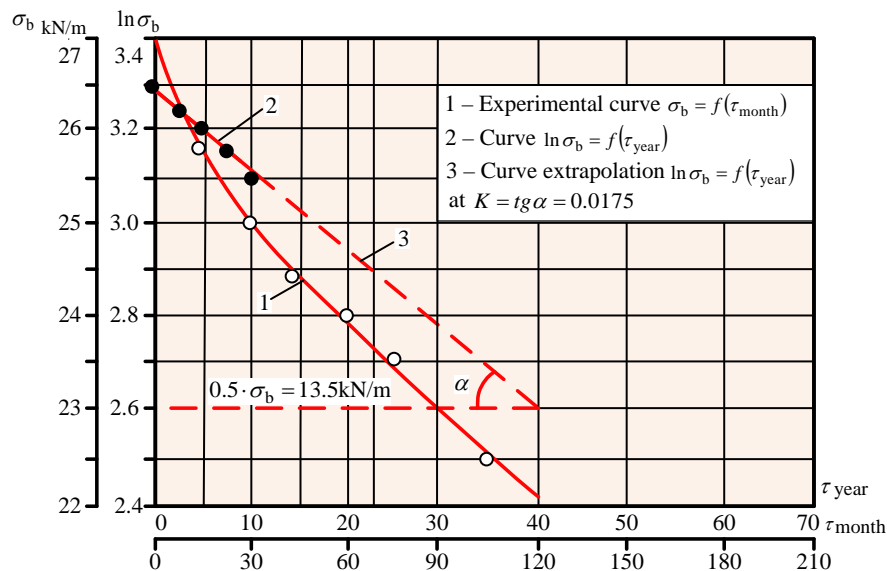


Figure 3. Diagram of changes of geomembrane strength at break depending on the time of observation.

Studies have shown the aging coefficient of the polymer geomembrane $K_{\epsilon} = \epsilon_{\tau} / \epsilon_0$ (where ϵ_0 is the initial value of the relative elongation of the geomembrane at break (σ_b); ϵ_{τ} is the relative elongation after exposure over time τ). On the diagram, in the logarithmic coordinates (Figure 3.2) during the exposure of the samples (10 years) and their further extrapolation, the service life of the geomembrane under water was equal to 70 years, and under the protective coating from the ground – 83 years. Under direct atmospheric exposure (ultraviolet radiation), curve 3 is characterized by a significant drop in values K_{ϵ} with the intersection of the limit line with $K_{\epsilon} = 0.5$ at $\tau = 25$ years.

Figure 3 shows the experimental curve 1 of the change in the geomembrane strength at break $\sigma_b = f(t_{\text{month}})$, which intersects the abscissa axis with $t = 120$ months or 10 years, curve 2 $\ln \sigma_b = f(t_{\text{month}})$ is built on a different time scale for clarity, which is built on the upper section based on the results of testing the geomembrane under a protective coating of ground, and on the bottom one, it is extrapolated as a straight line on a semi-logarithmic scale. We will use these data to calculate the longevity (service life) according to the Arrhenius equation, which has the following form:

$$\ln \delta_p = \ln \delta_{p_0} - K'' \cdot \tau \cdot e^{-\frac{Q}{E}}, \quad (4)$$

where δ_p is minimum strength, kN/m;

δ_0 is initial strength, kN/m;

Q is activation energy;

E is reaction energy;

K'' is the coefficient including the constants K and K' is a function of the concentration of substances, as well as their nature.

After transforming equation (4) we obtain an expression for determining the longevity (service life):

$$\tau = \frac{\ln \sigma_0 - \ln \sigma_p}{K'' \cdot e^{-\frac{Q}{E}}}, \quad (5)$$

where K'' is the coefficient determined by the slope of line 3, as $\text{tg} \alpha$:

$$K'' = \text{tg} \alpha = \frac{3.3 - 2.6}{40} = 0.0175.$$

Substituting the found value in equation (5), we obtain the value of the service life of the geomembrane according to the Arrhenius equation:

$$\tau = \frac{3.3 - 2.6}{0.0175 \cdot e^{-0.65}} = \frac{0.7}{0.0175 \cdot (1/1.912)} = 76.5 \text{ years},$$

where the ratio $\frac{Q}{E} = 0.65$ is taken.

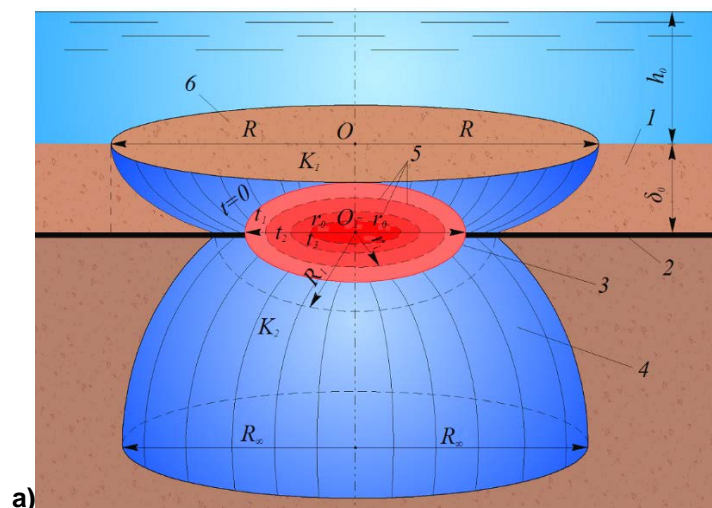
The obtained value of $\tau = 76.5$ years according to the Arrhenius equation closely matches the data in Figure 3.2 in the presence of water or a protective coating from the ground.

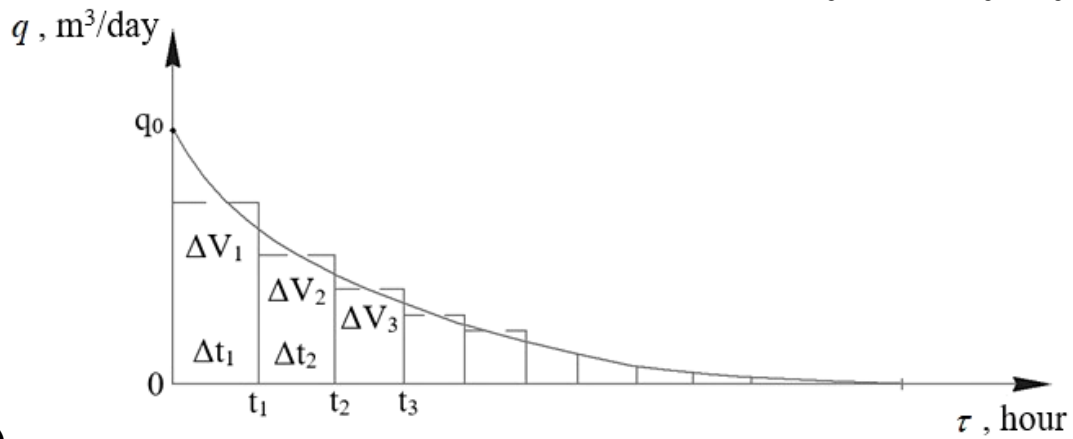
3.4. Technique for calculating the efficiency and longevity of the bentomat lining taking into account their self-healing

This technique for calculating efficiency (water permeability) is based on the assumption that during the operation of such lining the damage can happen, so they will be healed as a result of the regeneration of bentonite granules.

To calculate the water permeability of a screen made of bentomats (Ca-bentonite) with a protective ground layer (ground-film lining), we will use the method of successive change of steady states proposed by. It lies in the fact that the entire process of non-steady filtration is divided into a number of steady states, when damage is partially healed, where we will consider the filtration costs through the damage over a time interval $\Delta \tau$ to be constant, and the leakage volumes vary along a concave curve.

Figure 4 shows a diagram of the water permeability of the bentomat screen under conditions of healing.





b)

Figure 4. Scheme of water permeability of a bentomat screen with a protective layer of ground under conditions of damage self-healing:

a) design diagram of screen permeability; b) a graph of changes in costs and volumes of leakage through the screen;

1 – a protective layer of ground; 2 – seepage-control screen from bentomats;

3 – contour of the initial damage; 4 – domed filtering area at the base of the screen;

5 – contours of changes in the position of damage at time instants $\tau_1, \tau_2 \dots \tau_3$;

6 – filtration area in the protective layer of ground.

To calculate the water permeability in the conditions of healing of bentomat we will accept the following assumptions:

1. damage to the screen is formed during prolonged use of the canal due to significant deformation of the ground base under the screen;
2. the pressure on the screen will be assumed constant and appropriate to the normal operation of the canal;
3. healing of screen damage occurs due to repeated regeneration;
4. the boundaries of the damage healing contours are conditionally accepted around the circumference.

For the following screen healing contours:

$$q_i = \frac{2\pi^2 k_1 r_i (h_0 + \delta_0)}{\ln(8\delta_0 / \pi r_i)}, \quad (6)$$

where r_i is the radius of damage during healing.

The time interval (t) is determined by the formula:

$$\Delta\tau = \frac{\tau}{n_{\text{int}}}. \quad (7)$$

Taking the number of intervals ($n_{\text{int}} = 10$), $\Delta\tau$ will be as follows:

$$\Delta\tau = \frac{37.5}{10} = 3.75 \text{ hours.}$$

Then the radius of the hole in the screen during healing will be the following:

$$r_i = r_0 - n_{\text{int}} \cdot r_0, \quad (8)$$

where n_{int} is the number of intervals when healing damage.

The amount of water leakage during the time interval $\Delta\tau_i$ will be:

$$\Delta V_i = q_{\text{av},i} \cdot \Delta\tau_i, \quad (9)$$

where $q_{\text{av},i}$ is the average consumption for the healing time interval $\Delta\tau_i$,

$$q_{av.i} = \frac{q_i + q_{i-1}}{2}. \quad (10)$$

The total volume of leakage during filtration for the entire healing period (τ) is found as:

$$V_{fil} = \sum_{i=1}^{n_{int}} \Delta V_i = \sum_{i=1}^{n_{int}} q_{av.i} \cdot \Delta \tau_i. \quad (11)$$

With $k_2/k_1 < 10$ the calculated formula of the filtration flow will take into account the pressure in the hole (3) [12]. For the initial screen damage contour.

For the following healing contours:

$$q_i = \frac{2\pi^2 k_1 r_i (h_0 + \delta_0 - h_1)}{\ln(8\delta_0 / \pi r_i)}, \quad (12)$$

$$\text{where } h_1 = \frac{\pi^2 \sigma (h_0 + \delta_0) - 4H_\kappa \ln(8\delta_0 / \pi r_i)}{\pi^2 \sigma + 4 \ln(8\delta_0 / \pi z_i)};$$

$$\sigma = k_1 / k_2.$$

Let us consider an example of calculating the water permeability of a bentomat lining film based on self-healing of bentonite granules.

Initial data: $L_c = 10 \text{ km} = 10000 \text{ m}$, $\chi_c = 15 \text{ m}$, $k_1 = 1.0 \text{ m/day}$, $k_2 = 0.3 \text{ m/day}$, $\delta_0 = 0.5 \text{ m}$, $h_0 = 3.0 \text{ m}$, $d_0 = 50 \text{ mm} = 0.05 \text{ m} = 5.0 \text{ sm}$, $r_0 = d_0 / 2 = 0.05 / 2 = 0.025 \text{ m}$, $H_c = 0.5 \text{ m}$, $\tau = 37.5 \text{ hour}$, $n = 10$.

1. Let us determine the speed of healing of circle damage in the bentomat screen according to the formula:

$$v = \frac{r_0}{\tau}, \quad (13)$$

at $r_0 = 0.025 \text{ m}$:

$$v = \frac{0.025}{37.5} = 0.00067 \text{ m/hour} = 0.67 \text{ mm/hour}.$$

2. Let us determine the time interval $\Delta \tau_i$ by the formula (7):

$$\Delta \tau_i = \frac{\tau}{n_{int}} = \frac{37.5}{10} = 3.75 \text{ hours}.$$

3. The radius of change of the hole in the screen for the i -th interval is:

$$r_i = r_0 - n_{int} \cdot \Delta r,$$

where Δr is the change in the radius of damage in one time interval ($\Delta r = r_0 / n_{int} = 0.025 / 10 = 0.0025 \text{ m} = 2.5 \text{ mm}$).

4. Let us calculate the filtration leakage rate for the entire healing period, according to the formula (12):

at $r_0 = 0.025 \text{ m}$:

$$\begin{aligned} q_0 &= \frac{2\pi^2 k_1 r_0 (h_0 + \delta_0 - h_1)}{\ln(8\delta_0 / \pi r_0)} = \frac{2 \cdot 3.14^2 \cdot 1.0 \cdot 0.025 (3.0 + 0.5 - 2.21)}{\ln(8 \cdot 0.5 / 3.14 \cdot 0.025)} = \\ &= \frac{0.636}{3.93} = 0.162 \text{ m}^3/\text{day}, \end{aligned}$$

where:

$$h_1 = \frac{\pi^2 \sigma (h_0 + \delta_0) - 4H_k \ln(8\delta_0 / \pi r_0)}{\pi^2 \sigma + 4 \ln(8\delta_0 / \pi r_0)} =$$

$$\frac{3.14^2 \cdot 3.33(3.0 + 0.5) - 4 \cdot 0.5 \cdot \ln(8 \cdot 0.5 / 3.14 \cdot 0.025)}{3.14^2 \cdot 3.33 + 4 \cdot \ln(8 \cdot 0.5 / 3.14 \cdot 0.025)} =$$

$$= \frac{114.91 - 7.86}{32.83 + 15.72} = \frac{107.05}{48.56} = 2.21 \text{ m};$$

$$\sigma = k_1 / k_2 = 1.0 / 0.3 = 3.33.$$

The summary results of the calculation of the permeability of the bentomat through a single damage are presented in table 3.2 (at $h_0 = 3.0$ m, $\delta_0 = 0.5$ m, $d_0 = 0.05$ m, $k_1 = 1.0$ m/day, $k_2 = 0.3$ m/day, $\tau = 37.5$ hour).

5. The amount of leakage through a single damage to the ground-film lining made of bentomats according to the formula (12):

$$\text{at } \tau_1 = 3.75 \text{ hour, } q_{\text{av.1}} = \frac{0.162 + 0.195}{2} = 0.154 \text{ m}^3/\text{day},$$

$$\Delta V_1 = q_{\text{av.1}} \cdot \Delta \tau = 0.154 \cdot 0.156 = 0.0244 \text{ m}^3.$$

In accordance with the performed calculations and total leakage for the healing period $\tau = 37.5$, presented in Table 2, the total leakage (V) through possible single damage to the bentomat after its complete healing will be $V = 0.1223 \text{ m}^3$.

Then the total volume of filtration leaks through the total number of possible damages at $n = 10$ will be:

$$V_{\text{total } n=10} = V \cdot n = 0.1223 \cdot 10 = 1.223 \text{ m}^3.$$

Figure 5 shows diagrams of changes in filtration flow depending on the time of healing of a single damage, as well as the volume of water leakage through circular damage, which decreases due to the regeneration of bentonite and healing damage.

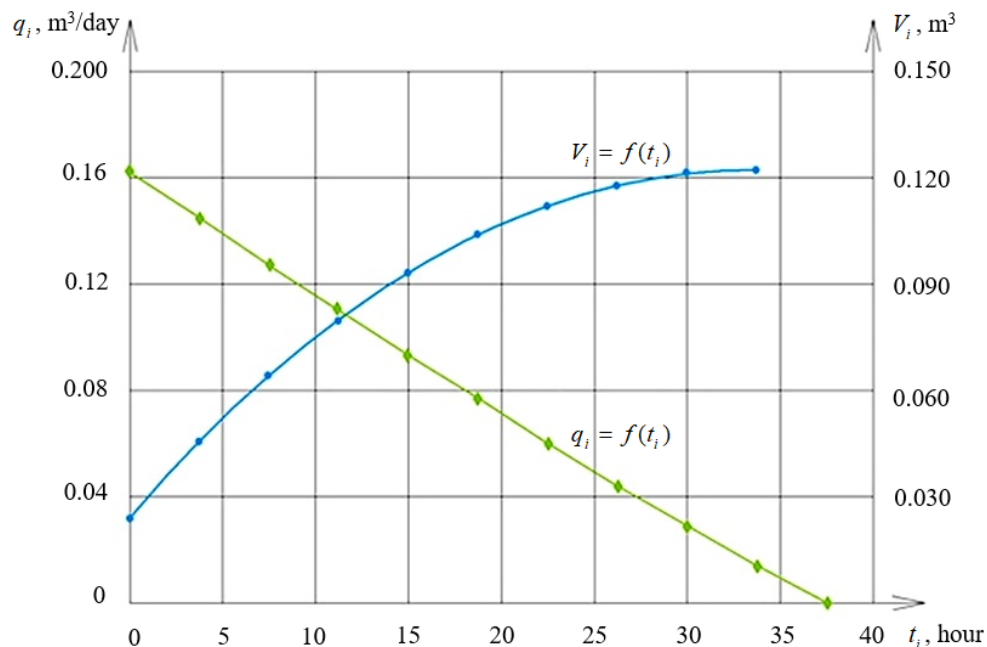


Figure 5. Diagrams of dependencies $q_i = f(\tau_i)$ and $V_i = f(\tau_i)$.

According to this diagram, the filtration flow curve $q_i = f(\tau_i)$ varies from the healing time period along a certain curve close to a straight-line dependence, and the curve $V_i = f(\tau_i)$ of the volume of water leakage through possible single damage to the bentomat is of the type related to the parabolic curve.

Table 2. Summary results of the calculation of water permeability through a single damage to the ground-film lining from bentomats.

Number of intervals $n_{\text{int}.i}$	Time interval $\Delta\tau_i$, hour	The time period for healing damage, τ_i , hour	The radius of the hole when healing damage, r_i , m	Piezometric pressure in the hole, h_{li} , m	Filtration flow rate for the time interval q_i , m ³ /day	The average filtration rate for the time interval $q_{sr.i}$, m ³ /day	Amount of leakage per time interval ΔV_i , m ³	Total leakage over a period of time V_i , m ³
0	0	0	0.0250	2.21	0.162			
1	3.75	3.75	0.0225	2.18	0.145	0.154	0.0244	0.0244
2	3.75	7.50	0.020	2.16	0.127	0.136	0.0213	0.0457
3	3.75	11.25	0.0175	2.13	0.110	0.118	0.0185	0.0642
4	3.75	15.00	0.0150	2.10	0.093	0.102	0.0158	0.0800
5	3.75	18.75	0.0125	2.06	0.077	0.085	0.0133	0.0933
6	3.75	22.50	0.0100	2.02	0.060	0.068	0.0107	0.1040
7	3.75	26.25	0.0075	1.96	0.044	0.052	0.0081	0.1121
8	3.75	30.00	0.0050	1.89	0.029	0.036	0.0057	0.1178
9	3.75	33.75	0.0025	1.77	0.014	0.022	0.0034	0.1212
10	3.75	37.50	0.0	–	0.0	0.007	0.0011	0.1223

6. The predicted service life (longevity) of the bentomat lining. The calculation is carried out according to the Rice equation [11]. The source data is taken according to analogues.

Initial data: $\Pi_{per.} = 5.1 \cdot 10^{-12}$, $\Pi_{\tau_0} = 2.2 \cdot 10^{-11}$, $k_{\sigma} = \frac{\sigma}{\sigma_0} = \frac{10}{12} = 0.83$, $\bar{\nu} = 0.04$,
 $m_{\Pi_{\tau_0}}^2 = 0.10 \cdot \Pi_{\tau_0}^2 = 0.10(2.2 \cdot 10^{-12})^2 = 0.484 \cdot (10^{-12})^2$.

The service life of the bentomat lining is determined by the formula [11]:

$$\tau\{P\} = \frac{(-\ln P_{GCL})}{\bar{\nu}} \exp\left[\frac{[\Pi_{per.} - (\Pi_{\tau} / k_{\sigma})]^2}{2m_{\Pi_{\tau_0}}^2}\right], \quad (14)$$

$$\tau\{P\} = \frac{(-\ln P_{GCL})}{\bar{\nu}_{\Pi}} \exp\left[\frac{[\Pi_{per.} - (\Pi_{\tau} / k_{\sigma})]^2}{2m_{\Pi_{\tau_0}}^2}\right] =$$

$$\tau\{P\} = \frac{(-\ln 0.99)}{0.04} \exp\left[\frac{[5.1 \cdot 10^{-12} - (2.2 \cdot 10^{-12} / 0.833)]^2}{2 \cdot 0.484 \cdot (10^{-12})^2}\right] = 129.5 \text{ years.}$$

Thus, the predicted service life of the bentomats with the adopted initial data will be about 130 years. According to research [20], the service life of a bentomat screen is 200 years.

3.5. Comparative analysis of the efficiency and longevity of various types of seepage-control canal linings

Using the data of calculations of the efficiency and reliability of seepage-control linings given above in paragraphs. 3.2 and 3.3, we will conduct a comparative analysis of various types of seepage-control linings. The summary results of the lining calculation are presented in Table 3.

As a criterion for the lining efficiency during comparison, we will use the averaged filtration coefficient of the lining calculated according to the theoretical formulas obtained by the methods of filtration theories (by the method of conformal mappings and the motion hodograph).

Comparing the value of the averaged filtration coefficient of concrete lining with the permissible value, we can see that the calculated value is more than the allowed value ($k'_{scr.} = 2.13 \cdot 10^{-5} \text{ m/s} > k'_{scr.nor.} = 0.55 \cdot 10^{-6} \text{ m/s}$), i. e. the necessary efficiency condition is not fulfilled here. This is due to the relatively high permeability of the concrete lining, which exceeds the permissible filtration

coefficient by 2.6 times. We can obtain similar data on other traditional lining such as: ground film and concrete film with a plastic film.

Table 3. Results of the calculation of the efficiency and reliability of different types of seepage-control canal linings.

The name of the efficiency and reliability indicators	Types of seepage-control linings					From bentomats (according to the company "NAUE" [2])
	Concrete	Ground-film (with a film)	Concrete-film (with a film)	Concrete-film (with geomembrane)	Ground-film (with geomembrane)	
1. The average coefficient of lining filtration, $k'_{scr.}$, m/s	$2.13 \cdot 10^{-5}$	$0.5 \cdot 10^{-9}$	$1.4 \cdot 10^{-9}$	$0.215 \cdot 10^{-10}$	$0.1 \cdot 10^{-10}$	$0.5 \cdot 10^{-11}$
2. Allowed filter coefficient, $k'_{scr.per.}$	$0.55 \cdot 10^{-6}$	$1 \cdot 10^{-8}$	$2 \cdot 10^{-8}$	$0.372 \cdot 10^{-6}$	$1.65 \cdot 10^{-6}$	$5 \cdot 10^{-11}$
3. The probability of fail safe performance, $P(t)$	0.95	0.90	0.90	0.99	0.990	0.999
4. The probability of lining failure, $Q(t)$	0.05	0.10	0.10	0.01	0.010	0.001
5. Longevity (service life) of lining, $\tau_{scr.}$, years	35.5	25.0	40.0	61.3	75.6	130.0

When comparing the data of the efficiency of concrete lining with concrete-film lining, including a geomembrane, we are convinced that the latter one has less permeability by $1 \cdot 10^4$ time, and, consequently, the efficiency of concrete-lining is 10,000 times higher than concrete. Such a high efficiency of concrete-film lining with a geomembrane is explained by an increase in its waterproofing properties due to the use of a geomembrane, which is characterized by high resistance to puncturing and other damages.

Even greater efficiency was obtained for a ground-film lining with a geomembrane, and compared to concrete lining it is $4.26 \cdot 10^6$ times.

The analysis of the calculation results in Table 3 shows that the greatest efficiency and reliability are for Bentofix linings from "NAUE" (Germany): by filtration coefficient – $0.5 \cdot 10^{-11}$ m/s. According to the calculation, the predicted service life of such a lining is about 130 years, which is 3.6 times higher than for concrete lining, 2.1 times higher than for concrete-film lining with a geomembrane and 1.7 times higher than for a ground-film lining with a geomembrane.

Table 4. Comparison of the obtained results with other authors on the leakage rate during the filtration through the damage of the bentonite covering.

Source data	Leakage rate due to initial screen damage, $q_0 = \text{m}^3/\text{day}$, according to the formulas				
	Authors (2)/(1)	V.N. Zhilenkova	J.P. Giroud at n		
			10	15	20
$h_0 = 3.0 \text{ m}$,	at $k_2 / k_1 < 10$				
$\delta_0 = 0.5 \text{ m}$,	0.162	$\frac{0.150}{7.4\%}$	$\frac{0.082}{45.3\%}$	$\frac{0.122}{24.7\%}$	$\frac{0.164}{-1.2\%}$
$d_0 = 0.05 \text{ m}$,		at $k_2 / k_1 \geq 10$			
$k_1 = 1.0 \text{ m/day}$,	0.439	$\frac{0.427}{2.7\%}$	$\frac{0.0334}{92.4\%}$	$\frac{0.0501}{88.6\%}$	$\frac{0.0668}{84.7\%}$
$k_2 = 3.0 \text{ m/day}$.					

Note:

1. The numerator is values q_0 , m^3/day , in the denominator there is a discrepancy with the authors' formulas, %.

2. In the formula of J. P. Giroud takes into account the number of damages n and the screen area on which they are located $A = 1 \text{ acre} = 4000 \text{ m}^2$.

Table 5. The comparison of the obtained results with other authors (companies) regarding the durability (service life) of the screen of bentonite coverings.

Source data	Screen life (lifetime), τ , years			
	Calculation by Rice equation (14)	According to BAM [20] using the Arrhenius equation		According to "Bentizole"
$\Pi_{dop} = 5.1 \cdot 10^{-12}$ $\Pi_{\tau 0} = 2.2 \cdot 10^{-11}$ $k_{\sigma} = 0.83$ $\bar{v}_p = 0.04$	129.5	at $t = 15^{\circ}\text{C}$ 200.0	> 400.0	Not limited

Table 6. The comparison of the obtained results with other authors (companies) regarding the durability (service life) of the screen of the geomembrane.

Source data	Screen life (lifetime), τ , years				
	Calculation using the Arrhenius equation (5)	According to Carpi	According to the German Institute of Technology (DIBT)	According to Polypine	According to [18]
$\sigma_{p0} = 26.5 \text{ kN/m}$ $\sigma_p = 22.0 \text{ kN/m}$ $K_{\varepsilon} = 0.5$	76.5	$\frac{200}{50}$	500	80	47–97

Note: The numerator shows data for closed geomembranes, the denominator – for open geomembranes.

The comparison of the obtained results with other authors on the consumption of leaks for filtration through the initial damage in the bentonite covering (Table 4) shows a satisfactory convergence with the formula of V.N. Zhilenkov, as well as the empirical formula of J.P. Giroud at $k_2 / k_1 < 10$. However, $k_2 / k_1 > 10$ in the case of J.P. Giroud's formula the results are erroneously low.

The results of the calculations of the screen durability (service life) of bentonite covering (Table 5) show similar results according to the Rice equation and the data of the Institute of BAM (Germany) at $t = 15^{\circ}\text{C}$. However, the second result of BAM – 400 years – is very much overestimated, and the last one according to "Bentizole" is not real.

The comparison of the obtained results on the durability of the screen from the geomembrane (Table 6) shows that the calculations made by the authors according to the Arrhenius equation (5) give close values of service life with the data [18] and "Polypine". At the same time, according to Carpi company, they are significantly overestimated, and the values τ according to DIBT (the German Institute for Technical Construction) - overstated many times (more than 5 times).

4. Conclusions

1. According to the results of the conducted researches the authors received new scientific results, which consist for the first time in estimation of efficiency (water permeability) of seepage-control lining from bentonite coverings taking into account their autogenous healing, as well as in the calculation method of the determination of durability of geosynthetic materials: bentonite coverings, geomembranes, which are confirmed by other studies.

2. The criteria for the efficiency and longevity of the seepage-control canals linings with anti-filter elements made of geomembranes and bentomats for water resistance, tensile strength, elongation and longevity (service life) have been formulated. The criteria for the efficiency of protection against end-to-end damage to the geomembrane and bentomats, hydraulic efficiency, the degree of destruction and the longevity have been proposed for protective coatings.

3. A technique to evaluate the efficiency and longevity of bentonite mats has been developed taking into account self-healing of possible damage due to the regeneration of Ca-bentonite. For the calculation, the method of successive change of steady states is used, when the unsteady filtering process through a single damage is divided into a number of steady states for a time interval $\Delta\tau$. Application of the technique is

illustrated by an example of calculation and graphical dependencies of changes in filtration flow $q_i = f(\tau_i)$ rate and leakage amount $V_i = f(\tau_i)$.

4. The Rice equation is used to calculate the predicted life of the bentomat lining which helped to obtain calculate dependence to determine the service life. The considered calculation example with given initial data allowed us to obtain a bentomat service life of about 130 years.

5. Based on the surveys of the Donskoy Principal Canal with Bentofix Na-bentonite linings, we have obtained a calculated assessment of the efficiency of such a lining for three criteria, which confirms the high efficiency of the bentomat compared to the ground channel of the canal, which is equal by the criterion $N_1 = 5 \cdot 10^6$ times, and also by efficiency with alternative options according to the criterion $N_2 = 1 \cdot 10^4 \div 8.3 \cdot 10^5$, the lining of bentomats exceeds all alternatives from $1 \cdot 10^4$ to $8.3 \cdot 10^5$ times and according to the criterion $N_3 = 1 \cdot 10^4 \div 1 \cdot 10^6$ times compared to filtration resistances.

6. The studies of changes in the coefficient of aging of the geomembrane made of HDPE polyethylene by relative elongation in the test basin for 8–10 years allowed to extrapolate them in a diagram in logarithmic coefficients and to obtain the service life of the geomembrane under a protective coating of ground of 0.5 m thick equal to $t = 83$ year; at the same time, the calculation by the Arrhenius equation gave a result close to extrapolation and is equal to $\tau = 76.5$ years.

7. A comparative analysis of the efficiency of various types of seepage-control linings showed that the bentomat linings with a filtration coefficient (that is respectively in 50–25 times less than the ground-film and concrete-film lining with a geomembrane and more than $4 \cdot 10^6$ time less than the most ineffective concrete lining) are the most effective. In addition, the bentomat lining has the highest service life of about 130 years, which is 3.66 times greater than for concrete lining.

5. Acknowledgement

This work was supported by a grant from the President of the Russian Federation for national support of young scientists and candidates of science (MK-33.04.2018.8).

References

1. The water strategy of the Russian Federation for the period until 2020. M.:NIAPriroda, 2009. 40 p. (rus)
2. Reclamation systems and facilities. Updated version of SNIIP 2.06.03-85: SP 100.13330.2016: conf. by the Ministry of Construction and Housing and Public Utilities of the Russian Federation 16.12.16: enter in force from 17.06.17. M.: Standartinform. 2016. p. 16. (rus)
3. Alimov, A.G. Improving the theoretical foundations, methods, and technique for studying the seepage-control efficiency of the protective lining of canals and reservoirs. *Hydrotechnical construction*. 2012. No. 6. Pp. 20–27.
4. Bandurin, M.A., Voloshukhin, V.A., Vanzha, V.V. Technology for Water Economy Monitoring of Technical State of Closed Drainage of Irrigation System: International Conference on Construction and Architecture: theory and practice of industry development. 2018. Pp. 214–218.
5. Solsky, S.V., Novikaya O.I., Kubetov S.V. Evaluation of the effectiveness of drainage and antifiltration devices of concrete dams on a rocky base (on the example of the Bureyskaya HPP) // *Magazine of Civil Engineering*. 2014. No 4. Pp.28–38
6. Kosichenko, Yu.M., Baev, O.A. Multilayer constructions of seepage-control coatings with bentonite mats and assessment of their comparative effectiveness. *Hydrotechnical construction*. 2019. No 3. Pp. 37–43.
7. Kosichenko, Yu.M., Baev, O.A. Primenenie bentonitovykh matov – put' k sozdaniyu neproniцаemyykh ekranov [The use of bentonite mats – the path to creating impermeable screens]. *Hydrotechnics*. 2019. No 1 (54). Pp. 74–77. (rus)
8. Kosichenko, Y.M., Baev, O.A. Water permeability of the polymer screen with a system of stilts of hydraulic structures. *Magazine of Civil Engineering*. 2018. No. 7. Pp. 64–73.
9. Bandurin, M.A. Diagnostics of the technical condition and assessment of the residual service life of waterworks of irrigation systems: abstract of a thesis. ... doctors of technical sciences: 01.06.02 / Bandurin Mikhail Alexandrovich; [Place of protection: The Russian Scientific Research Institute of Hydraulic Engineering and Land Reclamation named after A.N. Kostyakov]. Moscow. 2017. 41 p. (rus)
10. Glagovsky V.B, Solsky S.V, Lopatina M.G, Dubrovskaya N.V, Orlova N.L. Geosynthetic materials in hydraulic engineering construction. *Power technology and engineering*. 2014. No. 9. Pp. 23–27. (rus)
11. Kosichenko, Yu.M., Baev, O.A. Highly reliable constructions of anti-filtration coverings of canals and reservoirs, criteria of their efficiency and reliability. *Power technology and engineering*. 2014. No. 8. Pp. 52–56.
12. Kosichenko, Yu.M., Baev, O.A. Metody rascheta vodopronitsayemosti polimernyykh protivofiltratsionnykh ekranov gidrotekhnicheskikh sooruzheniy [Methods for calculating the permeability of polymer anti-filtration screens of hydraulic structures]. *Izvestiya VNIIG im. B.Ye. Vedenev*. 2017. Vol. 286. Pp. 10–21. (rus)
13. Giroud, J.P. Equations for calculating the rate of liquid migration through composite lines due to ge-omembrane defects. *Geosynthetics International*. 1997. Vol. 4. No. 3–4. Pp. 335–348.
14. Touze-Foltz, N., Rowe, R.K., Duquennoy, C. Liquid Flow Through Composite Liners due to geomembrane defects: analytical solutions for axi-symmetric and two-dimensional problems // *Geosynthetics International*. 2000. Vol. 6. No. 6. Pp. 455–479.
15. Baev, O.A., Kosichenko, Yu.M. Gidromekhanicheskoe reshenie zadachi vodopronicaemosti ekrana narushennoj sploshnosti [Hydromechanical solution to the problem of water permeability of the screen with broken continuity]. *Izvestia of the Russian Academy of Sciences. Mechanics of fluid and gas*. 2018. No. 4. Pp. 3–11. (rus)

16. Touze-Foltz, N., Giroud, J.P. Empirical equations for calculating the rate of liquid flow through composite liners due to geomembrane defects // *Geosynthetics International*. 2003. Vol. 10. No. 6. Pp. 215–233.
17. Giroud, J.P., Thiel, R.S., Kavazanjian E. Hydrated area of a bentonite layer encapsulated between two geomembranes // *Geosynthetics International*. 2004. Vol. 11. No. 4. Pp. 330–354.
18. Koerner, R.M., Hsuan, Y.G., Koerner, G.R. Lifetime predictions of exposed geotextiles and geomembranes // *Geosynthetics International*. 2017. Vol. 24. No. 2. Pp. 198–212.
19. Skuero, A.M., Basketti, G.L. Geomembranes - well-proven water-permeable systems in hydraulic structures // *International digest on hydraulic engineering and landfills*. 2007. Pp. 59–68.
20. Pryamitsky, A.V., Schlee, Yu. Bentonitovye maty kak al'ternativnyj material dlya protivofil'tracionnyh elementov gidrotekhnicheskikh sooruzhenij [Bentonite mats as an alternative material for seepage-control elements of hydraulic structures]. *Hydrotechnics XXI century*. 2010. No 1. Pp. 72–75. (rus)
21. AbdelRazek, A.Y., Kerry, Rowe R. Interface transmissivity of conventional and multicomponent GCLs for three permeants // *Geotextiles and Geomembranes*. 2019. Vol. 47. No. 1. Pp. 60–74.
22. Prabakaran, P.A., Sathyamoorthy, G.L., Adhimayan, M. An experimental and comparative study on canal lining exploitation geosynthetic material, cement mortar and material lining. *International Journal of Recent Technology and Engineering*. 2019. Vol. 7. No. 4. Pp. 81–83.
23. Cen, W.He, H.Li, D. Influence of geomembrane defect on seepage property of earth-rock dams and measures of seepage control // *Advances in Science and Technology of Water Resources*. 2017. Vol. 37. No. 3. Pp. 61–65.
24. Koerner, R.M. Koerner, G.R. Hsuan, Y. Exposed geomembrane geosynthetic clay liner composites for solid waste covers, liquid impoundment liners, and canal liners // *Geotechnical Special Publication*. 2016. No. 274. Pp. 22–35.
25. Koerner, G.R., Koerner, R.M. The durability of exposed geomembrane covers // *Geotechnical Special Publication* Issue. 2017. Vol. 276. Pp. 139–147.
26. Sainov, M.P., Zverev, A.O. Workability of high rockfill dam with a polymer face. *Magazine of civil Engineering*. 2017. No. 7. Pp. 76–83.
27. Zverev, A.O., Sainov, M.P., Lukichev R.V. Rezul'taty eksperimental'nogo issledovaniya polimernyh geomembran na dvuhosnoe rastyazhenie [The results of an experimental study of polymeric geomembranes on biaxial tension]. *Vestnik of the Eurasian Science*. 2018. No. 4. Book 10. Pp. 1–13.
28. Hydraulic engineering installations. Main provisions: SP 58.13330.2012: conf. by Ministry of Regional Development of the Russian Federation 29.12.11: enter in force from 01.01.13. M. 2012. 38 p.
29. Solsky, S.V., Orlova, N.L., Velichko, A.S. Crack self-healing in clay-cement concrete diaphragm of embankment dam. *Magazine of Civil Engineering*. 2018. No 1. Pp. 3–12.

Contacts:

Yuri Kosichenko, kosichenko-11@mail.ru

Oleg Baev, Oleg-Baev1@yandex.ru

© Kosichenko, Yu.M., Baev, O.A., 2020



DOI: 10.18720/MCE.96.5

Water-impact abrasion of self-compacting concrete

N.S. Ayoob, S.R. Abid*, A.N. Hilo, Y.H. Daek

Wasit University, Wasit-Kut, Iraq

* E-mail: sallal@uowasit.edu.iq

Keywords: abrasion, self-compacting concrete, steel fiber, fiber-reinforced concrete, impact

Abstract. Abrasion erosion is one of the serious problems that encounters the concrete surfaces exposed to speedy water flow in hydraulic structures, affects their service life and poses the need to expensive maintenance works. Some parts of the hydraulic structure like chute blocks and baffle piers in spillways are designed to face direct impact of water and waterborne materials. For such type of loading, the water-jet test method can be used to simulate the abrasion erosion of concrete surfaces. In this study, an experimental work was conducted to evaluate the abrasion erosion of self-compacting concrete under the effect of water impact. Plate specimens from six mixtures with 30, 40 and 50 MPa design strengths and with 0, 0.5, 0.75 and 1.0 % steel fiber contents were tested using the water-jet method. The results showed that increasing the strength from 30 to 40 MPa can reduce the abrasion losses by approximately 17 %, while using steel fibers with volumetric contents of 0.75 and 1.0 % can improve the abrasion resistance by more than 23 %. It was also concluded that the best percentage abrasion resistance improvement was gained when the strength of the plain specimens was increased to 50 MPa, which was 30 % compared to the plain 30 MPa sample.

1. Introduction

The reduction in concrete quality in structural members can in several cases be attributed to the inadequate compaction, which affects the strength and durability of the produced structural member. This problem was distinguished in Japan before 1990. Between 1988 and 1999, leading research works [1, 2] were conducted in the University of Tokyo to surpass this problem and produce a durable self-consolidating concrete. This type of concrete was first named as high performance concrete, then after, the term Self-Compacting Concrete (SCC) became more popular [3]. Several favorable characteristics can be named for SCC including self-consolidation under own weight, reduction in number of labor required, reduced noise in site, reduced construction period and avoidance of fresh-state concrete defects, which results in more durable surfaces [3, 4]. Any SCC mixture should have the characteristics of flowability, passing ability and segregation resistance. The limitations of the required SCC fresh properties and their tests are detailed in several standards, among the most important of which are the ACI 237-R [4] and the European Specifications EFNARC [5]. The first application of SCC was in Japan in 1990 where most of the reinforced concrete members of a building structure were cast using SCC. Then in 1991 it was used in the towers of the Shin-Kiba Ohashi prestressed concrete cable-styled bridge [3]. Since that it was extensively used around the world in buildings, bridge structures, tunnels, box-culverts and dam structures. In 2012, several important hydraulic structures in the Upper Gotvand dam in Khuzestan/Iran [6] were constructed using SCC. Among these structures is the pressure tunnel that includes four entrances with 11 m diameter each and total length of more than 5000 m.

One of the serious problems that affect the durability of hydraulic structures is the abrasion erosion of concrete surfaces subjected to high-speed water flow. This flow is mostly accompanied by waterborne materials, which might be as small as sand and gravel and as big as rocks. Such flow with such erodent materials causes shearing or impact abrasion forces that may lead to serious defects in the exposed surfaces. Two tests are being used during the current and last decades to qualitatively evaluate the abrasion erosion of concrete surfaces in hydraulic structures. The first is the standard ASTM C1138 [7] under water abrasion test method, while the second is the non-standard water jet test method developed by liu et al. [8]. The first simulates the abrasion erosion due to the movement of water and waterborne materials, where the direction of this movement is parallel to the concrete surface. In this method, the main cause of abrasion action is the

Ayoob, N.S., Abid, S.R., Hilo, A.N., Daek, Y.H. Water-impact abrasion of self-compacting concrete. Magazine of Civil Engineering. 2020. 96(4). Pp. 60–69. DOI: 10.18720/MCE.96.5



This work is licensed under a CC BY-NC 4.0

shearing frictional forces of water and erodent materials. On the other hand, the water jet method simulates the impact action of water and waterborne materials on surfaces that are normal to the direction of flow. Some valuable experimental research works were found in the literature on the abrasion erosion of different concrete types using the ASTM C1138 method [9–14] and the water jet method [15–20]. However, few trials were found in the literature on the evaluation of SCC abrasion, yet, none of which was under the effect of water and waterborne materials. Turk and Karatas [21] used the ASTM C779 [22] dry abrasion procedure to investigate the effect of the quantity of silica fume and fly ash in the concrete mixture on the SCC resistance to dry abrasion action. Their results showed that SCC was superior to normal concrete in abrasion resistance. The results also revealed that increasing silica fume and decreasing fly ash in the mixture lead to better abrasion resistance. Ghafoori et al. [23] used the same dry abrasion method (ASTM C779) to test SCC specimens. The authors found that SCC exhibited 50–70 % lower abrasion losses than ordinary concrete.

The inclusion of metallic or synthetic fibers to SCC may reduce its flowability, but can positively influence its strength and durability. Fibers are known to improve the physical properties of concrete when applied in sufficient quantities. Steel fiber can noticeably improve the resistance of concrete mixtures and reinforced concrete members to tensile, shear, flexural and torsional loads. It can reduce the crack width and improve the stiffness, ductility, surface hardness and resistance to impact loads [24–29]. Recent researches showed that steel fiber with volumetric contents of 0.3 to 1.0 % can reduce the surface abrasion losses. Liu et al. [15] showed that the inclusion of 1.0% of steel fiber led to lower abrasion losses by 39 %, while Horszczaruk [9] showed that the effect of fiber on abrasion resistance depends on many factors including its aspect ratio and distribution in the mixture, where 30 mm length steel fiber could retained lower abrasion losses by approximately 18% compared to plain mixture. Using the water-jet method, Ristic et al. [16] showed that 0.3 % of steel fiber could reduce the abrasion by approximately 9 to 15 %.

The literature review conducted in this research shows that although several experimental researches were found on the abrasion resistance of concrete under water flow effect, the available experimental data about this problem still much less than required. The response of several new concrete types still not well defined and the influence of several mixture ingredients still not well investigated. There still a need for more research works to improve the knowledge about the problem of abrasion erosion of concrete surfaces in hydraulic structures. Moreover, although SCC was used to construct many hydraulic structures, the reviewed literature reveals that none of the previous experimental researches tried to evaluate the impact abrasion erosion of SCC under water movement effect, especially with the presence of steel fibers. Therefore, this research tries to fill some gap of knowledge in this field by conducting an experimental work on the abrasion erosion of steel fiber-reinforced SCC under direct impact of water and waterborne materials.

2. Methods

The water jet test method was used in this work in order to estimate the resistance of SCC to the abrasion erosion that occurs due to direct impact of water and waterborne materials in hydraulic structures. For this purpose, six SCC mixtures were prepared and checked first for their filling, passing and segregation resistance abilities at the fresh state. Then, plate samples were prepared from the mixtures and kept in temperature-controlled water tank until testing date at age of 28 days.

2.1. Mixtures and materials

Basically, a SCC mixture was adopted from literature [30], then several trials were made to correct the quantities so that all required mixtures passes all SCC fresh properties tests. Six mixtures were prepared to study both the concrete strength and fiber content effects. The basic mixture has 30 MPa design strength but without fiber. For the same concrete strength, three other fibrous SCC mixtures with fiber contents of 0.5, 0.75 and 1.0 % were prepared, while two mixtures with higher design strengths of 40 and 50 MPa but without fiber were prepared to investigate the strength effect. To evaluate the strength of the prepared SCC mixtures, compressive strength and splitting tensile strength based on the ASTM standards were tested for all mixtures at the same day of abrasion test.

Different dosages of type R42.5 ordinary Portland cement were used in this investigation so as to produce SCC mixtures of different grades. A powder of limestone which is produced locally was added too but with constant small quantity of 70 kg/m³ as filler in order to provide better homogeneity for all mixtures, while 70 kg/m³ of silica fume was used with the 50 MPa strength mixture only. The course aggregate was crushed siliceous stone with maximum size of aggregate of 12.5 mm, while local siliceous sand was used as fine aggregate. To accommodate SCC mixtures with required workability and viscosity, Sika Viscocrete-5930 superplasticizer was added with different dosages based on trial mixtures. Straight micro-steel fiber was used with length and diameter of 15 and 0.2 mm, while its tensile strength was 2600 MPa. Table 1 shows the details of the prepared SCC mixtures.

Table 1. Proportions of SCC mixtures.

Mixture	Cement (kg/m ³)	FA (kg/m ³)	CA (kg/m ³)	Water (kg/m ³)	W/B	SP (kg/m ³)	Fiber (kg/m ³)
C30F0	400	1060	586	185.00	0.394	9.500	0.0
C30F0.5	425	1096	519	196.56	0.397	13.550	38.0
C30F0.75	425	1096	519	196.56	0.397	13.550	58.5
C30F1	435	1110	494	217.00	0.430	15.000	78.0
C40F0	500	990	586	200.00	0.351	10.250	0.0
C50F0	550	950	543	200.00	0.290	17.857	0.0

FA: Fine aggregate, CA: Coarse aggregate, W/B: Water to total binder ratio, SP: Superplasticizer

2.2. Fresh SCC tests

To ensure that the prepared mixtures fulfill the required fresh properties of SCC, six SCC fresh tests were adopted to validate the three main test categories which are the flowability, passing ability through steel bar reinforcement and resistance to segregation when cast from to deep sections. Three tests were adopted to check the flowability of the prepared mixtures, which are the slump flow [5, 31], T50 [5, 31] and V-funnel tests [5]. The former two tests were adopted for all mixtures, while the V-funnel test was carried out for the three plain SCC mixtures (C30F0, C40F0 and C50F0). On the other hand, the J-ring [5, 32] and L-box tests were used to check the passing ability through reinforcement obstacles. The L-shaped box was used in this study as per the standard dimensions of EFNARC [5]. This test was performed to evaluate the three plain mixtures only, while the J-ring test was used for the six SCC mixtures. Finally, the rapid penetration test was used according to the specifications of ASTM C 1712 [33] to evaluate the segregation resistance of the six SCC mixtures. Table 2 lists the acceptable records of the performed fresh properties tests according to both EFNARC and ASTM standards.

Table 2. Fresh SCC mix limitations.

Test	Limitations	
	EFNARC	ASTM
Slump flow (mm)	650-800	480-680*
		or 530-740**
T ₅₀ (sec)	2-5	2-5
ΔJ-ring (mm)	0-10	0-25 †
		25-50 ††
Penetration (mm)		0-10 †
		10-25††
L box	0.8-1	
V funnel (sec)	6-12	

* Single-operator precision ** Double-operator precision † No visible blocking †† Minimal to noticeable blocking
† Resistance to segregation †† Moderately resistance to segregation

2.3. The water-jet abrasion test

In this work, the water jet test was considered to experimentally simulate the abrasion of vertical SCC surfaces in hydraulic structures. In order to simulate the abrasion erosion that occurs in hydraulic structures due to the impact effect of the carried sediments, plate samples of 200×200×50 mm were tested under the direct high-pressurized water. The test was conducted at nine time steps of one-hour each. Thus, the specimens were exposed to the abrasion test for nine hours. The weight of the sample was recorded after each time step. The test procedure includes the pumping of water from a tank that contains 1 m³ of water, that is mixed with erodent materials, through a 200×10 mm nozzle at high pressure. In this test, the same procedure was used but using circular nozzle with a diameter of 50 mm. The velocity of the water jet was 20 m/s and the erodent material was graded sand with a concentration of 30 kg/m³. Figure 1 shows the water jet abrasion testing tank used in this investigation.



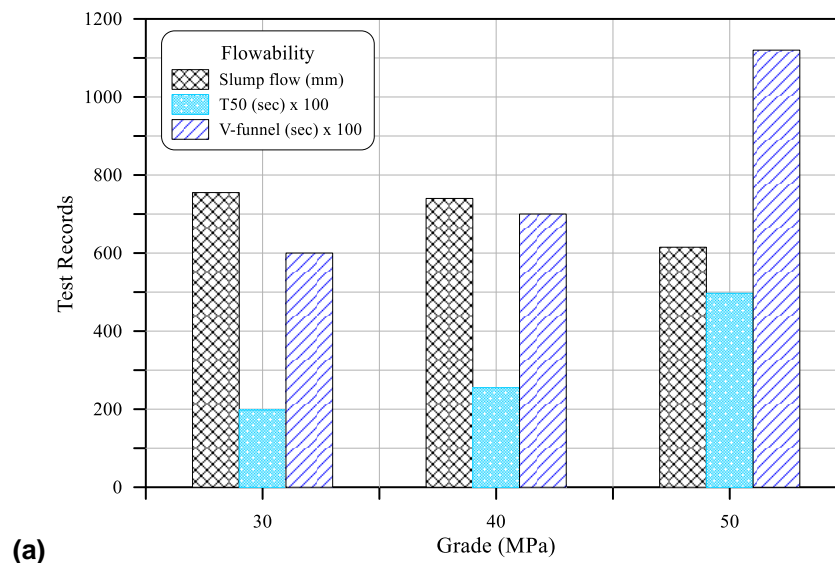
Figure 1. The used water-jet abrasion testing apparatus.

3. Results and Discussion

3.1. Results of Fresh Concrete Tests and Control Tests

Figures 2 and 3 display the results of fresh concrete tests. These figures show that the produced SCC mixtures fulfill the requirements of standard SCC with an appropriate flowability, average viscosity which is enough to prevent segregation and finally, acceptable passing ability according to the standards of ASTM and EFNARC.

Figure 2 shows that the flowability was reduced as the design strength increased. For mixtures of 40 and 50 MPa (without fiber), where the slump flow diameter was reduced by 2 and 18.54 %, the T_{50} flow time increased by 28.8 and 150 %, and the V-funnel time increased by 14.3 and 46.4 %, respectively, compared to the mixture of 30 MPa. The decrement of w/b ratio can be considered as the main cause of such behavior in spite of the increment of SP. This result is in agreement with the fact that in the range of acceptable slump deformability, the influence of minimizing the water content appears to be more controlling on flow time than superplasticizer (SP) influence [34]. The obstruction of J-ring increased by 60 and 80 % for grades of 40 and 50 MPa mixtures, respectively, compared to grade 30 MPa mixture, while the height ratio of L-box (H_2/H_1) decreased by 1 and 14 %, respectively. This obviously reflects the significant decrement of passing ability and higher blocking occurred by the decrement of water content. On the other hand, the segregation resistance was clearly enhanced as concrete grade increased. For mixtures of 40 and 50 MPa design strengths, the penetration test results reduced by 10 and 40 %, respectively, compared to the 30 MPa mixture. This result can be attributed to the increment in fine materials content and the noticeable reduction in w/b ratio.



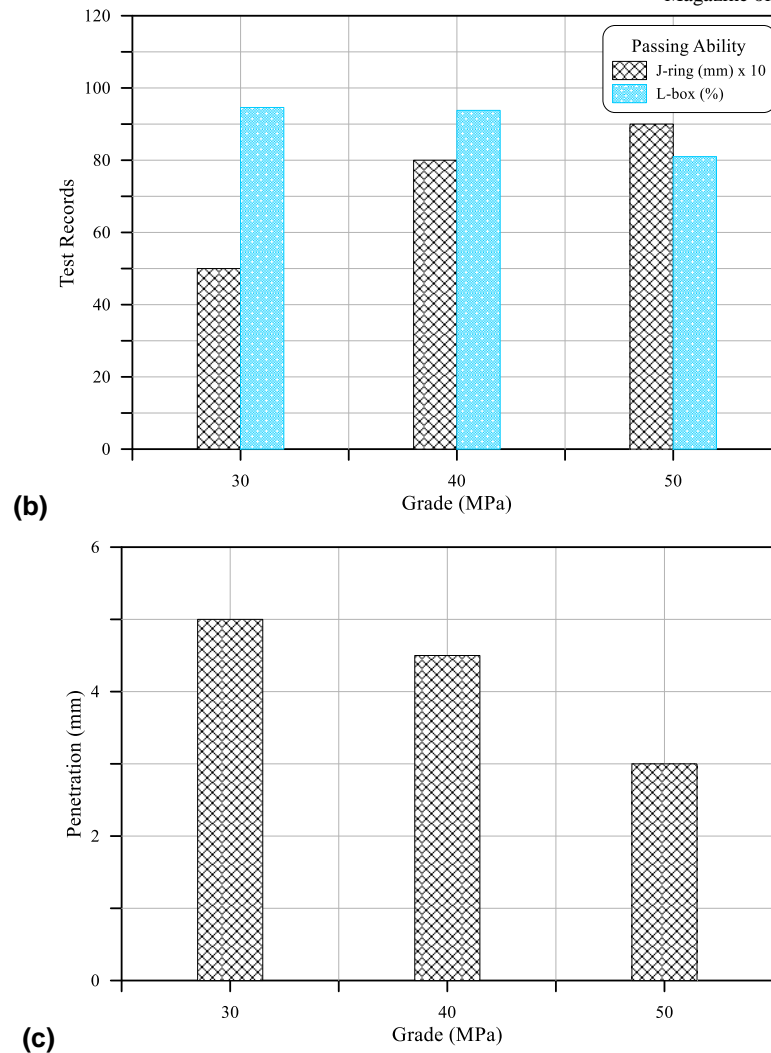


Figure 2. Fresh SCC tests of the mixtures with different design strengths (a) flowability tests (b) passing ability (c) segregation resistance.

Figure 3 shows that the inclusion of fibers negatively influences the fresh properties of SCC. As steel fiber content increased, slump flow test results clearly decreased in spite of the increase in w/b ratio and superplasticizer dosage. For example, for 1% fiber addition, the w/b ratio and SP increased by approximately 7.8 and 58%, respectively, while the slump flow diameter reduced by about 7.3% as compared with the slump flow for plain mixture. Similarly, the flow time increased due to steel fiber inclusion, while the J- ring obstruction increased by approximately 160, 180 and 300% for mixtures with 39, 58.5 and 78 kg/m³ of steel fiber, respectively. On the other hand, mixtures segregation was slightly increased but remained in the acceptable range, which returns to the use of larger water and superplasticizer quantities in order to attain appropriate flow and passing abilities.

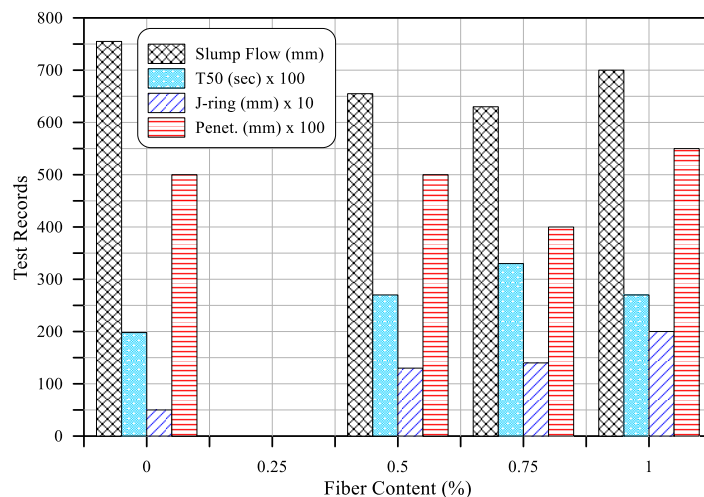


Figure 3. Fresh test results of fiber-reinforced mixtures.

3.2. Results of the Water Jet Abrasion Test

The decrease in the specimen weight due to abrasion was recorded in this investigation using the Percentage Abrasion Weight Loss (PAWL). It stands for the weight difference between the primary weight of each sample and its weight after a certain period of testing time, divided by its primary weight and multiplied by 100, as shown in the following equation, in which w_p and w_t are the primary weight and the weight of the specimen after (t) hours of testing, respectively:

$$PAWL(\%) = 100(w_p - w_t) / w_p \quad (1)$$

Figure 4 shows that the PAWL of all specimens significantly increased with testing time. The relation of PAWL with time seems to be linear for the 30 MPa specimen, while it is multi-linear for the higher grade specimens. Figure 5 shows that for the test specimens of grade 30 MPa, the PAWLs at testing times of 3, 6 and 9 hours were 0.43, 0.81 and 1.18 %, respectively. On the other hand, the PAWLs of grades 40 and 50 MPa for the same time sequence were 0.45, 0.71 and 0.97 % and 0.39, 0.69 and 0.83 %, respectively. It can be noticed that at all test intervals, the PALWs of grade 30 MPa were the highest except at the first three hours of testing in which grade 40 MPa exhibited higher PAWL, while the PAWLs of grade 50 MPa were permanently the lowest. Comparing the results at the end of the test, it is clear that the abrasion resistances of SCC mixtures with design strengths of 40 and 50 MPa were higher than that of 30 MPa by 17.8 and 30 %, respectively. These results are also shown in the final abraded surfaces shown in Figure 6, which shows that the 30 MPa specimen suffered higher surface abrasion losses.

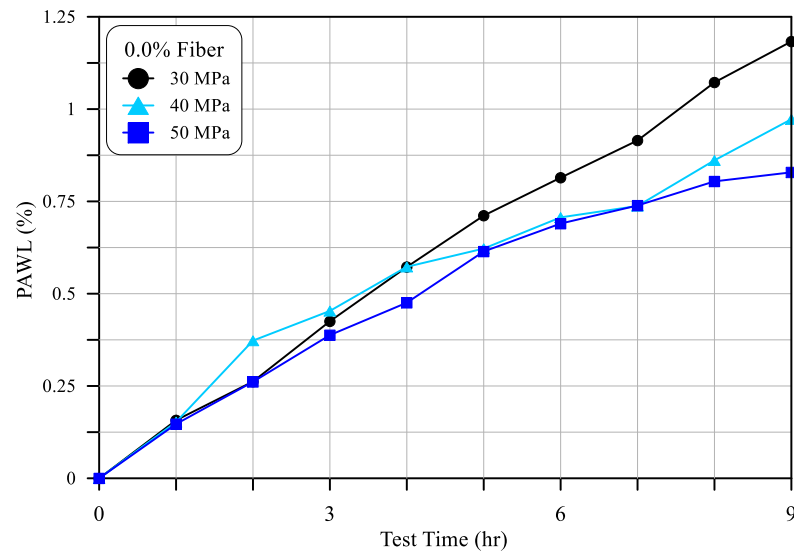


Figure 4. PAWL-testing time for different design concrete grades.

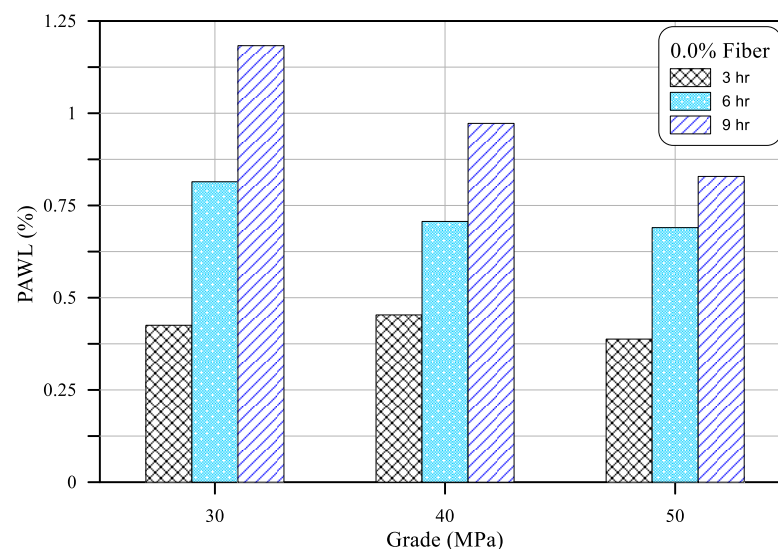


Figure 5. PAWL-concrete design grade after 3, 6 and 9 hours of abrasion testing.

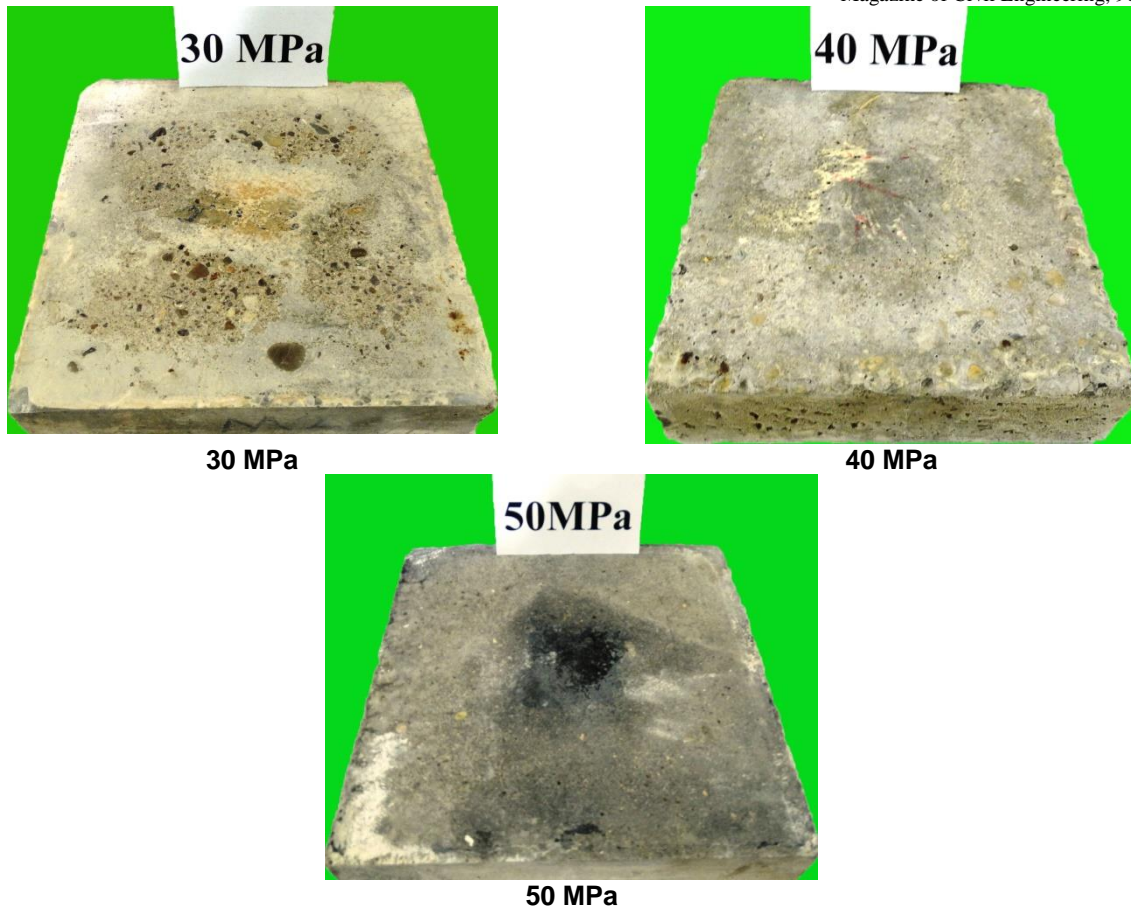


Figure 6. Abraded surfaces of the specimens with design strengths of 30, 40 and 50 MPa after 9 hours of abrasion testing.

Figure 7 shows the relation between the PAWL and various testing times for steel fiber contents of 0, 0.5, 0.75 and 1.0 % by volume. It is obvious that the effect of fiber content on the PAWL was not clear during the early hours of abrasion testing, while at the end of the test, the plain specimen with 0 % fiber exhibited the highest PAWL value of 1.18 %, while the specimen with 0.5 % fiber exhibited the second highest PAWL value of 0.95 %. On the other hand, specimens with 0.75 and 1.0 % fiber contents exhibited the smallest PAWL values of 0.906 and 0.903 %, respectively. Figure 8 shows the above discussed influence of steel fiber addition on the PAWL at various testing time intervals of 3, 6 and 9 hours. At the end of the test, the abrasion resistance of fibrous SCC specimens with 0.5, 0.75 and 1.0 % fiber contents was higher than the corresponding plain one by 19.7, 23.4 and 23.7 %. Pictures of the abraded surfaces of the four specimens after 9 hours of abrasion testing are shown in Figure 9. Another notice is that the fibrous specimens, especially those with fiber contents of 0.75 and 1.0 %, exhibited multilinear variation with time, where the slope of this relation changed after 4 hours of abrasion testing, while that of the plain specimen kept having approximately the same slope along the full test period.

From to Figures 4 to 9, an important note was observed, that is the final PAWL values for all fibrous specimens of grade 30 MPa were lower than that of plain sample of grade 50 MPa. Specimens of 0.5, 0.75 and 1.0 % fibers have lower PAWL values by 2.4, 6.8 and 7.1 %, respectively. This leads to a conclusion that increasing the strength of SCC has higher impact on abrasion resistance than adding micro-steel fibers with volumetric content up to 1.0 %, which is also a less expensive alternative. This result is more clear in Fig. 10, which shows the Percentage Increase in Abrasion Resistance (PIAR) for the three 30 MPa fibrous specimens (C30F0.5, C30F0.75 and C30F1) and the 40 and 50 MPa plain specimens (C40F0 and C50F0). The PIAR is calculated by dividing the difference of the final abrasion loss of any specimen and that of the reference specimen (C30F0) by the abrasion loss of the reference specimen. The figure obviously shows that the PIAR due to increasing the compressive strength from 30 to 50 MPa was the highest among all specimens, which was 30 %, while the inclusion of 1.0 % of steel fiber improved the abrasion resistance by approximately 24 %. However, it should also be noted that all fiber contents led to better abrasion resistance than increasing the strength by only 10 MPa. As it is shown in Table 1, the C50F0 mixture includes more than 45 % higher cement content and approximately 20 % lower w/b ratio. Such increase in cementitious materials and decrease in water content is enough to significantly improve the surface hardness, which leads to better resistance to impact abrasion forces. However, part of the better behavior of the 50 MPa specimen can be attributed the inclusion of silica fume. Where previous researches [15, 17, 35] showed that silica fume has positive impact on abrasion resistance of concrete.

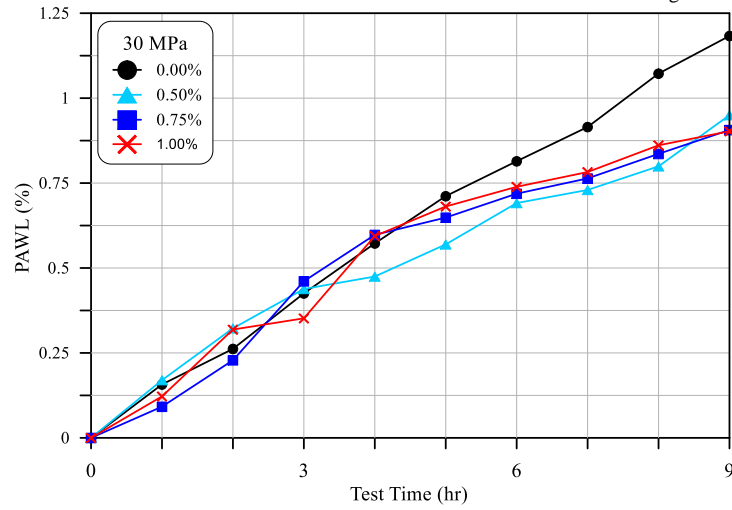


Figure7. PAWL-testing time of various steel fiber contents.

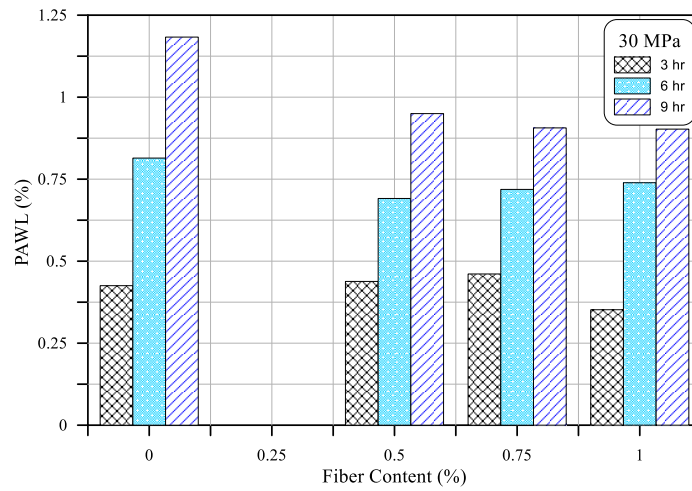


Figure 8. PAWL-fiber content after 3, 6 and 9 hours of abrasion testing.

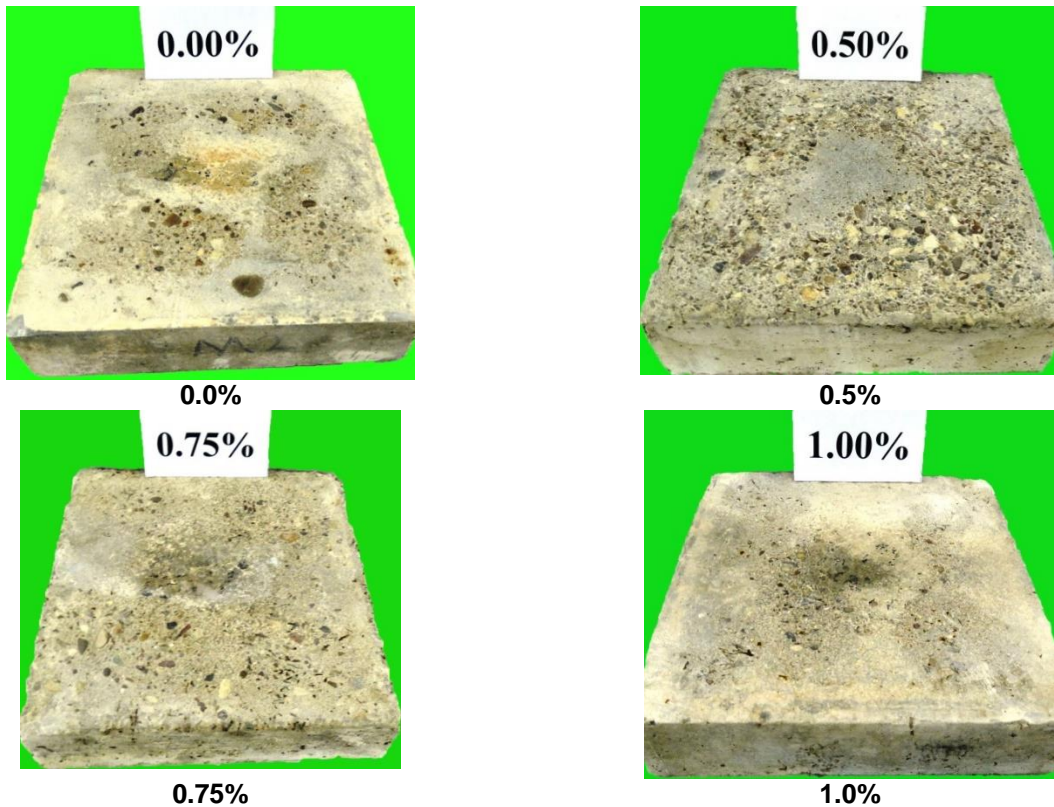


Figure 9. Abraded surfaces of the specimens with fiber contents of 0, 0.5, 0.75 and 1.0 % after 9 hours of abrasion testing.

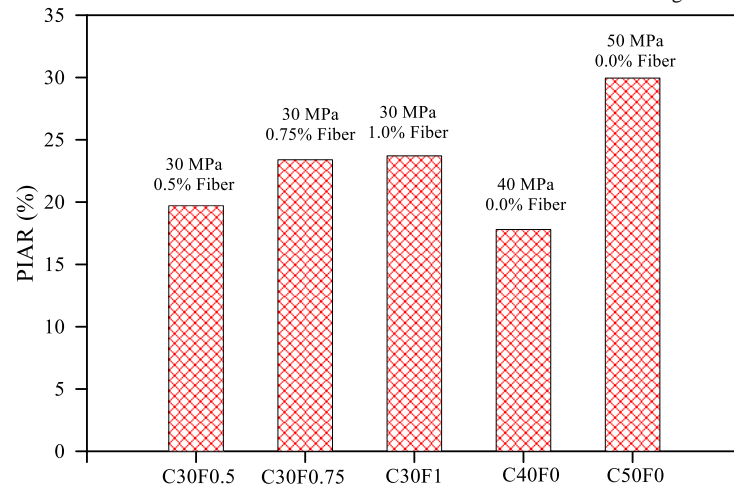


Figure10. PIAR of all specimens over the reference specimen with 30 MPa design strength and 0% fiber.

4. Conclusion

The water-jet method was used in this experimental investigation to conduct abrasion erosion tests on plate samples aiming to evaluate the abrasion resistance of SCC. Plain and steel fiber-reinforced SCC mixtures were prepared and tested. Three design concrete grades of 30, 40 and 50 MPa and four volumetric fiber contents of 0, 0.5, 0.75 and 1.0 % of steel fiber were adopted. Based on the test results of this study, the followings were concluded.

1. For all tested specimens, abrasion erosion weight loss increased as testing time increased. However, the behavior of the relationship between abrasion losses and time was different among the specimens. The reference plain specimen with design grade of 30 MPa exhibited continuous increase in abrasion losses with approximately the same slope, while the plain specimen with 50 MPa design grade and the fibrous specimens with 0.75 and 1.0 % of steel fiber (30 MPa) exhibited approximately a two-step linear behavior with time, where the slope of this relation decreased after 4 hours of abrasion testing indicating higher abrasion resistance.

2. During the full test period, the specimen with 50 MPa design grade showed the lowest abrasion losses among the plain specimens, while that with 30 MPa exhibited the highest abrasion losses along the last two thirds of the test time. At the end of the nine-hour test, the plain specimens with 30, 40 and 50 MPa suffered percentage weight losses of 1.18, 0.97 and 0.83 %, respectively. The better abrasion resistance of the 50 MPa mixture can be attributed to the higher quantity of cementitious materials and lower w/b ratio, which developed the surface hardness. The inclusion of silica fume can also be considered as one of the factors that led to the higher abrasion resistance of this mixture.

3. The effect of steel fiber on abrasion resistance was not clear during the early hours of the test, while it was obvious at the end of the test that the inclusion of 0.75 and 1.0 % of steel fiber can decrease the percentage abrasion losses by more than 23 %. The percentage abrasion losses of specimens with 0, 0.5, 0.75 and 1.0 % of steel fiber at the end of the test were 1.18, 0.95, 0.906 and 0.903 %, respectively.

4. The comparison among all tested specimens showed that increasing the strength by 10 MPa has a positive effect on the abrasion resistance of plain specimens with approximately 17 % decrease in abrasion losses. On the other hand, the inclusion of 0.75 and 1.0 % of steel led to better abrasion resistance by approximately 23 to 24 % compared to the plain specimen with the same grade (30 MPa). However, the best development in abrasion resistance was obtained when the design grade was increased from 30 to 50 MPa (no steel fiber), which was approximately 30 %.

5. Acknowledgements

The authors would like to thank the team of the Construction Materials Laboratory in the civil engineering department / Wasit University for their support.

References

1. Okamura, H., Ozawa, K. Mix-design for self-compacting concrete. Concrete Library of JSCE. 1995. 25. Pp. 107–120.
2. Nagamoto, N., Ozawa, K. Mixture proportions of self-compacting high performance concrete. ACI SP. 1997. 172. Pp. 623–636.
3. Okamura, H., Ouchi, M. Self-compacting concrete. Journal of Advanced Concrete Technology. 2003. 1. Pp. 5–15.
4. ACI Committee 237. Self-consolidating concrete. (ACI 237R-07). American Concrete Institute, USA. 2007. Pp. 1–30.
5. EFNARC. Specifications and guidelines for self-compacting concrete. EFNARC, UK. 2002. Pp. 1–32.

6. Zadeh, A.Z., Zafari, B., Yaminpour, M. Multifunctional use of self-compacting concrete as a fundamental material in dam construction: Upper Gotvand dam. *Key Engineering Materials*. 2015. 629–630. Pp. 391–398.
7. ASTM C1138-97. Standard test method for abrasion resistance of concrete (Underwater Method). ASTM International, West Conshohocken, USA. 1997. Pp. 1–4.
8. Liu, Y.W., Yen, T., Hsu, T.H. Abrasion erosion of concrete by water-borne sand. *Cement and Concrete Research*. 2006. 36. Pp. 1814–1820.
9. Horszczaruk, E. Hydro-abrasive erosion of high performance fiber-reinforced concrete. *Wear*. 2009. 267. Pp. 110–115.
10. Kryżanowski, A., Mikoš, M., Šušteršič, J., Ukrainczyk, V., Planinc, I. Abrasion resistance of concrete in hydraulic structures. *ACI Materials Journal*. 2009. 106. Pp. 349–356.
11. Horszczaruk, E. Abrasion resistance of high-performance hydraulic concrete with polypropylene fibers. *Tribologia*. 2012. 1. Pp. 63–72.
12. Mohebi, R., Behfarnia, K., Shojaei, M. Abrasion resistance of alkali-activated slag concrete designed by Taguchi method. *Construction and Building Materials*. 2015. 98. Pp. 792–798.
13. Abid, S., Hilo, A., Daek, Y. Experimental tests on the underwater abrasion of engineered cementitious composites. *Construction and Building Materials*. 2018. 171. Pp. 779–792.
14. Abid, S.R., Hilo, A.N., Ayoob, N.S., Daek, Y.H. Underwater abrasion of steel fiber-reinforced self-compacting concrete. *Case Studies in Construction Materials*. 2019. 11. Pp. 1-17.–
15. Liu, Y-W., Lee, C-C., Pann, K.S. Effects of fiber and silica fume reinforcement on abrasion resistance of hydraulic repair concrete. *Concrete Repair, Rehabilitation and Retrofitting II*, Edited by: Alexander et al. 2009. Pp. 877–880.
16. Ristic, N., Curcic, G.T., Grdic, D. Abrasion resistance of concrete made with micro fibers and recycled granulated rubber. *Zastita Materijala*. 2015. 56. Pp. 435–445.
17. Liu, Y.W. Improving the abrasion resistance of hydraulic-concrete containing surface crack by adding silica fume. *Construction and Building Materials*. 2007. 21. Pp. 972–977.
18. Grdic, Z.J., Curcic, G.A.T., Ristic, N.S., Despotovic, I.M. Abrasion resistance of concrete micro-reinforced with polypropylene fibers. *Construction and Building Materials*. 2012. 27. Pp. 305–312.
19. Dandapat, R., Deb, A. A probability based model for the erosive wear of concrete by sediment bearing water. *Wear*. 2016. 350–351. Pp. 166–181.
20. Abid, S.R., Shamkhi, M.S., Mahdi, N.S., Daek, Y.H. Hydro-abrasive resistance of engineered cementitious composites with PP and PVA fibers. *Construction and Building Materials Journal*. 2018. 187. Pp. 168–177.
21. Turk, K., Karatas, M. Abrasion resistance and mechanical properties of self-compacting concrete with different dosages of Fly ash/silica fume. *Indian Journal of Engineering and Materials Science*. 2011. 18. Pp. 49–60.
22. ASTM C779 / C779M-00. Standard test method for abrasion resistance of horizontal concrete surfaces. ASTM International, West Conshohocken, USA. 2000. Pp. 1–5.
23. Ghafoori, N., Najimi, M., Aqel, M.A. Abrasion resistance of self-consolidating concrete. *Journal of Materials in Civil Engineering*. 2014. 26. Pp. 296–303.
24. Ding, Y., Li, D., Zhang, Y., Azevedo, C. Experimental investigation on the composite effect of steel rebars and macro fibers on the impact behavior of high performance self-compacting concrete. *Construction and Building Materials*. 2017. 136. Pp. 495–505.
25. Travush, V.I., Konin, D.V., Krylov, A.S. Strength of reinforced concrete beams of high-performance concrete and fiber reinforced concrete. *Magazine of Civil Engineering*. 2018. 77(1). Pp. 90–100.
26. Abid, S.R., Abdul-Hussein, M.L., Ayoob, N.S., Ali, S.H., Kadhum, A.L. Repeated drop-weight impact tests on self-compacting concrete reinforced with micro-steel fiber. *Heliyon*. 2020. 6. Pp. 1–11.
27. Abbass, A., Abid, S., Özakça, M. Experimental investigation on the effect of steel fibers on the flexural behavior and ductility of high-strength concrete hollow beams. *Advances in Civil Engineering*. 2019. 2019. Pp. 1–13.
28. Yoo, D-Y., Moon, D-Y. Effect of steel fibers on the flexural behavior of RC beams with very low reinforcement ratios. *Construction and Building Materials*. 2018. 188. Pp. 237–254.
29. Abbass, A.A., Abid, S.R., Arna'ot, F.H., Al-Ameri, R.A., Özakça, M. Flexural response of hollow high strength concrete beams considering different size reductions. *Structures*. 2020. 23. Pp. 69–86.
30. Sahmaran, M., Yurtseven, A., Yaman, I.O. Workability of hybrid fiber reinforced self-compacting concrete. *Building and Environment*. 2005. 40. Pp. 1672–1677.
31. ASTM C1611. Standard test method for slump flow of self-consolidating concrete. ASTM International, West Conshohocken, USA. 2014.
32. ASTM C1621. Standard test method for passing ability of self-consolidating concrete by J-ring. ASTM International, West Conshohocken, USA.
33. ASTM C 1712. Standard test method for rapid assessment of static segregation resistance of self-consolidating concrete using penetration test. ASTM International, West Conshohocken, USA. 2014.
34. Felekoğlu, B., Türkel, S., Baradan, B. Effect of water/cement ratio on the fresh and hardened properties of self-compacting concrete. *Building and Environment*. 2007. 42. Pp. 1795–1802.
35. Cheng, T-C., Cheng, A., Huang, R., Lin, W-T. Abrasion properties of steel fiber reinforced silica fume concrete according to Los Angeles and water abrasion tests. *Materials Science (Medžiagotyra)*. 2014. 20. Pp. 498–502.

Contacts:

Nadheer Ayoob, natheers227@uowasit.edu.iq

Sallal Abid, sallal@uowasit.edu.iq

Ali Hilo, dralinasser@uowasit.edu.iq

Yasir Daek, yasirhd327@uowasit.edu.iq

© Ayoob, N.S., Abid, S.R., Hilo, A.N., Daek, Y.H., 2020



DOI: 10.18720/MCE.96.6

A probabilistic approach to estimation of the ultimate load of end-bearing piles on settlement criterion

S.A. Solovyev

Vologda State University, Vologda, Russia

* E-mail: ser6sol@yandex.ru

Keywords: pile, end-bearing pile, settlement, FORM, bearing capacity, reliability index

Abstract. Pile foundation is one of the most common types of foundations in the presence of soft soils. The safety of the entire structure depends on the pile foundation safety. Stochastic (probabilistic) modeling of load-bearing elements is a modern trend in the quantitative structural safety assessment. The article describes the probabilistic approach to estimate the bearing capacity (ultimate load) of end-bearing piles on settlement criterion. Design load and elastic modulus of a pile material are the main stochastic (random) parameters that determine the probability of end-bearing pile failure. The graphical model of failure and safety areas is proposed, on the basis of which conclusions can be drawn about the allowable load during the design and inspection of pile foundations. The numerical example shows that the method of pile reliability analysis based on FOSM (First Order Second Moment) gives similar results as the method on the basis on FORM (First Order Reliability Method). Therefore, for an accurate evaluation of the reliability index (according to the considered mathematical model), the first iteration of the FORM method is sufficient. Experimental modeling of pile behavior showed good convergence of the theoretical result with the experimental result based on the Monte Carlo method. For a comprehensive reliability analysis of end-bearing piles, it is necessary to consider a pile as a system (in terms of reliability theory).

1. Introduction

Pile foundations are one of the most common types of foundations in the presence of weak soils. There are two types of piles: friction piles and end-bearing piles. End-bearing piles transfer the load to the soil only by the pile's toe (lateral friction is ignored). The safety of whole structure depends on end-bearing piles safety. There is an important task to evaluate the maximum allowable load on the pile. In addition, the value of the allowable load should provide the pile reliability.

By Eurocode 0 "Basis of structural design", the reliability is the ability of a structure or a structural member to fulfill the specified requirements, including the design working life, for which it has been designed. Reliability covers safety, serviceability and durability of a structure and is usually expressed in probabilistic terms. The measure of reliability is the failure probability or safety probability. Structural reliability is a fundamental part of buildings and structures; reliability combines design problems, work planning, production and operation of buildings and structures [1]. As noted in [2], "reliability analysis has been a hot research topic in recent years, as the influences of uncertainty arising on loads, material properties, dimensions, and geometries become more and more profound". The research in [3] notes that reliability theory demonstrates the rapid growth and recognized importance for structural safety issues over the past decades. Reliability analysis allows to quantify the safety level of structure or structural element.

Reliability analysis has found applications in pile foundation engineering. The paper [4] proposes a two-dimensional axisymmetric numerical probabilistic modeling of an earth platform over clayey sand improved by stiff vertical piles using a finite-difference continuum approach; only the soil parameters are considered as random variables. The article [5] reviews the problems of piles probabilistic design in the North Sea. In [6] it is noted, that "reliability-based design (RBD), a hot issue in pile foundation engineering, has attracted more and more attention from engineers and researchers". The paper [6] also proposed a methodology to calculate the optimal ultimate base and shaft resistance factors for reliability-based design of driven piles by considering

Solovyev, S.A. A probabilistic approach to estimation of the ultimate load of end-bearing piles on settlement criterion. Magazine of Civil Engineering, 2020. 96(4). Pp. 70–78. DOI: 10.18720/MCE.96.6



This work is licensed under a [CC BY-NC 4.0](https://creativecommons.org/licenses/by-nc/4.0/)

the setup effects that can significantly enhance the ultimate shaft resistance after initial installation. T.V. Ivanova, I.U. Albert, B.G. Kaufman et al. [7] presented the probabilistic analysis of the friction pile behavior on the pile material and soil strength criterion.

There are several limit state criteria for axial loaded end-bearing pile: pile material strength, pile stability, strength of soil under a pile's toe and pile settlement. The calculation of the end-bearing pile settlement was often allowed not carried out because of its small value: only the pile material deformation was considered. For this reason, there is a lack of information about the reliability analysis of end-bearing piles by the deformation criterion. With the development of high-rise construction, the load on the piles has increased significantly, and end-bearing piles settlement can affect the stress-strain state or functioning of the structure.

Let us consider approaches to the estimation of end-bearing pile settlement. Generally, the settlement of end-bearing pile can be represented as the sum of two displacements:

$$s = s_s + s_p, \quad (1)$$

where s_s is pile settlement from soil deformation under the pile toe; s_p is pile settlement from pile material deformation (shortening).

Such an approach is implemented in mathematical models in various researches. A similar equation was proposed by X. Chen in [8]:

$$s = s_s + s_p = \frac{N}{AC_0} + \frac{Nl}{EA}, \quad (2)$$

where C_0 is the vertical reaction coefficient of the pile toe when the single axial limit compression strength of the rock sample is 1000 kPa, $C_0=300000$ kPa/m; s is pile tip settlement; N is an axial load; l is a pile length; E is an elastic module of pile body; A is the pile cross-section area;

In [9], the empirical equation was proposed for determining pile settlement:

$$s = \frac{d}{100} + \frac{Nl}{EA}, \quad (3)$$

where d is pile diameter.

In [10], the following approach was proposed to assess the settlement of a large diameter long pile:

$$s = \frac{2Nl}{5EA}. \quad (4)$$

Taking into account the notes in [11], the settlement of end-bearing pile also can be calculated by the equation:

$$s = s_s + s_p = \frac{1-\nu}{Gd} + \frac{Nl}{EA}, \quad (5)$$

where ν is soil Poisson's ratio under the pile toe and G is soil shear modulus under the pile toe.

In [12], G. Mylonakis proposed the extended dependence for determining the settlement of end-bearing pile:

$$s(z) = \frac{2N}{EAl} \sum_{m=0}^{\infty} \frac{K_0(\eta\alpha_m d/2) \cos \alpha_m z}{\alpha_m^2 \left[K_0(\eta\alpha_m d/2) + \frac{\pi d \eta G}{EA \alpha_m} K_1(\eta\alpha_m d/2) \right]}, \quad (6)$$

where K_0 , K_1 are modified Bessel functions of zero and first order; $\eta^2 = \frac{2}{1-\nu}$ is the later displacement

factor; $\alpha_m = \frac{\pi}{2l}(2m+1)$, $m = 0, 1, \dots, n$;

From an analysis of the above equations (2) - (6), it can be concluded about the generality of the proposed approaches.

Equation (6) has a similar dependence of variables as equation (5), if we transform model (5) to the form $N \leq \left(s_u - \frac{1-\nu}{G \cdot d} \right) \frac{EA}{l}$. However, using complex mathematical dependencies in the analysis of structural reliability can lead to a complex nonlinear problem that complicates its use in the engineering practice. Also, the complex nonlinear relationship between random (stochastic) parameters in (6) can lead to an underestimation of the actual reliability level due to big uncertainty (compared to semi-probabilistic approaches). In this regard, the equation (5) will be used in the further analysis. The algorithm considered below can be easily projected, for example, onto model (2) or similar mathematical models of limit state.

An important problem in end-bearing piles design is the presence of cracks in the rock base. The paper [13] analyzed a compilation of previously published and new data on the uniaxial compressive strength (UCS) of various rock types using the pore-emanated crack and the wing crack models. The presence of cracks in the rock base affects the pile deformability under axial load. The paper [14] described and analyzed an international experience in piles designing in a rock base with cracks.

New numerical methods for piles behavior modeling are also noteworthy. The research [15] proposed to determine pile settlement based on various three-dimensional finite element models. The paper [16] presents modeling of pile settlement using neural networks. For some geotechnical sites, it needs to consider the stability of pile as Timoshenko beam [17, 18]. In this paper, we consider only one criterion of the limit state – the settlement. Fundamental experimental studies of pile settlements are also considered in the A.A. Bartholomew research [19].

In this paper, the expansion and development of the provisions in [7] is proposed to consider a probabilistic approach to estimate end-bearing piles ultimate load on settlement criterion with design reliability level. The aim of the paper is a probabilistic analysis of ultimate load on axial loaded end-bearing pile on settlement criterion. It is required to solve such problems as: to determine which parameters are random (stochastic); to choose the method of reliability analysis; to analyze the influence of the variability of individual parameters on the overall pile reliability level and to compare the analytical solution with experimental data by Monte-Carlo simulation.

2. Methods

The values of stochastic (random) parameters in (5) are determined by tests and represent some statistical subset of the data. Stochastic parameters are indicated by a wavy line above the symbol. The mathematical model of the limit state (5) can be written as:

$$\tilde{N} \leq \left(s_u - \frac{1-\nu}{\tilde{G} \cdot d} \right) \frac{\tilde{E} \cdot A}{l}, \quad (7)$$

where s_u is ultimate value of pile settlement.

The elasticity modulus of the pile material and the shear modulus of soil under the pile toe are determined by the repeated tests, which allows to describe them by the normal distribution. The axial load on the pile is described by a combination of different probability distributions, which can also be generically reduced to normal. There are different approaches to assign the maximum allowable pile settlement [20–22].

Denote $\tilde{N} = X$ and $\left(s_u - \frac{1-\nu}{\tilde{G} \cdot d} \right) \frac{\tilde{E}A}{l} = Y$. The parameters of the normal distribution function for random variable X are taken as a mathematical expectation $E[X]$ and standard deviation σ_x of axial load $\tilde{N} = X$.

The expected value $E[Y]$ and standard deviation σ_y for Y on the first stage can be found by decomposing the function into a Taylor series:

$$E[Y] = \left(s_u - \frac{1-\nu}{E[G] \cdot d} \right) \frac{E[E] \cdot A}{l}; \quad \sigma_y = \sqrt{\left(\frac{\partial Y}{\partial G} \right)^2 \sigma_G^2 + \left(\frac{\partial Y}{\partial E} \right)^2 \sigma_E^2}.$$

The probability of pile non-failure by model (7) can be calculated as:

$$P = \Pr(X \leq Y) = \Phi \left(\frac{E[Y] - E[X]}{\sqrt{\sigma_y^2 + \sigma_x^2}} \right) = \Phi(\beta), \quad (8)$$

where $\Phi(\beta)$ is determined by the table values of the integral Laplace function (z-table); β is the reliability index.

Such an approach is called FOSM (First Order Second Moment). As $\sigma_x = E[X] \cdot CV_x$, where CV_x is axial load coefficient of variation, then safety condition by reliability index β of the end-bearing pile can be written as:

$$\beta \geq \frac{E[Y] - E[X]}{\sqrt{\sigma_y^2 + (E[X] \cdot CV_x)^2}}. \quad (9)$$

Reliability index β can be specified in a design assignment.

If condition (9) is not met, the design parameters are adjusted by reducing the allowable axial load or its variability; or by increasing the class of pile material, by changing pile geometric parameters or by conduction more stringent quality control of the piles material with rejection of piles which variation coefficient of elastic modulus is higher than required values.

After assigning the final design parameters of the pile and fulfilling the condition (9), it is necessary to clarify the value of the reliability index β . Since the limit state model is nonlinear, it is necessary to use FORM (First Order Reliability Method) algorithm to more accurately estimate the reliability index β of the pile. The FOSM method also fails to be invariant with different mathematically equivalent formulations of the same problem. As noted in [23], the first-order reliability method (FORM) is considered to be one of the most reliable computational methods and has become a basic method for structural reliability analysis.

The mathematical model of the limit state (7) can be written as:

$$g = \left(s_u - \frac{1-\nu}{\tilde{G} \cdot d} \right) \frac{\tilde{E} \cdot A}{l} - \tilde{N} \leq 0. \quad (10)$$

Then reliability index is:

$$\beta = \frac{E[g]}{\sigma_g}, \quad (11)$$

where the mathematical expectation of limit state function g is:

$$E[g] = g(E[N], E[G], E[E]) = \left(s_u - \frac{1-\nu}{E[G] \cdot d} \right) \frac{E[E] \cdot A}{l} - E[N]; \quad \text{and standard deviation is:}$$

$$\sigma_g = \sqrt{\left(\frac{\partial g}{\partial G} \right)^2 \sigma_G^2 + \left(\frac{\partial g}{\partial E} \right)^2 \sigma_E^2 + \left(\frac{\partial g}{\partial N} \right)^2 \sigma_N^2}.$$

For generality, denote: $\tilde{G}_2 = x_1$, $\tilde{E} = x_2$, $\tilde{N} = x_3$.

“Sensitivity factors” are calculated by equation:

$$\alpha_i = - \frac{\frac{\partial g}{\partial x_i} \sigma_{x_i}}{\left[\sum_{i=1}^n \left(\frac{\partial g}{\partial x_i} \sigma_{x_i} \right)^2 \right]^{1/2}}. \quad (12)$$

New x - and u - coordinates are calculated for the limit state function (10) as:

$$x_i^* = E[x_i] + \beta \cdot \sigma_{x_i} \cdot \alpha_i, \quad (13)$$

$$u_i^* = \frac{x_i^* - E[x_i]}{\sigma_{x_i}}. \quad (14)$$

New function values are calculated in the new coordinates: $g(x_i^*)$ and $\frac{\partial g(x_i^*)}{\partial x_i^*}$.

After that, a new reliability index β^* is determined by the equation:

$$\beta^* = \frac{g(x^*) - \sum \frac{\partial g(x^*)}{\partial x_i} \sigma_{x_i} u_i}{\left[\sum_{i=1}^n \left(\frac{\partial g(x^*)}{\partial x_i} \sigma_{x_i} \right)^2 \right]^{1/2}}. \quad (15)$$

Then iterations are repeated until the reliability index β converges.

3. Results and Discussion

Let us consider the proposed approach in example. Design parameters (and its statistical parameters) are given in Table 1.

Table 1. Parameters for pile stochastic analysis.

Parameter	Expected value	Standard deviation
Soil Poisson's ratio	0.35	-
Soil shear modulus, MPa	50	1.5
Pile diameter, m	0.35	-
Pile length, m	6	-
Elastic modulus, MPa	30000	800
Pile cross-section area, m ²	0.096	-
Allowable settlement, m	0.010	-

The Y expected value and standard deviation calculated by above equations as:

$$E[Y] = \left(s_u - \frac{1-v}{E[G] \cdot d} \right) \frac{E[E] \cdot A}{l} = \left(0.01 - \frac{1-0.35}{50 \cdot 0.35} \right) \frac{30 \cdot 10^3 \cdot 0.096}{6} = 4.811 \text{ MN.}$$

$$\sigma_y = \sqrt{\left(\frac{\partial Y}{\partial G} \right)^2 \sigma_G^2 + \left(\frac{\partial Y}{\partial E} \right)^2 \sigma_E^2} = \sqrt{0.287 + 16.16 \cdot 10^9} = 0.128 \text{ MN.}$$

As can be seen from the calculations, the variability of the soil shear modulus under the pile toe does not practically affect the overall variability of the pile bearing capacity according to the settlement criterion.

Let us take design reliability index $\beta=3$. There are different approaches to assign a design reliability index [2, 24, 25, etc.]. The Table 2 shows the values of allowable mathematical expectations of load $E[X]$ depending on the load coefficient of variation CV_x at a given reliability index β .

Table 2. Expected values of ultimate loads $E[X]$ at the different levels of load variation coefficients CV_x .

CV_x	0.01	0.03	0.05	0.10	0.15	0.20	0.25	0.30	0.35
$E[X]$, MN	4.404	4.267	4.087	3.650	3.284	2.981	2.728	2.515	2.332

Fig. 1 presents a diagram which reflects safety and failure areas in the appointment of the load statistical parameters: $E[X]$ and CV_x . Such diagrams can be used to estimate the allowable value of the load in the inspection or design of pile foundations.

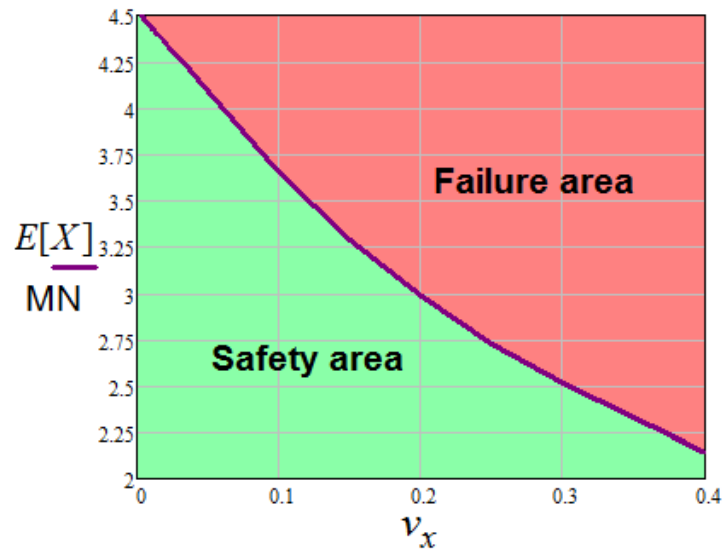


Figure 1. Diagram for ultimate load estimation.

Assume that the load is given by the following statistical parameters: $E[X] = 3.900$ MN; $CV_x = 0.07$; $\sigma_x = 0.273$ MN. As seen in Fig. 1, the pile is in the safety area by the settlement criterion. The reliability index in this case is:

$$\beta = \frac{E[Y] - E[X]}{\sqrt{\sigma_y^2 + (E[X] \cdot CV_x)^2}} = \frac{4.811 - 3.900}{\sqrt{0.128^2 + (3.900 \cdot 0.07)^2}} = 3.019.$$

The variability of the elastic modulus of the pile material contributes greatly to the solution uncertainty. The effect of the modulus change is analyzed in the table 3 at different coefficients of variation.

Table 3. Reliability index β at the different levels of pile elastic modulus expected value $E[E]$ and variation coefficient CV_E .

Coefficient of variation CV_E	Expected value of elastic modulus $E[E]$, MPa·10 ³								
	25	26	27	28	29	30	31	32	33
0.03	0.365	0.896	1.421	1.938	2.447	2.949	3.443	3.929	4.407
0.05	0.321	0.784	1.233	1.669	2.092	2.503	2.901	3.287	3.660
0.07	0.278	0.673	1.053	1.417	1.766	2.100	2.421	2.729	3.024
0.10	0.224	0.540	0.839	1.123	1.391	1.646	1.888	2.118	2.337
0.15	0.165	0.394	0.610	0.812	1.002	1.180	1.349	1.508	1.658
0.20	0.128	0.307	0.473	0.628	0.774	0.910	1.039	1.159	1.273

The Table 3 reflects the important role of quality control of physical and mechanical properties of pile materials (for example, concrete). Graphically, the table 3 data are shown in Fig. 2.

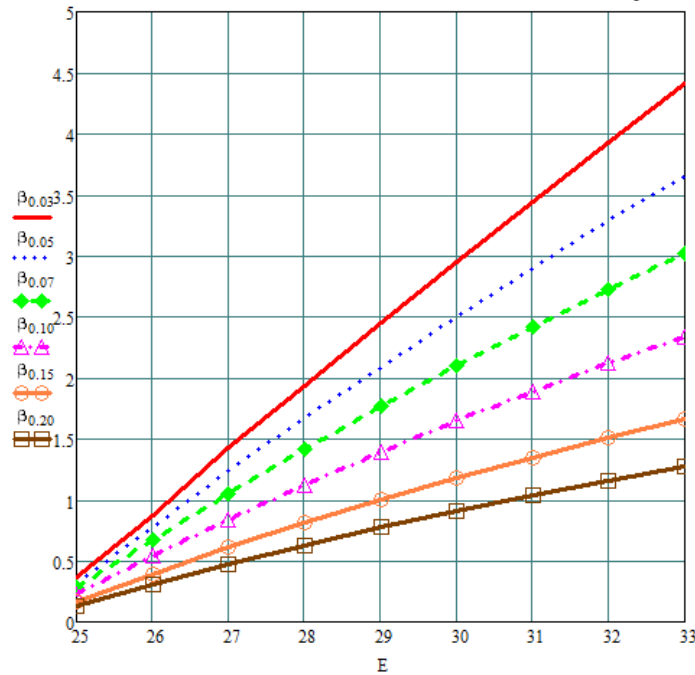


Figure 2. $\beta - E[E]$ diagrams at the different levels of variation coefficients for pile material elastic modulus E .

Fig. 2 shows that in order to provide a higher level of reliability, it is necessary to assign a greater expectation of the elasticity with an increase in its coefficient of variation. Diagram of the Fig. 2 type allows us to set the next parameters: 1) reliability index β (based on the results of nondestructive testing of existing piles); 2) the required minimum parameters of the designed piles at a given reliability index β .

Let us specify the value of β by the FORM approach.

Expected value and standard deviation of limit state function are:

$$E[g] = \left(s_u - \frac{1-\nu}{E[G]d} \right) \frac{E[E]A}{l} - E[N] = \left(0,01 - \frac{1-0,35}{50 \cdot 10^6 \cdot 0,35} \right) \frac{30 \cdot 10^9 \cdot 0,096}{6} - 3,9 \cdot 10^6 = 9,105 \cdot 10^5 \text{ N.}$$

$$\sigma_g = \sqrt{\left(\frac{\partial g}{\partial G} \right)^2 \sigma_G^2 + \left(\frac{\partial g}{\partial E} \right)^2 \sigma_E^2 + \left(\frac{\partial g}{\partial N} \right)^2 \sigma_N^2 =}$$

$$= \sqrt{\left(\frac{AE[E](\nu-1)}{d \cdot l \cdot E[G]^2} \right)^2 \sigma_G^2 + \left(\frac{A(s_{ult} - [\nu-1]/[d \cdot E[G]])}{l} \right)^2 \sigma_E^2 + \sigma_N^2}$$

$$\sigma_g = 3,016 \cdot 10^5 \text{ N.}$$

The reliability index (or Cornell index) is:

$$\beta = \frac{E[g]}{\sigma_g} = \frac{9,105 \cdot 10^5}{3,016 \cdot 10^5} = 3,019. \text{ Dimensionless}$$

Specify the parameters values for the next iteration by (12), (13) and (14) in table 4.

Table 4. Parameters for reliability index β^* evaluation.

	G	E	N
α	$1,777 \cdot 10^{-6}$	0.425	-0.905
x^*	$5,000 \cdot 10^7 \text{ Pa}$	$3,142 \cdot 10^{10} \text{ Pa}$	$2,687 \cdot 10^6 \text{ N}$
u^*	$7,432 \cdot 10^{-6}$	1.779	-3.785

New reliability index β^* by (15) is:

$$\beta^* = \frac{g(x^*) - \sum \frac{\partial g(x^*)}{\partial x_i} \sigma_{x_i} u_i}{\left[\sum_{i=1}^n \left(\frac{\partial g(x^*)}{\partial x_i} \sigma_{x_i} \right)^2 \right]^{1/2}} \rightarrow \beta^* = 3.019.$$

Based on the results of the FORM approach, we obtain the same reliability index as in the FOSM approach: $\beta = \beta^* = 3.019$. Consequently, the accuracy of the FOSM approach is enough to estimate the reliability index β even under different mathematical models of limit states - (7) or (10).

Statistical tests were carried out in MathCAD by the Monte Carlo method. Random values were given through the function $rnorm(1000, E[X], \sigma_x)$. According to the results of 1000 statistical tests, exceeding the limit state was recorded in 2 cases. The theoretical probability of pile non-failure in frequency is $(1000-2)/1000=0.9980$. This probability value is extremely close to the theoretical probability value of the reliability index $P = \Phi(\beta = \beta^* = 3.019) \approx 0.9987$.

Table 5. Comparison of reliability levels by FOSM, FORM and Monte-Carlo methods.

Method	FOSM	FORM	Monte-Carlo
Reliability level	0.9987	0.9987	0.9980

For a comprehensive assessment of reliability, it is necessary to identify the pile reliability according to other criteria of limit states (pile material, soil base strength, pile stability, etc.) and consider the pile foundation as a structural system [26, 27, etc.].

Target values for the reliability index β for various design situations, and for reference periods of 1 year and 50 years, are indicated in Appendix C, Eurocode 0 "Basis of structural design". For example, reliability index for serviceability limit state (for reference periods of 1 year) is $\beta = 2.9$. Joint Committee on Structural Safety (JCSS) Probabilistic Model Code sets target values for the reliability index β in dependence with a comparative cost of safety measures and failure consequences. However, the reliability index should be calculated individually for each structure (or structural element) based on the value of the acceptable risk [28].

4. Conclusions

1. The article describes the methods for end-bearing pile bearing capacity estimation and reliability analysis of settlement criterion;
2. The diagram of safety and failure areas is proposed for assigning and checking design of axial load statistic parameters on end-bearing piles;
3. It is shown by numerical example, that design load and elastic modulus of the pile materials are the main stochastic (random) parameters that determine the probability of end-bearing pile failure
4. Different mathematical models of limit states were analyzed by FOSM and FORM approaches. Results show that there is no "invariant" problem for FORM approach in that case;
5. Experimental modeling of random (stochastic) parameters of the end-bearing pile was carried out to verify the proposed approaches. A good convergence of theoretical results with experimental simulation data is established.

References

1. Priadko, I.N., Mushchanov, V.P., Bartolo, E., Vatin, N.I., Rudnieva, I.N. Improved numerical methods in reliability analysis of suspension roof joints. Magazine of Civil Engineering. 2016. 65(5). Pp. 27–41. DOI: 10.5862/MCE.65.3
2. Wang, P., Zhang, J., Zhai, H., Qiu, J. A new structural reliability index based on uncertainty theory. Chinese Journal of Aeronautics. 2017. 30(4). Pp. 1451–1458. DOI: 10.1016/j.cja.2017.04.008
3. Wang, C., Zhang, H., Li, Q. Moment-based evaluation of structural reliability. Reliability Engineering & System Safety. 2019. 181. Pp. 38-45. DOI: doi.org/10.1016/j.ress.2018.09.006
4. Hamrouni, A., Dias, D., Sbartai, B. Probabilistic analysis of piled earth platform under concrete floor slab. Soils and Foundations. 2017. 57. Pp. 828–839. DOI: 10.1016/j.sandf.2017.08.012

5. Schmoor, K.A., Achmus, M., Foglia, A., Wefer, M. Reliability of design approaches for axially loaded offshore piles and its consequences with respect to the North Sea. *Journal of Rock Mechanics and Geotechnical Engineering*. 2018. 10. Pp. 1112–1121. DOI: 10.1016/j.jrmge.2018.06.004
6. Bian, X., Xu, Z., Zhang, J. Resistance factor calculations for LRFD of driven piles based on setup effects. *Results in Physics*. 2018. 11. Pp. 489–494. DOI: 10.1016/j.rinp.2018.09.042
7. Ivanova, T.V., Albert, I.U., Kaufman, B.D., Shulman, S.G. The load-bearing capacity of hanging piles by the strength criterion of a pile or soil material. *Magazine of Civil Engineering*. 2016. 67(7). Pp. 3–12. DOI: 10.5862/MCE.67.1.
8. Chen, X. *Settlement calculation of high-rise buildings*. Springer Berlin. 2011. 430 p. DOI: 10.1007/978-3-642-15570-3
9. Prakash, S., Sharma, H.D. *Pile foundations in engineering practice*. New York: John Wiley & Sons. 1989. 784 p.
10. Zhou, Z., Wang, D., Zhang, L. Determination of large diameter bored pile's effective length based on Mindlin's solution. *Journal of Traffic and Transportation Engineering (English Edition)*. 2015. 2(6). Pp. 422-428.
11. Ter-Martirosyan, A.Z., Ter-Martirosyan, Z.G., Sobolev, Ye.S. Osadka i nesushchaya sposobnost dlinnykh svay konechnoy zhestkosti s ushirennoy pyatoy s uchetom nelineynykh svoystv okruzhayushchego grunta [Settlement and bearing capacity of long piles of finite rigidity with enlarged base with due regard for non-linear properties of surrounding ground]. *Zhilishchnoye stroitelstvo [Housing Construction]*. 2015. 9. Pp. 8-11. (rus)
12. Mylonakis, G. Winkler modulus for axially loaded piles. *Géotechnique*. 2001. 51(5). Pp. 455-461. DOI: 10.1680/geot.51.5.455.39972
13. Baund P., Wong T., Zhu W. Effects of porosity and crack density on the compressive strength of rocks. *International Journal of Rock Mechanics and Mining Sciences*. 2014. 67. Pp. 202-211. DOI: 10.1016/j.ijrmms.2013.08.031
14. Zertsalov M.G., Nikishkin M.V. Mirovoy opyt v proyektirovanii svay v skalnykh gruntakh [International experience in designing piles in rock]. *Vestnik MGSU*. 2011. 5. Pp. 120-127. (rus)
15. Hamderi, M. Comprehensive group pile settlement formula based on 3D finite element analyses. *Soils and Foundations*. 2018. 58(1). Pp. 1-15. DOI 10.1016/j.sandf.2017.11.012
16. Shahin, M.A. Load–settlement modeling of axially loaded steel driven piles using CPT-based recurrent neural networks. *Soils and Foundations*. 2014. 54(3). Pp. 515-522. DOI: 10.1016/j.sandf.2014.04.015
17. Lalin V. V., Yavarov A. V., Orlova E. S., Gulov A. R. Application of the Finite Element Method for the Solution of Stability Problems of the Timoshenko Beam with Exact Shape Functions. *Power Technology and Engineering*. 2019. 53. Pp. 449-454. DOI: 10.1007/s10749-019-01098-6
18. Perley Ye.M., Rayuk V.F., Belenkaya V.V., Almazov A.N. Svaynyye fundamenty i zaglublennyye sooruzheniya pri rekonstruktsii deystvuyushchikh predpriyatiy [Pile foundations and buried structures during reconstruction of existing enterprises]. Leningrad: Stroyizdat, 1989. 175 p. (rus)
19. Bartolomey, A.A., Omelchak, I.M., Yushkov, B.S. Prognoz osadok svaynykh fundamentov [Settlement forecast of pile foundations]. Moscow: Stroyizdat, 1994. 384 p. (rus)
20. Polishin, D.E., Tokar, R.A. Maximum Allowable Differential Settlement of Structures. *Proceedings of 4th International conference SMFE: London 1957*. 1. Pp. 402-406. URL: https://www.issmge.org/uploads/publications/1/41/1957_01_0085.pdf
21. Skempton, A.W., MacDonald, D.H. The Allowable Settlement of Buildings. *Proc. Inst. Of Civil Engineers: Part 3*. 1956. 5. Pp. 727–784.
22. Poulos, H.G. Tall building foundations: design methods and applications. *Innovative Infrastructure Solutions*. 2016. Pp. 1–10. DOI: 10.1007/s41062-016-0010-2
23. Lu, Z., Cai, C., Zhao, Y. et al. Normalization of correlated random variables in structural reliability analysis using fourth-moment transformation. *Structural Safety*. 2020. 82. DOI: 10.1016/j.strusafe.2019.101888
24. Ghassemi S.H., Nowak A.S. Target reliability for bridges with consideration of ultimate limit state. *Engineering Structures*. 2017. 152. Pp. 226–237. DOI: 10.1016/j.engstruct.2017.09.012
25. Sajedi, S., Huang, Q. Reliability-based life-cycle-cost comparison of different corrosion management strategies. *Engineering Structures*. 2019. 186. Pp. 52–63. DOI: 10.1016/j.engstruct.2019.02.018
26. Wang, Q., Wu, Z. Structural system reliability analysis based on improved explicit connectivity BNs. *KSCE Journal of Civil Engineering*. 2018. 22(3). Pp. 916–927. DOI: 10.1007/s12205-018-1289-7
27. Wang, J., Qiu, Z. The reliability analysis of probabilistic and interval hybrid structural system. *Applied Mathematical Modelling*. 2010. 34(11). Pp. 3648–3658. DOI: 10.1016/j.apm.2010.03.015
28. Koker N.D., Viljoen C., Day P. W. Risk-optimal sampling for reliability-based design. *Structural Safety*. 2020. 83. DOI: 10.1016/j.strusafe.2019.101896

Contacts:

Sergey Solovyev, ser6sol@yandex.ru



DOI: 10.18720/MCE.96.7

Impact of anchored CFRP on the torsional and bending behaviour of RC beams

R. Al-Rousan*, I. Abo-Msamh

Jordan University of Science and Technology, Irbid, Jordan

* E-mail: rzalrousan@just.edu.jo

Keywords: reinforced concrete, structural strength, structural models, bonding, torsion, flexural strength, fiber reinforced polymer

Abstract. The scientific problem considered in the study is indeed one of the problems in the modern theory of reinforced concrete. Despite a significant number of studies on the problem of bending with torsion, to date. There are no sufficiently reliable solutions to this problem that most fully reflect the physical nature of the problem. In the last two decades, using of Carbon Fiber Reinforced Polymers (CFRP) in strengthening of deficient reinforced concrete structural elements has been increased due to their ease of installation, low invasiveness, high corrosion resistance, and high strength to weight ratio. Strengthening damage structures is a relatively new technique. Therefore, the intent was to appear at the essential CFRP external strengthening technique that provides an efficient increase in the shear and flexural strengths as maintaining ductile failure mode. However, anchoring and debonding problems remains a challenge for the accomplishment of this technique. In this study, a novel application was implemented in which the CFRP sheet was integrated as external shear strengthening for RC beams. Therefore, this study investigated the behavior of simply supported RC beams strengthened externally with anchored CFRP composite using and subjected to combined bending and torsion using Nonlinear Finite Element Analysis (NLFEA). Seventeen models have been constructed and divided into four groups to scrutinize the effect of CFRP anchored depth and CFRP strip spacing. The performance of each beam was evaluated in terms of failure mode, CFRP strain, load-deflection and torsion-twist behavior, ultimate deflection, ultimate load capacity, ultimate angle of twist, ultimate torsion capacity, elastic stiffness, and energy absorption. The enhancement percentage increased with the increase of anchored depth and decreased with the increase of CFRP strip spacing. Finally, the external strengthening with anchored had a superior effect on the ultimate load, ultimate deflection, angle of twist, torsion elastic stiffness, energy absorption.

1. Introduction

In recent decades, repair and strengthening of reinforced concrete (RC) buildings and bridges have become increasingly common. Deficiencies in RC members may exist for several reasons, including changes in use of the structure, design and construction errors, and degradation due to environmental conditions [1–4]. RC members are commonly strengthened in flexure, shear, and/or confinement depending on the member loading conditions and type of enhancement needed [5–7]. In some cases, RC members are subjected to significant torsional moments, and the torsional strength needs to be enhanced. Accordingly, methods and design provisions for strengthening RC members in torsion are needed.

The Reinforced Concrete (RC) structural elements such as the peripheral beams in each floor of multi-storied buildings, ring beams at the bottom of circular tanks, edge beams of shell roofs, the beams supporting canopy slabs and the helical staircases are subjected to significant torsional loading in addition to flexure and shear. In reinforced concrete design, depending on the load transfer mechanism the torsion is classified as 'equilibrium torsion' and 'compatibility torsion'. Equilibrium torsion is induced in beams supporting lateral overhanging projections, and is caused by the eccentricity in the loading. In compatibility torsion, torsion is induced in a structural member by rotations (twists) applied at one or more points along the length of the member. The twisting moments induced are generally statically indeterminate and their analysis necessarily involves compatibility conditions. Hence it is named 'compatibility torsion'. The structural elements subjected to torsion show cracking if they are not designed and detailed properly. Further, change in loading or



deterioration of structural element cause the deficiency in torsional resistance. Also, in recent past earthquakes, it has been seen that structures showed failure and some have been severely damaged. Such disasters have demonstrated the need for retrofitting of seismically deficient structures. Retrofitting allows strengthening of elements to resist the strength demands predicted by the analysis, without significantly affecting the overall response of the structure.

The fiber reinforced polymer (FRP) has been proved to be a widely used strengthening material for deficient RC members. It has various well-known advantages such as high strength to weight ratio, high corrosive resistance, and easy-to-apply character. Many significant experimental and theoretical studies in the past have been carried out to understand the flexural [1, 2] and shear [3, 4] behaviors of RC members externally strengthened with FRP materials since the bending moments and shear forces are regarded as primary effects, whereas the torsional strengthening has not been studied in much depth, which was just initiated in 2001 [8–10]. Torsion can be considered as primary effect, however, in some special situations such as spandrel or curved beams, eccentrically loaded bridge girders, and bridge columns under seismic load. In this case, it is important to conduct deep researches on the torsional behavior of RC members strengthened with FRP materials, including experimental, numerical and analytical investigations.

Most of the test specimens in previous experimental investigations were solid rectangular RC beams externally strengthened with carbon or glass FRP (CFRP or GFRP) materials under monotonic torsion [11–13]. Few tests of RC box beams strengthened with CFRP sheets have been conducted under monotonic torsion [14] and under cyclic torque [15]. To understand the influence of strengthening schemes of FRP system on the effectiveness of upgrading in torsional resistance of RC members [16–23], the various FRP wrapping configurations have been investigated by considering the fiber orientation, the number of beam faces strengthened, the effect of number of FRP plies used, and the influence of anchors in U-wrapped test beams [16, 17]. The results have showed that the 45 spiral wrap is a much more efficient torsional strengthening scheme than vertical strips. Few researches on non-rectangular beams have been carried out in recent years. RC T-beams strengthened with different strengthening techniques under pure torsion [16] and combined shear and torsion [17] have been investigated. Spandrel RC beams strengthened with CFRP laminates also have been tested under torsion [18]. In addition, the torsional repair of damaged rectangular [19] and circular [20] RC columns with FRP materials, which helps to enhance the ultimate rotational strength, has been carried out in recent years.

Owing to the fact that experimental investigation costs much time and money, the finite element analysis (FEA) using commercial software is a beneficial supplement to the study of torsional behavior. Numerical studies on the cracking and crushing patterns [12], the damage simulation [24], the effect of CFRP and reinforcing steel bars on the contribution to the torsional behavior [10], and the torque–twist curves [23] of RC beams were performed through FEA softwares, such as ANSYS, ABAQUS, DIANA, Algor SAP and so on [25–29]. Therefore, essential issues to produce effective, economical, and successful CFRP strengthening were discussed. Also, the impact of anchored CFRP external strengthening on the behavior of reinforced concrete beams subjected to bending and torsion received miniature consideration. The scientific problem considered in the study is indeed one of the problems in the modern theory of reinforced concrete. Despite a significant number of studies on the problem of bending with torsion, to date. There are no sufficiently reliable solutions to this problem that most fully reflect the physical nature of the problem. In this study, a novel application was implemented in which the CFRP sheet was integrated as external shear strengthening for RC beams. A lack of literature regarding the behavior of simply supported RC beams strengthened externally with CFRP composite and subjected to combined bending and torsion are necessitated conducting the present investigation. The main objectives of this study are to predict the bending and torsion of RC beams strengthened externally with anchored CFRP composite using Nonlinear Finite Element Analysis (NLFEA) taking into account the effects of four major strengthening configuration including: 1) One layer of 50 mm U strip wrapping at 225 mm c/c with an additional layer of CFRP wrapping on both sides of the web; 2) One layer of 50 mm U strip wrapping at 175 mm c/c with an additional layer of CFRP wrapping on both sides of the web; 3) One layer of 50 mm U strip wrapping at 125 mm c/c with an additional layer of CFRP wrapping on both sides of the web; and 4) One layer of 50 mm U strip wrapping at 75 mm c/c with an additional layer of CFRP wrapping on both sides of the web. As a result, seventeen models have been constructed and subjected to combined bending and torsion. For this purpose, validation against the previous experimental study reported by Gesund et al. [30] is firstly simulated using ANSYS software. After that, a parametric study is extended for strengthened RC beams using different configurations of CFRP.

2. Methods

ANSYS software is a numerical method used to simplify the analysis of a variety of engineering problems. To reduce the complexity of load setup, effort, time and cost during the experimental testing, ANSYS software had been used by many researchers. It was recommended about this software to be used since their results achieved good agreement with experimental results. ANSYS is general-purpose software used in this study. Twenty-six full-scale models strengthened using CFRP are developed to carry out different investigated parameters.

2.1. Experimental Work Review

The validation process of the finite element model is based on the experimental work performed by Gesund et al. [30]. A total of twelve simply supported RC beams tested until failure under combined bending and torsion (Figure 1). The cross-section of the beam is 200 mm×200 mm with a 1600 mm clear span length. All beams were reinforced using three bars of tension reinforcement and two bars of compression reinforcement with a 13 mm nominal diameter. Besides, a 10 mm nominal diameter for closed stirrups was applied at 50 mm spacing c-c (Figure 1). The beams were loaded by two-point loads at the end of two-moment arms providing out of plane eccentricity. Hence the beams were subjected to the combined effect of bending and torsion (Figure 1).

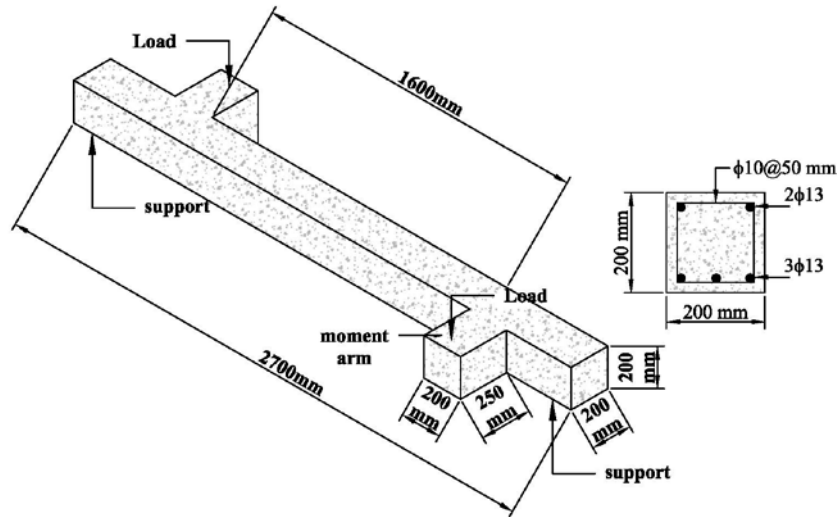


Figure 1. View of the model under load [30].

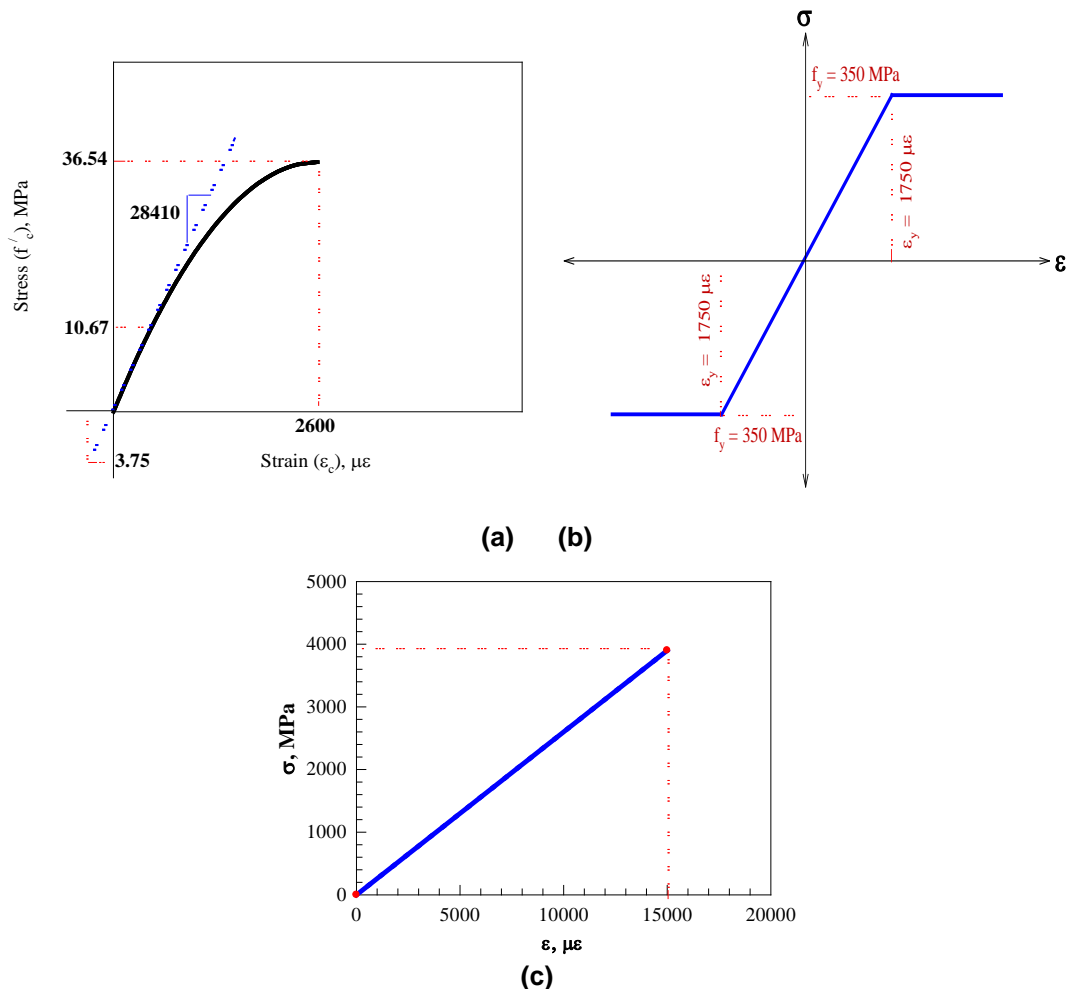


Figure 2. Stress-Strain Curve for (a) Concrete, (b) Steel, and (c) CFRP composite [25].

2.2. Description of Non-linear Finite Element Analysis (NLFEA)

Concrete is a brittle material having high compressive strength compared to tensile strength. The cylindrical compressive strength of concrete is 36.54 MPa. The elastic modulus of elasticity (E_c) and modulus of rupture (f_r) of concrete are 28410 MPa and 3.75 MPa, respectively, as shown in Figure 2(a). Concrete poisson's ratio is assumed 0.17 for all models. Shear transfer coefficient for open and closed cracks, β_t and β_c respectively, are important inputs needed for concrete, which indicate the condition of crack surface. In this study, a value of 0.2 and 0.9 is set for the β_t and β_c , respectively. Steel reinforcement is modeled as a bilinear isotropic material with 200 GPa for the elastic modulus of elasticity and 0.3 of poisson's ratio. Its behavior is assumed to be elastic-perfectly plastic, and the same assumption is set for tension and compression reinforcement with yielding stress of 350 MPa, as shown in Figure 2(b). Steel plates are added to the finite element model to avoid stress concentrations at the support and loading locations. These plates are steel type and defined as linear elastic isotropic material with 200 GPa for the elastic modulus of elasticity and 0.3 of poisson's ratio. Sika Wrap Hex 300C 0/90 is the CFRP type used in this study. It is a bi-directional material property with 0.166 mm thickness and having fibers in longitudinal and transverse directions. The linear elastic tensile stress-strain curve for CFRP composites is shown in Figure 2(c) and the detailed mechanical properties and poisson's ratio in all directions are shown in Table 1.

Table 1. CFRP composites properties.

Modulus of elasticity (GPa)		Poisson's ratio		Shear modulus of elasticity (GPa)		Ultimate tensile strength (MPa)	Ultimate strain
E_x	260	ν_{xy}	0.22	G_{xy}	106.6	3900	0.015
E_y	260	ν_{yz}	0.22	G_{yz}	106.6		
E_z	4.5	ν_{zx}	0.30	G_{zx}	1.73		

SOLID 45 is used to model the loading and supporting steel plates. This element is suitable to model the dimensional solid structures defined by eight nodes. There is a presence of translations in the three nodal directions; x, y, and z for each node. SOLID 65 is used to model the concrete which is suitable for tension cracking, crushing in compression and plastic deformations. It is a three-dimensional element defined by eight nodes. Each node has three degrees of freedom with a presence of translations in the three nodal directions; x, y, and z for each node. Steel reinforcement is modeled using link 180, which is a uniaxial tension-compression element. It includes two nodes, and each node has three degrees of freedom. This element can predict large deflection, large strain, rotation, creep, and plasticity. This element can predict large deflection, large strain, stress stiffening, creep, and plasticity. For CFRP, the SHELL 181 element type, having four nodes is used in modeling. It is chosen because it is appropriate to analyze thin layered applications. Three translations and three rotations are considered to include the six degrees of freedom at each node.

The concrete beam and steel plates were modeled as solid elements while steel reinforcement was modeled as link elements. In the case of strengthened RC beams, the CFRP sheets were modeled as shell element with a mesh size of 25 mm. To ensure the perfect bond between concrete and reinforcement, the link element of steel is connected between each adjacent Solid 65 elements, hence the same nodes are shared between the two materials. The same approach is used for the CFRP sheets to provide the perfect bonding as well as for the Steel plates. The geometry of the control and strengthened model, along with the reinforcement specimens are shown in Figure 3(a), Figure 3(b) and Figure 3(c), respectively. The meshing of the CFRP sheet for both fully U wraps and strips wrapping is also shown in Figure 3(d) and Figure 3(e), respectively.

The loads are applied on the two steel plates at the end of the moment arms as line loads distributed over nine nodes. The purpose of these moment arms is to provide the twisting of the main beam. To constrain the model, displacement boundary conditions are required. At the left end of the beam the U_x , U_y , and U_z displacements are set to zero to ensure hinge support. While roller support is added at the right end of the beam by setting zero value to the U_y displacement. Figure 4 shows the loads and boundary conditions of the model. The total applied load is divided into multiple load steps or load increments. Newton-Raphson equilibrium iterations give convergence at the end of each load increment within tolerance limit equal to (0.001) and a load increment of 0.22 kN. When large numbers of cracks appear throughout the concrete, the loads are applied gradually with smaller load increments.

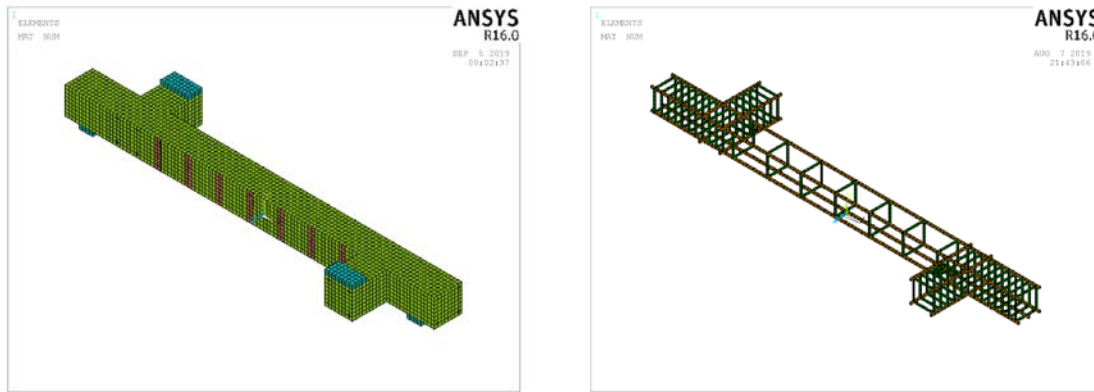


Figure 3. Geometry and meshing.

Table 2. Investigated parameters.

Group number	Beam number	CFRP strengthening configuration	CFRP Anchored Depth (mm)
Control	BC	Control beam without strengthening	0
Group 1	B1	One layer of 50 mm U strip wrapping at 225 mm c/c with an additional layer of CFRP wrapping on both sides of the web	50
	B2		100
	B3		150
	B4		200
Group 2	B5	One layer of 50 mm U strip wrapping at 175 mm c/c with an additional layer of CFRP wrapping on both sides of the web	50
	B6		100
	B7		150
	B8		200
Group 3	B9	One layer of 50 mm U strip wrapping at 125 mm c/c with an additional layer of CFRP wrapping on both sides of the web	50
	B10		100
	B11		150
	B12		200
Group 4	B13	One layer of 50 mm U strip wrapping at 75 mm c/c with an additional layer of CFRP wrapping on both sides of the web	50
	B14		100
	B15		150
	B16		200

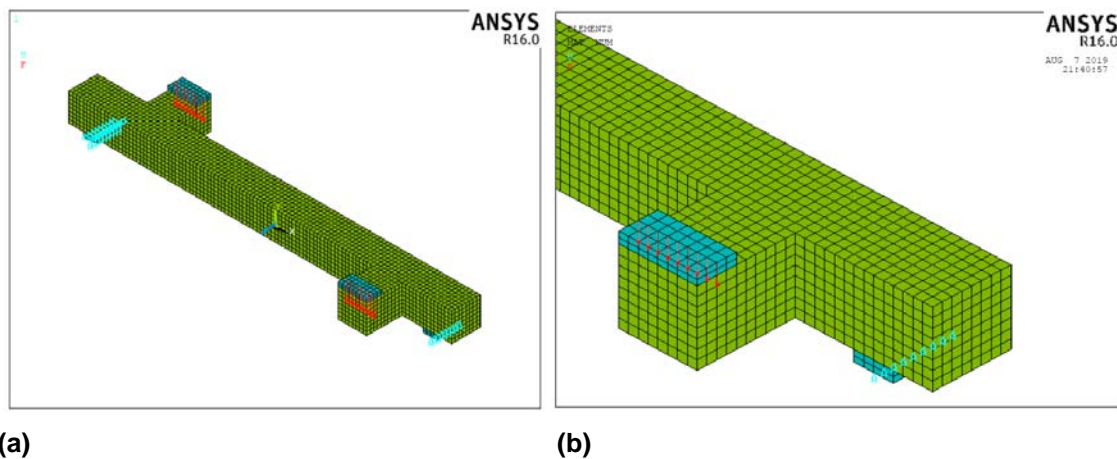


Figure 4. Loads and boundary conditions: (a) 3-D view and (b) Zoomed view.

2.3. Investigated Parameters

Twenty full-scale models strengthened using CFRP are developed to carry out different investigated parameters (Figure 5). A parametric study conducted in this research consists of four groups. The first group contains four models with one layer of 50 mm U strip wrapping at 225 mm c/c with an additional layer of CFRP wrapping on both sides of the web. Group 2 includes four models with one layer of 50 mm U strip wrapping at

175 mm c/c with an additional layer of CFRP wrapping on both sides of the web. The second group includes four models with one layer of 50 mm U strip wrapping at 175 mm c/c with an additional layer of CFRP wrapping on both sides of the web. The third group includes four models with one layer of 50 mm U strip wrapping at 125 mm c/c with an additional layer of CFRP wrapping on both sides of the web. The fourth group includes four models with one layer of 50 mm U strip wrapping at 75 mm c/c with an additional layer of CFRP wrapping on both sides of the web. A full description of the finite element modeling groups is shown in Table 2.

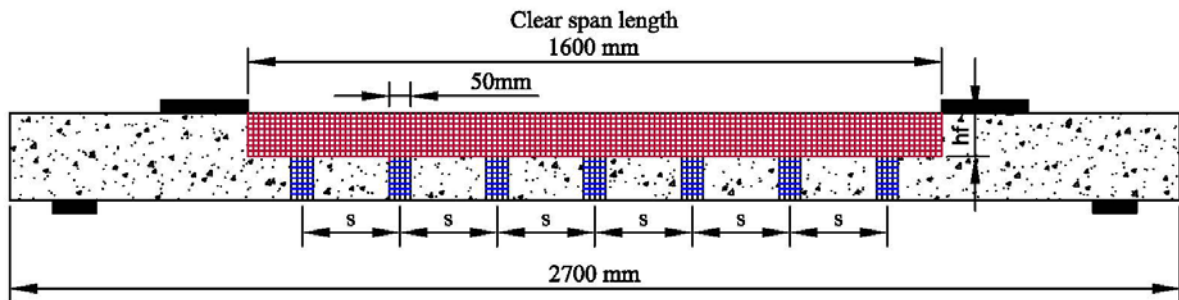
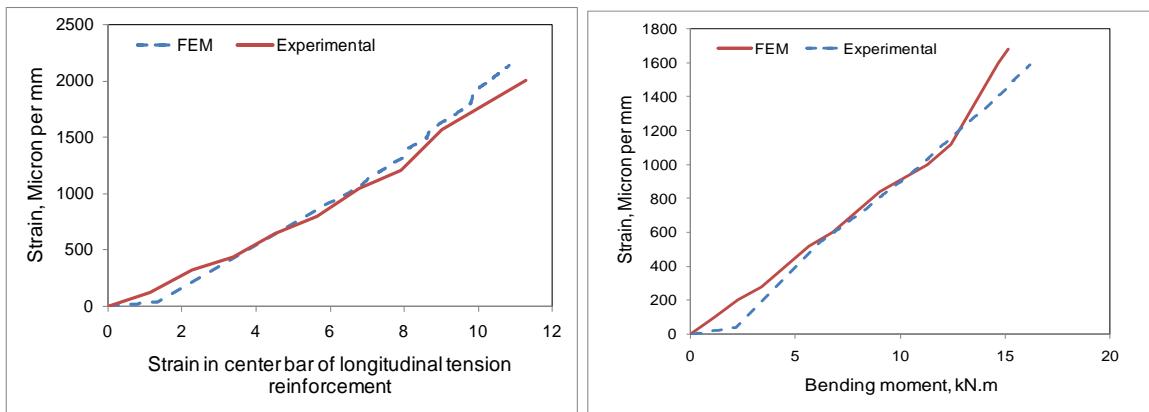


Figure 5. Schematic representation of simulated beams.

2.4. Validation Process

The validation process of the finite element model is based on the experimental work performed by Gesund et al. [30]. Bending and twisting moments at failure as well as the strain in the center bar of longitudinal reinforcement are compared with the NLFEA results. Figure 6 and Table 3 show good agreements between the finite element method and experimental results.



(a) Beam 2

(b) Beam 4

Figure 6. Validation of the NLFEA results.

Table 3. Validation summary.

Beam number	Torsion to Bending moment ratio	Bending moment at failure (kN.m)		The torsional moment at failure (kN.m)		Absolute Error %
		Experiment	FEM	Experiment	FEM	
2	1	11.52	10.9	11.52	10.9	5.3
4	0.5	15.14	16.2	7.6	8.1	-6.9

3. Results and Discussion

3.1. Failure Mode

Figure 7 shows the crack pattern for the typically simulated beams. The first crack at an integration point is shown with a red circle outline, the second crack with a green outline, and the third crack with a blue outline. The first crack initiated from the support and then propagated toward the top of the beam in a diagonal shape. Due to the lack of CFRP wrapping along the control beam, this propagation spreads at a faster rate with individual cracks along the beam compared to the strengthened beams. The FRP helps in distributing the stresses on the whole body of the beam. Also, the cracks were smaller and closer to each other, giving higher strength and capacity for those beams. All strengthened beams show almost similar diagonal cracks initiation. This is due to the reality of similar loading and boundary conditions and the reinforcement details. However, the fully FRP U-wrap inhibits the propagation of cracks more than FRP strips. The beam strengthened with Fully

FRP U wrap could sustain higher loads and deflections. The failure occurred due to the substantial wide diagonal cracks and concrete crushing followed by FRP failure.

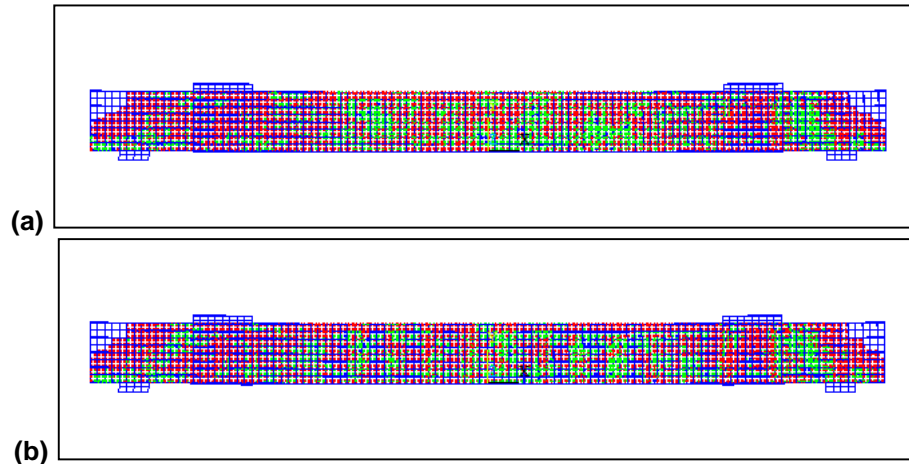


Figure 7. Crack pattern at failure: (a) control beam and (b) strengthened beams using FRP strips.

3.2. CFRP strain

Figure 8 shows the typical distribution of CFRP strain through the depth for all simulated beams. It is noticed that all simulated beams had CFRP strain below the maximum value of 15000 as shown in Table 4 and Table 5 as percentage of CFRP ultimate strain. Inspection of Table 5 reveals that the proposed anchorage system enhanced the efficiency of CFRP strips for Group#1 ($S = 225$ mm) from 15 % for un-anchored beams to 38 % for beam with anchored depth of 50 mm ($h_f = 0.25h$) and 65% for beam with anchored depth of 200 mm ($h_f = h$). This enhancement percentage increased with the decrease of CFRP strip spacing. The enhancement percentage of anchored system for Group#2 ($S = 175$ mm) is 43% for beam with anchored depth of 50 mm ($h_f = 0.25h$) and 69% for beam with anchored depth of 200 mm ($h_f = h$). Also, the enhancement percentage of anchored system for Group#3 ($S = 125$ mm) is 49% for beam with anchored depth of 50 mm ($h_f = 0.25h$) and 76% for beam with anchored depth of 200 mm ($h_f = h$). Finally, the strip spacing of 75 mm with anchorage enhanced the CFRP strain with a percentage of 54% for beam with anchored depth of 50 mm ($h_f = 0.25h$) and 85% for beam with anchored depth of 200 mm ($h_f = h$).

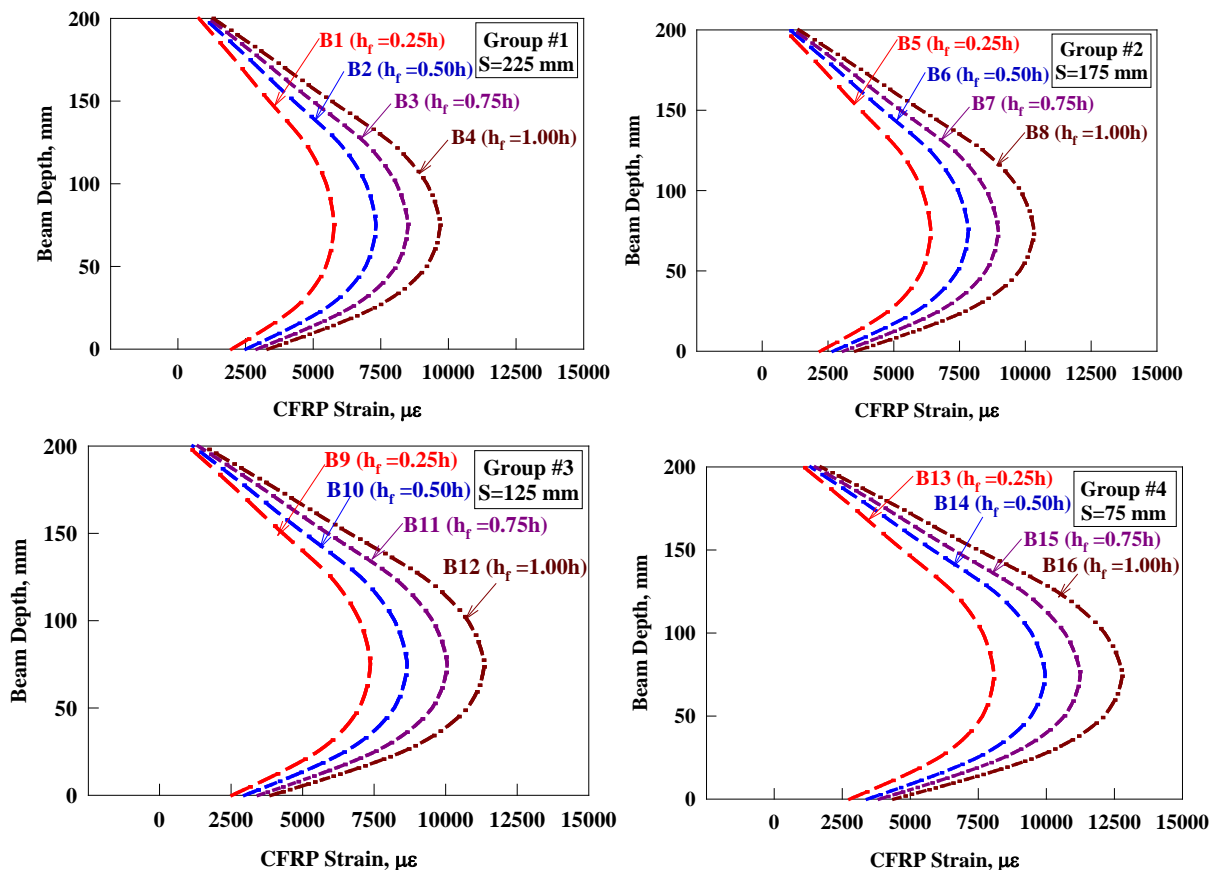


Figure 8. Typical CFRP strain versus beam depth.

3.3. Load-Deflection and Torsion-Twist Behavior

The load-deflection and torsion-twist curves are shown in Figure 9 and 10 respectively. The overall behaviour shown in Figure 9 and 10 indicates that the Anchored CFRP composite provided an increase in the torsional strength and twist at the peak load as well as the ultimate load capacity and corresponding deflection. In general, a linear behaviour before cracking with high torsional stiffness was observed for each strengthened anchored beam, and then the beam suffered an increase in the twist angle with small increasing of torque due to redistribution of forces from the concrete to the steel reinforcement. After this stage and before achieving the peak load, the behaviour became non-linear with a reduction in torsional stiffness.

The strengthened anchored beams exhibited larger twist and deflection at the peak load behaviour in the post-cracking stage due to yielding of the steel reinforcement and possibly slippage of the fibers in the composite. Table 4 illustrates the obtained results for all simulated models. The slope of each region of the load-deflection curves gives the elastic stiffness of the corresponding beam. All strengthened beams represent higher stiffness compared to the control beam in the three regions. Table 4 also shows the calculated energy absorption or area under the load deflection curves for all simulated models.

Table 4. Results for all simulated models.

Group number	Beam number	Ultimate load (kN)	Ultimate deflection (mm)	Ultimate torsion (kN.m)	Ultimate angle of twist (rad)	Elastic stiffness (kN/mm)	Energy absorption (kN.mm ²)	CFRP strain ($\mu\epsilon$)
Control	BC	27.8	3.05	0.0132	8.47	3.91	15.3	---
Group 1	B1	34.8	3.63	0.0153	10.62	4.12	22.8	5775
	B2	41.2	4.27	0.0181	12.57	4.14	31.8	7324
	B3	47.2	4.76	0.0210	14.40	4.26	40.6	8510
	B4	54.0	5.25	0.0244	16.45	4.41	51.1	9696
Group 2	B5	31.8	3.83	0.0164	9.70	3.56	22.0	6406
	B6	39.4	4.42	0.0191	12.01	3.82	31.4	7834
	B7	46.0	4.89	0.0217	14.02	4.03	40.6	8972
	B8	53.5	5.45	0.0254	16.32	4.21	52.6	10328
Group 3	B9	36.4	4.08	0.0177	11.09	3.83	26.7	7371
	B10	44.5	4.61	0.0205	13.55	4.14	36.9	8656
	B11	52.4	5.19	0.0234	15.96	4.33	49.0	10055
	B12	61.2	5.72	0.0276	18.65	4.59	63.1	11353
Group 4	B13	39.0	4.22	0.0179	11.90	3.97	29.7	8077
	B14	51.4	4.99	0.0223	15.68	4.42	46.3	9960
	B15	60.7	5.53	0.0259	18.49	4.71	60.5	11250
	B16	71.7	6.16	0.0302	21.85	4.99	79.7	12792

Table 5. Enhancement percentage with respect to control beam.

Group number	Beam number	Ultimate load (%)	Ultimate deflection (%)	Ultimate torsion (%)	Ultimate angle of twist (%)	Elastic stiffness (%)	Energy absorption (%)	ϵ_{CFRP}
Control	BC	0	0	0	0	0	0	---
Group 1	B1	25	19	25	16	5	49	$0.38\epsilon_{fu}$
	B2	48	40	48	37	6	108	$0.49\epsilon_{fu}$
	B3	70	56	70	59	9	165	$0.57\epsilon_{fu}$
	B4	94	72	94	85	13	234	$0.65\epsilon_{fu}$
Group 2	B5	44	26	44	24	14	80	$0.43\epsilon_{fu}$
	B6	78	45	78	44	23	158	$0.52\epsilon_{fu}$
	B7	107	60	107	64	29	232	$0.60\epsilon_{fu}$
	B8	141	79	141	93	35	331	$0.69\epsilon_{fu}$
Group 3	B9	64	34	64	34	23	119	$0.49\epsilon_{fu}$
	B10	100	51	100	55	33	203	$0.58\epsilon_{fu}$
	B11	136	70	136	77	39	301	$0.67\epsilon_{fu}$
	B12	176	88	176	109	47	417	$0.76\epsilon_{fu}$
Group 4	B13	76	38	76	35	27	143	$0.54\epsilon_{fu}$
	B14	132	64	132	69	42	280	$0.66\epsilon_{fu}$
	B15	174	81	174	96	51	396	$0.75\epsilon_{fu}$
	B16	223	102	223	129	60	553	$0.85\epsilon_{fu}$

Note: ϵ_{CFRP} is the strain in CFRP strips and ϵ_{fu} is the ultimate strain in CFRP strips of 15000 $\mu\epsilon$.

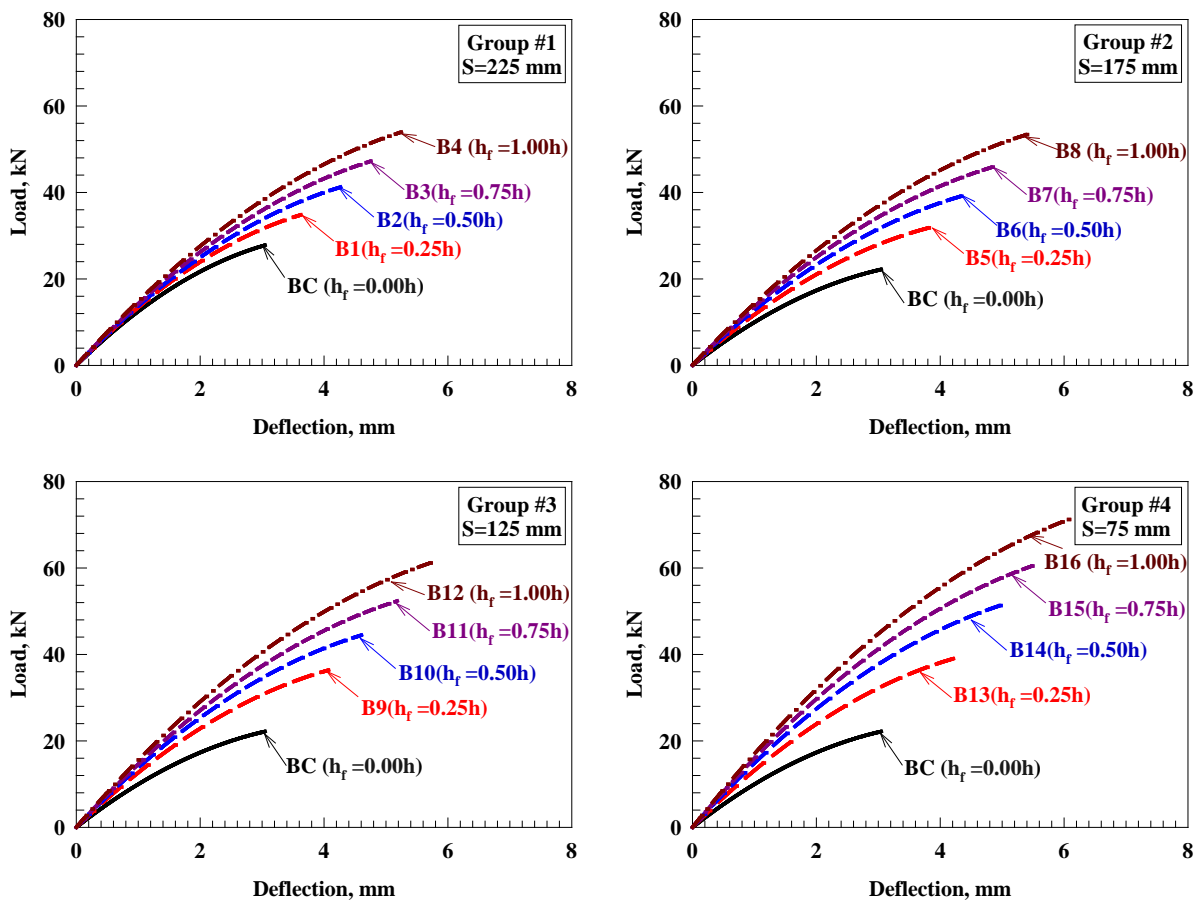
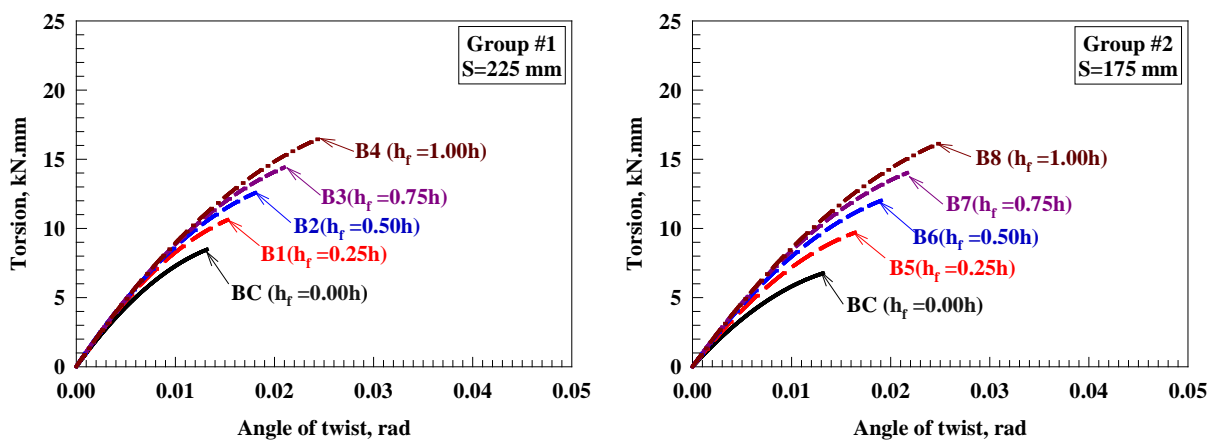


Figure 9. Typical load-deflection curve.

3.4. Ductility and strength ratios

The evaluation of beams for deformability (deflection) and strength (load capacity) shows the superlative performance of RC members. For strengthened RC members, deformability and strength can be related to the serviceability and ultimate load limit states, respectively, of the structural member and can be measured by calculating the strength and ductility ratios, respectively, as shown in Table 5. The strength and ductility ratios are defined as the ultimate load capacity and deflection, respectively, of CFRP strengthened beam divided by the ultimate deflection and load capacity of the un-strengthened beam (control). The ductility indicates how much the strengthened RC beams can sustain deformations without failure. The ductility ratio is defined as the ratio of the ultimate deflection of the strengthened beam to the ultimate deflection of the control beam (Table 5). Strength ratio also predicts the increase of load that the model can sustain.



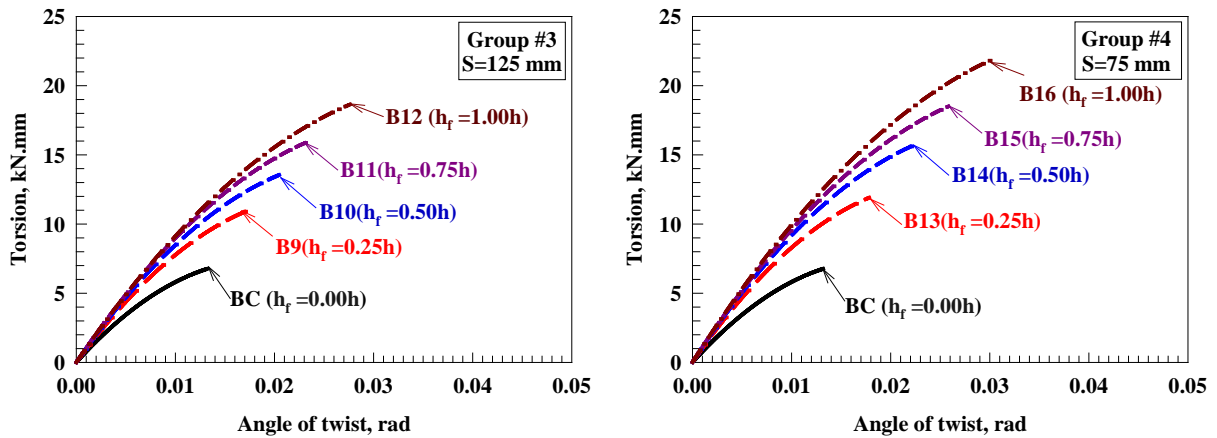


Figure 10. Typical Torsion-angle of twist curve.

Figure 11 and 12 show the strength and ductility ratios, respectively, for all simulated models. Inspection of Figure 11 reveals that the strength ratio enhancement percentage increased largely with the increase of anchored depth (h_f) and decreased with the increase of CFRP strip spacing (S). The strength ratio enhancement percentage (Figure 11) for beams strengthened (Group #1) with one layer of 50 mm U strip wrapping at 225 mm c/c with an additional layer of CFRP wrapping on both sides of the web is 25 %, 48 %, 70 %, and 94 % for CFRP anchored depth of 50 mm ($h_f = 0.25h$), 100 ($h_f = 0.50h$) mm, 150 mm ($h_f = 0.75h$), and 200 mm ($h_f = 1.00h$), respectively, with a significant average enhancement of 59 %. Also, the strength ratio enhancement percentage (Figure 11) for beams strengthened (Group #2) with one layer of 50 mm U strip wrapping at 175 mm (equivalent to 78 % of Group #1 spacing) c/c with an additional layer of CFRP wrapping on both sides of the web is 44 %, 78 %, 107 %, and 141 % for CFRP anchored depth of 50 mm ($h_f = 0.25h$), 100 ($h_f = 0.50h$) mm, 150 mm ($h_f = 0.75h$), and 200 mm ($h_f = 1.00h$), respectively, with an significant average enhancement of 93 % and this percentage is 1.56 times the percentage for Group#1 ($S = 225$ mm). In addition, the strength ratio enhancement percentage (Figure 11) for beams strengthened (Group #3) with one layer of 50 mm U strip wrapping at 125 mm (equivalent to 56 % of Group #1 spacing) c/c with an additional layer of CFRP wrapping on both sides of the web is 64 %, 100 %, 136 %, and 176 % for CFRP anchored depth of 50 mm ($h_f = 0.25h$), 100 ($h_f = 0.50h$) mm, 150 mm ($h_f = 0.75h$), and 200 mm ($h_f = 1.00h$), respectively, with an significant average enhancement of 119 % and this percentage is 2 times the percentage for Group#1 ($S = 225$ mm). While, the Group #4 beams (beams strengthened with one layer of 50 mm U strip wrapping at 75 mm (equivalent to 33 % of Group #1 spacing) c/c with an additional layer of CFRP wrapping on both sides of the web) had the largest average strength ratio enhancement percentage of 151 % and this percentage is 2.55 times the percentage for Group#1 ($S = 225$ mm). The strength ratio enhancement percentage for beams strengthened (Group #4) is 76%, 132%, 174%, and 223% (Figure 11) for CFRP anchored depth of 50 mm ($h_f = 0.25h$), 100 ($h_f = 0.50h$) mm, 150 mm ($h_f = 0.75h$), and 200 mm ($h_f = 1.00h$), respectively.

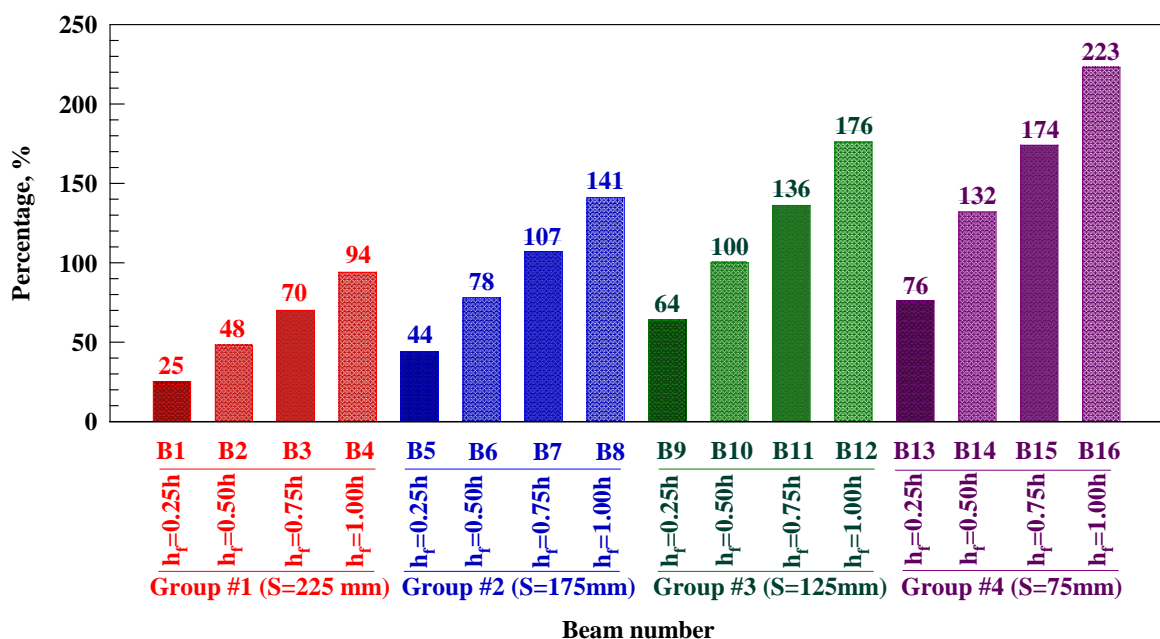


Figure 11. Enhancement percentage in ultimate load capacity (Strength ratio).

Figure 12 shows that the ductility ratio enhancement percentage slightly increased with the increase of h_f and decreased with the increase of S . The ductility ratio enhancement percentage (Figure 12) for beams strengthened (Group #1) with one layer of 50 mm U strip wrapping at 225 mm c/c with an additional layer of CFRP wrapping on both sides of the web is 19 %, 40 %, 56 %, and 72 % for CFRP anchored depth of 50 mm ($h_f = 0.25h$), 100 ($h_f = 0.50h$) mm, 150 mm ($h_f = 0.75h$), and 200 mm ($h_f = 1.00h$), respectively, with a significant average enhancement of 47 % (equivalent to 79 % of strength ratio enhancement). Also, the ductility ratio enhancement percentage (Figure 12) for beams strengthened (Group #2) with one layer of 50 mm U strip wrapping at 175 mm (equivalent to 78 % of Group #1 spacing) c/c with an additional layer of CFRP wrapping on both sides of the web is 26 %, 45 %, 60 %, and 79 % for CFRP anchored depth of 50 mm ($h_f = 0.25h$), 100 ($h_f = 0.50h$) mm, 150 mm ($h_f = 0.75h$), and 200 mm ($h_f = 1.00h$), respectively, with a significant average enhancement of 53 % (equivalent to 56 % of strength ratio enhancement) and this percentage is 1.25 times the percentage for Group#1 ($S = 225$ mm). In addition, the ductility ratio enhancement percentage (Figure 12) for beams strengthened (Group #3) with one layer of 50 mm U strip wrapping at 125 mm (equivalent to 56 % of Group #1 spacing) c/c with an additional layer of CFRP wrapping on both sides of the web is 34 %, 51 %, 70 %, and 88 % for CFRP anchored depth of 50 mm ($h_f = 0.25h$), 100 ($h_f = 0.50h$) mm, 150 mm ($h_f = 0.75h$), and 200 mm ($h_f = 1.00h$), respectively, with a significant average enhancement of 61 % (equivalent to 51 % of strength ratio enhancement) and this percentage is 1.5 times the percentage for Group#1 ($S = 225$ mm). While, the Group #4 beams (beams strengthened with one layer of 50 mm U strip wrapping at 75 mm (equivalent to 33 % of Group #1 spacing) c/c with an additional layer of CFRP wrapping on both sides of the web) had the largest average ductility ratio enhancement percentage of 71 % (equivalent to 47 % of strength ratio enhancement) and this percentage is 1.75 times the percentage for Group#1 ($S = 225$ mm). The ductility ratio enhancement percentage for beams strengthened (Group #4) is 38 %, 64 %, 81 %, and 102 % (Figure 12) for CFRP anchored depth of 50 mm ($h_f = 0.25h$), 100 ($h_f = 0.50h$) mm, 150 mm ($h_f = 0.75h$), and 200 mm ($h_f = 1.00h$), respectively.

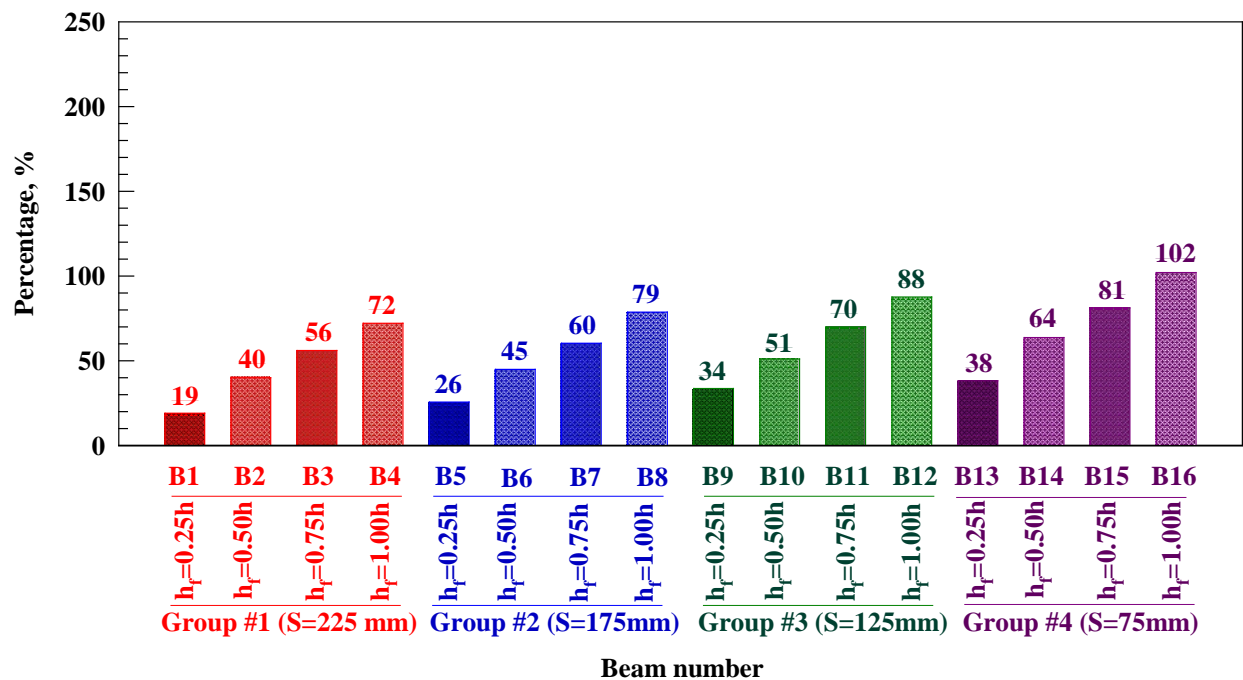


Figure 12. Enhancement percentage in ultimate deflection (ductility ratio).

3.5. Angle of twist ratio

The purpose of a torsion test is to determine the behavior reinforced concrete beam exhibits when twisted or under torsional forces as a result of applied moments that cause shear stress about the axis and angle of twist. The angle of twist can be defined as the angle through which the rotating machine element rotates or twists with respect to its free end as shown in Table 4. Torsional rigidity is the resistance against the torsional deformation or the minimum force required deforming the object by twisting or torsional rigidity is the amount of resistance a cross section has against torsional deformation in terms of twisting angle. Therefore, more angle of twist ratio (Table 5) caused higher torsional rigidity. Figure 13 shows the angle of twist ratio for all simulated models. Inspection of Figure 13 reveals the angle of twist ratio enhancement percentage slightly increased with the increase of h_f and decreased with the increase of S .

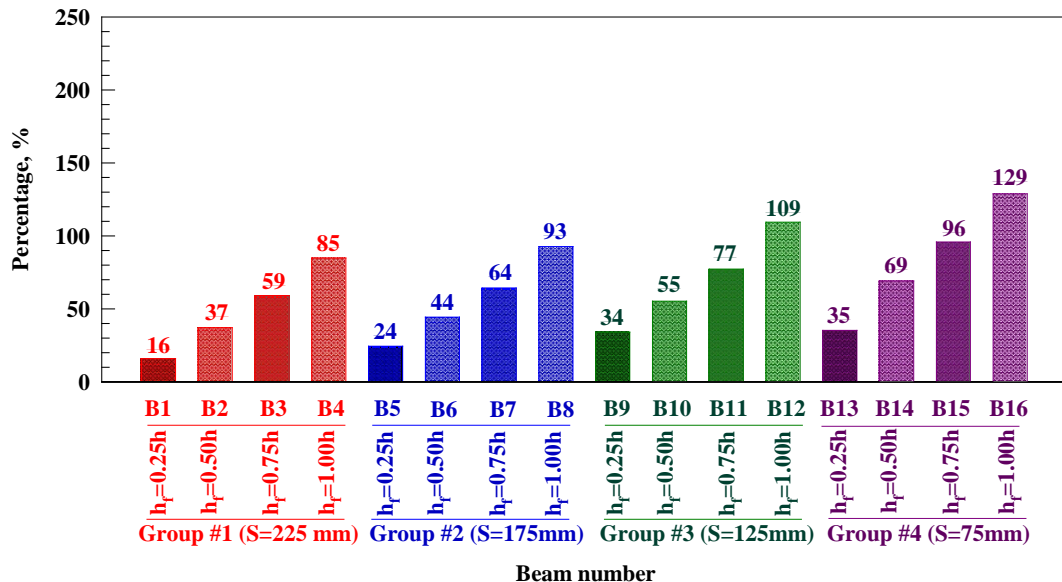


Figure 13. Enhancement percentage in ultimate angle of twist (angle of twist ratio).

The angle of twist ratio enhancement percentage (Figure 13) for beams strengthened (Group #1) with one layer of 50 mm U strip wrapping at 225 mm c/c with an additional layer of CFRP wrapping on both sides of the web is 16 %, 37 %, 59 %, and 85 % for CFRP anchored depth of 50 mm ($h_f = 0.25h$), 100 ($h_f = 0.50h$) mm, 150 mm ($h_f = 0.75h$), and 200 mm ($h_f = 1.00h$), respectively, with a significant average enhancement of 49 % (equivalent to 105 % of ductility ratio enhancement). Also, the angle of twist ratio enhancement percentage (Figure 13) for beams strengthened (Group #2) with one layer of 50 mm U strip wrapping at 175 mm (equivalent to 78 % of Group #1 spacing) c/c with an additional layer of CFRP wrapping on both sides of the web is 24 %, 44 %, 64 %, and 93 % for CFRP anchored depth of 50 mm ($h_f = 0.25h$), 100 ($h_f = 0.50h$) mm, 150 mm ($h_f = 0.75h$), and 200 mm ($h_f = 1.00h$), respectively, with a significant average enhancement of 56 % (equivalent to 108 % of ductility ratio enhancement) and this percentage is 1.15 times the percentage for Group#1 ($S = 225$ mm). In addition, the angle of twist ratio enhancement percentage (Figure 13) for beams strengthened (Group #3) with one layer of 50 mm U strip wrapping at 125 mm (equivalent to 56 % of Group #1 spacing) c/c with an additional layer of CFRP wrapping on both sides of the web is 34 %, 55 %, 77 %, and 109 % for CFRP anchored depth of 50 mm ($h_f = 0.25h$), 100 ($h_f = 0.50h$) mm, 150 mm ($h_f = 0.75h$), and 200 mm ($h_f = 1.00h$), respectively, with a significant average enhancement of 69 % (equivalent to 114 % of ductility ratio enhancement) and this percentage is 1.4 times the percentage for Group#1 ($S = 225$ mm). While, the Group #4 beams (beams strengthened with one layer of 50 mm U strip wrapping at 75 mm (equivalent to 33 % of Group #1 spacing) c/c with an additional layer of CFRP wrapping on both sides of the web) had the largest average angle of twist ratio enhancement percentage of 72 % (equivalent to 115 % of ductility ratio enhancement) and this percentage is 1.67 times the percentage for Group#1 ($S = 225$ mm). The angle of twist ratio enhancement percentage for beams strengthened (Group #4) is 35 %, 69 %, 96 %, and 129 % (Figure 13) for CFRP anchored depth of 50 mm ($h_f = 0.25h$), 100 ($h_f = 0.50h$) mm, 150 mm ($h_f = 0.75h$), and 200 mm ($h_f = 1.00h$), respectively.

3.6. Elastic stiffness ratio

The elastic stiffness determines the response of the crystal to an externally applied strain (or stress) and provides information about the bonding characteristics, mechanical and structural stability. The slope of the first stage of the load-deflection curve before initiation of the first main flexural crack is represented the elastic stiffness. For comparison, the elastic stiffness of each strengthened beam with CFRP sheets was normalized with respect to the control beams without CFRP sheets as shown in Table 5.

Figure 14 shows the elastic stiffness ratio for all simulated models. Inspection of Figure 14 reveals the elastic stiffness ratio enhancement percentage is classified as the least percentage in the investigated parameters in this study in which slightly increased with the increase of h_f and decreased with the increase of S . The elastic stiffness ratio enhancement percentage (Figure 14) for beams strengthened (Group #1) with one layer of 50 mm U strip wrapping at 225 mm c/c with an additional layer of CFRP wrapping on both sides of the web is 5 %, 6 %, 9 %, and 13 % for CFRP anchored depth of 50 mm ($h_f = 0.25h$), 100 ($h_f = 0.50h$) mm, 150 mm ($h_f = 0.75h$), and 200 mm ($h_f = 1.00h$), respectively, with a small average enhancement of 8 % (equivalent to 18 % of ductility ratio enhancement). Also, the elastic stiffness ratio enhancement percentage (Figure 14) for beams strengthened (Group #2) with one layer of 50 mm U strip wrapping at 175 mm (equivalent to 78 % of Group #1 spacing) c/c with an additional layer of CFRP wrapping on both sides of the web is 14 %, 23 %, 29 %, and 35 % for CFRP anchored depth of 50 mm ($h_f = 0.25h$), 100 ($h_f = 0.50h$) mm, 150 mm ($h_f = 0.75h$), and 200 mm ($h_f = 1.00h$), respectively, with a small average enhancement of 25 % (equivalent to 48 % of ductility ratio enhancement) and this percentage is 3.1 times the percentage for Group#1

($S = 225$ mm). In addition, the elastic stiffness ratio enhancement percentage (Figure 14) for beams strengthened (Group #3) with one layer of 50 mm U strip wrapping at 125 mm (equivalent to 56 % of Group #1 spacing) c/c with an additional layer of CFRP wrapping on both sides of the web is 23 %, 33 %, 39 %, and 47 % for CFRP anchored depth of 50 mm ($h_f = 0.25h$), 100 ($h_f = 0.50h$) mm, 150 mm ($h_f = 0.75h$), and 200 mm ($h_f = 1.00h$), respectively, with a small average enhancement of 35 % (equivalent to 58 % of ductility ratio enhancement) and this percentage is 4.3 times the percentage for Group#1 ($S = 225$ mm). While, the Group #4 beams (beams strengthened with one layer of 50 mm U strip wrapping at 75 mm (equivalent to 33 % of Group #1 spacing) c/c with an additional layer of CFRP wrapping on both sides of the web) had the largest average elastic stiffness ratio enhancement percentage of 45 % (equivalent to 63 % of ductility ratio enhancement) and this percentage is 5.5 times the percentage for Group#1 ($S = 225$ mm). The elastic stiffness ratio enhancement percentage for beams strengthened (Group #4) is 27 %, 42 %, 51 %, and 60 % (Figure 14) for CFRP anchored depth of 50 mm ($h_f = 0.25h$), 100 ($h_f = 0.50h$) mm, 150 mm ($h_f = 0.75h$), and 200 mm ($h_f = 1.00h$), respectively.

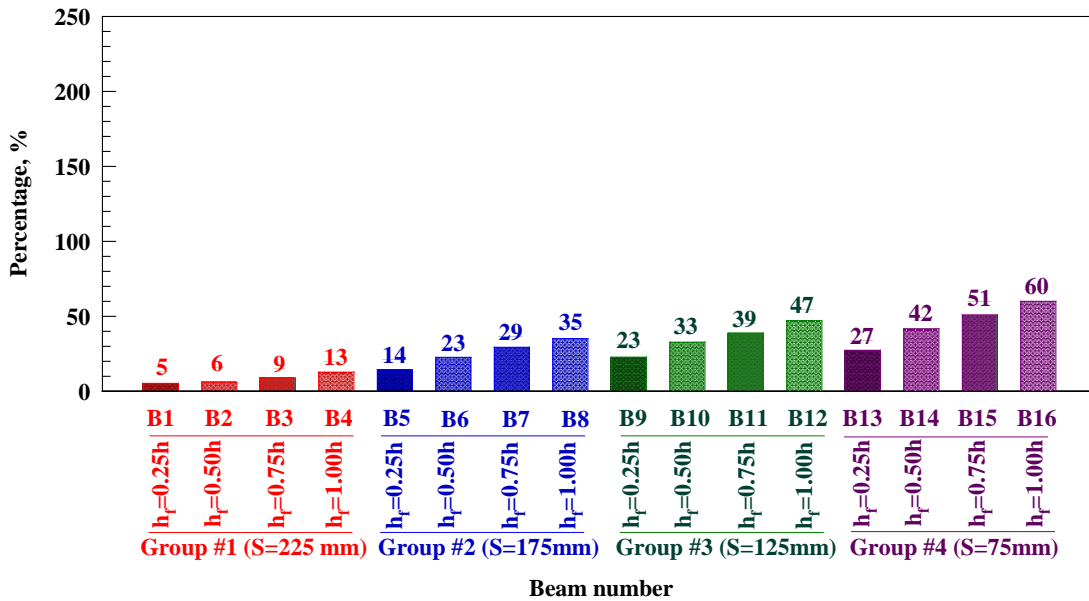


Figure 14. Enhancement percentage in elastic stiffness (elastic stiffness ratio).

3.7. Energy absorption ratio

In materials science and metallurgy, energy absorption or toughness is the ability of a material to absorb energy and plastically deform without fracturing. One definition of material toughness is the amount of energy per unit volume that a material can absorb before rupturing. Energy absorption is calculated as the entire area under the load-deflection curve. In addition, the energy absorption of each strengthened beam with CFRP sheets was normalized with respect to the control beams without CFRP sheets as shown in Table 5.

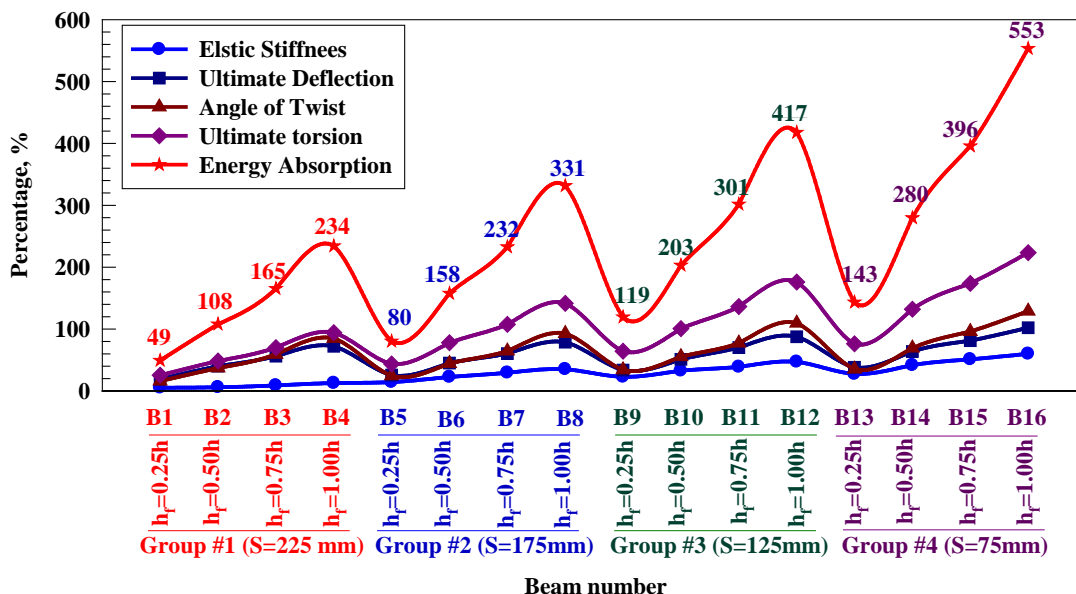


Figure 15. Enhancement percentage in energy absorption (energy absorption ratio).

Figure 15 shows the energy absorption ratio for all simulated models. Inspection of Figure 15 reveals the energy absorption ratio enhancement percentage is classified as the highest percentage in the investigated parameters in this study in which largely increased with the increase of h_f and decreased with the increase of S . The energy absorption ratio enhancement percentage (Figure 15) for beams strengthened (Group #1) with one layer of 50 mm U strip wrapping at 225 mm c/c with an additional layer of CFRP wrapping on both sides of the web is 49 %, 108 %, 165 %, and 234 % for CFRP anchored depth of 50 mm ($h_f = 0.25h$), 100 ($h_f = 0.50h$) mm, 150 mm ($h_f = 0.75h$), and 200 mm ($h_f = 1.00h$), respectively, with enormous average enhancement of 139 % (equivalent to 1692 % of elastic stiffness ratio enhancement). Also, the energy absorption ratio enhancement percentage (Figure 15) for beams strengthened (Group #2) with one layer of 50 mm U strip wrapping at 175 mm (equivalent to 78 % of Group #1 spacing) c/c with an additional layer of CFRP wrapping on both sides of the web is 80 %, 158 %, 232 %, and 331 % for CFRP anchored depth of 50 mm ($h_f = 0.25h$), 100 ($h_f = 0.50h$) mm, 150 mm ($h_f = 0.75h$), and 200 mm ($h_f = 1.00h$), respectively, with enormous average enhancement of 200 % (equivalent to 2438 % of elastic stiffness ratio enhancement) and this percentage is 1.44 times the percentage for Group#1 ($S = 225$ mm). In addition, the energy absorption ratio enhancement percentage (Figure 15) for beams strengthened (Group #3) with one layer of 50 mm U strip wrapping at 125 mm (equivalent to 56 % of Group #1 spacing) c/c with an additional layer of CFRP wrapping on both sides of the web is 119 %, 203 %, 301 %, and 417 % for CFRP anchored depth of 50 mm ($h_f = 0.25h$), 100 ($h_f = 0.50h$) mm, 150 mm ($h_f = 0.75h$), and 200 mm ($h_f = 1.00h$), respectively, with enormous average enhancement of 260 % (equivalent to 3166 % of elastic stiffness ratio enhancement) and this percentage is 1.87 times the percentage for Group#1 ($S = 225$ mm). While, the Group #4 beams (beams strengthened with one layer of 50 mm U strip wrapping at 75 mm (equivalent to 33 % of Group #1 spacing) c/c with an additional layer of CFRP wrapping on both sides of the web) had the largest average energy absorption ratio enhancement percentage of 343 % (equivalent to 4172 % of elastic stiffness ratio enhancement) and this percentage is 2.4 times the percentage for Group#1 ($S = 225$ mm). The energy absorption ratio enhancement percentage for beams strengthened (Group #4) is 143 %, 280 %, 393 %, and 553 % (Figure 14) for CFRP anchored depth of 50 mm ($h_f = 0.25h$), 100 ($h_f = 0.50h$) mm, 150 mm ($h_f = 0.75h$), and 200 mm ($h_f = 1.00h$), respectively.

3.8. Comparison of NLFEA with other results

Comparison of NLFEA with Vishnu et al. [31], the bending moment and torque for all specimens at first crack are closed to NLFEA. Due to FRP torsional resistance of beam is increased in all types of wrapping configuration. Maximum bending moment and torsional moment are resisted by FRP strengthening. Also, all specimens wrapped with GFRP show better torsional resistance compared to the control specimen. Results show an increase in structural behavior of the strengthened beam is almost the same performance as the NLFEA. Besides, Vishnu et al. [31] reached the same conclusion as NLFEA that the fully U wrap strengthening technique of RC beam with FRP is more efficient in resisting torsional moment compared to the vertical strip.

4. Conclusions

1. Integration of CFRP strips as anchored external shear CFRP strips in RC beams can be conducted with alleviate, which eliminates the need for decreasing the center to center spacing between CFRP strips.
2. The control beam shows a faster rate of diagonal crack propagation than the strengthened beams. This is due to the lack of CFRP wrapping along the beam. The failure occurred after substantial wide diagonal cracks and concrete crushing followed by CFRP rupture.
3. The using of anchored CFRP sheets along the top face of the beam as external strengthening in the enhancing of the beam shear integrity pre and post cracking, arresting the shear cracks and improving the structural performance and serviceability of simulated beam.
4. The efficiency of using CFRP strips increases as decreasing the center to center spacing between CFRP strips. For the same spacing, this efficiency increases as increasing the depth of anchored CFRP.
5. The external strengthening with anchored had a superior effect on the CFRP strain (15%–85%), ultimate load (25%–223%), ultimate deflection (19%–102%), angle of twist (16%–129%), torsion elastic stiffness (5%–60%), energy absorption (49%–553%).
6. The enhancement percentage increased with the increase of anchored depth and decreased with the increase of CFRP strip spacing.

References

1. Saadatmanesh, H., Ehsani, M. RC Beams Strengthened with GFRP Plates. I: Experimental Study. *Journal of Structural Engineering*. 1991.117(1). Pp. 3417–3433. DOI: 10.1061/(ASCE)0733-9445(1991)117:11(3417)
2. Wei, A., Saadatmanesh, H., Ehsani, M. RC Beams Strengthened with FRP Plates. II: Analysis and Parametric Study. *Journal of Structural Engineering*. 1991. 117(1). Pp. 3434–3455. DOI: 10.1061/(ASCE)0733-9445(1991)117:11(3434)
3. Chen, J., Teng, J. Shear capacity of fiber-reinforced polymer-strengthened reinforced concrete beams: fiber reinforced polymer rupture. *Journal of Structural Engineering*. 2003.129(1). Pp. 615–625. DOI: 10.1061/(ASCE)0733-9445(2003)129:5(615)

4. Chen, J.-F., Teng, J.-G. Shear capacity of FRP-strengthened RC beams: FRP debonding. *Construction and Building Materials*. 2003.17(1). Pp. 27–41. DOI: 10.1016/S0950-0618(02)00091-0
5. Volkova, A., Rybakov, V., Seliverstov, A., Petrov, D., Smignov, A. Lightweight steel concrete structures slab panels load-bearing capacity. *MATEC Web of Conferences*. 2018. 245. 08007. doi.org/10.1051/mateconf/201824508008
6. Vatin, N.I., Velichkin, V.Z., Kozinets, G.L., Korsun, V.I., Rybakov, V.A., Zhuvak, O.V. Precast-monolithic reinforced concrete beam-slabs technology with claydit blocks. *Construction of Unique Buildings and Structures*. 2018. 70(7). Pp. 43–59. DOI: 10.18720/CUBS.70.4
7. Rybakov, V.A., Kozinets, K.G., Vatin, N.I., Velichkin, V.Z., Korsun, V.I. Lightweight steel concrete structures technology with foam fiber-cement sheets. *Magazine of Civil Engineering*. 2018. 82(6). Pp. 103–111. DOI: 10.18720/MCE.82.10
8. Shen, K., Wan, S., Mo, Y.L., Jiang, Z. Theoretical analysis on full torsional behavior of RC beams strengthened with FRP materials. *Composite Structures*. 2018. 183(1). Pp. 347–357. DOI: 10.1016/j.compstruct.2017.03.084.
9. Jariwala, V.H., Patel, P., Purohit, S.P. Strengthening of RC beams subjected to combined torsion and bending with GFRP composites. *Procedia Engineering*. 2013. 51(1). Pp. 282–289. DOI: 10.1016/j.proeng.2013.01.038
10. Amulu, C.P., Zeagu, C.A. Experimental and analytical comparison of torsion, bending moment and shear forces in reinforced concrete beams using BS 8110, euro code 2 and ACI 318 provisions. *Nigerian Journal of Technology*. 2017. 36(3). Pp. 705–711. DOI: 10.4314/njt.v36i3.7.
11. Alabdulhady, M.Y., Sneed, L.H., Carloni, C. Torsional behavior of RC beams strengthened with PBO-FRCM composite—An experimental study. *Engineering Structures*. 2017. 136(1). Pp. 393–405. DOI: 10.1016/j.engstruct.2017.01.044
12. Ameli, M., Ronagh, H.R., Dux, P.F. Behavior of FRP strengthened reinforced concrete beams under torsion. *Journal of Composites for Construction*. 2007. 11(1). Pp.192–200. DOI: 10.1061/(ASCE)1090-0268(2007)11:2(192)
13. Chalioris, C.E. Tests and analysis of reinforced concrete beams under torsion retrofitted with FRP strips. *Computational Methods and Experimental Measurements XIII*. 2007. 46(1). Pp. 633–642. DOI: 10.2495/CMEM070631
14. Hii, A.K.Y., Al-Mahaidi, R. Experimental investigation on torsional behavior of solid and box-section RC beams strengthened with CFRP using photogrammetry. *Journal of Composites for Construction*. 2006. 10(1). Pp. 321–329. DOI: 10.1061/(ASCE)1090-0268(2006)10:4(321)
15. Jing, M., Raongjant, W., Li, Z. Torsional strengthening of reinforced concrete box beams using carbon fiber reinforced polymer. *Composite Structures* 2007. 78(1). Pp. 264–270. DOI: 10.1016/j.compstruct.2005.10.017
16. Chalioris, C.E. Torsional strengthening of rectangular and flanged beams using carbon fibre-reinforced-polymers—experimental study. *Construction and Building Materials*. 2008. 22(1). Pp. 21–29. DOI: 10.1016/j.conbuildmat.2006.09.003
17. Deifalla, A., Ghobarah, A. Strengthening RC T-beams subjected to combined torsion and shear using FRP fabrics: experimental study. *Journal of Composites for Construction*. 2010. 14(1). Pp. 301–311. DOI: 10.1061/(ASCE)CC.1943-5614.0000091
18. Salom, P.R., Gergely, J., Young, D.T. Torsional strengthening of spandrel beams with fiber-reinforced polymer laminates. *Journal of Composites for Construction*. 2004. 8(1). Pp. 157–162. DOI: 10.1061/(ASCE)1090-0268(2004)8:2(157)
19. He, R., Sneed, L.H., Belarbi, A. Torsional repair of severely damaged column using carbon fiber-reinforced polymer. *Aci Structural Journal*. 2014.111(1). Pp. 705–716. DOI: 10.14359/51686627
20. Yang, Y., Sneed, L., Saïidi, M.S., Belarbi, A., Ehsani, M., He, R. Emergency repair of an RC bridge column with fractured bars using externally bonded prefabricated thin CFRP laminates and CFRP strips. *Composite Structures* 2015. 133(1). Pp. 727–738. DOI: 10.1016/j.compstruct.2015.07.045
21. Gonzalez-Libreros, J.H., Sneed, L.H., D'Antino, T., Pellegrino, C. Behavior of RC beams strengthened in shear with FRP and FRCM composites. *Engineering Structures*. 2017. 150(1). Pp. 830–842. DOI: 10.1016/j.engstruct.2017.07.084.
22. Ghobarah, A., Ghorbel, M.N., Chidiac, S.E. Upgrading torsional resistance of reinforced concrete beams using fiber-reinforced polymer. *Journal of Composites for Construction*. 2002. 6(1). Pp. 257–263. DOI: 10.1061/(ASCE)1090-0268(2002)6:4(257)
23. Hii, A.K.Y., Al-Mahaidi, R. An experimental and numerical investigation on torsional strengthening of solid and box-section RC beams using CFRP laminates. *Composite Structures*. 2006. 75(1). Pp. 213–221. DOI: doi.org/10.1016/j.compstruct.2006.04.050
24. Ganganagoudar, A., Mondal, T.G., Suriya Prakash, S. Analytical and finite element studies on behavior of FRP strengthened RC beams under torsion. *Composite Structures*. 2016. 153(1). Pp. 876–885. DOI: 10.1016/j.compstruct.2016.07.014
25. Al-Rousan, R., Abo-Msamh, I. Bending and Torsion Behaviour of CFRP Strengthened RC Beams. *Magazine of Civil Engineering*. 2019. 92(8). Pp. 62–71. DOI: 10.18720/MCE.92.8
26. Mahmood, M.N. Nonlinear analysis of reinforced concrete beams under pure torsion. *Journal of Applied Sciences*. 2007. 7(22). Pp. 3524–3529. DOI: 10.3923/jas.2007.3524.3529
27. Prabaghar, A., Kumaran, G. Theoretical study on the behavior of rectangular concrete beams reinforced internally with GFRP reinforcements under pure torsion. *International Journal of Civil and Structural Engineering*. 2011. 2(2). Pp. 570–594. DOI: 10.6088/ijcser.00202010134.
28. Elwan, S.K. Torsion strengthening of RC beams using CFRP (parametric study). *Journal of Civil Engineering*. 2017. 21(4). Pp. 1273–1281. DOI: 10.1007/s12205-016-0156-7.
29. Zojaji, A.R., Kabir, M.Z. Analytical approach for predicting full torsional behavior of reinforced concrete beams strengthened with FRP materials. *Scientia Iranica*. 2012. 19(2). Pp. 51–63. DOI: 10.1016/j.scient.2011.12.004.
30. Gesund, H., Schuette, F.J., Buchanan, G.R., Gray, G.A. Ultimate strength in combined bending and torsion of concrete beams containing both longitudinal and transverse reinforcement. *Journal of the American Concrete Institute*. 1964. 61(12). Pp. 1509–1522. DOI: 10.1680/mac.1968.20.64.155.
31. Jariwala, V.H., Patel, P.V., Purohit, S.P. Strengthening of RC Beams Subjected to Combined Torsion and Bending with GFRP Composites. *Procedia Engineering*. 2013. 51(1). Pp. 282–289. DOI: 10.1016/j.proeng.2013.01.038

Contacts:

Rajai Al-Rousan, rzalrousan@just.edu.jo
 Isra'a Abo-Msamh, iabomsamh@gmail.com



DOI: 10.18720/MCE.96.8

Radiation changes of concrete aggregates under the influence of gamma radiation

A.V. Denisov

National Research Moscow State Civil Engineering University, Moscow, Russia

* E-mail: den-al-v@inbox.ru

Keywords: aggregates of concretes, radiation changes in volume and strength, influence of gamma radiation

Abstract. The work (in connection with the small study of the effects of gamma ray on concretes and their components) contains the results of calculation and analysis of radiation changes of concrete aggregates under the influence of gamma ray on the basis of analytical methods developed previously during the neutron irradiation process. The possibility of using these analytical methods in the case of exposure to gamma ray was substantiated. The relationship of the absorbed doses of gamma ray of different energies with the number of atoms displaced during irradiation was established. There is an assessment of radiation changes in the volume and strength of the main types of rocks - aggregates of concrete (igneous, sedimentary rocks and ores) under the influence of gamma ray with an average energy of 2 MeV and 5 MeV after irradiation to absorbed doses of 10^5 to 10^{11} Gy at 30 °C, 100 °C and 300 °C. For this, from the beginning, the radiation changes of the main rock-forming minerals were calculated, and on the ground of them, the radiation changes of rocks of concrete aggregates were calculated. It has been established that noticeable radiation changes of considered minerals and rock aggregates will occur only at absorbed doses of gamma ray of more than $1 \cdot 10^9$ – $1 \cdot 10^{10}$ Gy of gamma rays with an energy of 5 MeV and of $3 \cdot 10^9$ – $3 \cdot 10^{10}$ Gy for gamma rays with an energy of 2 MeV. The number of radiation changes grows with a rise in the absorbed dose and significantly decrease with an increase in the irradiation temperature for silicate class minerals and silicate rocks. The greatest radiation changes under the influence of gamma ray at 30 °C are observed in silicate minerals and rocks, especially olivine pyroxenes, hornblende, dunite, peridotite, pyroxenite, and gabbro. Moreover, even with an absorbed dose of gamma ray of 10^{11} Gy, the radiation changes are not large (increase in volume is not more than 0.36 %, decrease in strength is not more than 8.7 %). As the temperature increases, the ratio in the magnitude of radiation changes of different materials changes.

1. Introduction

Significant radiation changes in concrete could occur under the influence of ionizing radiation. In this regard, the radiation resistance of concrete used in buildings with various nuclear facilities determines the safety of operation of these buildings for both the operating staff and the environment as a whole.

The most significant radiation changes in concrete occur under the influence of neutrons of nuclear reactors. In this connection the influence of neutron radiation in concrete and their components (aggregates, minerals, cement stone) was investigated and adequately described in literature, for example in [1-22]. There are methods for the analytical determination of radiation changes in the following materials described in [8, 9, 10, 11, 12, 14, 22]:

- minerals of concrete aggregate [8, 14, 22] and cement stone [11,14] under the influence of neutrons according to the data on the fluence and neutron spectrum, irradiation temperature;
- materials of concrete aggregate according to data on radiation changes in crystals of the composing minerals them [9, 14];
- concretes according to data on radiation changes in their components (aggregates and cement stone) [10, 12, 14].



At the same time, significant volumes of concrete in buildings with nuclear facilities are exposed to gamma radiation. However, the effect of gamma ray on concrete is less studied. There are only a few data on the effect of gamma radiation on concrete obtained in [1, 2, 21, 23–27], discussed in the reviews [6, 7, 13, 15, 21] and on the effect of gamma radiation on the cement stone [25, 26, 28–31], indicating that they have small radiation changes under the influence of gamma radiation.

The effect of gamma ray on concrete aggregates and the contribution of radiation-induced changes in aggregates to radiation-induced changes in concrete under the influence of gamma ray have hardly been studied. This is due to the opinion based on the results of the study of ceramic materials [32, 34] that gamma ray does not cause noticeable changes in the properties of inorganic materials. This view was confirmed in the works of [33, 35], which show that the ability to displace atoms under the influence of gamma ray is 100 to 10,000 times lower than under the influence of neutrons.

However, the studies described in the papers [1, 2, 6, 7, 13, 15, 21, 23–31] were performed after exposure to the absorbed dose of gamma radiation no more than $1.5 \cdot 10^9$ Gy. The result of a study of the effects of higher absorbed doses has not been found in literature. At higher absorbed doses, the number of displaced atoms and changes in material properties may be more significant. In addition, studies of the aggregate materials, which are more radiation-sensitive than ceramics, are not available in the literature. In this regard, studies of radiation changes in concrete aggregate materials under the influence of gamma ray are of considerable practical interest.

The purpose of this work is to assess radiation changes in the main varieties of concrete aggregates under the influence of gamma ray in a wide range of absorbed doses and radiation temperatures.

Due to the lack of data in the literature on significant radiation changes of the aggregates and their minerals under the influence of gamma ray, radiation changes of these materials were evaluated by calculation.

In achieving the goal, the following known provisions in accordance with [8, 9, 14], were taken into account:

- Changes in the basic properties of concrete aggregate materials are caused by the displacement of atoms in their minerals, leading to the accumulation of radiation defects in them.
- Changes in volume and strength are of greatest interest.
- Radiation changes in the volume and strength of concrete aggregate materials can be calculated by radiation changes in the size and volume of the minerals that compose them on the basis of the analytical method tested during neutron irradiation, described in the works [9, 14].
- Radiation changes in the volume and size of mineral crystals can be calculated on the base of the number of displaced atoms and the radiation temperature. This analytical method based on neutron radiation, is described in the works [8, 14].

In order to achieve this goal, the following objectives of the study were set and solved:

- To justify the possibility of using the existing analytical methods listed above, which have been tested under the influence of neutrons, to determine the results of gamma radiation exposure.
- To establish the dependence of the number of displaced atoms in minerals of concrete aggregates under the action of gamma radiation on the absorbed dose and the energy of gamma quanta.
- To calculate, using the well-known analytical method presented in [8, 14] for neutron irradiation, radiation changes in the volume and size of crystals of the main minerals of concrete aggregates after irradiation with gamma radiation to various absorbed doses.
- To calculate, using the available analytical method presented in [9, 14] for neutron irradiation, the radiation changes of the volume and strength of the main materials of concrete aggregates after irradiation with gamma radiation to various absorbed doses.
- To analyze the results obtained and establish the absorbed doses and conditions under which it is necessary to take into account the radiation changes in the materials of concrete aggregates under the influence of gamma radiation.

2. Methods

When substantiating the possibility of using the above existing analytical methods tested under the influence of neutrons, the following circumstances were taken into account for the results of exposure to gamma ray:

- In accordance with the existing method for the analytical determination of radiation changes in minerals under the influence of neutrons, radiation changes in the volume and size of minerals, although they are not the same for different minerals, are determined by the calculated number of displaced atoms and the

irradiation temperature. In this regard, the most important for substantiating the possibility of using this analytical method when exposed to gamma ray is the condition that the same number of displaced atoms when irradiated with neutrons and gamma ray cause approximately equal radiation changes.

- Although atom displace efficiency in gamma radiation is 100 to 10,000 times lower than that of neutrons, the number of basic radiation defects (vacancies, interstitial atoms), their distribution in the crystal lattice and the effect on the properties for equal values of number of displaced atoms and irradiation temperature should be approximately the same. For neutrons of different energies, the efficiency of atomic displacement also differs significantly from each other. However, differences in the results of irradiation of minerals with neutron fluxes with different proportions of neutrons of different energies are quite well excluded when the radiation changes are linked to the calculated number of displaced atoms in [14].

- However, there is an opinion [37], that the number and distribution of radiation defects in the space may depend on the speed of displacement of atoms, which is less under the influence of gamma ray than under the influence of neutrons. However, this was not found in existing studies when irradiating minerals with neutrons at different neutron flux densities.

- In accordance with the existing method for the analytical determination of radiation changes in concrete aggregates, radiation changes in the volume and mechanical properties are determined by changes in the size and volume of minerals, their moduli of elasticity, grain size of minerals, and the modulus of elasticity of the material. The reasons for the change in the size and volume of minerals do not play a significant role. This is shown by the results of a positive-used of this method when heating the rocks presented in [36]. In this regard, this analytical method can be used when exposed to gamma ray.

To calculate the number of displaced atoms under the influence of gamma ray, we used the cross sections for the formation of displaced atoms $\sigma_d(E_g)$, calculated in [33] for atoms of building materials (mainly with the atomic number $4 \div 14$):

- $\sigma_d(E_g) = 0.1 \cdot 10^{-24} \text{ cm}^2$ for gamma rays with an energy of 2 MeV;

- $\sigma_d(E_g) = (0.2 - 0.5) \cdot 10^{-24} \text{ cm}^2$ for gamma rays with an energy of 5 MeV

By analogy with neutron radiation, considered in [8, 14], the number of displaced atoms n_{CM} when irradiated by gamma ray in the minerals should be determined by the formulas:

$$n_d = \sum_{i=1}^m [\sigma_d(E_{gi}) F_g(E_{gi})] \quad (1)$$

- when exposed to gamma rays with different energies E_{gi} (for $i = 1 - m$);

$$n_d = \sigma_d(E_g) F_g(E_g) \quad (2)$$

- when exposed to gamma rays with one energy E_g or average energy E_g ,

- where $\sigma_d(E_{gi})$ and $\sigma_d(E_g)$ are the cross sections for the formation of displaced atoms upon exposure to gamma rays with energy E_{gi} and E_g , cm^2 ;

- $F_g(E_{gi})$ and $F_g(E_g)$ are fluence of γ -quantum with energy E_{gi} and E_g , γ -quantum/ cm^2 .

In accordance with [39] the following coefficients $k_{D_g/F_g}(E_g)$ as the ratios of the dose-to-the-level gamma-quanta-dependent gamma-quanta energy E_g :

$$k_{D_g/F_g}(E_g) = (4.4 - 5.6) \cdot 10^{-12} \text{ Gy}/(\gamma\text{-quantum}/\text{cm}^2) \approx 5 \cdot 10^{-12} \text{ Gy}/(\gamma\text{-quantum}/\text{cm}^2) \text{ for gamma-rays with energy } E_g = 1 \text{ MeV};$$

$$k_{D_g/F_g}(E_g) = (7.5 - 9.2) \cdot 10^{-12} \text{ Gy}/(\gamma\text{-quantum}/\text{cm}^2) \approx 8 \cdot 10^{-12} \text{ Gy}/(\gamma\text{-quantum}/\text{cm}^2) \text{ for gamma rays with energy } E_g = 2 \text{ MeV};$$

$k_{D_g/F_g}(E_g) = (1.39 - 1.6) \cdot 10^{-11} \text{ Gy}/(\gamma\text{-quantum}/\text{cm}^2) \approx 1.5 \cdot 10^{-11} \text{ Gy}/(\gamma\text{-quantum}/\text{cm}^2)$ for gamma rays with energy $E_g = 5 \text{ MeV}$.

In accordance with [8, 14] the change in the volume of minerals under the influence of gamma ray was calculated by the formulas:

$$\frac{\Delta V}{V} = \begin{cases} \frac{a(T) \left(\frac{\Delta V}{V} \right)_{M.M} (e^{b(T)n_d} - 1)}{\left(\frac{\Delta V}{V} \right)_{M.M} + a(T) \cdot e^{b(T)n_d}} & \text{-- at } a(T) \neq \infty \text{ and } \beta(T) \neq 0 \\ \left(\frac{\Delta V}{V} \right)_{M.M} (1 - e^{-b(T)n_d}) & \text{-- at } a(T) = \infty \text{ and } \beta(T) = 0 \end{cases} \quad (3a)$$

$$\left(\frac{\Delta V}{V} \right)_{M.M} (1 - e^{-b(T)n_d}) \text{ -- at } a(T) = \infty \text{ and } \beta(T) = 0 \quad (3b)$$

where $\frac{\Delta V}{V}$ is the relative increase in the volume of crystals or unit cells of the mineral, %.

$\left(\frac{\Delta V}{V} \right)_{M.M}$ increase in the volume of the crystal of the mineral in a state of saturation, %

$a(T)$ and $b(T)$ are the parameters depending on the irradiation temperature, determined by the formulas:

$$a(T) = \alpha(T) / \beta(T) \quad (4)$$

$$b(T) = \beta(T) \left(\frac{\Delta V}{V} \right)_{M.M} + \alpha(T), \quad (5)$$

where $\alpha(T)$ and $\beta(T)$ are the parameters depending on the irradiation temperature.

Taking into account the work [8, 14], the change in the size of the crystals of minerals along various axes under the action of gamma ray was calculated by the formula:

$$\frac{\Delta \ell}{\ell} = a_1 + a_2 \frac{\Delta V}{V} + a_3 \left(\frac{\Delta V}{V} + a_4 \right)^{a_5}, \quad (6)$$

where $a_1 - a_5$ are the parameters.

In this work, we used the parameters of equations (3a)–(6) obtained and presented in [8, 14].

In accordance with [9, 14], the change in the volume of rocks of concrete aggregates under the action of gamma ray was calculated by the formulas:

$$\frac{\Delta V_{AG}}{V_{AG}} = \left(\frac{\Delta V}{V} \right)_1 = 3 \left(\frac{\Delta \ell}{\ell} \right)_{M.M} - a_M \frac{E_0}{E_{M.M} \sqrt{d_{GR}}} \cdot \frac{1 - V_{M.RED}}{V_{M.RED}} \text{ -- at } \left(\frac{\Delta V}{V} \right)_1 \geq \left(\frac{\Delta V}{V} \right)_2 \quad (7a)$$

$$\frac{\Delta V_{AG}}{V_{AG}} = \left(\frac{\Delta V}{V} \right)_2 = \left(\frac{\Delta V}{V} \right)_{AD.M} + \frac{3 \Delta \varepsilon_{AVE}}{1 + 2.2 a_M / (\sqrt{d_{GR}} 3 \Delta \varepsilon_{AVE})} \text{ -- at } \left(\frac{\Delta V}{V} \right)_1 < \left(\frac{\Delta V}{V} \right)_2, \quad (7b)$$

where $\left(\frac{\Delta \ell}{\ell} \right)_{M.M}$ is the maximum of the values of the radiation values of radiation-induced dimensional changes in the most expanding direction of the crystals composing the material of minerals, %;

$a_M = 3.4 \cdot 10^{-2} \% \text{ cm}^{0.5}$ is the complex parameter of the model;

E_0 is modulus of elasticity of the material at zero porosity, MPa;

d_{GR} is average size of crystals composing the material of minerals, cm;

$E_{M.M}$ is the modulus of elasticity of crystals having an expansion $\left(\frac{\Delta\ell}{\ell}\right)_{M.M}$ along the axis where the expansion $\left(\frac{\Delta\ell}{\ell}\right)_{M.M}$ takes place, MPa;

$\Delta\varepsilon_{AVE}$ is the average difference between the deformations of the crystals along various axes composing the material of minerals, %;

$V_{M.RED}$ is the relative volumetric content of mineral crystals with expansion, $\left(\frac{\Delta\ell}{\ell}\right)_{M.M}$, reduced to the isotropic case, but taking into account the anisotropy of radiation deformations and the presence of crystals with expansion $\left(\frac{\Delta\ell}{\ell}\right)_{M.i}$, (differing by a value of no more $\xi_p = a_M / \sqrt{d_{AVE}}$), rel. units;

$\left(\frac{\Delta V}{V}\right)_{AD.M}$ is an increase in the volume of material (in %) associated with a free change in the volume of mineral crystals composing it, determined by the formula:

$$\left(\frac{\Delta V}{V}\right)_{AD.M} = \sum_{i=1}^n \left[\left(\frac{\Delta V}{V}\right)_i V_i \right], \quad (8)$$

where $\left(\frac{\Delta V}{V}\right)_i$ and V_i is the radiation change in volume (in %) and the relative volume content of the minerals composing the material (in rel. units).

Values $\Delta\varepsilon_{AVE}$ and $V_{M.RED}$ by [9, 14] were determined by the formulas:

$$\Delta\varepsilon_{AVE} = \sum_{i=1}^n \sum_{j=1}^3 \left[\left(\frac{\Delta\ell}{\ell}\right)_{ij} - \frac{1}{3} \left(\frac{\Delta V}{V}\right)_{AD.M} \left| \frac{V_i}{3} \right| \right] \quad (9)$$

$$V_{M.RED} = \frac{n_{M.M} \cdot V_{M.M}}{3} + \sum_{i=1}^n \left[\frac{n_{M.i} \cdot V_{M.i}}{3} \frac{\left(\frac{\Delta\ell}{\ell}\right)_{M.i} E_{M.i}}{\left(\frac{\Delta\ell}{\ell}\right)_{M.M} E_{M.M}} \right] \leq 1 \quad (10)$$

where $\left(\frac{\Delta\ell}{\ell}\right)_{ij}$ is the increase in the size of the crystals of the i-th mineral along the j-th axis ($j = 1 \dots 3$ along the axes a, b and c) of the crystal, %;

$n_{M.M}$ and $n_{M.i}$ are the number of axes in the crystals along which the expansion occurs $\left(\frac{\Delta\ell}{\ell}\right)_{M.M}$ and $\left(\frac{\Delta\ell}{\ell}\right)_{M.i}$;

$V_{M.M}$; $V_{M.i}$; $E_{M.M}$; $E_{M.i}$ are the relative volume content (in rel. units) and the moduli of normal elasticity (in MPa) of mineral crystals having an expansion of $\left(\frac{\Delta\ell}{\ell}\right)_{M.M}$ and $\left(\frac{\Delta\ell}{\ell}\right)_{M.i}$.

The elastic moduli of mineral crystals along various axes were taken according to [39].

The radiation changes in the indicators of the mechanical properties of the aggregates were calculated by the formula [9, 14]:

$$\frac{R_{AG}}{R_{AG0}} = \exp \left[- \frac{\left(\frac{\Delta V_{AG}}{V_{AG}} \right)_{CR}}{A_{AG} \left(\frac{\Delta V_{AG}}{V_{AG}} \right)_{CR} + B_{AG}} \right], \quad (11)$$

where $\frac{R_{AG}}{R_{AG0}}$ is the residual value of the mechanical property R_{AG} after radiation exposure relative to the strength before irradiation R_{AG0} , rel. units;

A_{AG} and B_{AG} are the complex parameters of the model, the values are given in the works [9, 14].

$\left(\frac{\Delta V_{AG}}{V_{AG}} \right)_{CR}$ is an increase in the volume of material due to the formation of cracks is determined by the formula:

$$\left(\frac{\Delta V_{AG}}{V_{AG}} \right)_{CR} = \frac{\Delta V_{AG}}{V_{AG}} - \sum_{i=1}^n \left[\left(\frac{\Delta V}{V} \right)_i V_i \right] + \sum_{i=1}^n \left[\left(\frac{\Delta V}{V} \right)_i V_i u_i \right], \quad (12)$$

where u_i is the fraction of the increase in mineral crystals due to the formation of microcracks in the crystal, taken according to the data of [9, 14].

Relative changes in strength are calculated by the formula:

$$\frac{\Delta R_{AG}}{R_{AG0}} = \left(\frac{R_{AG}}{R_{AG0}} - 1 \right) \cdot 100\% , \quad (13)$$

where $\frac{\Delta R_{AG}}{R_{AG0}}$ are the relative changes in strength, as the ratio of the absolute change in strength ΔR_{AG} to strength before irradiation R_{AG0} , %.

The calculations of radiation changes were carried out for the following main rock-forming minerals:

- silicate class minerals - quartz, potassium feldspar-microcline, plagioclases (oligoclase and labrador), pyroxenes (enstatite, diopside), hornblende, olivine, serpentine;
- carbonate class minerals - calcite, dolomite;
- oxide-ore class minerals (hematite, magnetite).
- quartz glass.

The radiation changes in minerals were used to calculate the radiation changes in aggregate rocks: granite, diorite, gabbro, basalt, pyroxenite, peridotite, dunite, sandstone, limestone, and enriched hematite and magnetite ore.

When choosing the rocks, the following circumstances were taken into account:

- granites, diorites, gabbros, basalts, sandstones, limestones are the most common rocks;
- pyroxenites, peridotites, dunites, hematite and magnetite ore are examples of the most radiation-resistant rocks when irradiated with neutrons;
- sandstones and limestones were used as aggregates of concrete investigated after exposure to gamma ray in [1, 2, 24];
- hematite and magnetite ores are used for the preparation of particularly heavy concrete, effective for protection against radiation.

The characteristics of the mineral composition, the average size of the crystals of minerals and the elastic modulus of the rocks considered in the work are shown in table 1.

Although the mineral composition, structure, and properties of these rocks can vary in a rather wide range, the use of the accepted average characteristics can be considered to estimate the values of their radiation changes under the influence of gamma ray.

Table 1. The characteristics of the mineral composition, the average size of the crystals of minerals, and the modulus of elasticity of the rocks considered in this paper.

No.	Name of the rock	Mineral composition in the form of mineral content in %	Average crystal size of minerals, cm	Modulus of elasticity, MPa
1	Granite	Quartz – 25 %, Microcline – 40 %, Oligoclase – 20 %, Hornblende – 15 %	0.3	$6 \cdot 10^4$
2	Diorite	Oligoclase – 70 %, Microcline – 5 %, Hornblende – 25 %	0.3	$8 \cdot 10^4$
3	Gabbro	Enstatite, Diopside – 50 %, Labrador – 50 %	0.3	$10 \cdot 10^4$
4	Basalt	Enstatite, Diopside – 50 %, Labrador – 40 %, Glass – 10 %	0.01	$10 \cdot 10^4$
5	Pyroxenite	Enstatite, Diopside – 90 %, Olivine – 10 %	0.1	$12 \cdot 10^4$
6	Peridotite	Enstatite, Diopside – 40 %, Olivine – 40 %, Serpentine – 20 %	0.1	$12 \cdot 10^4$
7	Dunitite	Enstatite, Diopside – 10 %, Olivine – 90 %	0.1	$12 \cdot 10^4$
8	Sandstone	Quartz – 50 %, Microcline – 25 %, Oligoclase – 25 %	0.03	$6 \cdot 10^4$
9	Limestone	Calcite – 75 %, Dolomite – 25 %	0.03	$8 \cdot 10^4$
10	Hematite ore (enriched)	Hematite – 100 %	0.01	$25 \cdot 10^4$
11	Magnetite ore (enriched)	Magnetite – 100 %	0.01	$27 \cdot 10^4$

First, using the formulas (1)–(6), the radiative changes in the volume and size of the crystals of the minerals that make up these rocks were calculated: quartz, microcline, oligoclase, hornblende, calcite and dolomite. Then, according to formulas (7)–(13), radiation changes in the volume and strength of granite, sandstone, and limestone with the accepted characteristics of the mineral composition, structure, and properties were calculated.

Considering the data of [14], the radiation changes of the considered minerals and rocks were calculated after the following exposure to gamma ray:

- gamma ray with an average energy of 2 MeV at absorbed doses from $1 \cdot 10^5$ to $1 \cdot 10^{11}$ Gy for materials of radiation protection of technological equipment of nuclear power plants;

- gamma ray with an average energy of 5MeV at absorbed doses from $1 \cdot 10^5$ to $1 \cdot 10^{11}$ Gy for radiation protection materials of nuclear reactors.

The radiation changes were calculated for cases of irradiation at temperatures of 30 °C, 100 °C, and 300 °C. In this case, changes in materials under the action of heating associated with irradiation (thermal changes) were not considered, since they are independent of radiation changes, they are determined and can be taken into account by other methods, for example, according to [36].

3. Results and Discussion

The dependences necessary for calculating the number of displaced atoms in concrete aggregate minerals were found based on the values of the atomic displacement cross sections $\sigma_d(E_g)$, calculated in [33] for atoms of building materials and the known relations $k_{D_g/F_g}(E_g)$ between the absorbed dose and gamma-ray fluence, which depend on the energy of gamma-rays E_g .

Based on the values of $\sigma_d(E_g)$ and $k_{D_g/F_g}(E_g)$ and of formula (2) shown in the research methodology, the following dependence of the number of displaced atoms (in fractions of a unit) in aggregate minerals when irradiated with gamma ray on the absorbed dose in Gy of gamma ray of different energy was established and accepted for calculations:

$$n_d = 1.1 \cdot 10^{-14} \cdot D_g - \text{at gamma ray energy } E_g = 2 \text{ MeV}; \quad (14)$$

$$n_d = 3.3 \cdot 10^{-14} \cdot D_g - \text{at gamma ray energy } E_g = 5 \text{ MeV.} \quad (15)$$

It can be seen that the absorbed dose of gamma ray with an energy of 5 MeV corresponds to a 3 times larger number of displaced atoms than gamma ray with an energy of 2 MeV. In this connection, the absorbed dose of gamma quanta with an average energy of 2 MeV is equivalent to 1/3 of the absorbed dose of gamma quanta with an energy of 5 MeV in the efficiency of atomic displacement. This circumstance was taken into account when graphically presenting the calculation results. All calculation results are presented depending on the absorbed dose equal to the absorbed dose of gamma rays with an energy of 5 MeV or equal to 1/3 of the absorbed dose of gamma rays with an energy of 2 MeV.

The calculation results according to formulas (1) - (5) taking into account formulas (14) and (15) of radiation changes in the volume of the examined minerals from the absorbed dose of gamma ray in the range of 10^5 – 10^{11} Gy and the irradiation temperature from 30 to 300 °C are given on Figures 1 to 5.

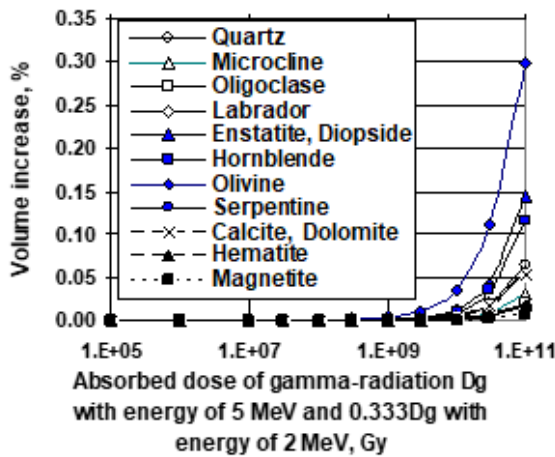


Figure 1. Dependence of the calculated radiation increase in the volume of various minerals on the absorbed dose of gamma ray with an average energy of 5 MeV and 2 MeV at an irradiation temperature of 30 °C.

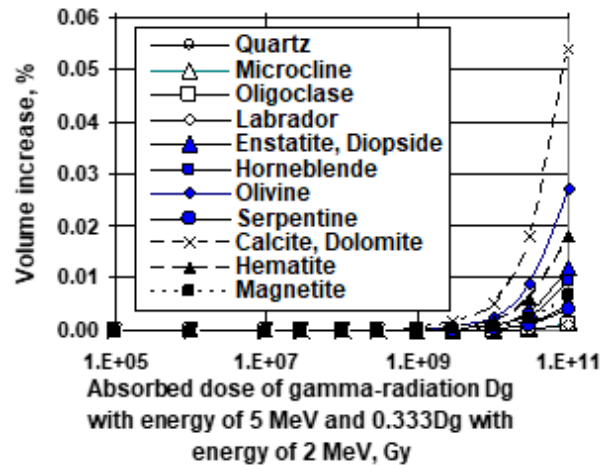


Figure 2. Dependence of the calculated radiation increase in the volume of various minerals on the absorbed dose of gamma ray with an average energy of 5 MeV and 2 MeV at an irradiation temperature of 100 °C.

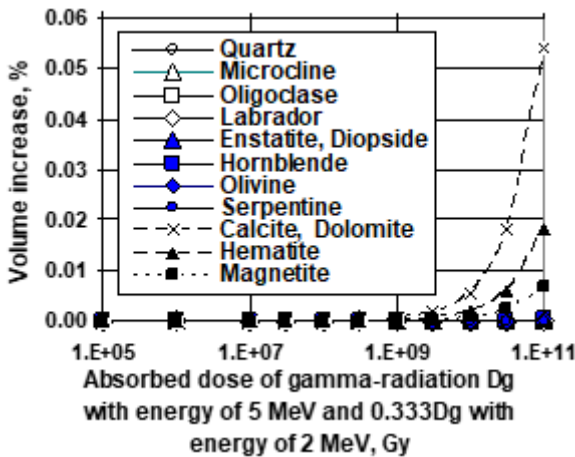


Figure 3. Dependence of the calculated radiation increase in the volume of various minerals on the absorbed dose of gamma ray with an average energy of 5 MeV and 2 MeV at an irradiation temperature of 300 °C.

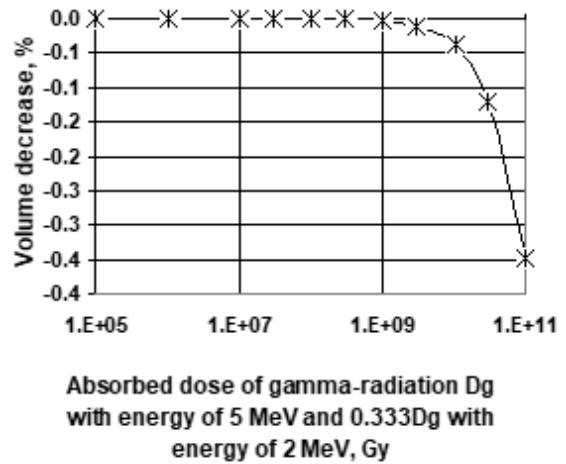


Figure 4. The dependence of the calculated radiation decrease in the volume of quartz glass on the absorbed dose of gamma ray with an average energy of 5 MeV and 2 MeV at irradiation temperatures from 30 to 300 °C.

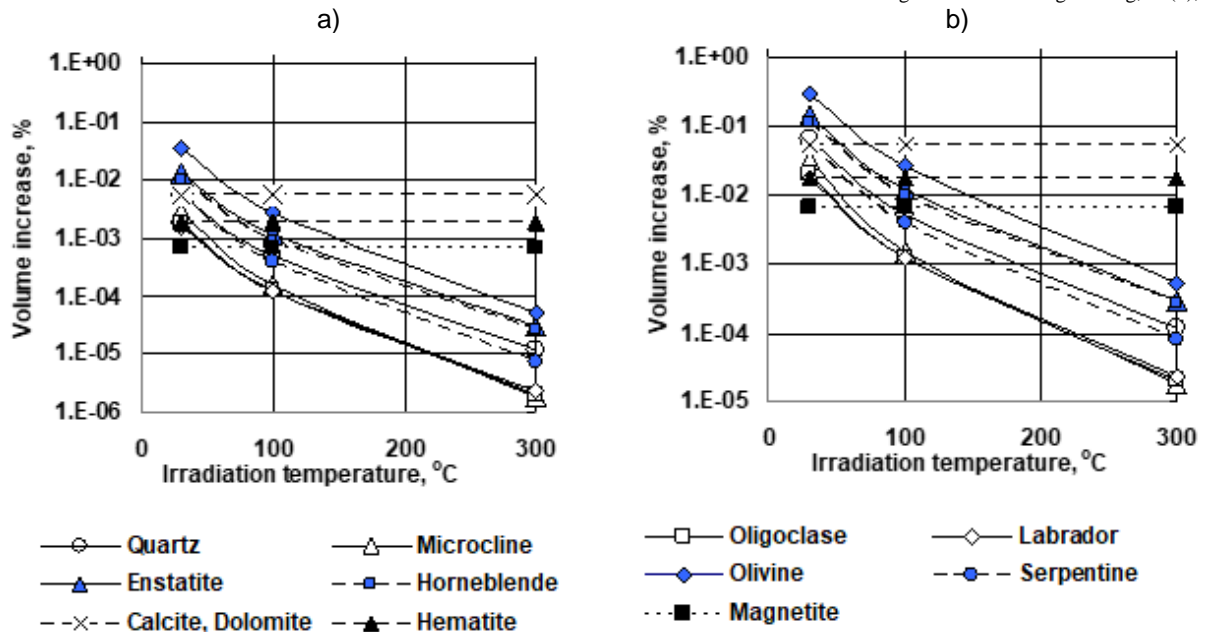


Figure 5. Dependence of the calculated radiation increase in the volume of various minerals on the irradiation temperature at an absorbed dose of gamma ray with an average energy of 5 MeV $1 \cdot 10^{10}$ Gy (a) and $1 \cdot 10^{11}$ Gy (b)

The calculation results indicate that noticeable radiation changes in the considered minerals will occur only at absorbed doses of gamma ray greater than $D_{g0} = 1 \cdot 10^9 - 1 \cdot 10^{10}$ Gy for gamma rays with an energy of 5 MeV and $D_{g0} = 3 \cdot 10^9 - 3 \cdot 10^{10}$ Gy for gamma rays with an energy of 2 MeV. The radiation changes in volume rise with an increase in the absorbed dose and decrease in silicate class minerals with an increase in the irradiation temperature.

At 30 °C, according to the calculation results, the largest radiation increase in volume in the studied range of absorbed doses will occur in minerals of silicate class minerals.

The maximum increase in volume during irradiation at 30 °C will be observed in olivine (up to 0.3 %). A 2–2.5 times smaller increase in volume will occur in pyroxenes of diopside and enstatite (up to 0.15 %) and hornblende (up to 0.12 %). 4.6–5.5 times a smaller increase in volume will be observed in quartz (up to 0.065 %), serpentine, calcite, dolomite (up to 0.055 %). A 10–16 times smaller increase in volume will occur in the microcline minerals (up to 0.03 %) and oligoclase, labrador, hematite (up to 0.018–0.020 %). A minimal increase in volume will be observed in magnetite (up to 0.007 %). In quartz glass, regardless of the irradiation temperature, a decrease in volume will occur (up to -0.3 %).

With an increase in the irradiation temperature from 30 °C to 100 °C and 300 °C, the radiation changes in the silicates class minerals decrease, while the radiation changes of carbonate class minerals (calcite, dolomite) and iron oxides (hematite, magnetite) do not change. Moreover, the effect of temperature increases with the rise of irradiation temperature. At 100 °C the increase in the volume of silicates decreases by 11–18 times, and at 300 °C it decreases by 400–1800 times in comparison with a change in volume at 30 °C. In this regard, the ratio between radiation changes in the volume of various minerals changes, the upper and lower boundaries of the changes in volume decrease, and the increase in the volume of silicate class minerals becomes smaller than that of carbonates and iron oxides.

In the case of irradiation at 100 °C in the studied range of absorbed doses, the maximum volume increase will be observed in minerals of the carbonate class—calcite and dolomite (up to 0.055 %). An approximately twofold smaller increase in volume will occur in olivine (up to 0.027 %). A 3.7-fold smaller increase in volume will be observed in hematite (0.018 %). A 4.5–5.6 times smaller volume increase will occur in pyroxenes of enstatite, diopside (up to 0.012 %) and hornblende (up to 0.096 %). An 8-fold smaller increase in volume will be observed in magnetite (up to 0.0067 %). 10.8–13.5 times a smaller increase in volume will occur in quartz (up to 0.005 %) and serpentine (up to 0.004 %). A slight, 36–45 times smaller increase in volume will be observed in microcline, oligoclase and labrador (up to 0.0012–0.0015 %).

In the case of irradiation at 300 °C in the studied range of absorbed doses, a maximum increase in volume will also be observed in calcite and dolomite of carbonate class minerals (up to 0.055 %). A 3.7-fold smaller increase in volume will occur in hematite (0.018 %). An 8-fold smaller increase in volume will be observed in magnetite (up to 0.0067 %). For the remaining studied minerals, the increase in volume will not be significant (at 100–3000 times less) and will be 0.000018–0.00053 %.

The results of calculations by formulas (7)–(13) of radiation changes in the volume and compressive strength of the considered rocks - aggregates of the absorbed dose of gamma ray are shown in Figures 6–12.

The calculation results indicate that, as with minerals, noticeable radiation changes in the considered minerals will occur only at absorbed doses of gamma ray greater than $D_{g0} = 1 \cdot 10^9 - 1 \cdot 10^{10}$ Gy for gamma rays with an energy of 5 MeV and $D_{g0} = 3 \cdot 10^9 - 3 \cdot 10^9$ Gy for gamma rays with an energy of 2 MeV. The radiation changes in volume rise with an increase in the absorbed dose and decrease in rocks, consisting of silicates, with an increase in the irradiation temperature.

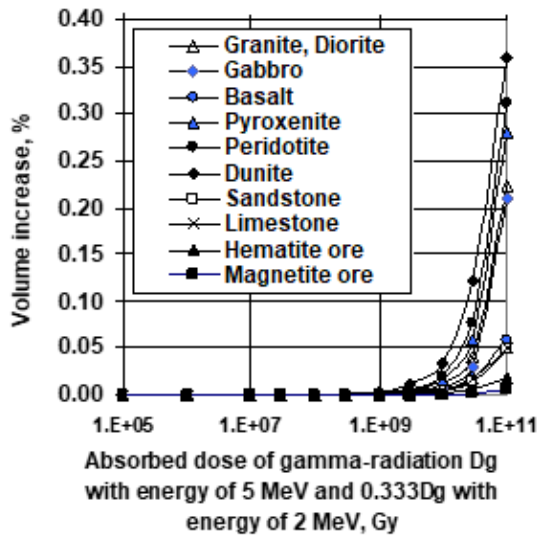


Figure 6. Dependence of the calculated radiation increase in the volume of various concrete aggregate rocks on the absorbed dose of gamma ray with an average energy of 5 MeV and 2 MeV at an irradiation temperature of 30 °C.

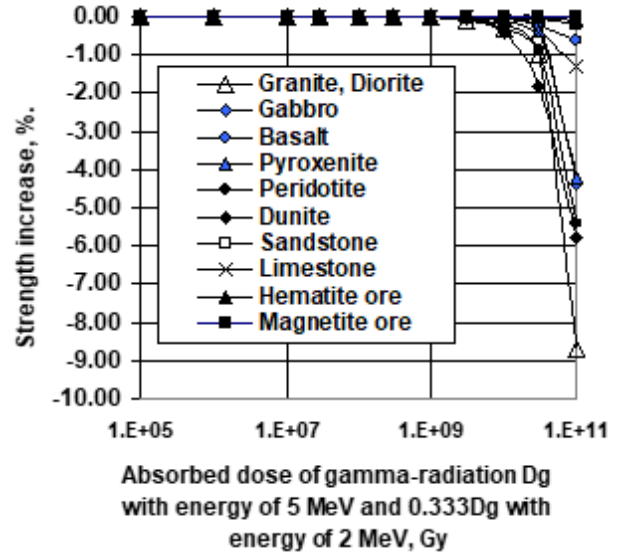


Figure 7. Dependence of the estimated residual strength of various concrete aggregate rocks on the absorbed dose of gamma ray with an average energy of 5 MeV and 2 MeV at an irradiation temperature of 30 °C.

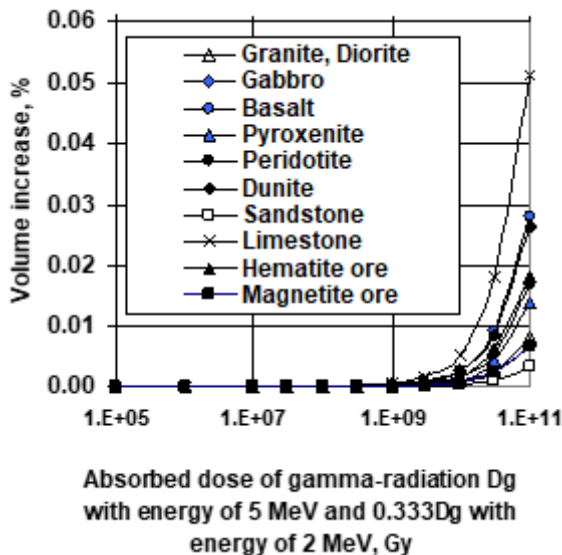


Figure 8. Dependence of the calculated radiation increase in the volume of various concrete aggregate rocks on the absorbed dose of gamma ray with an average energy of 5 MeV and 2 MeV at an irradiation temperature of 100 °C.

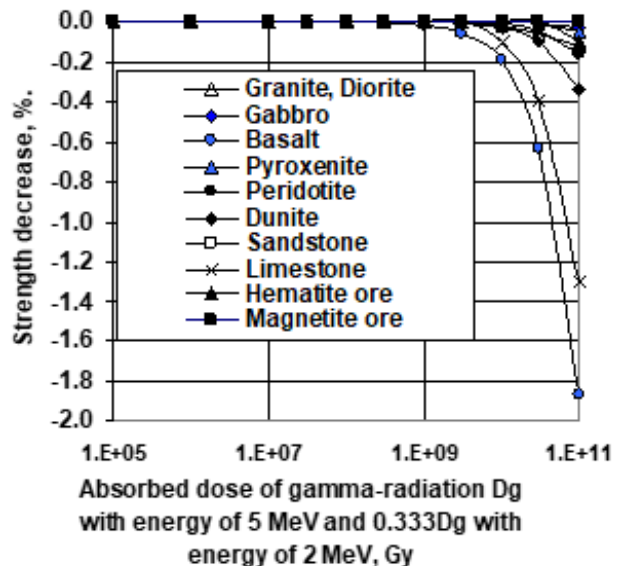


Figure 9. Dependence of the estimated residual strength of various concrete aggregate rocks on the absorbed dose of gamma ray with an average energy of 5 MeV and 2 MeV at an irradiation temperature of 100 °C.

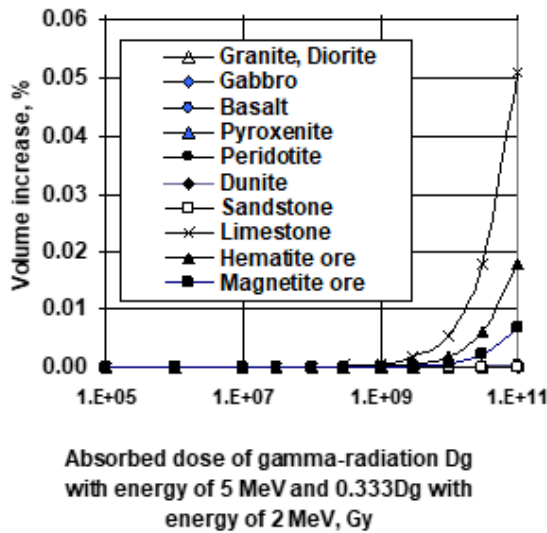


Figure 10. Dependence of the calculated radiation increase in the volume of various concrete aggregate rocks on the absorbed dose of gamma ray with an average energy of 5 MeV and 2 MeV at an irradiation temperature of 300 °C.

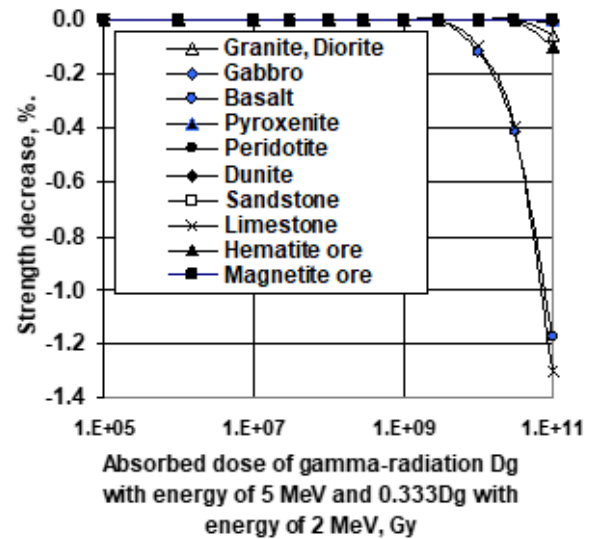


Figure 11. Dependence of the estimated residual strength of various concrete aggregate rocks on the absorbed dose of gamma ray with an average energy of 5 MeV and 2 MeV at an irradiation temperature of 300 °C.

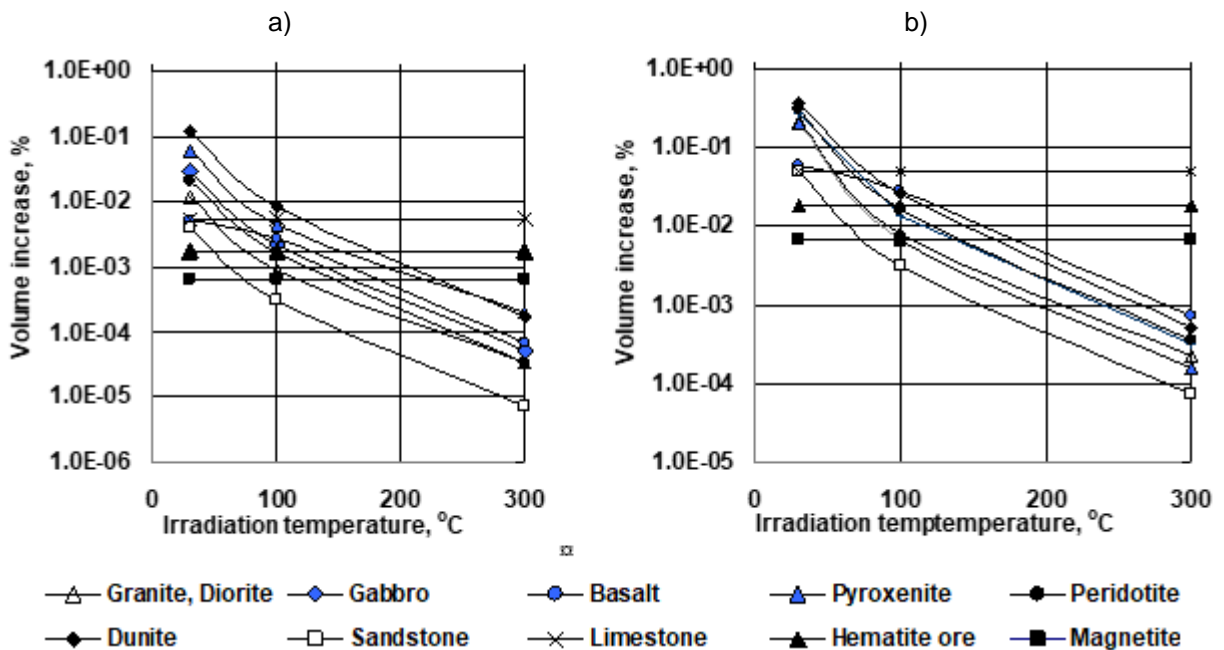


Figure 12. Dependence of the calculated radiation increase in the volume of various concrete aggregate rocks on the irradiation temperature for an absorbed dose of gamma radiation with an average energy of 5 MeV 1.10¹⁰ Gy (a) and 1.10¹¹ Gy (b)

At 30 °C, according to the results of calculations, the greatest increase in volume and decrease in strength under the influence of gamma radiation in the studied range of absorbed doses will occur in rocks consisting of silicate class minerals.

The largest volume increase during irradiation at 30 °C will be observed in dunite (up to 0.36 %), peridotite (up to 0.31 %) and pyroxenite (up to 0.28 %). 1.4–1.7 times a smaller increase in volume will occur in granite, diorite (up to 0.22 %) and gabbro (up to 0.21 %). 4.7–7 times less a smaller increase in volume will be observed in basalt (up to 0.059 %), sandstone (up to 0.050 %), limestone and dolomite (up to 0.051 %). The smallest increase in volume will occur in hematite ore (up to 0.018 %) and magnetite ore (up to 0.0066 %).

The greatest decrease in strength during irradiation at 30 °C will be observed for granite (up to -8.7 %). Almost two times lesser decrease in strength will occur in dunite (up to -5.8 %), peridotite (up to -5.4 %), pyroxenite (up to -4.2 %) and gabbro (-4.3 %). In other rocks, the decrease in strength is not significant and amounts to -1.3 % or less, but decreases in the direction: limestone (up to -1.3 %) → basalt (up to -0.6 %) → hematite and magnetite ore (up to - 0.1 %).

With an increase in the irradiation temperature from 30 °C to 100 °C and 300 °C, the radiation changes of silicate aggregate rocks decrease, but the radiation changes of carbonate and ore aggregate rocks do not change. Moreover, the effect of temperature increases with increasing irradiation temperature. At 100 °C, an increase in the volume of silicate rocks except for basalt decreases by 13–31 times, and at 300 °C it decreases by 300–970 times compared with a change in volume at 30 °C. In basalt, the decrease is ≈ 2 times at 100 °C and ≈ 80 times at 300 °C. In this regard, the ratio between radiation changes in the volume of various silicate and carbonate, ore rocks varies, the upper and lower boundaries of volume changes decrease, and the increase in the volume of silicate rocks becomes less than that of carbonate and ore rocks.

In the case of irradiation at 100 °C in the studied range of absorbed doses, the maximum increase in volume will be observed in limestone (up to 0.051 %). An approximately twofold smaller increase in volume will occur in basalt (up to 0.028 %) and dunite (up to 0.026 %). 2.8–3.7 times a smaller increase in volume will be observed in hematite ore (0.018 %), peridotite (up to 0.017 %) and pyroxenite (up to 0.014 %). In 6.2–7.3, a smaller increase in volume will occur in granite and diorite (up to 0.008 %), gabbro (up to 0.007 %) and magnetite ore (up to 0.007 %). A minimal and insignificant increase in volume will be observed in sandstone (up to 0.0032 %).

The decrease in strength during irradiation at 100 °C will be insignificant in all rocks, since it does not exceed -1.8 %. However, it decreases in the direction: basalt (up to -1.8 %) → limestone (up to -1.3 %) → dunite (up to 0.3 %) → other rocks (up to -0.2 %).

In the case of irradiation at 300 °C in the studied range of absorbed doses, the maximum increase in volume will be observed in limestone (up to 0.051 %). A 2.8 times smaller increase in volume will occur in hematite ore (up to 0.018 %). A 7.3-fold smaller increase in volume will be observed in magnetite ore. In other rocks, the increase in volume is not significant and does not exceed 0.0007 %.

The decrease in strength during irradiation at 300 °C will be even less significant than during irradiation at 100 °C. The greatest decrease in strength will be -1.3 % for limestone and -1.2 % for basalt. In other rocks, the decrease in strength will not be significant (no more than -0.1 %).

Thus, the radiation changes of aggregates of concrete and their minerals under the influence of gamma ray at the considered absorbed doses can be significant only at absorbed doses of more than 10^9 Gy. Radiation changes increase with the absorbed dose. However, even with an absorbed dose of 10^{11} Gy, the radiation changes are not large (an increase in volume of not more than 0.36 %, a decrease in strength of not more than 8.7 %). Since, in accordance with the existing analytical methods [10, 12, 14] the changes in concrete are close to changes in aggregates, the radiation changes in concrete under the influence of gamma ray at the considered absorbed doses will not be large either.

Since the available experimental data on concretes were obtained in [1, 2, 6, 7, 13, 15, 21, 23–27] at absorbed doses of less than $1.5 \cdot 10^9$ Gy, the radiation-induced changes in concrete found in these works are mainly caused by changes in their cement stone.

It is important that the calculated radiation changes of minerals and aggregate rocks under the influence of gamma ray are much less than the maximum changes established by neutron radiation (increase in volume to 18–23 %, decrease in strength to 100 % in silicate materials, increase in volume to 3 % in carbonate and oxide materials). In this regard, it is of interest to evaluate what absorbed doses of gamma ray are necessary to achieve the same effects as under the influence of neutrons.

According to [14], the indicated maximum radiation changes in the aggregate rocks are observed at the following approximate values of the damaging neutron fluences (with an energy of more than 10 KeV):

- $1 \cdot 10^{20}$ neutron/cm² for silicate materials at 30 °C;
- $3 \cdot 10^{20}$ neutron/cm² for silicate materials at 100 °C;
- $10 \cdot 10^{20}$ neutron/cm² for silicate materials at 300 °C;
- $(1-10) \cdot 10^{20}$ neutron/cm² for carbonate materials and materials based on iron oxides.

For the neutron spectra of the main reactors used in these studies, the fluences of $1 \cdot 10^{20}$ – $10 \cdot 10^{20}$ neutron/cm² correspond to the fraction of displaced atoms $n_{CM} = 0.14$ – 1.4 , since the average cross section for atomic displacement is $\sigma_{CM}(E_n) = 1400 \cdot 10^{-24}$ cm². Then, to obtain under the action of gamma ray the same maximum effects as under the action of neutrons in accordance with formulas (14) and (15), the following absorbed to gamma ray are necessary:

$$D_g = n_{CM} / 1.1 \cdot 10^{-14} = (0.14 - 1.4) / 1.1 \cdot 10^{-14} = 1.3 \cdot 10^{13} - 1.3 \cdot 10^{14} \text{ Gy} - \text{at gamma ray energy } E_g = 2 \text{ MeV};$$

$$D_g = n_{CM} / 3.3 \cdot 10^{-14} = (0.14 - 1.4) / 3.3 \cdot 10^{-14} = 4.2 \cdot 10^{12} - 4.2 \cdot 10^{13} \text{ Gy} - \text{at gamma ray energy } E_g = 5 \text{ MeV}.$$

Such high absorbed doses of gamma ray to radiation protection concrete in modern nuclear facilities are not achievable. Therefore, radiation changes under the influence of gamma ray, commensurate with the maximum radiation changes under the influence of neutrons, are practically impossible at currently operating nuclear facilities.

It is also of interest to evaluate the contribution of radiation changes due to gamma ray to radiation changes in the radiation protection materials of nuclear reactors, which are simultaneously affected by neutrons and gamma ray.

It can be made in the following way:

According to [40], the ratio φ_n / φ_g of the density of the damaging neutron flux (with an energy of more than 10 KeV) φ_n (neutron/(cm²·s)) to the energy flux density of gamma ray φ_g (MeV/(cm²·s)) behind the nuclear reactor vessel is:

- $\varphi_n / \varphi_g \approx 0.05 \text{ MeV}^{-1}$ – for uranium-graphite and water-cooled thermal neutron reactors;

- $\varphi_n / \varphi_g \approx 3 \text{ MeV}^{-1}$ – for fast neutron reactors.

Then the ratio $n_{d.g} / n_{d.n}$ of the number of displaced atoms under the action of gamma ray $n_{d.g}$ with gamma ray energy $E_g = 5 \text{ MeV}$ (average energy behind the reactor vessel) to the number of displaced atoms under the action of neutrons $n_{d.n}$ with the cross sections for the formation of displaced atoms $\sigma_d(E_g) = 0.5 \cdot 10^{-24} \text{ cm}^2$ and $\sigma_d(E_n) = 1400 \cdot 10^{-24} \text{ cm}^2$ will be:

$$n_{d.g} / n_{d.n} = \varphi_n / \varphi_g \cdot \frac{\sigma_d(E_g)}{E_g \cdot \sigma_d(E_n)} = 0.05 \cdot \frac{0.5 \cdot 10^{-24}}{5 \cdot 1400} = 3.6 \cdot 10^{-6} \text{ – for uranium-graphite and water-cooled thermal neutron reactors;}$$

$$n_{d.g} / n_{d.n} = \varphi_n / \varphi_g \cdot \frac{\sigma_d(E_g)}{E_g \cdot \sigma_d(E_n)} = 3 \cdot \frac{0.5 \cdot 10^{-24}}{5 \cdot 1400} = 2.1 \cdot 10^{-4} \text{ – for fast-neutron reactors.}$$

Since $n_{d.g} / n_{d.n}$ is much less than 1, the effect of gamma ray on the radiation changes of minerals and rock-aggregates of concrete, and hence concrete, radiation protection of nuclear reactors under the simultaneous exposure to neutrons and gamma ray can be neglected. In this regard, the radiation changes under the influence of gamma ray must be taken into account when gamma ray only is exposed to materials with absorbed doses of more than 10^9 Gy .

It is characteristic that the results of evaluating the gamma ray effect on minerals and rocks do not correspond to the opinion that silicate minerals and rocks receive the largest and smallest radiation changes upon exposure based on the results of irradiation of minerals and rocks with high neutron fluences. When irradiated with neutrons with the formation of a large number of displaced atoms, the largest radiation changes are obtained by quartz, feldspars and including them granites, diorites (with coarser grains especially), sandstones, and much smaller changes – by serpentine, pyroxenes, hornblende, olivine and including them gabbro, basalts, diabases, pyroxenites, peridotites and dunites. Under the gamma ray influence of the considered absorbed dose values, the maximum changes from silicate materials will occur in olivine, pyroxenes and including them dunite, peridotite, pyroxenite, and the minimum changes will occur in quartz, serpentine, feldspars (microcline, oligoclase, labrador) and including them sandstone and basalt. The intermediate radiation changes will be observed in granites, diorites and gabbro, to the compositional features of which the influence of their coarse-grained structure is added.

Further computational research should be devoted to:

- assessment of radiation changes in cement stone based on existing experimental data on concrete irradiation;
- assessment of radiation changes in concrete with various aggregates under the influence of gamma ray in a wide range of absorbed doses and radiation temperatures based on the results of the assessment of radiation changes in aggregates and cement stone.

Such an assessment can also be performed on the basis of the above considered methods for the analytical determination of radiation changes in concrete and its components.

4. Conclusion

1. The paper assesses the radiation changes of concrete aggregates under the influence of gamma ray based on analytical methods developed previously during the study of neutron radiation influence. The possibility of using these analytical methods in the case of exposure to gamma ray is discussed and justified in this paper.

2. For practical use of these analytical methods, the relationship between the absorbed dose of gamma radiation of different energies and the number of atoms displaced during irradiation has been established. It was found that the absorbed dose of gamma radiation with an energy of 5 MeV corresponds to 3 times more displaced atoms than the absorbed dose of gamma radiation with an energy of 2 MeV.

3. As a result of the calculations, the radiation changes of the main types of rocks - concrete aggregates (igneous, sedimentary rocks and ores) under the influence of gamma radiation with an average energy of 2 MeV and 5 MeV after irradiation to absorbed doses from 10^5 to 10^{11} Gy at 30 °C, 100 °C and 300 °C were estimated. For this purpose, the radiation changes of the main rock-forming minerals were calculated, and the radiation changes of rocks of concrete aggregates were calculated from them.

4. It has been established that the noticeable radiation changes in the examined minerals and aggregate rocks will occur only at absorbed doses of gamma ray greater than $D_{g0} = 1 \cdot 10^9 - 1 \cdot 10^{10}$ Gy for gamma rays with an energy of 5 MeV and $D_{g0} = 3 \cdot 10^9 - 3 \cdot 10^{10}$ Gy for 2 MeV gamma rays. The radiation changes in the volume of minerals increase with a rise in the absorbed dose and decrease in silicate class minerals and silicate rocks with an increase in the irradiation temperature.

5. At 30 °C, the largest increase in volume under the influence of gamma radiation in the studied range of absorbed doses will occur in minerals of the silicate class. The maximum increase in volume during irradiation at 30 °C will occur in olivine (up to 0.3 %). A minimal and insignificant increase in volume will be observed in magnetite (up to 0.007 %). The radiation change in the volume of minerals decreases in the direction: olivine-pyroxenes (diopside, enstatite) →hornblende→quartz, serpentine, calcite, dolomite→microcline, oligoclase, labrador, hematite→magnetite.

6. With an increase in the irradiation temperature from 30 °C to 100 °C and 300 °C, the radiation changes of silicate class minerals decrease, while the radiation changes of carbonate class minerals (calcite, dolomite) and iron oxides (hematite, magnetite) do not change. Moreover, the effect of temperature increases with the rise of irradiation temperature. At 100 °C, the radiation increase in the volume of silicates decreases by 11–18 times and becomes insignificant and at 300 °C it decreases by 400–1800 times compared with the change in volume at 30 °C and becomes insignificant. In this regard, the ratio between radiation changes in the volume of various minerals changes, the upper and lower boundaries of the changes in volume decrease, and the increase in the volume of silicate class minerals becomes smaller than that of carbonates and iron oxides.

7. In quartz glass, regardless of the irradiation temperature, there will be a decrease in volume (up to -0.3%).

8. Radiation changes in the volume of rocks of concrete aggregates increase with an increase in the absorbed dose and decrease in rocks consisting of minerals of the silicate class with an increase in the irradiation temperature.

9. At 30 °C, according to the results of calculations, the greatest increase in volume and decrease in strength under the influence of gamma radiation in the studied range of absorbed doses will occur in rocks consisting of silicate class minerals.

10. The largest increase in volume under the influence of gamma radiation during irradiation at 30 °C will be observed in dunite (up to 0.36 %), peridotite (up to 0.31 %) and pyroxenite (up to 0.28 %). The smallest, insignificant increase in volume will occur in magnetite ore (up to 0.0066 %). The radiation change in the volume of rocks decreases in the direction of: dunite, peridotite and pyroxenite→granite, diorite and gabbro (up to 0.22 %)→basalt, sandstone, limestone and dolomite (up to 0.059%)→magnetite ore (up to 0.018 %)→hematite ore.

11. The greatest decrease in strength during irradiation at 30 °C will be observed in granite (up to -8.7 %). Almost half less reduction of strength will occur in dunite (up to -5.8 %), peridotite (up to -5.4 %), pyroxenite (up to -4.2 %) and gabbro (-4.3 %). In other rocks, the reduction of strength is not significant and is -1.3 % or less, but it decreases in the direction of: limestone (to -1.3 %)→basalt (to -0.6 %)→hematite and magnetite ore (to -0.1 %).

12. With an increase in the irradiation temperature from 30 °C to 100 °C and 300 °C, the radiation changes of silicate aggregate rocks decrease, while the radiation changes of carbonate and ore aggregate

rocks do not change. At 100 °C, the increase in the volume of silicate rocks in addition to basalt decreases by 13-31 times, and at 300 °C decreases by 300–970 times compared to the change in volume at 30 °C. In basalt, the decrease is about 2 times at 100 °C and about 80 times at 300 °C. In this regard, the ratio between the radiation changes in the volume of various silicate and carbonate, ore rocks changes, the upper and lower limits of volume changes are reduced, and the increase in the volume of silicate rocks become less than of carbonate and ore rocks. Radiation changes in strength with increasing irradiation temperature change similarly to changes in volume.

13. In general, it can be noted that even with the absorbed dose of 10^{11} Gy gamma ray the changes of rocks-concrete aggregates are not great (an increase in volume is no more than 0.36 %, a decrease in strength is no more than 8.7 %). In this regard, the changes in concrete under the influence of gamma ray at the considered absorbed doses will not be significant.

14. The calculated radiation changes of minerals and rock aggregates of concrete under the action of gamma radiation are much smaller than the maximum changes established during neutron irradiation (an increase in volume is to 18–23 %, a decrease in strength is to 100 % in silicate materials, an increase in volume is to 3 % in carbonate and oxide materials). According to the results of calculations, the radiation changes under the action of gamma ray, commensurate with the maximum radiation changes under the action of neutrons in nuclear facilities operating at the present time are practically impossible.

15. The calculations have shown that the influence of gamma ray on the radiation changes of minerals and rock aggregates of concrete, and therefore concrete, the radiation protection of nuclear reactors with the simultaneous exposure to neutrons and gamma ray can be neglected. In this regard, the radiation changes under the influence of gamma radiation must be taken into account when only gamma ray is applied to materials and when absorbed doses are greater than 10^9 Gy.

References

- Kelly, B., Brocklehurst, J., Mottershead, D., McNearney, S. The Effects of Reactor Radiation on Concrete. Proceedings of the Second Information Meeting on Pre Stress Concrete and Reactor Pressure Vessels and their Thermal Isolation. EUR-4531, 1969. Pp. 237–265.
- Gray, B.S. The Effect of Reactor Radiation on Cements and Concrete. Proceedings of an information exchange meeting on results of concrete irradiation programmes. EUR 4751 f-e Brussels (Belgium), April 19, 1971. Commission of the European Communities, Luxembourg, 1972. Pp. 17-39
- Elleuch, L., Dubois, F., Rappeneau, J. Effects of Neutron Radiation on Special Concretes and Their Components. Special Publication of The American Concrete Institute SP-34, 1972. Pp. 1071–1108.
- Dubrovskiy, V.B., Lavdanskii, P.A., Pergamenshchik, B.K., Solovyev, V.N. Radiatsionnaya stoykost materialov [Radiation Stability of Materials Handbook]. Spravochnik. Pod obshey red. V.B. Dubrovskogo. Ed. V.B. Dubrovskiy. Moscow: Atomizdat, 1973. 264 p.(rus)
- Dubrovskiy, V. B. Radiatsionnaya stoykost stroitelnykh materialov [Radiation Stability of building materials] Moscow: Stroyizdat, 1977. 278 p.(rus)
- Hilsdorf, H.K., Kropp, J., Koch, H. J. The effects of nuclear radiation on the mechanical properties of concrete. Proceedings of the Douglas McHenry International Symposium on Concrete and Concrete Structures, ACI SP 55-10, American Concrete Institute, Mexico City, Mexico, 1978. Pp. 223–251.
- Kaplan, M.F. Concrete Radiation Shielding. Concrete Design and Construction Series. Harlow: Longman Scientific, 1989. 457 p.
- Denisov, A.V., Dubrovskiy, V.B., Krivokoneva, G.K. Radiatsionnyye izmeneniya mineralov zapolniteley betonov i ikh analiticheskoye opredeleniye [Radiation-induced changes in concrete aggregates minerals and analytical determination]. Voprosy atomnoy nauki i tekhniki. 1984. No 2 (18). Pp. 31–40. (rus)
- Denisov, A. V., Dubrovskiy, V.B. Analiticheskoe opredeleniye radiatsionnogo izmeneniya svoystv materialov zapolniteley betonov [Analytical determination of radiation changes in the properties of concrete aggregate materials]. Voprosy atomnoy nauki i tekhniki. 1984. No. 2(18). Pp. 45–57. (rus)
- Muzalevskiy, L.P. Prognozirovaniye stepeni izmeneniya prochnosti i radiatsionnykh deformatsiy betona [Forecasting of degree of change of durability and radiating deformations of concrete]. Trudy Tretey Vsesoyuznoy nauchnoy konferentsii po zashchite ot ioniziruyushchih izlucheniye yaderno-tekhnicheskikh ustanovok [Works of the Third All-Union scientific conference on protection from ionising radiation of Nuclear-technical installations]. Vol. 5. Tbilisi: Iz-vo TGU, 1985. Pp. 116–125. (rus)
- Denisov, A.V., Dubrovskiy, V.B., Yershov, V.Yu. et. al. Radiatsionno -Temperaturnyye izmeneniya svoystv portlandcementnogo kamnya betona i avismosti dlya ih prognozirovaniya [Radiation -thermal changes of properties of hardened cement paste and functions for their predictions]. Voprosy atomnoy nauki i tekhniki. 1989. No. 2. Pp. 20–35. (rus)
- Muzalevskiy, L.P. Radiatsionnyye izmeneniya tyazhelykh betonov i metod ikh analiticheskogo opredeleniya [Radiating changes of heavy concrete and method of their analytical definition]. Dissertatsiya na soiskaniye uchenoy stepeni kandidata tekhnicheskikh nauk [Candidate of technical sciences (PhD) dissertation]. Moscow, 1989. 240 p. (rus)
- Fillmore, D.L. Literature Review of the Effects of Radiation and Temperature on the Aging of Concrete. Technical Report INEL/EXT-04-02319. Idaho National Engineering and Environmental Laboratory. Bechtel BWXT Idaho, LLC. Prepared for the Central Research Institute of Electric Power Institute. September 2004.
- Denisov, A.V., Dubrovskiy, V.B., Solovev, V.N. Radiatsionnaya stoykost mineralnykh i polimernykh stroitelnykh materialov [Radiating stability of mineral and polymer c building materials]. Moscow: Izdatelskiy dom MEI, 2012. 284 p. (rus)
- William, K., Xi, Y., Naus, D. A review of the effects of radiation on microstructure and properties of concretes used in Nuclear Power Plants. Tech. Rep. NUREG/CR -7171 ORNL/TM - 2013/263, US Nuclear Regulatory Commission, Oak Ridge National Laboratory. 2013.
- Field, K.G., Remec, I., Le Pape, Y. Radiation effects in concrete for nuclear power plants – Part I: Quantification of radiation exposure and radiation effects. Nuclear Engineering and Design. 2015. 282. Pp. 126–143.

17. Le Pape, Y., Field, K.G., Remec, I. Radiation effects in concrete for nuclear power plants, Part II: Perspective from micromechanical modeling. *Nuclear Engineering and Design*. 2015. 282. Pp. 144–157.
18. Giorla, A., Vaitova, M., Le Pape, Y., Stemberk, P. Meso-scale modeling of irradiated concrete in test reactor. *Nuclear Engineering and Design*. 2015. Vol. 295. Pp. 59–73.
19. Pomaro, B. A Review on Radiation Damage in Concrete for Nuclear Facilities. Experiments to Modeling. *Modelling and Simulation in Engineering*. 2016. Pp 1-10. Article ID 4165746. <https://doi.org/10.1155/2016/4165746> (date of application: 19/01/2020)
20. Rosseel, T.M., Maruyama, I., Le Pape, Y., Kontani, O., Giorla, A.B., Remec, I., Wall, J.J., Sircar, M., Andrade, C., Ordonez, M. Review of the Current State of Knowledge on the Effects of Radiation on Concrete. *Journal of Advanced Concrete Technology*. 2016. 14(7), Pp. 368-383. DOI:10.3151/jact.14.368.
21. Maruyama, I., Kontani, O., Takizawa, M., Sawada, S., Ishikawa, S., Yasukouchi, J., Sato, O., Etoh, J., Igari, T. Development of the soundness assessment procedure for concrete members affected by neutron and gamma-irradiation. *Journal of Advanced Concrete Technology*. 2017. 15. Pp. 440–523. DOI:10.3151/jact.15.440.
22. Le Pape, Y., Alsaid, M.H.F., Giorla, A.B. Rock-forming minerals radiation induced volumetric expansion – revisiting the literature data. *Journal of Advanced Concrete Technology*. 2018. 16. Pp.191–209. DOI: 10.3151/jact.16.191
23. Sommers, J.F., Gamma radiation damage of structural concrete immersed in water. *Health Physics*. 1969. 16. Pp. 503–508.
24. McDowall, D.C. The Effect of Gamma Irradiation on the Creep Properties of Concrete. Proceedings of an information exchange meeting on results of concrete irradiation programmes. EUR 4751 f-e Brussels (Belgium), April 19, 1971. Commission of the European Communities, Luxembourg, 1972. Pp. 55–69
25. Vodák, F., Trtík, K., Sopko, V., Kapičková, O., Demo, P. Effect of γ -Irradiation on Strength of Concrete for Nuclear Safety Structures. *Cement and Concrete Research*. 2005. 35. Pp. 1447–1451.
26. Lowinska-Kluge, A., Piszora, P. Effect of gamma irradiation on cement composites observed with XRD and SEM methods in the range of radiation dose 0-1409 MGy. *Acta Physica Polonica-Series A General Physic.*, 2008. 114. Pp. 399–411.
27. Kitsutaka, Y., Matsuzawa, K. The effect of gamma radiation on the fracture properties of concrete. Proceedings of FraMCoS-7, May 23-28, 2010. *Fracture Mechanics of Concrete and Concrete Structures - Recent Advances in Fracture Mechanics of Concrete*. Korea Concrete Institute, Seoul, ISBN 978-89-5708-180-8. Pp. 61–64.
28. Vodák, F., Vydra, V., Trtík, K., Kapičková, O. Effect of γ -irradiation on Properties of Hardened Cement Paste. *Materials and Structures*. 2011. 44. Pp. 101–107.
29. Kontani, O., Ichikawa, Y., Ishizawa, A. Irradiation Effects on Concrete Durability of Nuclear Power Plants. Proceedings of ICAPP 2011, Nice, France, May 2-5, Paper 11361.
30. Kontani, O., Sawada, S., Maruyama, I., Takizawa, M., Sato, O. Evaluation of irradiation effects on concrete structure: gamma-ray irradiation tests on cement paste. Proceedings ASME 2013 Power Conference, Boston, USA 29 July-1 August 2013. New York, USA: American Society of Mechanical Engineers, 2013-98099.
31. Ishikawa, S., Maruyama, I., Takizawa, M., Etoh, J., Kontani, O., Sawada, S. Hydrogen Production and the Stability of Hardened Cement Paste under Gamma Irradiation. *Journal of Advanced Concrete Technology*. December 2019.17. Pp. 673–685. DOI: 10.3151/jact.17.673.
32. Kircher, J. F., Bowman, R. E. Effects of Radiation on Material and Components. Eds. Reinhold, New York: Chapman and Hall, 1964. 690 p.
33. Pergamenschik, B.K., Samotayev, A. V. Raschet chisla smeshchennykh atomov v kvartse pri obluchenii v reaktore [Calculation of the number of displaced atoms in quartz during irradiation in the reactor]. *Materialy i konstruksii zashchit yadernykh ustanovok*. Sbornik trudov MISI. 1974. № 114 (kafedra Stroitelstva yadernykh ustanovok). Pp. 102–112. (rus)
34. Kovalchenko, M.S., Ogorodnikov, M.S., Rogovoy, Yu.I., Krayniy, A. G. Radiatsionnoye povrezhdeniye tugoplavkikh soyedineniy [Radiation damage to refractory compounds]. Moscow: Atomizdat, 1979. 160 p.
35. Kwon, J., Motta, A.T. Gamma displacement cross-sections in various materials. *Annals of Nuclear Energy*. 2000. No. 27. Pp. 1627–1642.
36. Denisov, A.V., Sprince, A. Analytical determination of thermal expansion of rocks and concrete aggregates. *Magazine of Civil Engineering*. 2018. No. 4. Pp.151–170. DOI: 10.18720/MCE.80.14
37. Kelly, B. Radiatsionnoye povrezhdeniye tverdykh tel [Irradiation Damage of Solids]. *Perevod s angl.* Moscow: Atomizdat, 1970. 240 p. (rus)
38. Mashkovich, V.P., Kudryavtseva, A.V. Zashchita ot ioniziruyushchih izlucheniy [Protection against ionizing radiation]. *Spravochnik [Handbook] – 4 –ye izd. pererab. i dlop.* Moscow: Energoatomzdat, 1995. 496 p. (rus)
39. *Spravochnik fizicheskikh konstant gornykh porod [Handbook of physical constants of rocks. Edited by S. Clarke]. Pod red. S. Klarka ml.* Moscow: MIR, 1969. 543 p.(rus)
40. Dubrovskiy, V.B., Pergamenschik, B.K. Dopuskayemye radiatsionnyye nagruzki na betonnyu zashchitu yadernykh reaktorov [Permissible radiation loads on concrete shielding of nuclear reactors]. *Energeticheskoye stroitelstvo*. 1969. No 9. Pp. 74-75. (rus)

Contacts:

Aleksandr Denisov, den-al-v@inbox.ru



DOI: 10.18720/MCE.96.9

Analytical dependence of the deflection of the spatial truss on the number of panels

M.N. Kirsanov

National Research University "Moscow Power Engineering Institute", Russia, Moscow

* E-mail: c216@ya.ru

Keywords: spatial truss, exact solution, induction, deflection, wind load, asymptotics, Maple

Abstract. A statically definable girder truss consists of two flat side trusses with parallel belts and descending braces, connected along the upper and lower belt by horizontal ties. The truss at the corners has four supports, the vertical reaction of one of which is selected from the equilibrium condition of the structure as a whole. Several types of external load are considered: the load in the middle of the span, vertical, evenly distributed over the nodes of the upper or lower belt, and uniform horizontal (wind), applied to the nodes of the upper belt. The forces in the rods and supports are determined by the method of cutting out the nodes. The deflection is found by the Maxwell-Mohr formula under the assumption of linear elasticity of the rods. The dependence of the deflection on the number of panels is obtained from solving problems for trusses with a consistently increasing number of panels. Generalization of these solutions to an arbitrary number of panels is found using special operators of the Maple computer mathematics system. Using the Maple operators, we derive and solve homogeneous linear recurrent equations that satisfy the coefficients of the desired formula. The found dependence has the form of a polynomial in the number of panels. Curves of the deflection dependence on the number of panels, the load and the size of the structure are constructed. Some asymptotic properties of the obtained solution are found. Formulas for the dependence of forces in the most stretched and compressed rods on the size of the structure, the load, and the number of panels that can be used to analyze the strength and stability of the structure are derived.

1. Introduction

In most analytical and numerical calculations of spatial trusses, the structure is replaced by separate flat trusses that carry the main load. The work of links is not taken into account. Modern computer mathematics systems allow for analytical calculations of spatial structures taking into account the forces in all rods.

The task is to determine the analytical dependence of the deflection of the spatial truss (Fig. 1) on the number of panels under different loading of the truss. The construction of a mathematical model of the structure, the calculation of forces in the rods, and the inductive derivation of the desired formulas are performed in the system of analytical transformations Maple [1]. Previously, a similar problem for flat trusses in analytical form was solved by the induction method in works [2–9], spatial — in works [10, 11]. The original algorithm for analytical calculation of lattice systems (planar, spatial, statically definable and statically indeterminate) was developed in [12]. The only drawback of the method is that it is not possible to obtain compact calculation formulas for the dependence, for example, of the deflection on the number of panels or any periodicity elements. In [13], non-linearity is taken into account in the calculation of frames.

The used calculation algorithm can be transferred almost without changes to other computer mathematics systems, which have a block for determining the General terms of sequences and solving a system of linear algebraic equations in symbolic form. In addition to Maple, the Mathematica system meets these requirements most of all, and to a lesser extent, the Reduce, Derivative, and Maxima systems.



2. Methods

2.1. Truss scheme. The calculation of the forces in the bars

The construction under consideration consists of two inclined flat trusses with parallel belts and descending struts of length $c = \sqrt{a^2 + d^2 + h^2}$ (Fig. 1, 2), connected on the lower and upper panel by tie rods on the long sides.

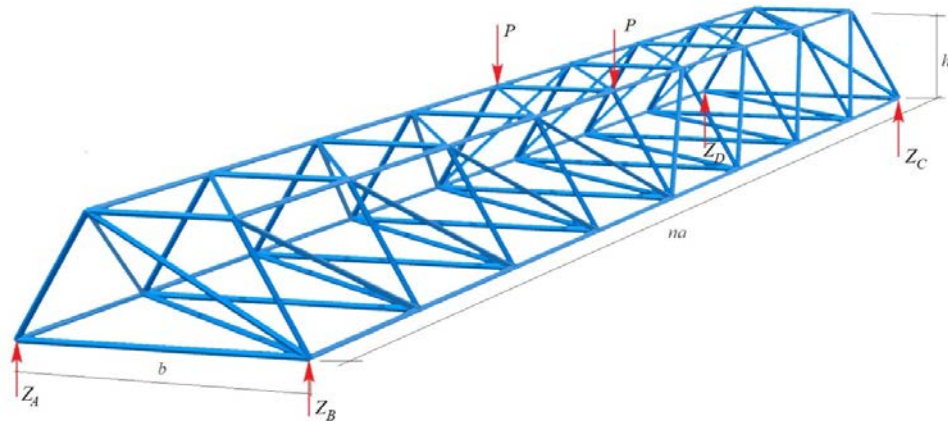


Figure 1. Vertical load in the middle of the span, $n=2k=8$.

The design is statically definable with n panels and contains $n_s = 12(n+1)$ rods. Supports located at three corners of the truss are modeled with six rods. Three rods simulate a spherical support A , two rods—a cylindrical D , one vertical — a movable in the plane hinge B . All connections of the rods in the design are hinged. The upper face of the spatial truss is a rectangular truss with length na and width $b - 2d$ with struts of length $d = \sqrt{a^2 + (b - 2d)^2}$ (Fig. 2). Instead of the fourth support, a vertical force $Z_C = P_{sum} / 4$ is applied to node C in the case of a symmetrical load P_{sum} (centered in the middle or evenly distributed across all nodes).

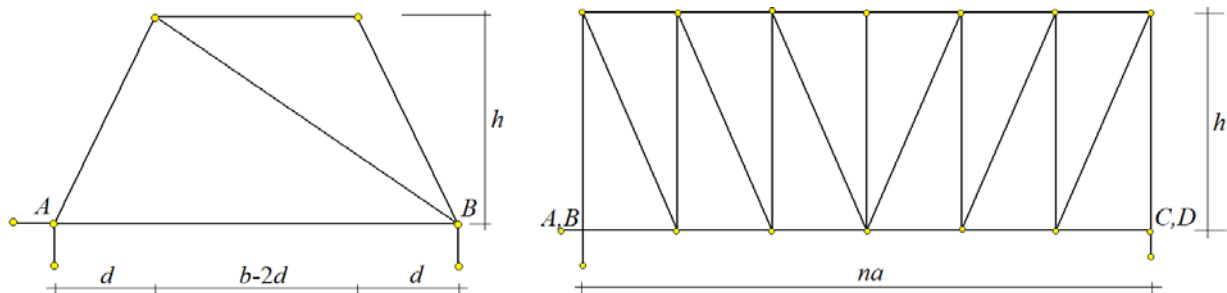


Figure 2. The size of the truss, $n=6$.

If the corner C were fixed to a real hinge support, the structure would become statically indeterminate once, but the result of solving the static indeterminability problem would give the same result, provided that all vertical supports have the same stiffness and length. The number of panels we choose is even $n = 2k$, so that the deflection of the truss can be judged by the vertical displacement of the nodes of its middle section.

To determine the forces in the rods, we use the program [1], which is based on drawing up and solving a system of equilibrium equations for nodes in symbolic form. The geometry of the truss is based on the coordinates of nodes at specified lengths of bars and the number of panels. The origin of coordinates is placed in the corner A , the axis x directed from A to B , y — longitudinal, z — vertical (Fig. 3):

$$\begin{aligned} x_i &= b, x_{i+n+1} = 0, x_{i+2n+2} = b - d, x_{i+3n+3} = d, \\ y_i &= y_{i+n+1} = y_{i+2n+2} = y_{i+3n+3} = a(i-1), \\ z_i &= z_{i+n+1} = 0, z_{i+2n+2} = z_{i+3n+3} = h, \quad i = 1, \dots, n+1. \end{aligned} \quad (1)$$

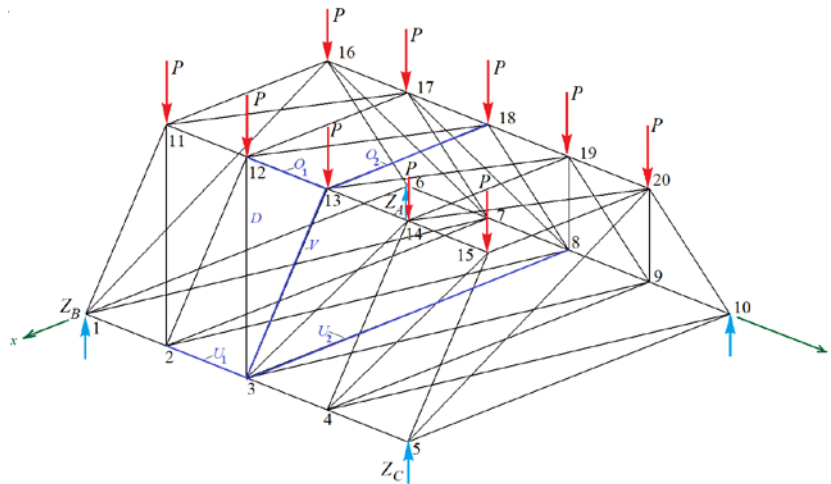


Figure 3. Numbering of nodes and rods. Uniform vertical load on the upper belt, $n=2k=4$.

The spatial structure of the truss that determines the order of connecting rods is defined by conditional vectors that have rod numbers directed along the rods and contain the numbers of the ends of the rods (the numbers of the corresponding nodes). The longitudinal bars of the lower truss belt, for example, are defined by the following vectors

$$N_i = [i, i + 1], N_{i+n} = [i + n + 1, i + n + 2], i = 1, \dots, n.$$

Other bars of the structure are set in the same way.

The square matrix of the equilibrium equations of nodes size $n_s \times n_s$ is formed from the guiding cosines of forces, which are calculated from the coordinates of their ends. For a statically defined truss $n_s = 3m$, where $m = 4(n + 1)$ is the number of nodes. The matrix G is divided into three lines for each node. These lines record the guide cosines of the rods attached to the node. Information about the rods in the node is contained in the vectors N_i , $i = 1, \dots, n_s$. Rows of the matrix with numbers $3i - 2$, $i = 1, \dots, n_s$ correspond to the projection of forces on the x axis, rows $3i - 1$ — projections on the y axis, rows of the type $3i$ — projections on the vertical z axis:

$$G_{3N_{i,1}-3+j,i} = l_{j,i} / L_i, G_{3N_{i,2}-3+j,i} = -l_{j,i} / L_i, j = 1, 2, 3, i = 1, \dots, n_s,$$

where $l_{1,i} = x_{N_{i,2}} - x_{N_{i,1}}$, $l_{2,i} = y_{N_{i,2}} - y_{N_{i,1}}$, $l_{3,i} = z_{N_{i,2}} - z_{N_{i,1}}$ are conditional projections of rods on the coordinate axis — L_i , $i = 1, \dots, n_s$ the length of the rods. Projections of the external load are recorded in the right part of the system of equilibrium equations. Solving a system of equations gives forces in all rods (including support rods).

To analyze the stability of compressed truss rods, you can use the calculation data to get the dependencies of the forces in them on the number of panels. Consider the six rods in the middle of the truss span that are potentially the most dangerous in terms of loss of stability or tensile strength (Fig. 3). Inductive analysis provides the following solutions for uniform load across the upper belt:

$$O_1 = Pak^2 / (2h), O_2 = -Pd / h, U_1 = Pa(k^2 - 1) / (2h), U_2 = 0, V = -Pg / h, D = Pc / (2h).$$

In the case of forces in the middle of the span (Fig. 1):

$$O_1 = -Pak / (2h), O_2 = 0, U_1 = Pa(k - 1) / (2h), U_2 = -Pd / h, V = 0, D = Pc / (2h).$$

To determine the force dependence on the number of panels, first calculate a series of trusses with a consistently increasing number of panels. The **rgf_findrecur** operator of the Maple system finds recurrent equations for the sequence of obtained analytical expressions of effort, and the **rsolve** operator, solving these equations, gives the already sought dependencies. The most complex equation was found when determining the force in the longitudinal rod of the lower belt U_1 the action of a uniform load:

$$U_{1,k} = 3U_{1,k-1} - 3U_{1,k-2} + U_{1,k-3}.$$

In all other cases, the forces are constant or the dependencies of the forces on k are fairly obvious, and you do not need to use a computer math system to derive the formulas. Numerical analysis of the obtained solution shows that under the condition of constant span and total load $P_{sum} = 2P(n+1)$ for a changing number of panels $n=2k$, all relative forces $U_1' = U_1 / P_{sum}$, $O_1' = O_1 / P_{sum}$, $O_2' = O_2 / P_{sum}$, $D' = D / P_{sum}$, $V' = V / P_{sum}$ in the rods asymptotically tend to their limit: $\lim_{k \rightarrow \infty} U_1' = L / (16h) = \tilde{S}$,

$\lim_{k \rightarrow \infty} O_1' = -\tilde{S}$. The curves in Figure 4 are constructed at $L = 100$ m, $h = 5$ m, and $d = 1$ m. Note that the forces in this section of the truss do not depend on the width b of the truss along the lower belt.

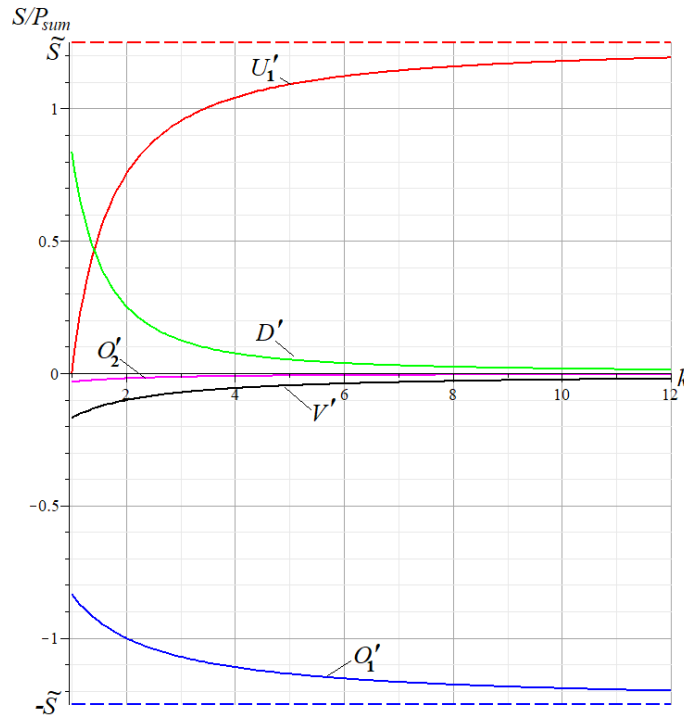


Figure 4. Dimensionless critical stress in the rods, depending on the number of panels.

In addition, the Maple graphical tools allow you to get a picture of the distribution of forces on the rods for a fixed number of panels. In figure 5, the calculation results for $k = 4$, $a=b=4$ m, $h=2$ m, $d=1$ m show compressed and unloaded rods in blue, and stretched rods in red. The thickness of the lines is proportional to the force modulus. The number indicates the value of the force in the rod related to the load P . The calculation shows that, as expected, the forces in the rods of the belts increase towards the middle of the span. The longitudinal bars of the upper belt are compressed, the lower — stretched. In the side panels (inclined), the reverse pattern is found somewhat unexpectedly. All rods in these panels are most loaded at the ends of the structure near the supports. The connections of the upper belt have very small compressive forces, while in the lower belt all the rods (except the extreme ones) are not strained at all.

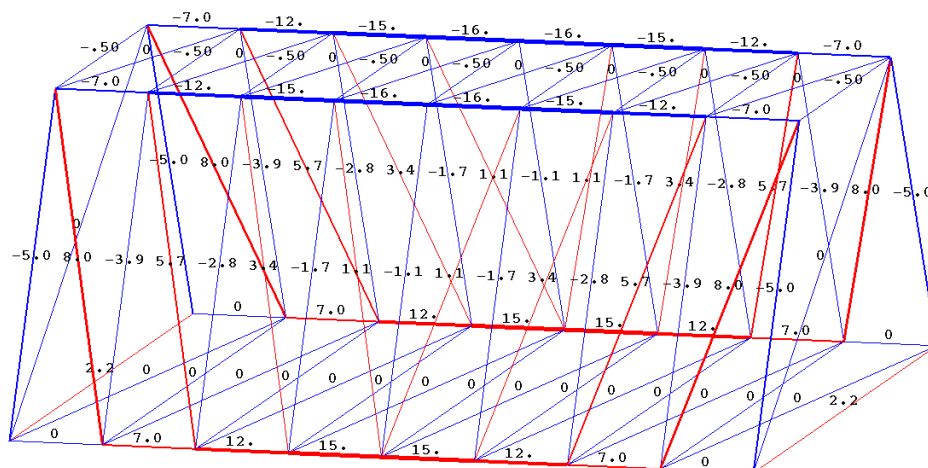


Figure 5. The forces in the rods, $k=4$.

2.2. Deflection from the action of a vertical load

A more difficult problem arises in the derivation of the formulas for deflection. Consider three types of vertical load on the truss. To calculate the deflection, use the Maxwell-Mohr formula

$$\Delta = \sum_{j=1}^{n_s-6} \frac{S_j s_j l_j}{EF}, \quad (2)$$

where E and F is the elastic modulus of the rods and their cross-sectional area, l_j and S_j is the length and force in the j -th rod from the action of a given load, s_j is the force from the unit load applied to the upper belt nodes in the middle of the span. Calculations of deflection of trusses with a consistently increasing number of panels using the formula (2) show that the type of expression for any values of k does not change. This is typical for regular systems [14] and is manifested not only in static problems [2–10], but also in dynamics [15]. For the case of a load applied to the upper belt nodes (Fig. 3), we have:

$$\Delta_I = P(C_{1,k}a^3 + C_{2,k}c^3 + C_{3,k}g^3 + C_{4,k}bd^2) / (2h^2EF). \quad (3)$$

The coefficients in this relationship form sequences whose common members can be determined using the already mentioned **rgf_findrecur** and **rsolve** operators of the Maple system. For the coefficient at a^3 , the **rgf_findrecur** operator returns a fifth-order equation

$$C_{1,k} = 5C_{1,k-1} - 10C_{1,k-2} + 10C_{1,k-3} - 5C_{1,k-4} + C_{1,k-5}.$$

The **rsolve** operator gives a solution to this equation

$$C_{1,k} = k^2(5k^2 + 1) / 6.$$

Other coefficients have a simple form and are obtained in the same way:

$$C_{2,k} = k^2, \quad C_{3,k} = k(k+2), \quad C_{4,k} = k+1/2:$$

The calculation shows that in the case of a load applied uniformly to the nodes of the lower belt, the type of expression (2) for the deflection does not change much:

$$\Delta_{II} = P(C_{1,k}a^3 + C_{2,k}(c^3 + g^3) + C_{3,k}bd^2) / (2h^2EF). \quad (4)$$

The coefficients here have the form $C_{1,k} = k^2(5k^2 + 1) / 6$, $C_{2,k} = k^2$, $C_{3,k} = k+1/2$.

Similarly, for a concentrated load in the middle of the span, we have

$$\Delta_{III} = P(C_{1,k}a^3 + C_{2,k}(c^3 + g^3) + C_{3,k}bd^2) / (2h^2EF), \quad (5)$$

where $C_{1,k} = k(2k^2 + 1) / 3$, $C_{2,k} = k$, $C_{3,k} = 3/2$.

A linear combination of three solutions, Δ_I , Δ_{II} and Δ_{III} gives a formula for calculating a truss with a fairly wide set of loads, including the weight of the structure itself.

2.3. Deformations from the action of a lateral load

One of the advantages of the applied algorithm for solving the problem of truss deformation, in addition to its analytical form, is the ease with which it can be reconfigured to another load. The main costs for generating formulas are spent on modeling the truss grid and debugging the solution. Replacing the load is reduced only to replacing the vector of the right part of the system of equilibrium equations. Consider the wind effect on structures [16]. It is obvious that due to the low windage of the structure, this load has a very small effect on the deformation of the truss [17]. Let us model this effect with a lateral horizontal load evenly distributed over the nodes of the upper belt (Fig. 8). As in the previous cases of loading, we will apply a load modeling the support to the free corner C of the lower belt truss. We find the load value from the equation of moments relative to the y axis: $Z_C = -P(n+1)h / (2b)$. With this action, we actually replaced the procedure for revealing static uncertainty if there was a vertical support rod in this corner. As a result of induction we have the following simple solution for the vertical displacement of the point M :

$$\Delta_{IV} = P(2k + 1)(g^3 + bd^2) / (2hbEF). \tag{6}$$

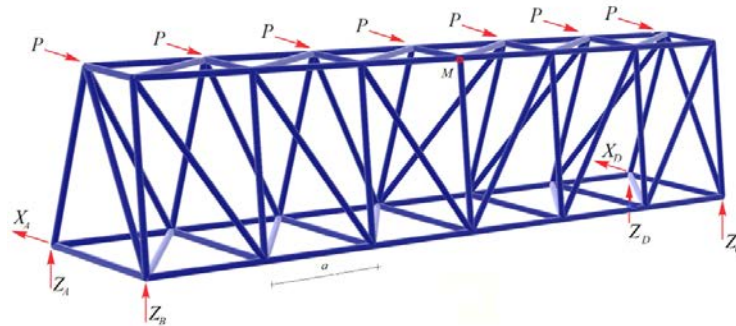


Figure 6. Lateral (wind) load, $k=3$.

3. Results and Discussion

It is best to evaluate the obtained solutions based on numerical calculations performed using the found formulas for specific tasks.

The curves of the dependence of the dimensionless deflection $\Delta' = \Delta_I EF / (P_{sum} L)$ on the number of panels constructed using the formula (3) for the case of a uniform vertical load along the upper belt, provided that the span of the structure $L = na = 100m$ is constant, and the total load $P_{sum} = 2(n + 1)P$ on the truss show the presence of a pronounced extreme (Fig. 7). Calculations were made for $h=3m$, $b=4m$. the oblique asymptote is also Observed. Using the Maple methods, you can calculate the slope of the asymptote. We get:

$\lim_{k \rightarrow \infty} \Delta' / k = f^3 / (4h^2 L)$, where $f = \sqrt{h^2 + d^2}$. The expression for the extreme point itself cannot be obtained in analytical form, but the figure shows that the position of this point on the axis k is almost independent of the size d .

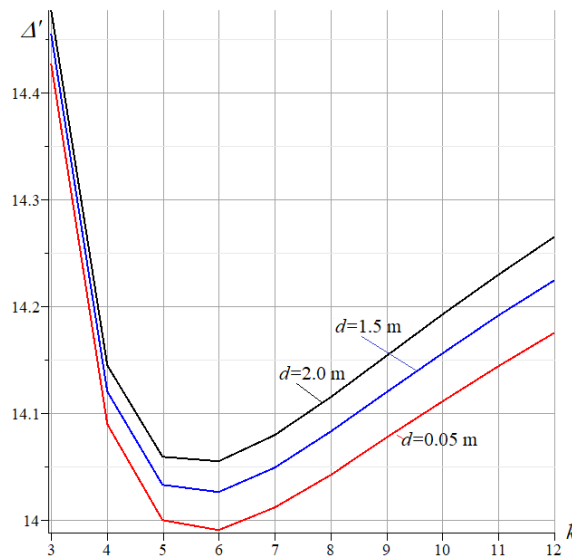


Figure 7. Dependence of dimensionless deflection on the number of panels.

If we trace the dependence of the deflection of the truss under the action of a uniform load on the height of the truss h (Fig. 8), then you can also notice the extremum ($h = 8m$), although very weakly expressed. These curves are constructed at $L = na = 60m$, $b = 8m$, $k = 40$. If the cross-section of the truss is rectangular (the width at the top is equal to the width at the bottom, or $d = 0$), the deflection is expected to be smaller. The other extreme is the degenerate case $b = 2d$, or the triangular section. The deflection here is greater, but from the point of view of saving material, this case is also interesting for the designer.

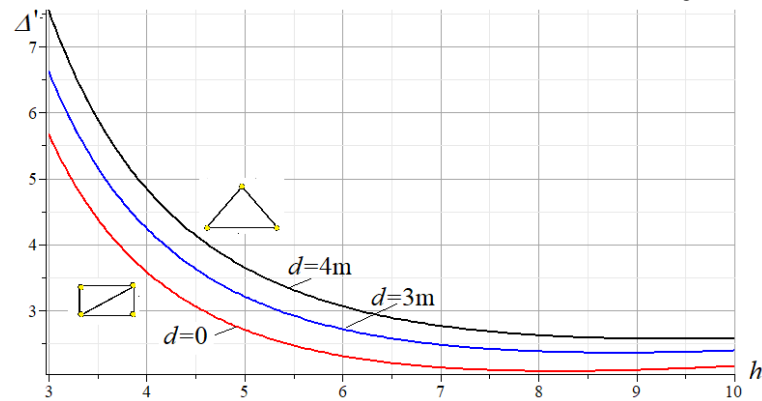


Figure 8. Dependence of the deflection on the height of the truss.

Formulas (4) and (5) for other vertical loads give similar curves, differing only in scale. For the horizontal load, as expected, the deflection is several orders of magnitude less than that of the vertical one. The minimum deflection is also detected, however, at unrealistically low truss heights (9). With a span length of $L = 100$ m, $d = 1$ m, this minimum corresponds to 1.5 m. In this setting, the width of the truss b plays a significant role. As the width increases, the truss becomes more rigid.

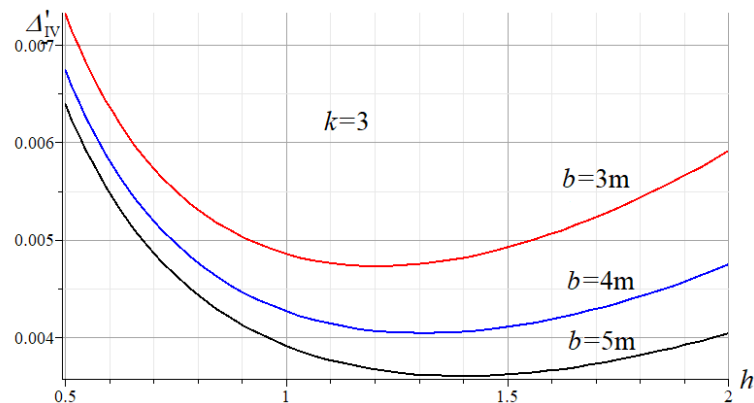


Figure 9. Dependence of the deflection of the truss on the action of the wind load on the height.

The main advantage of analytical solutions that include not only the size of the structure and load, but also the number of panels, is the ability to apply calculation formulas to structures with a large or very large number of rods. If numerical methods inevitably begin to accumulate counting errors when the number of rods in an object increases [18–26], then the accuracy of the calculation formula obtained by induction does not change and is determined only by the adequacy of the design model used. Another advantage of the obtained solution is the ability to perform optimization [27–35] of the truss by mathematically analyzing the formula, quickly compare options for building parameters and find optimal combinations of sizes and number of panels. Extreme points are found on the graphs based on the found formulas, which suggest the appropriate optimal design parameters to the designer. Analysis of forces in the truss also revealed an unexpected and unusual distribution of forces in the bars of the side panels of the truss.

4. Conclusions

A mathematical model of a spatial beam truss is constructed. An algorithm for displaying accurate analytical solutions for the forces in the rods and deflections of the structure under the action of various types of loads has been developed. The obtained solutions proved to be quite compact, suitable both for evaluating the performance of real structures of this type, and for testing numerical solutions performed in standard packages based on the finite element method. The applied modeling and analysis algorithm can be applied to other regular systems, both planar and spatial.

References

1. Kirsanov, M.N. Analysis of the buckling of spatial truss with cross lattice. Magazine of Civil Engineering. 2016. 64. Pp. 52–58. DOI: 10.5862/MCE.64.5
2. Voropay, R.A., Domanov, E.V. The dependence of the deflection of a planar beam truss with a complex lattice on the number of panels in the system Maple. Postulat. 2019. No. 1. P. 12
3. Arutyunyan, V.B. Analytical calculation of the deflection street bracket for advertising. Postulat. 2019. No.1 <http://e-postulat.ru/index.php/Postulat/article/download/2300/2340>
4. Voropay, R.A., Domanov, E.V. Analytical solution of the problem of shifting a movable support of a truss of arch type in the Maple system. Postulat. 2019. No. 1. <http://e-postulat.ru/index.php/Postulat/article/download/2345/2386>

5. Ilyushin, A.S. The formula for calculating the deflection of a compound externally statically indeterminate frame. *Structural mechanics and structures*. 2019. Vol. 3. No. 22. Pp. 29–38.
6. Egorov, S.S. The inductive method of solving the problem of deflection of the symmetric core structures of complex shape in the system Maple for arbitrary number of panels. *Science Almanac*. 2017. 3-3 (29). Pp. 254–257. DOI: 10.17117/na.2017.03.03.254 <http://ucom.ru/doc/na.2017.03.03.254.pdf>
7. Tinkov, D.V. Comparative analysis of analytical solutions to the problem of truss structure deflection. *Magazine of Civil Engineering*. 2015. No. 5. Pp. 66–73. (rus) DOI: 10.5862/MCE.57.6
8. Smirnova, A.A., Rakhmatulina, A.R Analytical calculation of the displacement of the truss support. *Science Almanac*. 2017. No. 2-3(28). Pp. 275–278. https://elibrary.ru/download/elibrary_28913800_87609841.pdf
9. Rakhmatulina, A.R., Smirnova, A.A. The dependence of the deflection of the arched truss loaded on the upper belt, on the number of panels. *Science Almanac*. 2017. No. 2-3(28). Pp. 268–271. https://elibrary.ru/download/elibrary_28913798_61471993.pdf
10. Kirsanov, M.N. Analytical calculation of deflection of rectangular spatial roof structure. *Proceedings of the Moscow State University of Civil Engineering*. 2018. Vol. 13. No. 5(116). Pp. 579–586. DOI: www.dx.doi.org/10.22227/1997-0935.2018.5.579-586]
11. Kirsanov, M.N. The deflection of spatial coatings with periodic structure. *Magazine of Civil Engineering*. 2017. 76. Pp. 58–66. DOI: 10.18720/MCE.76.6
12. Rybakov, L.S. Linear theory of a flat orthogonal grid. *Mekhanika tverdogo tela*. 2001. No. 4. Pp. 106–118. (rus)
13. Galishnikova, V.V., Dunaiski, P., Pahl, P.J. Geometrically Nonlinear Analysis of Plane Trusses and Frames SUN MeDIA, Stellenbosch (Republic of South Africa), 2009. Pp. 382. doi:10.18820/9781920109998.
14. Hutchinson, R.G., Fleck, N.A. Microarchitected cellular solids – the hunt for statically determinate periodic trusses. *ZAMM Z. Angew. Math. Mech.* 2005. Vol. 85. No. 9. Pp. 607–617 DOI: 10.1002/zamm.200410208
15. Kirsanov, M.N. The property of embedding of natural frequencies spectra of regular mechanical systems. *Structural mechanics and structures*. 2019. No. 2(21). Pp. 40–49.
16. Petersen, O.W., Oiseth, O., Lourens, E. Investigation of dynamic wind loads on a long-span suspension bridge identified from measured acceleration data. *Journal of Wind Engineering and Industrial Aerodynamics*. 2020. Vol. 196. Pp. 104045. <https://doi.org/10.1016/j.jweia.2019.104045>
17. Zhou, Q., Ma, B., Zhu, Q., Zhang, H. Investigation on wind loads on angle-steel cross-arms of lattice transmission towers via direct force measurement. *Journal of Wind Engineering and Industrial Aerodynamics*. 2019. Vol. 191. Pp. 117–126. doi: 10.18820/9781920109998.
18. Rybakov, V.A., Gamayunova, O.S. Stress-state elements frame structures from thin-walled rods. *Construction of Unique Buildings and Structures*. 2013. No. 7(12). Pp. 79–123. (rus)
19. Rybakov, V.A., Al Ali, M., Pantelev, A.P., Fedotova, K.A., Smirnov, A.V. Bearing capacity of rafter systems made of steel thin-walled structures in attic roofs. *Magazine of Civil Engineering*. 2017. No. 8. Pp. 28–39. doi: 10.18720/MCE.76.3.
20. Vatin, N.I., Havula, J., Martikainen, L., Sinelnikov, A.S., Orlova, A.V., Salamakhin, S.V. Thin-walled cross-sections and their joints: tests and fem-modelling. *Advanced Materials Research*. 2014. No. 945–949. Pp. 1211–1215. DOI: 10.4028/www.scientific.net/AMR.945-949.1211
21. Tushina, V.M. Semi-rigid steel beam-to-column connections. *Magazine of Civil Engineering*. 2017. 73. Pp. 25–39. doi: 10.18720/MCE.73.3.
22. Tushina, O.A., Danilov, A.I. The stiffness of rigid joints of beam with hollow section column. *Magazine of Civil Engineering*. 2016. 64. Pp. 40–51. doi: 10.5862/MCE.64.4
23. Gusakova, N.V., Filyushina, K.E., Gusakov, A.M., Minaev, N.N. Selection criteria of space planning and structural solutions of low-rise buildings. *Magazine of Civil Engineering*. 2017. 75. Pp. 84–93. doi: 10.18720/MCE.75.8.
24. Travush, V.I., Fedorova, N.V. Survivability of structural systems of buildings with special effects. *Magazine of Civil Engineering*. 2018. 81. Pp. 73–80. doi: 10.18720/MCE.81.8
25. Siriguleng, B., Zhang, W., Liu, T., Liu Y. Z. Vibration modal experiments and modal interactions of a large space deployable antenna with carbon fiber material and ring-truss structure. *Engineering Structures*. 2019. Pp. 109932. <https://doi.org/10.1016/j.engstruct.2019.109932>
26. Cheng, J., Xu, M., Xu, H. Mechanical performance analysis and parametric study of double-deck plate-truss composite steel girders of a three-tower four-span suspension bridge. *Engineering Structures*. 2019. Vol. 199. Pp. 109648. <https://doi.org/10.1016/j.engstruct.2019.109648>
27. Serpik, I.N., Alekseytsev, A.V. Optimization of flat steel frame and foundation posts system. *Magazine of Civil Engineering*. 2016. 61. Pp. 14–24. doi: 10.5862/MCE.61.2
28. Topping, B.H.V. Shape optimization of skeletal structures: a review. *Journal of Structural Engineering*. 1983. Vol. 109. No. 8. Pp. 1933–1951 [https://doi.org/10.1061/\(ASCE\)0733-9445\(1983\)109:8\(1933\)](https://doi.org/10.1061/(ASCE)0733-9445(1983)109:8(1933))
29. Kaveh, A., Laknejadi, K. A hybrid evolutionary graph-based multi-objective algorithm for layout optimization of truss structures. *Acta Mechanica*. 2013. Vol. 224. No. 2. Pp. 343–364. DOI: 10.1007/s00707-012-0754-5
30. Tinkov, D.V., Safonov, A.A. Design Optimization of Truss Bridge Structures of Composite Materials. *Journal of Machinery Manufacture and Reliability*, 2017. Vol. 46. No. 1. Pp. 46–52. DOI: 10.3103/S1052618817010149
31. Pholdee, N., Bureerat, S. Comparative performance of meta-heuristic algorithms for mass minimisation of trusses with dynamic constraints. *Advances in Engineering Software*. 2014. Vol. 75. Pp. 1–13.
32. Lieu, Q.X., Do, D.T.T., Lee, J. An adaptive hybrid evolutionary firefly algorithm for shape and size optimization of truss structures with frequency constraints. *Computers & Structures*. 2018. Vol. 195. Pp. 99–112. <https://doi.org/10.1016/j.compstruc.2017.06.016>
33. Alekseytsev, A.V. Evolutionary optimization of steel trusses with the nodal joints of rods. *Magazine of Civil Engineering*. 2013. 40. Pp. 28–37. DOI: 10.5862/MCE.40.3
34. Alekseytsev, A.V., Akhremenko, S.A. Evolutionary optimization of prestressed steel frames, *Magazine of Civil Engineering*. 2018. 73. Pp. 32–42. DOI: 10.18720/MCE.81.4.
35. Serpik, I.N., Alekseytsev, A.V., Balabin, P.Y. Mixed Approaches to Handle Limitations and Execute Mutation in the Genetic Algorithm for Truss Size, Shape and Topology Optimization. *Periodica Poly-technica Civil Engineering*. No. 61(3). 2017. Pp. 471–482.

Contacts:Mikhail Kirsanov, c216@ya.ru

© Kirsanov, M.N., 2020



DOI: 10.18720/MCE.96.10

Spatial natural vibrations of viscoelastic axisymmetric structures

M.M. Mirsaidov*, **Sh.O. Khudainazarov**

Tashkent Institute of Irrigation and Agricultural Mechanization Engineers, Tashkent, Uzbekistan

* E-mail: theormir@mail.ru

Keywords: axisymmetric structures, high-rise smokestacks, spatial vibrations, eigenfrequency, vibration decrement, dynamic characteristics, viscoelasticity, dissipative properties

Abstract. A mathematical model, methods and algorithm to assess the spatial natural vibrations of axisymmetric structures are given in the paper taking into account the variability of the slope and structure thickness in the framework of the viscoelastic theory of shells. Dissipative properties of the material are taken into account by the Boltzmann-Volterra hereditary theory of viscoelasticity. The spatial natural vibrations of high-rise ventilation pipes of the Armenian nuclear power plant (NPP) and smokestacks of the Novo-Angren, Syrdarya, Azerbaijan and Ekibastuz thermal power plants (TPP) were studied taking into account the elastic and viscoelastic properties of their material. The reliability of results was verified by comparing the results obtained with the exact solution of a number of test problems, as well as by comparing the results with the results of field experiments. It was found that when the viscoelastic properties of structure material are taken into account, the decrement of their vibrations weakly depends on the values of eigenfrequency. Along with this, the dangerous range of earthquake frequencies includes not only the bending frequencies of the structure, but the spatial ones as well.

1. Introduction

As a rule, high-rise smoke and ventilation pipes, cooling towers of thermal and nuclear power plants (TPP and NPP) and protective shells of NPP are considered as axisymmetric structures. They are unique structures in their design features and geometric dimensions. Today, a great number of different axisymmetric high-rise structures are being operated and erected all over the world; one of such structures is a high-rise smoke stack, the height of which reaches up to 150 m–600 m [1, 2].

If for pipes of a height of about 50 m, the ratio of the wall thickness δ to the radius R of its middle surface at the base is $\delta/R=1/5\div 1/7$, then for the pipes of a height of 250–300 m – $\delta/R=1/12\div 1/15$, and for the pipes of a height of 420 m, the ratio δ/R is $\delta/R\approx 1/23$. With increasing height H and radius R , the wall thickness δ of the pipe grows slowly [1, 2]. Besides, along the height of the pipe, its radius, cone thickness and slope change, gradually moving from a conical section to a cylindrical one.

In the existing building norms of many countries, an elastic cone-shaped console with a constant slope is used as a calculation model for such structures; it does not take into account such features as real geometry, structural features and dissipative properties of their material, which have a direct impact on the value of dynamic characteristics of structure.

The reliability of such structures is largely determined by the accuracy of dynamic calculations, which in turn depends on the correct choice of structure design model and exact determination of its dynamic characteristics.

In the dynamics of structures, the study of dynamic characteristics (i.e., eigenfrequencies, modes and decrements of vibration) of structures occupies a special place, since the dynamic characteristics are a passport of the structure and make it possible to judge the dynamic properties of the structure as a whole, without even examining its behavior under various effects.



Determination of eigenfrequencies and vibration modes even for elastic structures is a self-contained and rather difficult task. When accounting for dissipative properties of the material, the determination of structure dynamic characteristics is complicated by an order of magnitude.

The first attempts at a theoretical description of dissipative properties of materials are associated with the names of Voigt, Maxwell, and Kelvin. Further, new models were proposed, and known models were improved to describe dissipative processes occurring in various systems during dynamic processes. However, the results obtained did not always agree well with experimental data.

To eliminate this, other, more adequate models were used that take into account dissipative processes in the material, such as the model with hysteresis absorption or hereditary viscoelastic models of the Boltzmann-Volterra type, although their implementation is rather difficult and experimental materials are scarce [3–10].

Recently, when determining the natural frequencies and vibration modes of various high-rise structures, much attention has been paid to accounting for elastic properties of structure material only.

For instance:

- an experimental determination of dynamic characteristics of high-rise monolithic reinforced concrete buildings was considered in [11] and the results obtained were recommended for certification of buildings;
- the energy method for estimating the cylindrical shells vibration was given in [12], where the effect of uniform external pressure and symmetrical boundary conditions on eigenfrequency of homogeneous and multilayer isotropic cylindrical shells was studied;
- the oscillatory process of rigid composite cylindrical shells taking into account the bending behavior of stiffness ribs and their effect on eigenfrequencies of a shell, a change in its thickness and boundary conditions were studied in [13];
- in [14] the eigenfrequencies of a cylindrical shell were studied at different boundary conditions;
- change in dynamic characteristics of the structure in order to detect damage to reinforced concrete building structures was considered in [15];
- to effectively evaluate the eigenfrequency and attenuation coefficient, a reliable mathematical model was proposed in [16] based on the use of the probability distribution function of eigenfrequency.
- along with this, the stress-strain state, dynamic behavior, and wave phenomenon in various systems were studied in [17–26], taking into account the design features.

These are just some of the studies devoted to the determination of dynamic characteristics of various designs and systems.

The above review of well-known studies shows that the dynamic characteristics of spatial axisymmetric structures, such as ventilation and smokestacks of nuclear and heat power plants, are evaluated differently in different works, and each theory or method used has its advantages and disadvantages.

Therefore, the development of an adequate model, effective methods and algorithm for assessing the dynamic characteristics of high-rise axisymmetric structures, taking into account their design features and dissipative properties of their material, is an urgent task of the mechanics of a deformable rigid body.

The aim of this study is to develop an adequate mathematical model, methods and algorithm for solving the problem of spatial natural vibrations of viscoelastic axisymmetric structures using the theory of shells and studying the dynamic characteristics (i.e., frequency and decrement of vibrations) of real structures, as well as comparing the results with the results of field experiments.

2. Methods

Consider a high axisymmetric structure (Fig. 1), modeled as an axisymmetric viscoelastic shell with a rectilinear axis, with a variable slope and a variable wall thickness, the lower part of the structure ($z=0$) is on a rigid base, and the upper ($z=H$) is free. The spatial natural vibrations of the structure under consideration are investigated (Fig. 1).

To determine the dynamic characteristics of the structures (Fig. 1), it is necessary to study spatial natural vibrations, i.e. the structure motion in which all of its points oscillate according to the same harmonic law - real or complex one - with different amplitudes in the absence of external influences, i.e.

$$\vec{u}(\vec{x}, t) = \vec{u}^*(\vec{x}) e^{-i\omega t} \quad (1)$$

Here $\vec{u}^*(\vec{x}) = \{u_z(\vec{x}), u_\theta(\vec{x}), u_r(\vec{x})\}$ is the displacement vector of the structure point (Fig. 1) in the directions of the coordinate axes $\vec{x} = \{z, \theta, r\}$, respectively.

In the case of conservative systems ω , $\bar{u}^*(\bar{x})$ are the frequency and natural vibration of the structures. In the case of non-conservative systems ω , $\bar{u}^*(\bar{x})$ are the complex quantities, i.e. $\omega = \omega_R - i\omega_I$, the real part ω_R of the complex parameter ω in its physical essence is the frequency of free damped vibrations of the structure, and the imaginary part ω_I accurate to the sign is equal to the damping coefficient of vibrations and determines the dissipative properties of the structure as a whole.

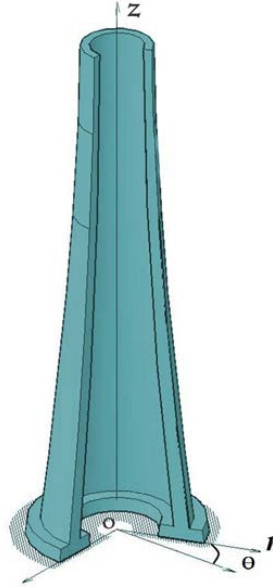


Figure 1. Model of axisymmetric structure.

To simulate the process of structure strain (Fig. 1) under its natural vibrations, the principle of virtual displacements is used according to which the sum of all active forces acting on the structure, including the inertia forces on virtual displacements, is zero, i.e.:

$$-\int_F (\tilde{M}_s \delta\gamma_s + \tilde{M}_\theta \delta\gamma_\theta + \tilde{M}_{s\theta} \delta\gamma_{s\theta} + \tilde{N}_s \delta\varepsilon_s + \tilde{N}_\theta \delta\varepsilon_\theta + \tilde{N}_{s\theta} \delta\varepsilon_{s\theta}) dF - \int_F \rho(\ddot{u}\delta u + \ddot{v}\delta v + \ddot{w}\delta w) dF = 0 \quad (2)$$

In this case, kinematic boundary conditions are used

$$z = 0: \bar{u} = 0; \frac{\partial w}{\partial z} = 0 \quad (3)$$

Here:

$\bar{u}(\bar{x}, t) = \{u(\bar{x}, t), v(\bar{x}, t), w(\bar{x}, t)\}$; $\bar{x} = \{z, \theta, r\}$ are the coordinates of the point in cylindrical coordinates;

u, v, w are displacements in the directions of axes (z, θ, r) of cylindrical coordinates, respectively; $\tilde{M}_s, \tilde{M}_\theta, \tilde{M}_{s\theta}, \tilde{N}_s, \tilde{N}_\theta, \tilde{N}_{s\theta}$ are bending, torsional and membrane forces; $\delta\gamma_s, \delta\gamma_\theta, \delta\gamma_{s\theta}, \delta\varepsilon_s, \delta\varepsilon_\theta, \delta\varepsilon_{s\theta}$ are isochronous variations in the curvature and components of the strain tensor; $\delta u, \delta v, \delta w$ - variations of displacements in longitudinal, circumferential and tangent directions; ρ is the density of the shell material.

The relationship between the components of the forces and strains at an arbitrary point of the structure (Fig. 1) is taken in the form:

$$\begin{aligned} \tilde{N}_s &= \tilde{\lambda}(\varepsilon_s + \nu\varepsilon_\theta); \tilde{M}_s = \tilde{\mu}(\gamma_s + \nu\gamma_\theta) \\ \tilde{N}_\theta &= \tilde{\lambda}(\varepsilon_\theta + \nu\varepsilon_s); \tilde{M}_\theta = \tilde{\mu}(\gamma_\theta + \nu\gamma_s); \\ \tilde{N}_{s\theta} &= \tilde{K}\varepsilon_{s\theta}; \tilde{M}_{s\theta} = \tilde{G}\gamma_{s\theta} \end{aligned} \quad (4)$$

where

$$\tilde{\lambda} = \frac{\tilde{E}h}{1-\nu^2}; \tilde{\mu} = \frac{\tilde{E}h^3}{12(1-\nu^2)}; \tilde{K} = \frac{\tilde{E}h}{2(1+\nu)}; \tilde{G} = \frac{\tilde{E}h^3}{12(1+\nu^2)}$$

To describe the viscoelastic properties of the material, the Boltzmann-Volterra hereditary theory [5–8] is used according to which the long-term elastic modulus is expressed by the integral operator

$$\tilde{E}[\varphi] = E \left[\varphi(t) - \int_0^t \Gamma(t-\tau)\varphi(\tau)d\tau \right] \quad (5)$$

E is the instant modulus of elasticity of the material;

$\Gamma(t-\tau)$ is the kernel of relaxation.

If the function $\varphi(t)$ has the form

$$\varphi(t) = \psi(t)e^{-i\omega_R t} \quad (6)$$

where ψ is a slowly changing function of time, i is an imaginary unit, ω_R is a real constant.

Assuming that the integral terms in (5) are small compared to $\varphi(t)$, and using the freezing method [5, 6, 8], the integral relation (5) can be reduced to the complex one, i.e.:

$$\tilde{E}[\varphi] \approx E \left[1 - \Gamma^c(\omega_R) - i\Gamma^s(\omega_R) \right] \psi, \quad (7)$$

where

$$\begin{aligned} \Gamma^c(\omega_R) &= \int_0^{\infty} \Gamma(\tau) \cos \omega_R \tau d\tau, \\ \Gamma^s(\omega_R) &= \int_0^{\infty} \Gamma(\tau) \sin \omega_R \tau d\tau, \end{aligned} \quad (8)$$

Γ^S , Γ^C are the sines and cosines of the image of Fourier kernel $\Gamma(\tau)$.

The relationship between the components of the strain tensor and the displacement vector is described by Cauchy relations

$$\begin{aligned} \varepsilon_s &= \frac{\partial u}{\partial s} \\ \varepsilon_\theta &= \frac{1}{r} \frac{\partial v}{\partial \theta} + \frac{1}{r} (w \cos \varphi + u \sin \varphi) \\ \varepsilon_{s\theta} &= \frac{1}{r} \frac{\partial u}{\partial \theta} + \frac{\partial v}{\partial s} - \frac{1}{r} v \sin \varphi \\ \gamma_s &= -\frac{\partial^2 w}{\partial s^2} \\ \gamma_\theta &= -\frac{1}{r^2} \frac{\partial^2 w}{\partial \theta^2} + \frac{\partial v}{\partial \theta} \frac{\cos \varphi}{r^2} - \frac{\partial w}{\partial s} \frac{\sin \varphi}{r} \\ \gamma_{s\theta} &= 2 \left(-\frac{1}{r} \frac{\partial^2 w}{\partial s \partial \theta} + \frac{\sin \varphi}{r^2} \frac{\partial w}{\partial \theta} + \frac{\cos \varphi}{r} \frac{\partial v}{\partial s} - \frac{\sin \varphi \cos \varphi}{r^2} v \right) \end{aligned} \quad (9)$$

Here s is the coordinate measured along the neutral line of the shell; φ is the angle between the tangent to the generatrix and the axis z of the shell; r is the variable radius of the middle surface of the shell.

Substituting (1) into (2), (3), (4), (9), taking into account (7), reduces the problem under consideration to a complex variational eigenvalue problem of the form

$$\begin{aligned}
& - \int_F (\bar{M}_s \delta \gamma_s + \bar{M}_\theta \delta \gamma_\theta + \bar{M}_{s\theta} \delta \gamma_{s\theta} + \bar{N}_s \delta \varepsilon_s + \bar{N}_\theta \delta \varepsilon_\theta + \bar{N}_{s\theta} \delta \varepsilon_{s\theta}) dF + \\
& + \rho \omega^2 \int_F (u^* \delta u^* + v^* \delta v^* + w^* \delta w^*) dF = 0
\end{aligned} \tag{10}$$

$$z = 0: \bar{u}^* = 0; \delta \left(\frac{dw^*}{ds} \right) = 0$$

Now, the problem under consideration of finding the eigenfrequencies and natural modes of viscoelastic shell vibrations (Fig. 1) has been reduced to finding the constant ω^2 - ($\omega = \omega_R - i\omega_I$) and vector function $\bar{u}^*(\bar{x}) - (\bar{u}^*(\bar{x}) = \bar{u}_R^*(\bar{x}) - i\bar{u}_I^*(\bar{x}))$, satisfying equation (10) for any kinematic virtual displacement $\delta \bar{u}^*$.

When solving the variational problem (10) on the spatial natural vibrations of a viscoelastic axisymmetric shell (Fig. 1), the solution along one coordinate is taken in the form of an exact trigonometric (in the circumferential direction at the angle θ) dependence

$$\begin{aligned}
u^*(s, \theta) &= \bar{u}(s) \cos n\theta \\
v^*(s, \theta) &= \bar{v}(s) \sin n\theta \\
w^*(s, \theta) &= \bar{w}(s) \cos n\theta
\end{aligned} \tag{11}$$

$n = 0, 1, 2, \dots$ is number of harmonics, the finite element discretization is used along coordinate s with finite elements in the form of a truncated cone with 8 degrees of freedom.

The finite element method (FEM) procedure described in [27] allows us to reduce the variational problem (10) to a complex algebraic eigenvalue problem for a structure (Fig. 1):

$$([\bar{K}] - \omega^2 [M]) \{\bar{z}\} = 0, \tag{12}$$

where $[\bar{K}]$ is the complex stiffness matrix, the value of which depends on the sought for parameter ω_R ; $[M]$ is the matrix of the structure mass; $\omega = \omega_R - i\omega_I$ is the complex eigenfrequency; $\{\bar{z}\} = \{z_R\} - i\{z_I\}$ is the complex eigenvector corresponding to the eigenfrequency ω of the structure.

Usually, the order of the equations to be solved (12) exceeds 1500. Therefore, the eigenvalues $\lambda = \omega^2$ of algebraic equation (12) are found using the Muller method [28], because there is no other, more efficient method for calculating complex eigenvalues, and the eigenvector $\{\bar{z}\}$ is determined by the Gauss method using specially developed algorithms and a calculation program for IBM. The entire calculation process outlined in this section is automated and runs on an IBM PC. An author's certificate of the Intellectual Property Agency under the Ministry of Justice of the Republic of Uzbekistan was obtained for the developed software.

3. Results and Discussion

3.1. Study of the method and algorithm convergence when solving model problems

In this section, consider the convergence and the solutions accuracy obtained on model problems of natural vibrations for cylindrical shells, taking into account the elastic and viscoelastic properties of the material. The obtained solutions are compared with the known exact solutions.

Task 1.

The axisymmetric own vibrations of an elastic cylindrical shell are considered here. The boundary conditions are: both ends of the shell are hinged, i.e.:

$$u|_{z=0} = 0; w|_{z=0} = 0; w''|_{z=0} = 0$$

$$u|_{z=L} = 0; w|_{z=L} = 0; w''|_{z=L} = 0 \tag{13}$$

In the calculation, the following initial data were used:

$$r_1/r_2=0.98; L/r_2=6.0.$$

The shell material is hypothetical, its elastic modulus is E , the density is ρ , and the Poisson's ratio is ν : $E/\rho=1.0$; $\nu=0.3$.

where r_1, r_2 are the inner and outer radii of the cylinder; L is the shell length.

When solving the problem under consideration (at $n=0$ in expression (11)) we obtain axisymmetric eigenfrequencies of the shell. The task is to determine the axisymmetric frequencies of elastic cylindrical shells.

Table 1 shows a comparison of axisymmetric eigenfrequencies of an elastic cylindrical shell obtained by exact solution and using the finite element method.

An analysis of the comparison shows a satisfactory agreement between the numerical results and the exact solution.

Task 2.

The axisymmetric natural vibrations of a viscoelastic cylindrical shell with a hinged support at the ends are considered, i.e. the conditions are similar to (13). Geometrical and mechanical parameters of a shell, are similar to the ones in Task 1.

The Boltzmann–Volterra hereditary theory with the Rzhantsyn–Koltunov relaxation kernel in the form of [6–8] was used to describe the viscoelastic properties of the shell material:

$$\Gamma(t) = Ae^{-\beta t} t^{\alpha-1} \quad (14)$$

with parameters $A=0.008$; $\beta=0.05$; $\alpha=0.1$.

The results obtained are presented in Table 1, which shows the complex eigenfrequencies of a viscoelastic cylindrical shell obtained by exact solution and using the finite element method.

Table 1. Natural frequencies of an elastic and viscoelastic cylindrical shell.

No. of eigen frequency	Eigenfrequencies			
	Elastic shell		Viscoelastic shell	
	Exact solution	Solutions obtained using the developed algorithm	Exact solution	Solutions obtained using the developed algorithm
ω_1	0.5152	0.5153	$0.5132-i3.090 \cdot 10^{-4}$	$0.5144-i3.096 \cdot 10^{-4}$
ω_2	0.8959	0.8962	$0.8925-i5.223 \cdot 10^{-4}$	$0.8944-i5.344 \cdot 10^{-4}$
ω_3	0.9732	0.9734	$0.9695-i5.643 \cdot 10^{-4}$	$0.9716-i5.653 \cdot 10^{-4}$
ω_4	0.9877	0.9880	$0.9840-i5.724 \cdot 10^{-4}$	$0.9859-i5.731 \cdot 10^{-4}$
ω_5	0.9930	0.9937	$0.9896-i5.754 \cdot 10^{-4}$	$0.9899-i5.769 \cdot 10^{-4}$

Analysis of the solutions of test problems (tasks 1, 2) allows us to draw the following conclusions:

The obtained eigenfrequencies and their comparison with the exact ones show satisfactory accuracy of the numerical results for elastic and viscoelastic shells.

Summarizing the results obtained, it can be stated that the studies of the convergence of numerical solutions, and their comparison with the exact ones, show the reliability and validity of the developed methods and compiled software for PC-IBM when solving problems of natural vibrations of elastic and viscoelastic shell-like structures.

3.2. Study of spatial natural vibrations of high stacks taking into account elastic properties of the material

In this section, consider the spatial natural vibrations (frequencies and modes) of high-rise smoke stacks of the Novo-Angren, Syrdarya, Azerbaijan and Ekibastuz TPPs and the ventilation pipe of the Armenian NPP according to the theory of shells in elastic statement using the developed methods and PC-IBM calculation programs.

In calculations, a high-rise smokestack is modeled by an elastic axisymmetric shell of variable thickness with separate variable slopes of both internal and external surfaces that describe the real geometry of the structures.

All geometric dimensions of the considered structures are taken from design documentation. Some of geometric dimensions of these structures are as follows (H is height, R is outer diameter and h is pipe wall thickness, z is pipe mark from the base of the structure):

Smokestack of the Novo-Angren TPP, $H = 325.0$ m; at the mark: $z = 0.0$ m: $R = 19.0$ m, $h = 1.10$ m; at the mark: $z = 325.0$ m: $R = 8.35$ m, $h = 0.40$ m.

Smokestack of Syrdarya TPP, $H = 325.0$ m; at the mark: $z = 0.0$ m: $R = 21.0$ m, $h = 0.85$ m; at the mark: $z = 325.0$ m: $R = 6.00$ m, $h = 0.22$ m.

Smokestack of the Azerbaijan TPP, $H = 330.0$ m; at the mark: $z = 0.0$ m: $R = 19.0$ m, $h = 1.00$ m; at the mark: $z = 330.0$ m: $R = 7.52$ m, $h = 0.60$ m.

Smokestack of Ekibastuz TPP, $H = 420.0$ m; at the mark: $z = 0.0$ m: $R = 22.0$ m, $h = 1.20$ m; at the mark: $z = 420.0$ m, $R = 7.10$ m, $h = 0.30$ m.

Ventilation pipe of the Armenian NPP, $H = 150.0$ m; at the mark: $z = 0.0$ m: $R = 8.45$ m, $h = 0.90$ m; at the mark: $z = 150.0$ m, $R = 2.35$ m, $h = 0.16$ m.

The parameters of the physico-mechanical characteristics of the material under consideration are taken as:

$$E = 2.9 \times 10^4 \text{ MPa}; \nu = 0.17; \rho = 2.5 \text{ t/m}^3; \Gamma(t) = 0.0.$$

For all the aforementioned high-rise smokestacks, non-axisymmetric natural vibrations corresponding to different numbers (n) of harmonics were studied. At harmonic number $n = 0$, the spatial form splits into axisymmetric and torsional vibration modes.

For axisymmetric vibrations of a shell in one-dimensional problem, there is a one-dimensional equivalent – longitudinal vibrations of a beam, and for torsional vibrations of the shell a one-dimensional equivalent is torsional vibration of a beam. At $n = 1$, for non-axisymmetric vibrations of the shell, there also exists a one-dimensional equivalent – bending vibrations of a beam. At ($n = 2, 3, \dots$) non-axisymmetric vibrations of one-dimensional equivalents do not exist.

For all stacks listed above, at each harmonic ($n = 0, 1, 2, 3, \dots$), at least 5 eigenfrequencies were obtained and the corresponding vibration modes were constructed.

Table 2 shows the spatial (at $n = 0, 1, 2, 3, \dots$) eigenfrequencies for some high-rise stacks obtained using the developed methods and software.

Table 2. Frequency of spatial natural modes of vibration (rad/sec) of structures (high-rise stacks) obtained in elastic statement.

No. of harmonics	Novo-Angren TPP			Ekibastuz TPP			Syrdarya TPP		
	ω_1	ω_2	ω_3	ω_1	ω_2	ω_3	ω_1	ω_2	ω_3
$n=0$ torsion.	20.10	34.92	55.70	17.76	29.05	45.36	24.42	39.92	60.43
$n=0$ axisym.	24.66	49.78	81.84	20.51	40.04	65.48	27.43	53.56	87.16
$n=1$	1.89	6.30	14.29	1.27	4.09	9.20	2.96	7.59	16.38
$n=2$	13.02	15.75	19.29	11.92	14.69	16.59	11.23	15.85	19.65
$n=3$	36.89	38.31	40.11	26.99	35.86	39.31	32.30	35.05	44.31
$n=4$	68.51	70.67	73.48	54.54	60.32	69.02	56.79	64.01	73.19
$n=5$	107.35	109.18	116.12	76.07	90.20	97.38	86.63	98.79	105.06

(tr – torsional, as – axisymmetric frequencies)

In the studies conducted at the Institute of Earth Physics of the Academy of Sciences of the Russian Federation [29] it was found that the predominate periods of soil vibrations during strong earthquakes are within the range of 0.1–0.5 sec.

When analyzing the values of obtained eigenfrequencies of the structures under consideration, there is a probability that they would coincide with the ground motion frequency during the earthquake; this can lead

to a dangerous phenomenon – resonant vibrations of a pipe. This indicates that in assessing the seismic resistance of such structures, one cannot limit oneself by only a few bending eigenmodes of vibration (at $n=1$).

3.3. Study of spatial own vibrations of high-rise stacks taking into account viscoelastic properties of the material

In this section, spatial natural vibrations (frequencies, modes and decrements of vibrations) of the above structures in viscoelastic statement (i.e. considering viscoelastic properties of the structure material) are studied using the developed methods and PC-IBM computation. The structures under consideration are modeled by a viscoelastic axisymmetric shell with a variable slope and thickness, which makes it possible to take into account their real geometry.

To describe the viscoelastic properties of the material, the Boltzmann-Volterra hereditary theory with the Rzhanytsyn-Koltunov kernel is used (14).

The choice of viscoelastic models to describe the properties of structure material (concrete) is explained by the closeness of experimental and theoretical results obtained for the stress state of concrete [30]. The parameters of the relaxation kernel are found on the basis of the technique [8], the essence of which lays in the comparison of experimental creep curve and the theoretical curve. In this work, the theoretical strain values for various time instants are tabulated in detail and the curves are plotted for a wide range of kernel parameters A, β, α .

To determine the values of the kernel parameters for concrete, several experimental creep curves for concrete, presented in [30], were processed. By superimposing the obtained experimental curve on the assemblage (set) of theoretical curves [8] and shifting it to the abscissa and ordinate axes, we find the one theoretical curve that coincides with experimental one. The values corresponding to this theoretical curve are taken as the sought for values of the kernel parameters.

In the problem to be solved below, the parameters of the relaxation kernel (14) for concrete were used, obtained with the above method from experimental creep curves given in [30]:

$$A=0.0194; \beta=0.00000014; \alpha=0.075.$$

All geometric dimensions of the above structures are taken from design documentation. Some dimensions of these structures are given in section 3.2 of this paper.

Table 3 shows the complex eigenfrequencies of spatial vibrations obtained for the above listed structures using the developed methods and software taking into account viscoelastic properties of the structure material.

Table 3. The frequency of spatial natural vibrations (rad/sec) of structures (high-rise stacks) obtained in viscoelastic statement.

No. of harmonic s	Novo-Angren TPP			Ekibastuz TPP			Syrdarya TPP		
	$\omega_1 = \omega_{1R}$	$\omega_2 = \omega_{2R}$	$\omega_3 = \omega_{3R}$	$\omega_1 = \omega_{1R}$	$\omega_2 = \omega_{2R}$	$\omega_3 = \omega_{3R}$	$\omega_1 = \omega_{1R}$	$\omega_2 = \omega_{2R}$	$\omega_3 = \omega_{3R}$
	$-i\omega_{1I}$	$-i\omega_{2I}$	$-i\omega_{3I}$	$-i\omega_{1I}$	$-i\omega_{2I}$	$-i\omega_{3I}$	$-i\omega_{1I}$	$-i\omega_{2I}$	$-i\omega_{3I}$
$n=0$ torsion.	22.14-	44.46-	74.22-	18.38-	36.09-	59.27-	24.64-	48.40-	79.09-
	-i0.32	-i0.60	-i0.95	-i0.27	-i0.49	-i0.77	-i0.35	-i0.64	-i1.01
$n=0$ axisym.	18.01-	31.44-	50.36-	15.89-	26.12-	40.94-	21.02-	35.99-	54.67-
	-i0.26	-i0.43	-i0.67	-i0.24	-i0.37	-i0.55	-i0.31	-i0.49	-i0.72
$n=1$	1.66-	5.58-	12.76-	1.10-	3.61-	8.18-	2.19-	6.74-	14.65-
	-i0.03	-i0.09	-i0.19	-i0.02	-i0.06	-i0.13	-i0.04	-i0.11	-i0.22
$n=2$	12.55-	14.04-	17.54-	10.62-	13.12-	14.84-	10.01-	14.17-	17.60-
	-i0.19	-i0.21	-i0.26	-i0.16	-i0.19	-i0.22	-i0.15	-i0.21	-i0.26
$n=3$	33.22-	34.53-	36.16-	24.25-	32.29-	36.31-	29.07-	31.57-	39.98-
	-i0.46	-i0.47	-i0.49	-i0.34	-i0.45	-i0.49	-i0.41	-i0.44	-i0.54
$n=4$	64.29-	64.31-	66.58-	49.38-	54.55-	62.48-	51.34-	57.94-	66.32-
	-i0.84	-i0.83	-i0.86	-i0.66	-i0.72	-i0.81	-i0.68	-i0.76	-i0.86
$n=5$	98.43-	100.31-	105.50-	68.94-	81.86-	93.69-	79.85-	91.43-	97.88-
	-i1.23	-i1.25	-i1.31	-i0.89	-i1.04	-i1.18	-i1.02	-i1.15	-i1.22

The real parts (ω_R) of eigenfrequencies ($\omega = \omega_R - i\omega_I$) given in Table 3 are the frequencies of structure natural vibrations and the imaginary parts (ω_I) carry information about the damping coefficients of structure vibrations.

Comparison of the results presented in Table 2 (elastic statement) and Table 3 (viscoelastic statement), shows that the real part of the complex frequencies is less than the corresponding values of the eigenfrequencies obtained in elastic statement, and the logarithmic decrement $\delta = -2\pi \frac{\omega_I}{\omega_R}$ slightly decreases with increasing frequency number. This means that an account for viscoelastic properties of the structure material leads to a weak dependence of the logarithmic decrement of vibrations on frequency.

Table 4 shows the comparison between the periods of bending vibrations obtained by one-dimensional theory (in elastic statement) and by the theory of shells (in elastic and viscoelastic statements) and the results of field experiments [17, 31].

Table 4. Periods of bending vibrations of various smokestacks.

High-rise smoke stacks	No. of period	Vibrations periods (sec)			
		Elastic statement		Viscoelastic statement	Field experiment
		One-dimensional theory	Theory of shells (at $n=1$)	Theory of shells (at $n=1$)	
Novo-Angren TPP	T_1	3.26	3.32	3.8	3.4
	T_2	0.91	0.99	1.12	1.0
	T_3	0.38	0.44	0.49	0.5
	T_4	0.21	0.25	0.28	0.3
Syrdarya TPP	T_1	2.5	2.12	2.88	2.8
	T_2	0.80	0.83	0.93	0.9
	T_3	0.33	0.38	0.42	0.4
	T_4	0.19	0.23	0.25	0.2
Armenian NPP	T_1	1.56	1.42	2.03	1.6
	T_2	0.46	0.46	0.52	0.5
	T_3	0.21	0.22	0.24	0.2
	T_4	0.11	0.12	0.14	-

An analysis of the above results shows that the values of bending vibrations periods obtained in field experiments [17, 31] and the ones found theoretically by the developed method are quite close.

Table 5 shows the values of logarithmic decrement of vibrations of the Novo-Angren TPP high smokestack obtained by field experiment [17] and the ones found theoretically for the three lower bending modes (at $n=1$), using the developed methods and software that take into account viscoelastic properties of the structure material.

Table 5. Logarithmic decrement of bending vibrations of the Novo-Angren TPP smokestack.

Decrement definition method	Logarithmic decrement		
	δ_1	δ_2	δ_3
Experimental	0.15	0.25	0.37
Theoretical	0.121	0.102	0.094

Significant differences in the values of experimentally and theoretically determined logarithmic decrement (Table 5), especially for the second and third modes, are apparently explained by a failure to consider dry friction and energy entrainment from the structure to infinity.

4. Conclusions

1. A mathematical model, methods and algorithm to study the spatial natural vibrations of axisymmetric structures, with account for dissipative properties of the material are developed based on the hereditary theory of viscoelasticity in the framework of the theory of shells.

2. The reliability of the developed methods and algorithms was verified by solving a number of test problems and comparing the results obtained by known exact solutions and the results of field experiments.

3. The spatial natural vibrations of a number of real axisymmetric structures (ventilation and smokestacks of nuclear power plants and thermal power plants) were studied taking into account the elastic and viscoelastic properties of the structure material of the structure.

4. It was revealed that not only the frequencies of bending modes of vibration are in the dangerous range of earthquakes frequencies, but also some other modes of spatial vibrations of structures, determined by the theory of shells.

5. It was found that the value of the logarithmic decrement of structure vibrations when accounting for viscoelastic properties of the structure material weakly depends on eigenfrequencies of vibrations.

References

- Duzhikh, F.P., Osolovsky, V.P., Ladygichev, M.G. *Promyshlennyye dymovye i ventilyacionnye truby: Spravochnoye izdanie* [Industrial smoke and ventilation pipes: Reference publication]. M.: Teplotekhnika, 2004. 464 p. (rus)
- Dinamicheskiy raschet spetsialnykh inzhenernykh sooruzheniy i konstruksiy. *Spravochnik proektirovshika* [Dynamic calculation of special engineering structures and buildings. Designer reference]. M.: Stroyizdat, 1986. 462 p. (rus)
- Bolotin, V.V. *Random vibrations of elastic systems*. Moscow Energetics Institute Moscow, USSR Translated from the Russian edition by I. Shenkman English translation edited by H.H.E. Leipholtz University of Waterloo, Waterloo, Ontario, Canada, 1984. 463 p. doi: 10.1007/978-94-017-2842-3
- Guz, A.N. *Fundamentals of the Three-Dimensional Theory of Stability of Deformable Bodies*. translated by Maria Kashtalian. Structural stability. 1999. 1. Title. II. Series. 553 p. doi 10.1007/978-3-540-69633-9
- Mirsaidov, M.M., Sultanov, T.Z. *Theory and Methods of Strength Assessment of Earth Dams*. Lambert Akademik Publishing. Saarbrücken/ Deutschland/ Germany/. 2015. 341 p.
- Mirsaidov, M.M., Sultanov, T.Z. Use of linear heredity theory of viscoelasticity for dynamic analysis of earthen structures. *Soil Mechanics and Foundation Engineering*. 2013. 49 (6), Rr. 250-256. doi: 10.1007/s11204-013-9198-8
- Rzhanitsyn, A.R. *Teoriya polzuchesti* [Creep theory]. M.: Stroyizdat, 1968. 416 p. (rus)
- Koltunov, M.A. *Polzuchest i relaksatsiya* [Creep and relaxation]. M.: Higher school, 1976. 267 p. (rus)
- Betten, J. *Creep Mechanics*. Engineering. Springer-Verlag Berlin Heidelberg. 2008. 361p. doi: <https://doi.org/10.1007/978-3-540-85051-9>
- Naumenko, K., Altenbach, H. *Modeling of Creep for Structural Analysis*. Engineering. Martin-Luther-Universität Halle- Wittenberg Halle Germany. 2007. 215 p. <https://doi.org/10.1007/978-3-540-70839-1>
- Sergeevtsev, E.Yu., Zubkov, D.A., Rummyantsev, A.A. *Izuchenie dinamicheskikh karakteristik vysotnogo zdaniya* [Studying the dynamic characteristics of a high-rise building]. Bulletin of MGSU. 2011. No. 4. Pp.266-272. (rus)
- Isvandzibaev, M.R., Jamaluddin, H., Hamzah, R.I.R. Natural frequency characteristics of thin-walled homogeneous and manifold layered cylindrical shells under pressure using energy method. *J. Cent. South Univ.* 2014. Vol. 21. No. 2. Pp. 521–532. <https://doi.org/10.1007/s11771-014-1970-z>
- Hemmatnezhad, M., Rahimi, G.H., Ansari, R. On the free vibrations of grid-stiffened composite cylindrical shells. *Acta Mechanica*. 2014. Vol. 225. No. 2. Pp. 609–623. <https://doi.org/10.1007/s00707-013-0976-1>
- Iqbal, Z., Naeem, M.N., Sultana, N. Vibration characteristics of FGM circular cylindrical shells using wave propagation approach. *Acta Mechanica*. 2009. Pp. 208-237. <https://doi.org/10.1007/s00707-009-0141-z>
- Consuegra, F., Irfanoglu, A. Variation of Small Amplitude Vibration Dynamic Properties with Displacement in Reinforced Concrete Structures. *Experimental Mechanics*. 2012. Vol. 52. No. 7. Pp. 817–828. <https://doi.org/10.1007/s11340-011-9590-0>
- Hwang, J.-S., Noh, J.-T., Lee, S.-H., Kareem, A. Experimental Verification of Modal Identification of a High-rise Building Using Independent Component Analysis. *International Journal of Concrete Structures and Materials*. 2019. 13:4. <https://doi.org/10.1186/s40069-018-0319-7>
- Mirsaidov, M., Khamraev, P., Shalimov, A. *Eksperimentalnoye i teoreticheskoye opredelenie dinamicheskikh karakteristik dimovykh trub* [Experimental and theoretical determination of dynamic characteristics of smoke stacks]. Construction and Architecture. 1985. series 14, No. 4. M.: 1985. Pp. 17–20. (rus)
- Mirsaidov, M.M., Safarov, I.I., Teshayev, M.Kh. Dynamics of Structurally Inhomogeneous Lamellar and Shell Mechanical Systems. Part 1. *Applied Mathematics and Physics (JAMP)*. 2019. Vol. 7. No. 10. Pp. 2283–2302. doi: 10.4236/jamp.2019.710155
- Bakhodirov, A.A., Sultanov, K.S. Wavees in a Viscoelastic Bar Surrounded by Soils under Smooth Loading. *Mechanics of Solids*. 2014. Vol. 49. No. 3. Pp. 349–359. <https://doi.org/10.3103/S002565441403011X>
- Sultanov, K.S., Loginov, P., Ismoilova, S., Salikhova, Z. Wave processes in determining mechanical characteristics of soils. *E3S Web of Conferences*. 2019. Vol. 97. P. 04009. doi: 10.1051/e3sconf/20199704009
- Khudayarov, B.A., Komilova, K., Turaev, F.Z. Numerical Modeling of pipes conveying gas-liquid two- phase flow. *E3S Web of Conferences*. 2019. Vol. 97. Pp. 05022. doi: 10.1051/e3sconf/20199705022
- Khudayarov, B.A., Turaev, F.Z. Mathematical simulation of nonlinear oscillations of viscoelastic pipelines conveying fluid. *Applied Mathematical Modelling*. 2019. Vol. 66. Pp. 662–679. doi: 10.1016/j.apm.2018.10.008
- Usarov, M.K. Buckling of orthotropic plates with bimoments. St. Petersburg. *Magazine of Civil Engineering*. 2015. No. 1(53). Pp. 80–90. doi: 10.5862/MCE.53.8
- Toshmatov, E.S., Usarov, M., Usarov, D.M. Dynamic methods of spatial calculation of structures based on a plate model // *E3S Web of Conferences*. 2019. Vol. 97. P. 04065. doi: 10.1051/e3sconf/20199704072
- Ishmatov, A.N., Mirsaidov, M. Nonlinear vibrations of an axisymmetric body acted upon by pulse loads. *Soviet Applied Mechanics*. 1991. 27(4). Pp. 388–394. doi: 10.1007/BF00896519
- Mirsaidov, M., Troyanovskii, I.E. Forced axisymmetric oscillations of a viscoelastic cylindrical shell. *Polymer Mechanics*. 1975. Vol. 11. No. 6. Pp. 953–955. doi: 10.1007/BF00857626
- Bate, K.-J., Wilson, E.L. *Numerical methods in finite element analysis*. Publisher: New Jersey (etc.), Prentice-Hall. 1976. 448 p.

28. Muller, D.E. A Method for Solving Algebraic Equations Using an Automatic Computer. *Mathematical Tabl.* 1956. Pp. 208-215.
29. Polyakov, S.V. *Posledstviya silnyx zemletryaseniy* [The consequences of strong earthquakes]. M.: Stroyizdat, 1978. 311 p. (rus)
30. *Polzuchest i usadka betona jelezobetonnyx konstruksiy* [Creep and shrinkage of concrete reinforced concrete structures]. Ed. by S. V. Alexandrovsky. M.: Stroyizdat, 1976. 351 p. (rus)
31. Artishchev, V.P., Poghosyan, O.K. *Eksperimentalno - teoreticheskoye opredelenie dinamicheskikh xarakteristik ventilyatsionnoy trubi visotoy 150 m* [Experimental - theoretical definition of dynamic characteristics of 150 m high ventilation pipe]. Ref. information. *Earthquake-resistant construction. Ser. 14.* M.: 1977. Pp. 33–36. (rus)

Contacts:

Mirziyod Mirsaidov, theormir@mail.ru

Sherzod Khudainazarov, scherzodshox77@mail.ru

© Mirsaidov, M.M., Khudainazarov, Sh.O., 2020



DOI: 10.18720/MCE.96.11

Actual thermophysical characteristics of autoclaved aerated concrete

N. Vatin^{a*}, S.V. Korniyenko^b, A.S. Gorshkov^c, I.I. Pestryakov^a, V. Olshevskiy^a

^a Peter the Great St. Petersburg Polytechnic University, St. Petersburg, Russia

^b Volgograd State Technical University, Volgograd, Russia

^c Saint Petersburg State University of Industrial Technologies and Design, St. Petersburg, Russia

* E-mail: vatin@mail.ru

Keywords: thermal conductivity, moisture, humidity, energy conservation, energy efficiency, housing, insulation, walls, autoclaved aerated concrete blocks, construction

Abstract. The characteristics of autoclaved aerated concrete blocks was tested and analyzed in comparing with Standards' requirements. The results of the study show that the actual thermophysical characteristics of autoclaved aerated concrete blocks, cut from product samples of the three largest manufacturers, in most cases do not coincide with the values declared by the manufacturers and presented in the standards prepared with their direct participation. The mismatch between the calculated and actual values of the thermal conductivity of materials and products used in the installation of external walling, leads to an increase in transmission heat losses through the external walls and the waste of thermal energy for heating and ventilation of buildings. In this regard, a radical review of the values declared by manufacturers, as well as the standards on the basis of which the products are manufactured, and their correct presentation in the current regulatory documents are required.

1. Introduction

Autoclaved cellular concrete products are widely used in construction [1–3]. Basically, such products in the form of autoclaved aerated concrete blocks are used in external and internal walls mortar [1, 4–7], to a lesser extent - as part of rib precast and cast-in-situ floors [8].

AAS is about four times lower, and thermal resistance is 11 times higher [9, 10]. AAC is most effective in warm and hot climates [5, 11–13]. AAC-compliant construction in hot and dry climates reduces residential energy consumption by 7 % [9]. The article [5] evaluates the energy efficiency of three types of exterior walls (prefabricated wooden frame walls, AAC and brick walls) in Southeast Europe. The results of the analysis show that the wall structure with AAC has the best environmental characteristics, while the brick wall has the best thermal characteristics in intermittent heating mode among the studied types of walls.

Unsteady heat transfer in wall structures with AAC is also considered in [14–17]. High energy-saving effect is also observed in the construction of multi-apartment buildings from AAC in three climatic zones of Greece [13]. The low cost of blocks reduces the estimated payback period of investments for reducing energy resources [18–20]. The article [1] summarizes design solutions for load-bearing and non-bearing stone walls, as well as describes construction methods aimed at increasing the efficiency and productivity of building construction, including using wall structures made of AAC.

In the manufacture of blocks used industrial waste [21–25]. This allows you to get the material with the necessary heat and humidity characteristics [21], reduce thermal conductivity [4, 22], increase thermal storage properties [26], improve the capillary-porous structure of the material [23], get high energy saving effect and reduce CO₂ emissions [24], increase moisture-proofing properties of structures [24]. Disposal in the production of AAC can significantly reduce the volume of solid waste landfill [28].

The main objective of the study [29] was to classify the properties of AAC in terms of physical (microstructure, density), chemical, mechanical (compressive and tensile strength, elastic modulus, shrinkage during drying) and operational (thermal insulation, moisture transfer, durability, fire resistance and sound

Vatin, N., Korniyenko, S.V., Gorshkov, A.S., Pestryakov, I.I., Olshevskiy, V. Actual thermophysical characteristics of autoclaved aerated concrete. Magazine of Civil Engineering. 2020. 96(4). Pp. 129–137. DOI:10.18720/MCE.96.11



This work is licensed under a CC BY-NC 4.0

insulation) characteristics. The articles [29, 30] present the results of theoretical studies that have shown the advantages of using AAC in wall enclosures.

However, as shown in the works [6, 7] on the example of the Central Russian Upland cold climate, the use of single-layer external walls with AAC and two-layer wall structures in the form of AAC with brick lining carries thermal risks due to the significant influence on the thermal protection of buildings of the edge zones. Such structures without additional thermal insulation have virtually no reserve for thermal protection and energy saving. To reduce the heat engineering risks in the design of buildings, it is necessary, first of all, to improve the constructive solution of the marginal zones. Another measure to increase the level of thermal protection of buildings is the use of additional thermal insulation along the entire plane of the wall.

The mismatch between the actual and declared by the manufacturer thermophysical characteristics of building materials is one of the main reasons for the deterioration of thermal comfort in the premises and the decrease in energy efficiency of operated buildings [31]. In publications does not assess the conformity of actual and declared AAC characteristics with the literature, which makes it difficult to find effective structural solutions for external walls using AAC. From this point of view, the task is certainly relevant.

This article deals with the strength and thermophysical test results made on the basis of the masonry samples of cellular autoclave curing concrete (aerated concrete blocks) with the use of polyurethane adhesive or concrete adhesives [32, 33].

In this work calculation of vapor permeability of walls from gas-concrete blocks is made [34]. The purpose of this study is to verify the thermophysical characteristics of AAC, declared by different manufacturers, as well as contained in the standards of different countries, which have a significant difference [35].

2. Materials and Methods

Tests were conducted at the St. Petersburg Polytechnic University (Russia).

As part of the study, products were selected from three different manufacturers, conventionally marked with numbers 1, 2 and 3. The lower the serial number, the greater the volume of production produced by this manufacturer:

- manufacturer 1: grade for density D 400 (declared by the manufacturer);
- manufacturer 2: grade D 500 (density declared by the manufacturer);
- manufacturer 3: D 500 grade (declared by the manufacturer).

The choice of manufacturers is due to the fact that they are the largest and are located on the territory of St. Petersburg and the Leningrad Region (Russia), and also most actively sell their products in St. Petersburg to private consumers through DIY networks.



Figure 1. Measurement of thermal conductivity of samples.



Figure 2. The excitatory method for determining the sorption moisture of samples.



Figure 3. Testing a masonry fragment in the climate chamber.



Figure 4. Determination of vapor permeability of samples.

As part of the study, the following types of tests were performed (Figures 1–4):

- determination of average density in accordance with Russian State Standard GOST 12730.1;
- determination of thermal conductivity in accordance with Russian State Standard GOST 7076;
- determination of sorption moisture in accordance with Russian State Standard GOST 24816;
- determination of vapor permeability in accordance with Russian State Standard GOST 25898;
- testing of a masonry fragment in a climate chamber according to Russian State Standard GOST 26254.

Total was made:

- 18 samples with a size of 100×100×100 mm – 6 from each manufacturer to determine the average density of the material in a dry state;
- 15 samples of size 250×250×50 mm — 5 samples from each manufacturer to determine the thermal conductivity of the material in a dry state;
- 21 samples of arbitrary shape – 7 from each manufacturer to determine the sorption moisture of the material;
- 15 samples with a diameter of 100 mm and a thickness of 30 mm – 5 samples from each manufacturer to determine the vapor permeability of the material.

To determine the thermal conductivity and humidity of the model structure in a climate chamber, a masonry fragment of AAC blocks was made on 150 mm thick adhesive. A masonry fragment is made of blocks declared by the manufacturer of the brand in average density D500 (manufacturer 2). Design tests were conducted for 66 hours. In the cold compartment of the climate chamber, the air temperature was minus 30 ± 1 °C automatically, in the warm compartment – air temperature $+ 20 \pm 1$ °C, relative humidity 50 ± 5 %. After the end of the experiment, a study was conducted of the distribution of moisture over the thickness of the test masonry fragment. For this purpose, 6 cellular concrete samples 25 mm in diameter were sequentially drilled from the central part of the fragment. The sampling step was also 25 mm.

3. Results and Discussion

3.1. AAC density test results

An analysis of the results of AAC medium density tests shows that products from only one manufacturer (manufacturer 2) correspond to the declared density brand. Products manufactured by manufacturer 1 in terms of average density (426 kg/m^3) correspond to the upper permissible density limit for products of the declared brand in density (D 400), which should not exceed 428 kg/m^3 (with a variation coefficient of 2 %). In this case, three of the six tested samples exceed the upper permissible limit. If the coefficient of variation in density of the batch produced exceeds 2 %, then the tested samples will not correspond to the declared brand in density D400. Products manufactured by manufacturer 3 with an average density of 536 kg/m^3 do not even correspond to the upper permissible limit for the average density, which, with a coefficient of variation of 2 %, should not exceed 535 kg/m^3 . In fact, the products from which the samples were taken and tested correspond to the D600 density brand with the manufacturer's D500 density brand declared.

The test results show a significant variation in the density of the tested samples, which may indicate a sufficiently high value of the coefficient of variation in density for the batch of products from which the tested samples were taken. Only for products of one manufacturer, there is a slight variation in the deviation of the results of individual tests from the average density value.

3.2. AAC dry conductivity test results

AAC dry heat conductivity test results are presented in Table 1.

Table 1. The actual thermal conductivity of AAC in the dry state (at a temperature of 25 °C).

Sample	Thermal conductivity [W / (m·K)]		
	Manufacturer 1 (D400)	Manufacturer 2 (D500)	Manufacturer 3 (D500)
1	0.108	0.124	0.148
2	0.108	0.127	0.151
3	0.110	0.129	0.145
4	0.110	0.126	0.152
5	0.107	0.127	0.153
Average value	0.109	0.127	0.150

Table 2 shows the actual thermal conductivity for AAC in the dry state with a density of about 500 kg/m³ according to foreign studies [2, 4, 9, 21, 24]. Figure 5 shows a comparison of the obtained AAC dry heat conductivity test results with foreign studies presented in Table 2. The test results are shown in Figure 5 with dashed lines for AAC manufacturers 2 and 3 (grade D500). Figure 5 shows that the obtained test results and data from foreign studies have good consistency, which indicates the reliability of the obtained experimental values of thermal conductivity.

Table 2. Actual thermal conductivity AAC (D500).

No	Author	Thermal conductivity [W/(m·K)]
1	[9]	0.140
2	[21]	0.120
3	[4]	0.124
4	[24]	0.160
5	[2]	0.130
6	Our results	0.127–0.150

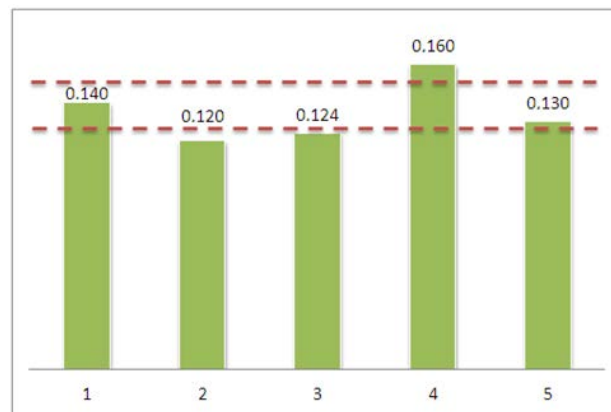


Figure 5. Comparison of the obtained results with the data of other researchers.

A comparison of the dry thermal conductivity values of dry AAC declared in Russian and international standards and the actual thermal conductivity of AAC of various grades by density is presented in Figure 6.

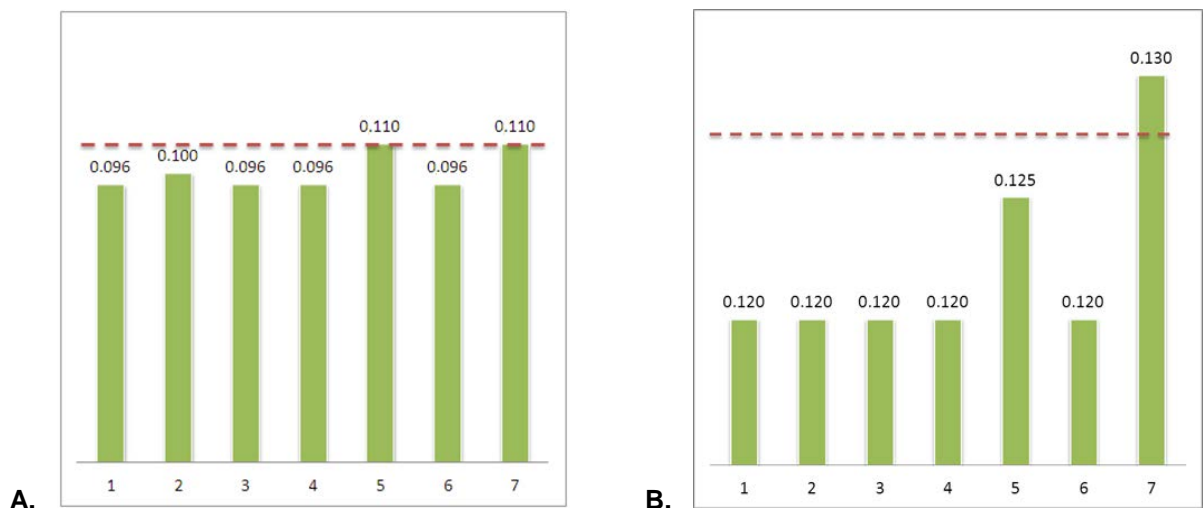


Figure 6. Thermal conductivity AAC in the dry state.

Dashed line shows measurements' results.

A – density grade D400 (manufacturer 1).

B – density grade D500 (manufacturers 2 and 3).

The bars on the bar charts show the standard requirements in accordance to:

1 – Russian State Standard GOST 31359;

2 – Russian State Standard GOST 25485;

3 – Standard 2.9.136 of National Association of Constructors (Russia);

4 – Standard 3.1 of National Association of Autoclaved Aerated Concrete Manufacturers (Russia);

5 – Russian State Building Code SP 50.13330;

6 – EN 1745 ($\lambda_{50/50}$);

7 – EN 1745 ($\lambda_{90/90}$).

The analysis of the results shows that the measurement results for the blocks of the brand in terms of average density D500 do not correspond to the thermal conductivity values specified in most Russian standards. The values of $\lambda_{90/90}$, established in the international standard EN 1745, as well as the data of the Russian standard SP 50.13330, correspond to the measurement results for brand products with an average density of D400 (manufacturer 1). The $\lambda_{90/90}$ values according to EN 1745 correspond to the actual data for the brand products in terms of average density D500 (manufacturer 2). The actual values of thermal conductivity of manufacturer's samples 3 (not shown in Figure 6) correspond to the values of $\lambda_{90/90}$ established in the EN1745 standard for brand products with an average density of D600.

A significant difference between the actual thermal conductivity values of AAC products from the requirements of the standards is one of the main reasons for the deterioration of thermal comfort in rooms and the decrease in energy efficiency of operated buildings.

3.3. AAC thermal conductivity test results at different humidity

The results of tests of thermal conductivity of AAC grade average density D 500 at a humidity close to 2 and 5% are presented in Table 3.

Table 3. Thermal conductivity of wet products from AAC brand D 500.

Sample	First test cycle		Second test cycle	
	Humidity,% by mass	Thermal conductivity, W / (m·K)	Humidity,% by mass	Thermal conductivity, W / (m·K)
1	2.1	0.137	5.2	0.176
2	2.0	0.140	4.8	0.187
3	2.0	0.143	4.7	0.190
4	1.8	0.135	5.0	0.186
5	2.2	0.145	5.0	0.182
Average value	2.02	0.14	4.94	0.184

Figure 7 shows a generalized dependence of AAC thermal conductivity on humidity, averaged over all tested samples.

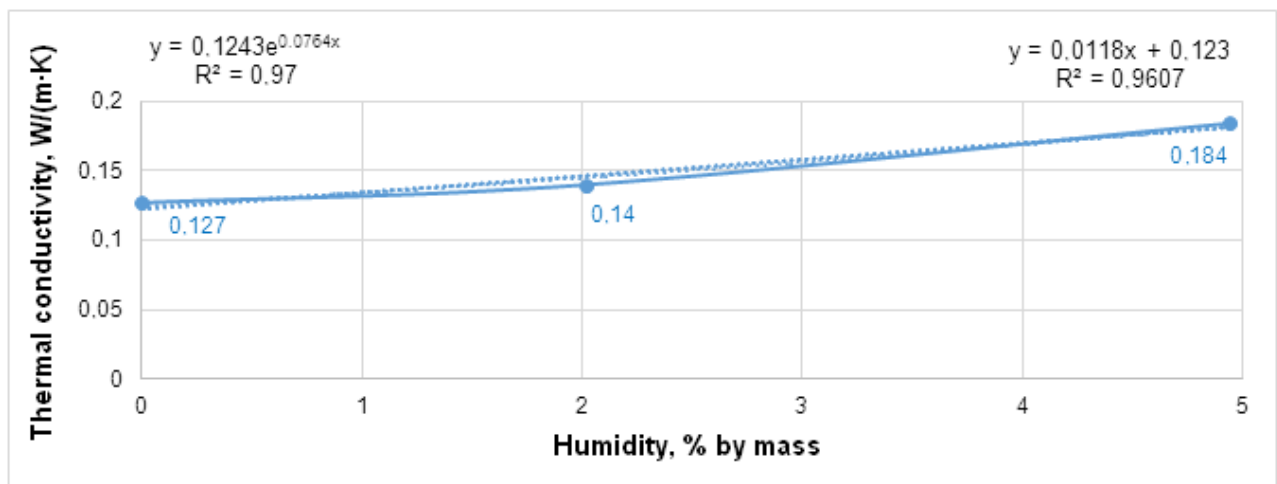


Figure 7. AAC thermal conductivity vs. humidity.

From the data presented in Fig. 7, it follows that the maximum determination coefficient (R^2) corresponds to the exponential dependence of the thermal conductivity of AAC on humidity. To compare the results, Fig. 7 also shows the linear dependence $\lambda(w)$. In the international standard ISO 10456, the dependence of the thermal conductivity of building materials on humidity is also represented by an exponential function of the form:

$$\lambda_w = \lambda_o \exp[f_w(w_2 - w_1)], \quad (1)$$

where λ_o is the measured value of thermal conductivity in the dry state, W/(m·K); f_w is the coefficient establishing for the exponential dependence the proportionality between the thermal conductivity and humidity of the building material; w_2 is the moisture content of the material,%, for conditions 2 (for a given humidity

other than 0 %); w_1 is the moisture content of the material, %, for conditions 1 (initial conditions), for example, at a moisture content of zero.

For five tested samples from one manufacturer, the experimental dependence of AAC thermal conductivity on humidity can be described by an equation of the form (see Figure 7):

$$\lambda_w = 0.1243 \exp[0.0764(w_2 - w_1)]. \quad (2)$$

An analysis of the results shows that the discrepancy between the obtained experimental data and the declared values of thermal conductivity AAC at different humidity according to the Russian State Standard GOST 31359 is due to the discrepancy between the initial values of the thermal conductivity of the material in the dry state (0.1243 W/(m·K) in according to the test results of the control batch of samples, 0.12 W/(m·K) in according to GOST 31359), and the mismatch of the coefficients f_w (0.0764 % and 0.0405 %, respectively).

3.4. AAC sorption moisture test results

AAC sorption moisture test results are presented in Table 4.

Table 4. Sorption humidity AAC.

Manufacturer	Density grade declared by the manufacturer	Equilibrium sorption humidity, % by mass,	
		with relative air humidity at 80%	with relative air humidity at 97%
1	D400	3.3	9.3
2	D500	4.0	15.9
3	D500	2.9	9.6

From a comparison of the measurement results presented in table 4, with standard values from regulatory documents follows:

1. The AAC actual sorption humidity of all three manufacturers at a relative humidity of 80 % does not exceed 4 % specified in Russian State Standard GOST 31359, Standard 2.9.136 of National Association of Constructors (Russia), Standard 3.1 of National Association of Autoclaved Aerated Concrete Manufacturers (Russia) when establishing the equilibrium moisture content of aerated concrete by weight for operating conditions A.

2. The actual sorption humidity AAC of all three manufacturers at a relative humidity of 97 % significantly exceeds 5 % specified in Russian State Standard GOST 31359, Standard 2.9.136 of National Association of Constructors (Russia), Standard 3.1 of National Association of Autoclaved Aerated Concrete Manufacturers (Russia) when establishing the equilibrium moisture content of aerated concrete by weight for operating conditions B.

3. For products of one of the manufacturers (manufacturer 2), the AAC actual sorption humidity at a relative humidity of 97 % reaches 16 %. This can be explained by the fact that the equilibrium sorption moisture of aerated concrete depends not only on the density of the products, but also on the composition of the initial raw materials.

3.5. AAC vapor permeability test results

AAC vapor permeability test results are presented in Table 5.

Table 5. Vapor permeability AAC (average values).

Manufacturer	Density grade declared by the manufacturer	Permeance [kg·Pa ⁻¹ ·s ⁻¹ ·m ⁻¹]
1	D400	6.39·10 ⁻¹¹
2	D500	4.72·10 ⁻¹¹
3	D500	5.00·10 ⁻¹¹

Comparison of the data presented in Table 5 with Standards' values shows the following:

1. Actual vapor permeability of AAC of manufacturer 1 (6.39·10⁻¹¹ kg·Pa⁻¹·s⁻¹·m⁻¹) coincides with the value provided by Russian State Standard GOST 31359 for the average density D400 declared by the manufacturer of the brand.

2. The actual values of vapor permeability AAC manufacturer 2 ($4.72 \cdot 10^{-11} \text{ kg} \cdot \text{Pa}^{-1} \cdot \text{s}^{-1} \cdot \text{m}^{-1}$) and manufacturer 3 ($0.65 \text{ ng} \cdot \text{Pa}^{-1} \cdot \text{s}^{-1} \cdot \text{m}^{-2}$) do not match the value presented in Russian State Standard GOST 31359 for the declared brand manufacturer for the average density of D500 ($5.00 \cdot 10^{-11} \text{ kg} \cdot \text{Pa}^{-1} \cdot \text{s}^{-1} \cdot \text{m}^{-1}$).

The observed difference between the actual and declared vapor permeability values of cellular concrete suggests that the properties of cellular concrete depend not only on their density, but also on the quality of the feedstock.

3.6. AAC Masonry Test Results

The test results of the AAC fragment of masonry from in a climate chamber are presented in Figures 8 and 9.

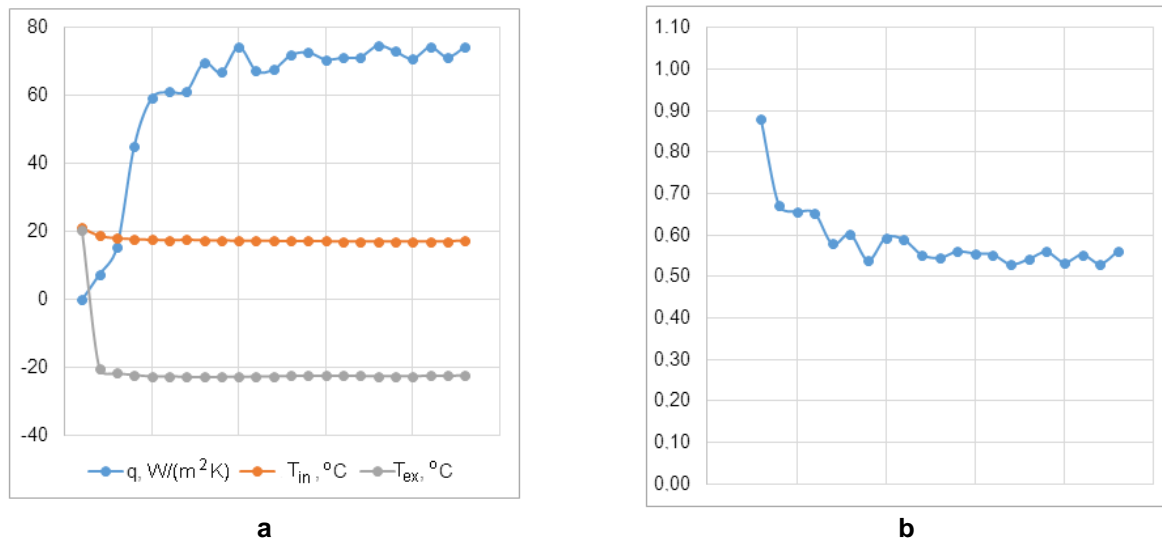


Figure 8. The results of measurements of parameters in the climatic chamber (a) and calculation of thermal resistance, $\text{m}^2 \cdot \text{K/W}$, of the studied fragment (b).

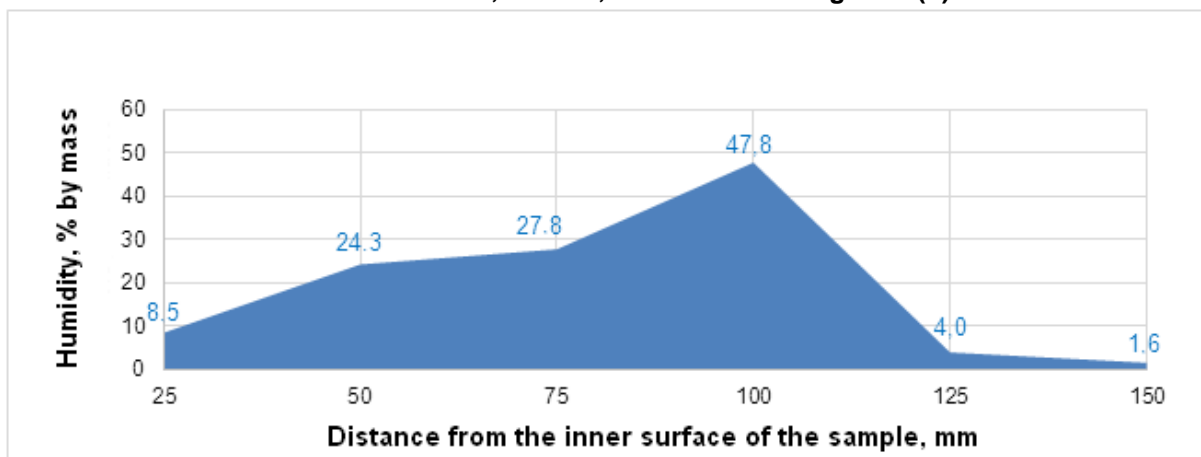


Figure 9. Moisture distribution over the thickness of the AAC wall structure.

Despite the fact that the moisture distribution over the thickness of the tested masonry fragment, shown in Figure 9, is obtained for a conditional (model) masonry with a thickness of 150 mm, this distribution is indicative from the point of view of a qualitative display of the main features of the humidity regime of real wall fencing. It can be seen from the graph (see Figure 9) that the plane of maximum wetting of the masonry is at a distance of 2/3 of its thickness when counting from the inner surface of the test fragment, i.e. correlates with the data specified in clause 9.1 of Russian State Building Code SNiP 23-02-2003 for a homogeneous (single-layer) wall.

In the plane of maximum humidification at low temperatures, moisture freezes and creates a low-permeability barrier for water vapor, which leads to further accumulation of moisture in front of it. Behind this barrier, due to the low resistance to vapor permeation of a section of the structure located between the condensation plane and the outer surface, the masonry is dried.

The initial AAC humidity measured before testing is 5.7 %. The average AAC humidity in the composition of the test masonry fragment after the experiment was 19 %.

The thermal conductivity of the masonry under these conditions can be calculated. As the calculated value of thermal resistance, we take the value of $0.54 \text{ m}^2 \text{ K/W}$, obtained as a result of laboratory tests of a fragment of a wall enclosure in a climate chamber (see Figure 8). Then, with the thickness of the test fragment equal to 150 mm, the thermal conductivity without taking into account the influence of mortar joints of the masonry will be $0.278 \text{ W}/(\text{m}\cdot\text{K})$. It is seen that an increase in operational humidity and freezing of moisture in the pores of the material leads to a significant increase in the thermal conductivity of the masonry.

4. Conclusion

The literature does not assess the conformity of the actual and declared characteristics of autoclaved aerated concrete blocks (AAC), which makes it difficult to find effective structural solutions for exterior walls using AAC.

1. The results of the study show that the actual thermophysical characteristics of autoclaved aerated concrete blocks (AAC), cut from product samples of the three largest manufacturers, in most cases do not coincide with the values declared by the manufacturers and presented in the standards prepared with their direct participation.

2. The mismatch between the calculated and actual values of the thermal conductivity of materials and products used in the installation of external walling, leads to an increase in transmission heat losses through the external walls and the waste of thermal energy for heating and ventilation of buildings. In this regard, a radical review of the values declared by manufacturers, as well as the standards on the basis of which the products are manufactured, and their correct presentation in the current regulatory documents are required.

References

- Hendry, E.A.W. Masonry walls: Materials and construction. *Construction and Building Materials*. 2001. 15(8). Pp. 323–330. DOI:10.1016/S0950-0618(01)00019-8.
- Narayanan, N., Ramamurthy, K. Structure and properties of aerated concrete: A review. *Cement and Concrete Composites*. 2000. 22(5). Pp. 321–329. DOI:10.1016/S0958-9465(00)00016-0.
- Campanale, M., Moro, L. Autoclaved aerated concrete: experimental evaluation of its thermal properties at high temperatures. *High Temperatures -- High Pressures*. 2015. 44(5). Pp. 369–382. URL: <https://web.b.ebscohost.com/abstract?direct=true&profile=ehost&scope=site&authtype=crawler&jml=00181544&AN=110456869&h=gNgCCCFY5h8uKRCy%2FOQ%2BtvO85dG5jQfnx8L37uW9%2B1zw1JxzpXbhdLZSXJYBsyIwWUNyQGIEhvZwMeR%2BI63w%3D%3D&url-f&resultNs=AdminWebAuth&result> (date of application: 12.02.2020).
- Tasdemir, C., Sengul, O., Tasdemir, M.A. A comparative study on the thermal conductivities and mechanical properties of lightweight concretes. *Energy and Buildings*. 2017. 151. Pp. 469–475. DOI:10.1016/j.enbuild.2017.07.013.
- Maoduš, N., Agarski, B., Kočetov Mišulić, T., Budak, I., Radeka, M. Life cycle and energy performance assessment of three wall types in south-eastern Europe region. *Energy and Buildings*. 2016. 133. Pp. 605–614. DOI:10.1016/j.enbuild.2016.10.014.
- Korniyenko, S.V., Vatin, N.I., Gorshkov, A.S. Thermophysical field testing of residential buildings made of autoclaved aerated concrete blocks. *Magazine of Civil Engineering*. 2016. 64(4). Pp. 10–25. DOI:10.5862/MCE.64.2.
- Korniyenko, S. Complex analysis of energy efficiency in operated high-rise residential building: Case study. *E3S Web of Conferences*. 2018. 33. DOI:10.1051/e3sconf/20183302005.
- Parashchenko, N.A., Gorshkov, A.S., Vatin, N.I. Partially rib precast and cast-in-situ floors with cellular-concrete blocks. *Magazine of Civil Engineering*. 2011. 24(6). Pp. 50–55. DOI:10.5862/MCE.24.7. URL: [https://engstroy.spbstu.ru/userfiles/files/2011/6\(24\)/parashenko_perekrytiya.pdf](https://engstroy.spbstu.ru/userfiles/files/2011/6(24)/parashenko_perekrytiya.pdf) (date of application: 12.02.2020).
- Radhi, H. Viability of autoclaved aerated concrete walls for the residential sector in the United Arab Emirates. *Energy and Buildings*. 2011. 43(9). Pp. 2086–2092. DOI:10.1016/j.enbuild.2011.04.018.
- Ulykbanov, A., Sharafutdinov, E., Ramazanova, E., Shon, C.-S. Thermal conductivity of aerated concrete based on response surface method. *Materials Science Forum*. 2018. 917 MSF. Pp. 342–346. DOI:10.4028/www.scientific.net/MSF.917.342.
- Al-Jabri, K.S., Hago, A.W., Al-Nuaimi, A.S., Al-Saidy, A.H. Concrete blocks for thermal insulation in hot climate. *Cement and Concrete Research*. 2005. 35(8). Pp. 1472–1479. DOI:10.1016/j.cemconres.2004.08.018.
- Al-Mudhaf, H.A., Attiogbe, E.K. Performance of autoclaved aerated-concrete masonry walls in Kuwait. *Materials and Structures/Materiaux et Constructions*. 1996. 29(191). Pp. 448–452.
- Balaras, C.A., Droutsas, K., Argiriou, A.A., Asimakopoulos, D.N. Potential for energy conservation in apartment buildings. *Energy and Buildings*. 2000. 31(2). Pp. 143–154. DOI:10.1016/S0378-7788(99)00028-6.
- Gorshkov, A., Vatin, N., Nemova, D., Tarasova, D. Definition of the overturning and holding moments for floor-by-floor leaning walls made from aerated concrete blocks. *Applied Mechanics and Materials*. 2014. 633–634. Pp. 897–903. DOI:10.4028/www.scientific.net/AMM.633-634.897.
- Vatin, N., Gorshkov, A., Rymkevich, P., Nemova, D., Tarasova, D. Nonstationary thermal conduction through the building envelope. *Applied Mechanics and Materials*. 2014. 670–671. Pp. 365–369. DOI:10.4028/www.scientific.net/AMM.670-671.365.
- Gorshkov, A.S., Rymkevich, P.P., Vatin, N.I. Simulation of non-stationary heat transfer processes in autoclaved aerated concrete-walls. *Magazine of Civil Engineering*. 2014. 52(8). DOI:10.5862/MCE.52.5.
- Gorshkov, A.S., Rymkevich, P.P. A diagram method of describing the process of non-stationary heat transfer. *Magazine of Civil Engineering*. 2015. 60(8). Pp. 68–82. DOI:10.5862/MCE.60.8.
- Gorshkov, A.S., Vatin, N.I., Rymkevich, P.P., Kydrevich, O.O. Payback period of investments in energy saving. *Magazine of Civil Engineering*. 2018. 78(2). Pp. 65–75. DOI:10.18720/MCE.78.5.
- Gorshkov, A., Murgul, V., Oliynyk, O. Forecasted Payback Period in the Case of Energy-Efficient Activities. *MATEC Web of Conferences*. 2016. 53. DOI:10.1051/mateconf/20165301045.

20. Gorshkov, A., Vatin, N., Nemova, D., Shabaldin, A., Melnikova, L., Kirill, P. Using life-cycle analysis to assess energy savings delivered by building insulation. *Procedia Engineering*. 2015. 117(1). Pp. 1080–1089. DOI:10.1016/j.proeng.2015.08.240.
21. Drochytka, R., Zach, J., Korjenic, A., Hroudová, J. Improving the energy efficiency in buildings while reducing the waste using autoclaved aerated concrete made from power industry waste. *Energy and Buildings*. 2013. 58. Pp. 319–323. DOI:10.1016/j.enbuild.2012.10.029.
22. Kurama, H., Topçu, I.B., Karakurt, C. Properties of the autoclaved aerated concrete produced from coal bottom ash. *Journal of Materials Processing Technology*. 2009. 209(2). Pp. 767–773. DOI:10.1016/j.jmatprotec.2008.02.044.
23. Koronhalyova, O. Moisture storage capacity and microstructure of ceramic brick and autoclaved aerated concrete. *Construction and Building Materials*. 2011. 25(2). Pp. 879–885. DOI:10.1016/j.conbuildmat.2010.06.098.
24. Haik, R., Peled, A., Meir, I.A. The thermal performance of lime hemp concrete (LHC) with alternative binders. *Energy and Buildings*. 2020. 210. DOI:10.1016/j.enbuild.2019.109740.
25. Qu, X., Zhao, X. Previous and present investigations on the components, microstructure and main properties of autoclaved aerated concrete – A review. *Construction and Building Materials*. 2017. 135. Pp. 505–516. DOI:10.1016/j.conbuildmat.2016.12.208.
26. Roberz, F., Loonen, R.C.G.M., Hoes, P., Hensen, J.L.M. Ultra-lightweight concrete: Energy and comfort performance evaluation in relation to buildings with low and high thermal mass. *Energy and Buildings*. 2017. 138. Pp. 432–442. DOI:10.1016/j.enbuild.2016.12.049.
27. Shea, A., Lawrence, M., Walker, P. Hygrothermal performance of an experimental hemp-lime building. *Construction and Building Materials*. 2012. 36. Pp. 270–275. DOI:10.1016/j.conbuildmat.2012.04.123.
28. Thongtha, A., Maneewan, S., Punlek, C., Ungkoon, Y. Investigation of the compressive strength, time lags and decrement factors of AAC-lightweight concrete containing sugar sediment waste. *Energy and Buildings*. 2014. 84. Pp. 516–525. DOI:10.1016/j.enbuild.2014.08.026.
29. Jun, F., Yue, Y., JiaBin, Y. Water permeation simulation of autoclaved aerated concrete blocks using the Lattice Boltzmann method. *Magazine of Civil Engineering*. 2019. 89(5). Pp. 106–114. DOI:10.18720/MCE.89.9.
30. Jin, H.-Q., Yao, X.-L., Fan, L.-W., Xu, X., Yu, Z.-T. Experimental determination and fractal modeling of the effective thermal conductivity of autoclaved aerated concrete: Effects of moisture content. *International Journal of Heat and Mass Transfer*. 2016. 92. Pp. 589–602. DOI:10.1016/j.ijheatmasstransfer.2015.08.103.
31. Gorshkov A.S., Pestryakov I.I., Korniyenko S.V., Vatin N.I., Olshevskiy V.Ya. Actual thermal insulation properties of cellular autoclave curing concretes. *Construction of Unique Buildings and Structures*. 2018. 68(5). Pp. 75–104. DOI:10.18720/CUBS.68.7. URL: www.unistroy.spbstur (date of application: 12.02.2020).
32. Grinfeldi, G.I., Gorshkov, A.S., Vatin, N.I. Tests results strength and thermophysical properties of aerated concrete block wall samples with the use of polyurethane adhesive. *Advanced Materials Research*. 2014. 941–944. Pp. 786–799. DOI:10.4028/www.scientific.net/AMR.941-944.786.
33. Gorshkov, A.S., Vatin, N.I. Properties of the wall structures made of autoclaved cellular concrete products on the polyurethane foam adhesive. *Magazine of Civil Engineering*. 2013. 40(5). Pp. 5–19. DOI:10.5862/MCE.40.1.
34. Vatin, N., Gorshkov, A., Nemova, D., Gamayunova, O., Tarasova, D. Humidity conditions of homogeneous wall from gas-concrete blocks with finishing plaster compounds. *Applied Mechanics and Materials*. 2014. 670–671. Pp. 349–354. DOI:10.4028/www.scientific.net/AMM.670-671.349.
35. Gorshkov, A.S., Sokolov, N.A. Inconsistency in Russian and international standards in the determination of the design values of thermal conductivity of building materials and products. *Magazine of Civil Engineering*. 2013. 42(7). DOI:10.5862/MCE.42.2.

Contacts:

Nikolai Vatin, vatin@mail.ru

Sergey Korniyenko, svkorn2009@yandex.ru

Alexander Gorshkov, alsgor@yandex.ru

Igor Pestryakov, iscvisota@mail.ru

Vyacheslav Olshevskiy, 79119199526@yandex.ru

© Vatin, N., Korniyenko, S.V., Gorshkov, A.S., Pestryakov, I.I., Olshevskiy, V., 2020



DOI: 10.18720/MCE.96.12

The effect of simulated ambient conditions on durability of concrete

A.M.O. Wedatalla, Y.J. Yanmin*

Northeast Forestry University, Harbin, China

* E-mail: jiayanmin@nefu.edu.cn

Keywords: high-strength concrete, concrete permeability, fly ash, silica fume, concrete durability

Abstract. This study aimed to assess the impact of ambient conditions on the internal microstructure of high-strength concrete (HSC) samples. A scanning electron microscope (SEM) was used with X-ray microanalysis to study the relationship between ambient conditions and the durability of concrete. The concrete specimens were cast at a temperature of 25 ± 1 °C and cured under three different conditions: standard curing, steam curing, and dry curing at 50 °C. Conventional Portland cement, crushed aggregate, and natural sand were used in the production of all specimens. Three water binder ratios were typically used: 0.3, 0.35, and 0.4. Three different mixes were also used, containing different binders: 450, 520, and 480 kg/m³. In this study, 30 % fly ash was used in all mixes, while silica fume partly replaced this in a ratio of 0 %, 5 %, and 10 % by weight of cement in the concrete mixes, respectively. Additionally, the effect of ambient conditions was estimated by computing the compressive strength, flexural strength, microhardness, permeability, and the microstructure of concrete. The relationship between these concrete properties was obtained. SEM and energy-dispersive X-ray spectroscopy (EDX) were used to confirm the results for samples cured under all conditions. HSC was obtained that exhibited desirable properties when additional cement materials such as silica and fly ash were used to form homogeneous concrete with a smooth surface; the concrete had low permeability and high durability. It was concluded that it was possible to produce concrete with low permeability and durability within a harsh environment.

1. Introduction

Durability [1] is one of the most important properties required of materials used in the civil and construction industries. Concrete's ability to withstand weathering, chemical attack, abrasion, or any other deterioration process that it is exposed to during its lifetime is termed concrete durability. The proportions of materials and the mixtures used should be tailored to maintain the concrete's integrity and protect the steel reinforcement from metal corrosion [2].

Because concrete is the most commonly used construction material because of its cost-effective durability, there is a high demand for improvements to the sustainability of concrete technology through partially replacement of Portland cement with other supplementary cementing materials (SCM). The durability of concrete can be significantly reduced when it is exposed to harsh conditions because of the potential electrochemical corrosion of the steel reinforcement and the potential physical degradation of the concrete itself. The durability of concrete can be improved considerably by incorporating SCM. Owing to pozzolanic activity and the fill effect, the use of SCM can produce a high-performance concrete that possesses improved mechanical properties and reduced permeability, improving its durability [3–7].

The hydration of Portland cement is enhanced by the chemical reactions (e.g. pozzolanic activity) of the additional cementitious materials within the SCM. Increasing industrial support of the Portland SCM market has significantly reduced CO₂ emissions during concrete production and its continued support can lead to the production of more sustainable concrete and environmentally sound materials [8].

Although, the pozzolanic reactions of SCM generally have the same base (i.e., reactions with calcium hydroxide), the structure of the hydration products, the speed of the pozzolanic reactions, and the length of the development time required to improve the characteristics of the hardened cement paste vary significantly with SCMs [9–14].



The contribution of the SCM and reduction of the w/c ratio leads to the production of high-performance concrete (HPC) containing a more homogeneous microstructure than conventional concrete. The addition of SCM (individually or in combination) enhances the strength and durability of concrete due to the reduction in porosity of the cement paste and at the interface transition zone [15].

Merida et al. [4] suggested that the use of natural volcanic pozzolan, replacing 5 % by weight of the cement in an HPC mix, positively influenced the durability of samples cured in a sulfate medium. The pozzolan modified the microstructure of the concrete and reduced its porosity. Over time, the pozzolanic effect increased, reducing the porosity exhibited by the concrete due to natural mixing in the formation of CSH with bonding properties comparable to those formed in the mineral cement.

Bentz et al. [16] concluded that the pozzolanic reaction could significantly reduce the amount of cement required in concrete production and could provide the concrete with resistance to harsh environments.

Janina Setina et al. [17] reported that nano silica and wood ashes were potential additives that could improve concrete properties. Owing to their chemical composition, they participated in pozzolanic reactions and enhanced concrete durability. Atis et al. [18] reported that if the concrete contained additional cementitious materials (e.g. fly ash, granular blast furnace slag, or active silica debris) and was exposed to hot and dry conditions immediately after molding, the healing become even more essential. Ramezaniapour et al. [19] reported that exposure to a dry environment at room temperature after casting caused the strength of concrete to drop by approximately 38 % for concrete containing 25 % ground-granulated blast-furnace slag (GGBFS), and by approximately 50 % for concrete containing 25 % fly ash, 50 % GGBFS, or a high volume of fly ash. They concluded that concrete containing SCMs is more significantly affected by curing in dry conditions and demonstrates a significant reduction in strength compared with the strength of wet cured concrete. Although considerable research has been conducted on concrete and its durability, the properties of concrete and their improvement for use under harsh environmental conditions must be studied further. Because construction sites are mostly in non-ideal climates including concrete casting and treatment, this paper highlights the effects of these conditions on concrete casting and provides some guidelines for improving the quality of the cast concrete as well as a basis for further research. This study aims to assess the impact of ambient conditions on the internal microstructure of high-strength concrete. A scanning electron microscope (SEM) was used with X-ray microanalysis to study the relationship between ambient conditions and the durability of concrete. In this study, we chose to use different mixtures to study the effect of the ambient conditions on the durability of concrete containing fly ash and active silica.

2. Methods

2.1. Mix features and Materials

As is well known, concrete durability is the dominant factor affecting the integrity of concrete structures over time. Therefore, when concrete mixes or concrete elements are used in severe environments, the concrete should be rich in cementitious materials. These factors, in addition to the decrease in the water-to-binder (w/b) ratio, should be taken into account in order to produce concrete with low permeability, which is the dominant factor determining durability. To ensure that the tests could detect the effect of a larger number of factors on the strength of the concrete, orthogonal test analysis was adopted. In addition, orthogonal test analysis was used in order to reduce the cost of test materials. In this study, we used orthogonal experimental design and analysis to determine the concrete mixes which were then used in the tests to study the effect of ambient conditions on concrete durability.

We used nine mixes with three different w/b ratios (0.30, 0.35, and 0.40), three different binders (450, 480, and 520 kg) with three different percentages of fly ash (30 %, 50 %, and 70 %), and three different percentages of silica fume (0 %, 5 %, and 10 %) relative to the mass of cement used. A common trend in concrete technology is to use compressive strength as a quantitative measure for the other properties of hardened concrete [20]. After performing a laboratory test and analyzing the results for nine mixes, we chose the optimal mix for each w/b ratio to focus on the effects of the ambient conditions on the durability of high-strength concrete (HSC). We found that a mix containing 30% fly ash yielded the best result with different percentages of silica fume.

In regard to the considerations mentioned above, the main components of the designed concrete mixtures shown in Table 4 were as follows:

- Ordinary Portland cement (OPC) corresponding to P.O. 42.5 [21], with a specific surface area of 350 m²/kg was used.
- The binder contents were 450, 480, and 520 kg/m³ and the w/b ratios were 0.30, 0.35, and 0.4, respectively, for each mix.
- Each of the two pozzolanic materials were used as an additive to the cement in a ratio of 30 % fly ash by weight for each mix and in a ratio of 0 %, 5 %, and 10 % silica fume by weight, respectively.

- - The OPC and SCM's chemical compositions are shown in Table 1.
- - Table 2 depicts the specific gravity, crushing value, and water absorption rate of coarse aggregate (crushed limestone) and fine aggregate (natural river aggregate). The classification of coarse aggregates is as per JTG/T F30-2014 [22], as presented in Table 3.
- - A suitable level of flowability was obtained by using a high range water reducer (HRWR) at a dosage of 1.8 %, 1.5 %, and 1.5 % of the binder material's weight. According to the flow test code [23], the slumps obtained were as follows: 200 mm for mix 1 and 400 mm for mix 2 and mix 3.
- - The sand to coarse aggregate ratio was (0.4:0.6) by weight.

Table 1. Chemical composition of cement and SCMs.

Oxide compounds (mass%)	PC	Silica fume	Fly ash
SiO ₂	21.12	69.3	59.1
Al ₂ O ₃	5.62	27.70	38.9
Fe ₂ O ₃	3.22	1.20	-
CaO	65.95	1.30	0.87
MgO	1.82	0.20	0.71
SO ₃	2.30	0.30	0.42
Density (g/cm ³)	2.80	2.50	2.75
Physical properties			
C ₃ A	7.2	-	-
C ₄ AF	11.4	-	-
C ₃ S	59.2	-	-
C ₂ S	18.8	-	-
Ignition loss	0.5	-	-

Table 2. Absorption, specific gravity, and crushing value of coarse aggregate and fine aggregate.

Aggregate	Absorption (%)	Crushing value (%)	Bulk specific gravity
Coarse > 5mm	1.73	19.46	2.58
Fine < 5mm	2.32	-	2.50

Table 3. Grading of coarse aggregates.

Sieve opening, mm	Passed (%)	Remaining (%)
26.5	100	0-5
19	70	25-40
16	40	50-70
9.5	20	70-90
4.75	5	90-100
2.36	0	95-100

2.2. Specimen preparation

The concrete specimens were prepared in conditions that were representative of the summer months. The representative month was July, where the temperature can reach 50 °C and the relative humidity (RH) can reach 80 %–90 % (hot and high RH) due to proximity to the ocean, but can also fall below 10 % (hot and low RH). The samples were molded in the morning to meet the requirements for casting in hot weather according to ACI 305 [24]. The specimens were placed in a steamy environment to meet the first condition (hot and high RH), and the other specimens were placed in a dry oven to meet the second condition (hot and low RH). Some concrete specimens were placed in water (standard curing) at a temperature of 20 °C and RH of 80 %–90 %.

Table 4. Mixture proportions.

	w/b ratio	Water	Binder kg/m ³	Cement kg/m ³	FA kg/m ³ 30 %	SF kg/m ³	Sand kg/m ³	Aggregate kg/m ³	Water reducers %	Density (kg/m)
Mix 1	0.30	135	450	315	135	0% (0)	706	1060	1.8	2351
Mix 2	0.35	182	520	338	156	5% (26)	660	990	1.5	2352
Mix 3	0.4	192	480	288	144	10% (48)	682	1023	1.5	2377

3. Results and Discussion

3.1. Compressive strength

The results of the compressive strength tests for the concrete mixes are shown in Table 5 for the three curing times and for various other curing conditions. Compressive strength was determined based on 100 mm cubic specimens. These results are plotted against curing time in Figures 1–3. When comparing the oven and 50 °C steam cured concrete with standard cured (in water) concrete, the compressive strength increased for different ratios. The percentage increases at 7, 14, and 28 day cure-time for oven cured mixes 1, 2, and 3 were: (4%, 3%, and 8%); (28%, 19%, and 1.5%); and (17%, 10%, and -18%), respectively. The percentage increases for steam cured concrete were: (-13%, -5%, and 9%); (37%, 34%, and 19%); and (27%, 28%, and 15%), respectively. It was observed that the compressive strength of mix 3, which had a w/b ratio of 0.4, 10% added silica fume, and a 28 day cure time, dropped by 18% due to the effect of the dry conditions. This seemed to agree with the results of a previous investigation by Ramezaniyanpour et al. [19] and Atiş et al. [18]. Although the dry condition simulated in this investigation was more extreme than that in the previous investigations, the reduction in compressive strength was lower. In order to study the efficiency of the curing process, analysis was conducted on the ratio of compressive strength at all curing temperatures and times to that of standard curing. Eq. 1 reflects the curing efficiency:

$$E = \frac{F_x}{F_s} \geq 1 \quad (1)$$

where F_x is compressive strength at the different curing temperature (steam curing, oven curing).

F_s is compressive strength at standard curing.

Table 6 and Figure 4 depict the efficiency of curing at 7, 14, and 28 days. It could be shown that all curing temperatures for both the steam cure and oven cure had an efficiency of greater than one, except for the steam cure of mix 1 at 7 and 14 days and the dry oven cure of mix 3 at 28 days. Additionally, it was observed that the efficiency was high at early cure times and decreased for longer cure times.

Table 5. Compressive strength for all mixes.

cure time (days)	w/b=0.30, 50 °C			w/b=0.35, 50 °C			w/b=0.4, 50 °C		
	STANDARD CURING	DRY OVEN	STEAM	STANDARD CURING	DRY OVEN	STEAM	STANDARD CURING	DRY OVEN	STEAM
7 days	65	68	58	38	53	60	40	48	55
14 days	67	69	64	46	57	70	44	49	61
28 days	74	76	77	67	68	83	58	49	68

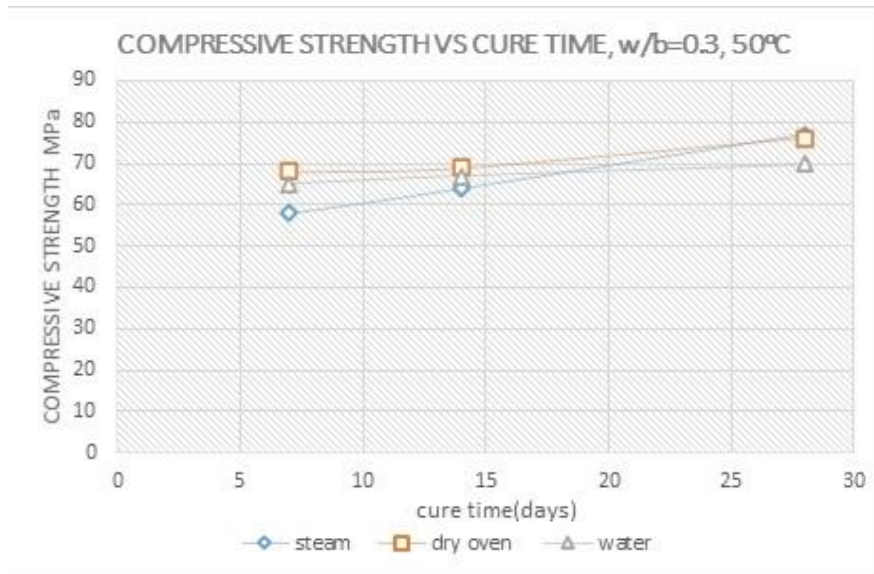


Figure 1. Mix 1 Compressive Strength Development with respect to cure time for mixes cured under varying conditions.

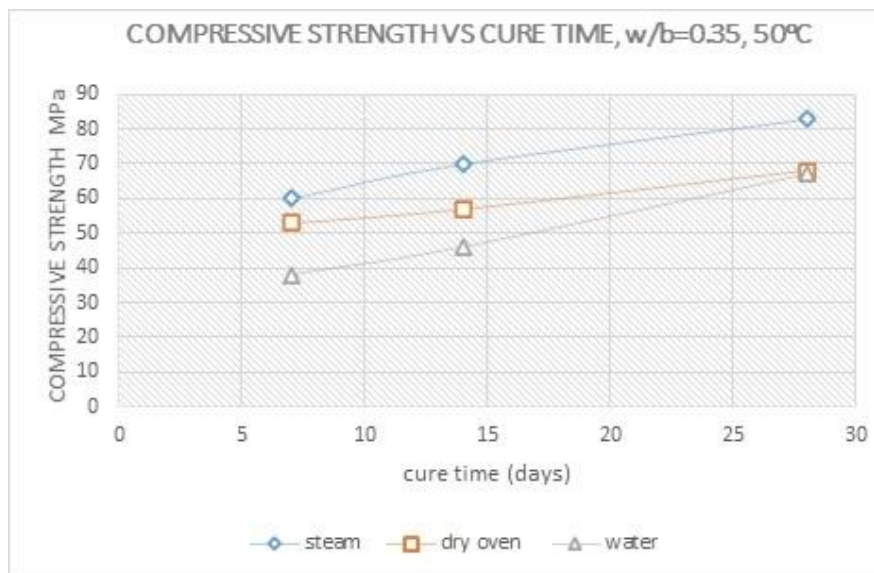


Figure 2. Mix 2 Compressive Strength Development with respect to cure time for mixes cured under varying conditions.

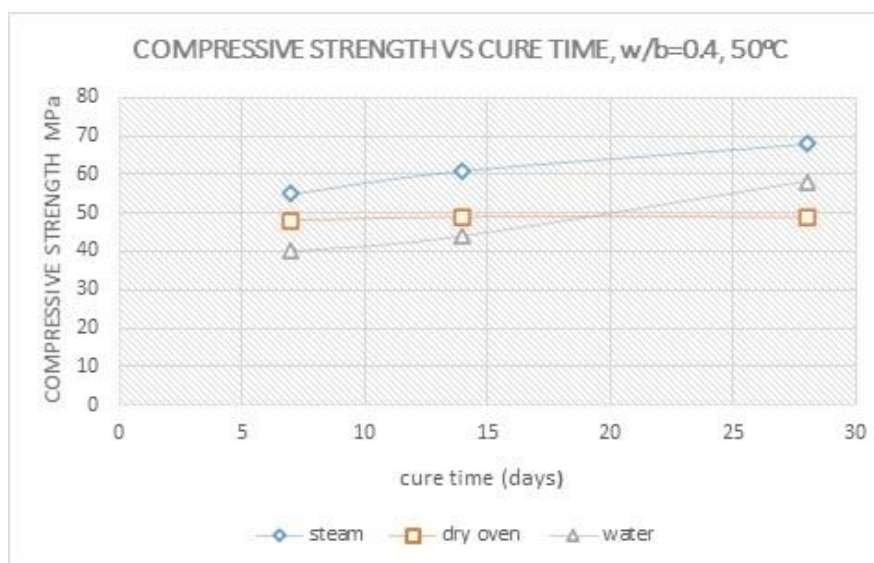


Figure 3. Mix 3 Compressive Strength Development with respect to cure time for mixes cured under varying conditions.

Table 6. The effect of curing efficiency on compressive strength for all mixes.

AGE (days) curing	w/b=0.30, 50 °C		w/b=0.35, 50 °C		w/b=0.4, 50 °C	
	*EO %	*ES %	EO %	ES%	EO %	ES %
7 days	1.046154	0.892308	1.394737	1.578947	1.2	1.375
14 days	1.029851	0.955224	1.23913	1.521739	1.113636	1.386364
28 days	1.027027	1.040541	1.014925	1.238806	0.844828	1.172414

* EO, ES: the efficiency of oven and steam curing respectively.

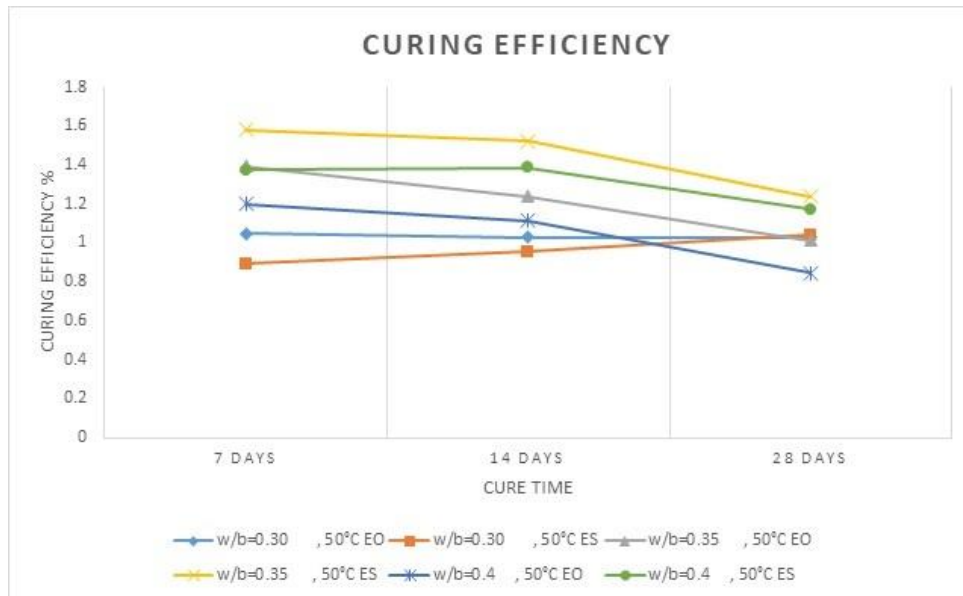


Figure 4. The effect of Curing Efficiency on Compressive Strength for all mixes with respect to cure time.

Statistical analysis was performed to set up a linear relationship between the compressive strength obtained by steam curing (hot and high humidity) and dry oven curing (hot and low humidity). The relationships that were set up are presented in Figure 5 and show that there is a strong linear relationship between the two conditions mentioned above. A strong linear relation was observed at low w/b ratios and decreased with an increase in the w/b ratio. Additionally, the concrete became more sensitive to dry conditions when its silica fume contents [18] were $R^2 = 0.9996$ at w/b = 0.3, $R^2 = 0.9651$ at w/b = 0.35, and $R^2 = 0.7106$ at w/b = 0.4. The hot and dry environment caused water evaporation and the limited hydration affected the silica fume in HSC because of the effect of the drying [25]. High curing temperature can speed up the hydration of cement [26] and the pozzolanic reaction [27] and produce calcium silicate hydrate (C-S-H), which is an important product of cement hydration that increases the strength of concrete. The elevated curing temperature may lead to micro cracking, a process in which the precipitation of portlandite and ettringite are centered in and around cracks, which affects the properties of the concrete.

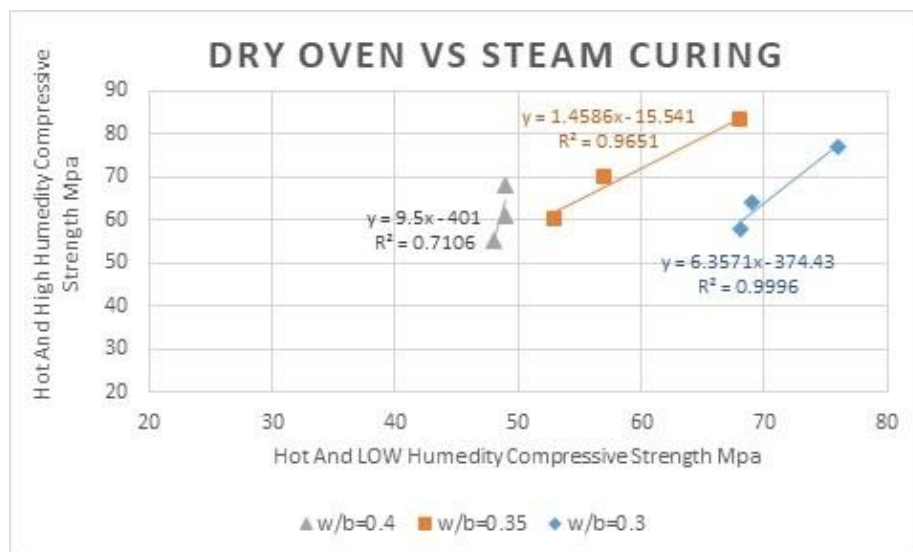


Figure 5. The relationship between steam cured and dry oven cured compressive strength for all concrete mixes.

3.2. Micro hardness

The micro hardness experiment is a reliable method of describing the microstructural properties of hardened concrete and the interface transition zone (ITZ) [28]. In this study, this test method was used to describe the influence of ambient conditions on the properties of the concrete's ITZ. The micro hardness values reported in the ITZ were the result of the concrete being exposed to the three curing conditions mentioned in the previous sections (steam, dry oven, and standard curing). Figures 6, 7, and 8 show the variation in micro hardness values, which were measured using the Vickers's hardness test at the ITZ. An increase in micro hardness was observed over time [29] for standard and steam curing conditions, while it decreased with cure time for the dry curing condition. The relationships between the compressive strength and the micro hardness are shown in Figures 9, 10, and 11. The concrete was strong (positive) for standard and steam curing conditions and strong (negative) for the dry curing condition for all mixtures except mix 2 with $w/b=0.35$. The regression for the standard curing condition showed that R^2 ranged from 0.82 to 0.95. While for the steam curing condition, R^2 ranged from 0.8 to 0.99, increasing with an increase in w/b ratio and with an increase in the percentage of active silica. However, an opposing regression trend was observed in the dry curing condition of 0.9198 at $w/b=0.3$ and 0.9249 at $w/b=0.4$, while the unexpected regression at $w/b=0.35$ R^2 0.0418 may be due to an empirical error.

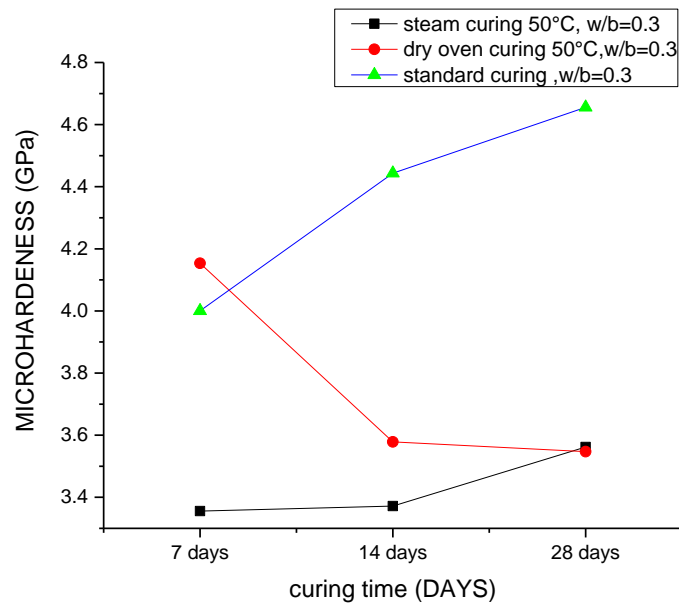


Figure 6. Mix 1 Micro Hardness Development with respect to curing time for mixes cured under varying conditions.

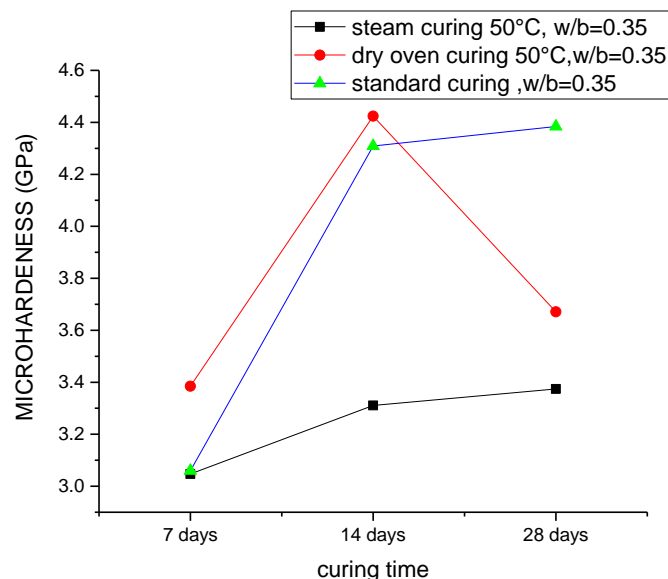


Figure 7. Mix 2 Micro Hardness Development with respect to curing time for mixes cured under varying conditions.

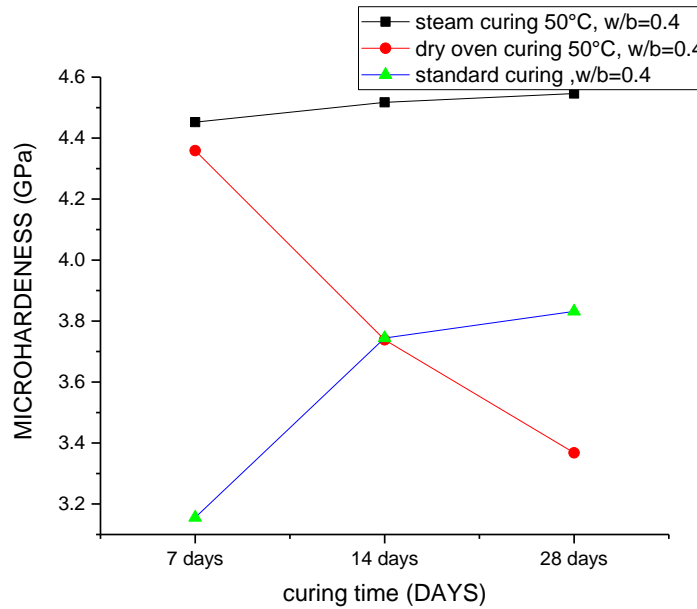


Figure 8. Mix 3 Micro Hardness Development with respect to curing time for mixes cured under varying conditions.

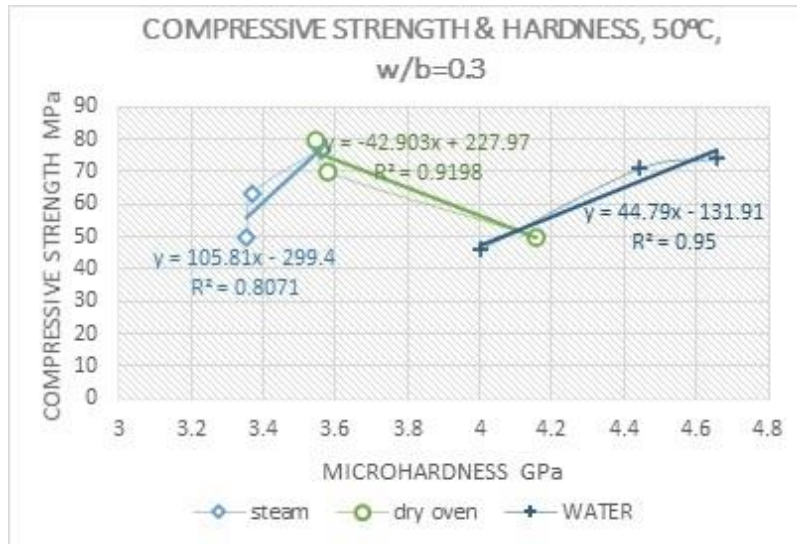


Figure 9. Mix 1 relationship between Compressive Strength and Micro Hardness for mixes cured under varying conditions.

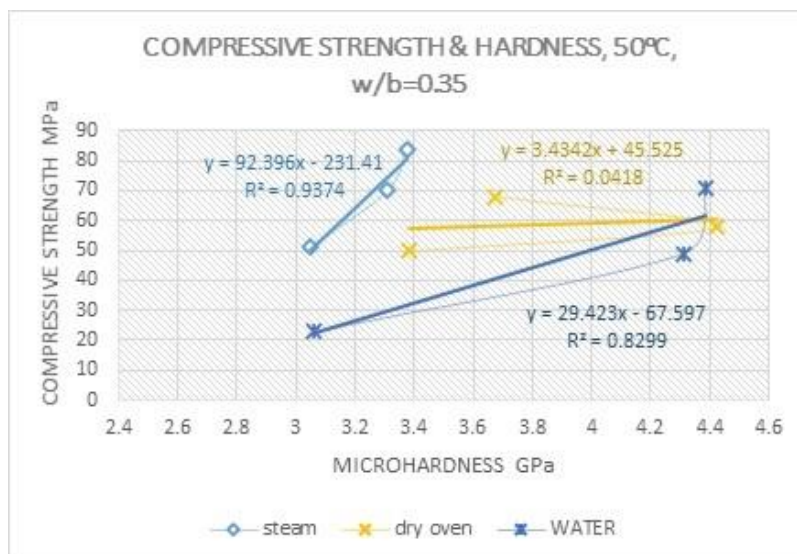


Figure 10. Mix 2 relationship between Compressive Strength and Micro Hardness for mixes cured under varying conditions.

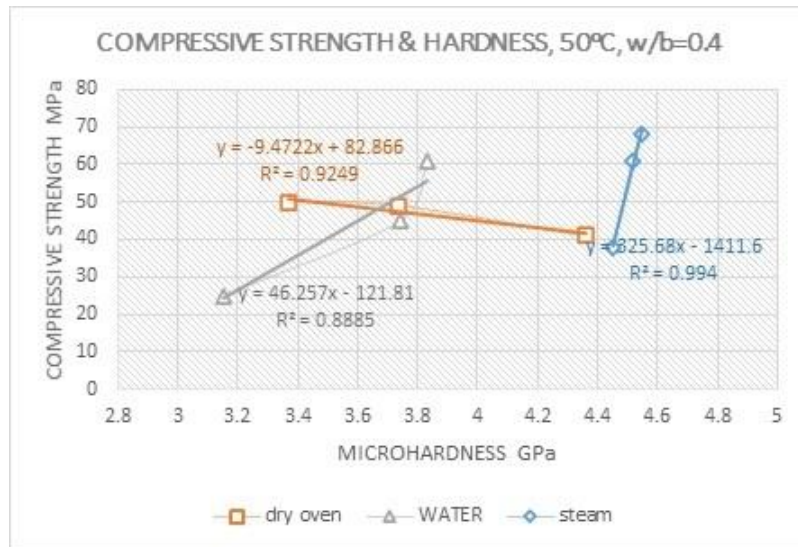


Figure 11. Mix 3 relationship between Compressive Strength and Micro Hardness for mixes cured under varying conditions.

3.3. Flexural strength

Flexural strength was determined based on 40×10×10 mm concrete beam specimens in accordance with the Standard Test Method for determining the mechanical properties of ordinary concrete (GB/T 50081-2002).

Figures 12 to 14 show the flexural strength of specimens of all mixes. It can be seen from Figure 12. for mix 1 that dry curing at 50 °C yielded a flexural strength that was lower than that of normal cured concrete at a curing time of 7 and 28 days by 16.7 % and 40 %, respectively. Figure 13 for mix 2, shows that the flexural strength of specimens cured for seven days in the oven was 30 % greater than that of specimens cured under normal curing conditions, whereas the flexural strength achieved with normal curing at 28 days was higher than that achieved using the dry curing condition by 14.3 %. Figure 14. for mix 3 shows that the flexural strength of samples cured for seven days using standard curing was 22.3 % less than that of specimens cured in the oven, whereas the flexural strength of specimens cured for 28 days using standard curing was 37 % greater than that of specimens cured under dry oven conditions. Figures 13 and 14 show that the flexural strength of specimens cured for seven days using standard curing was lower than that of samples cured under dry conditions. It was found that the specimens cured for 28 days under dry conditions had lower flexural strength than specimens cured using standard curing due to the fact that the high temperatures affected the strength for longer curing times. The hot and dry environment caused water vaporization and limited the effect of hydration, affecting the concrete properties, especially for the concrete containing the silica fume because it was particularly affected by the drying action [18].

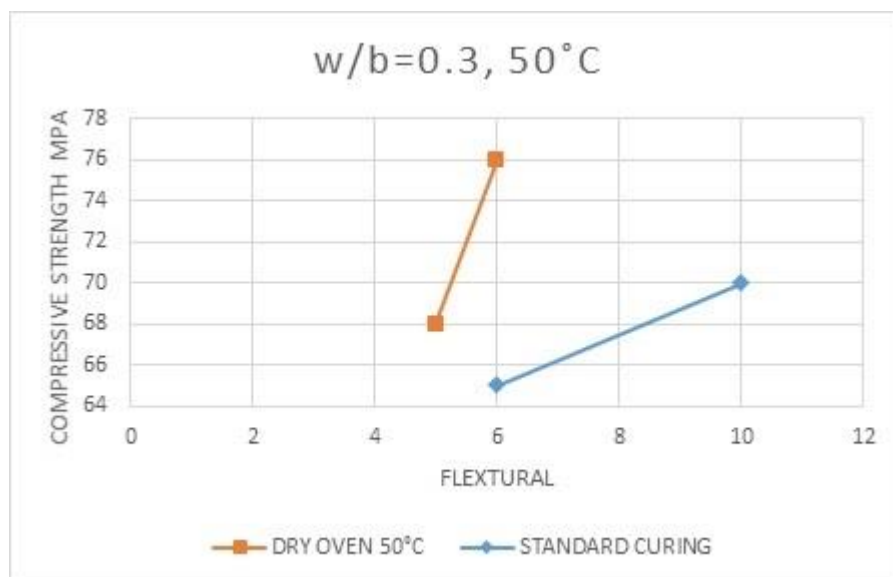


Figure 12. Mix 1 Compressive Strength VS. Flexural Strength for mixes cured under varying conditions.

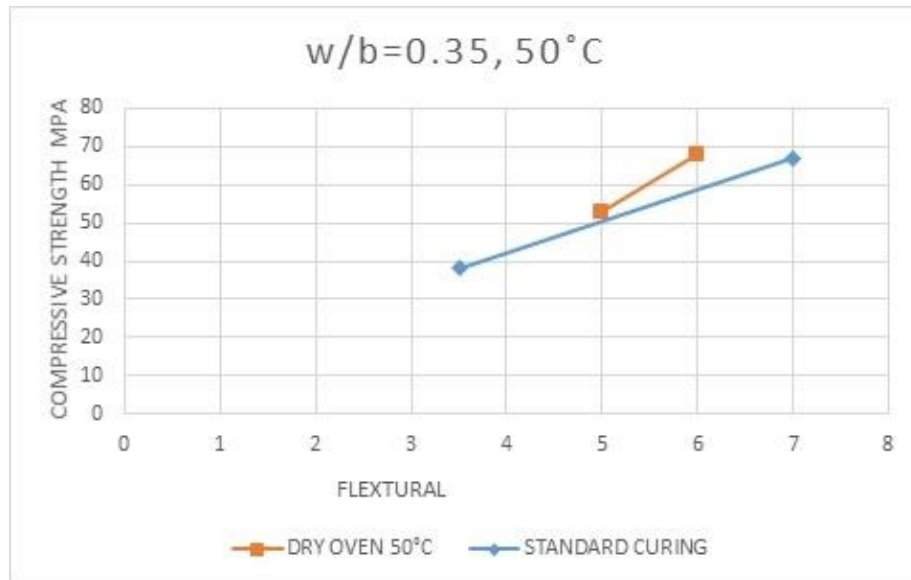


Figure 13. Mix 2 Compressive Strength VS. Flexural Strength for mixes cured under varying conditions.

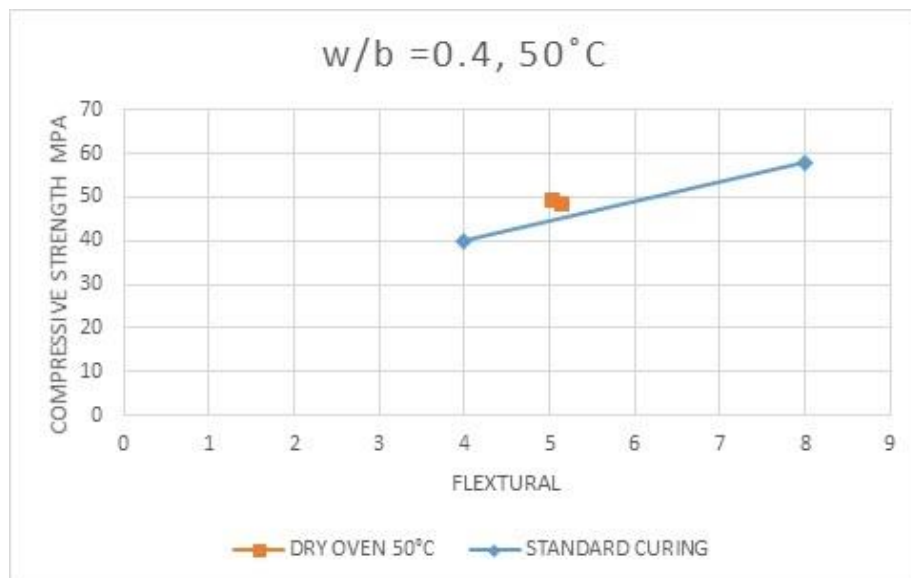


Figure 14. Mix 3 Compressive Strength VS. Flexural Strength for mixes cured under varying conditions.

3.4. Water absorption test

The results of the water absorption test performed on all concrete mixtures cured under both steam and dry conditions are plotted in Figures 15–17. It can clearly be seen that the water absorption of each mixture decreased with increasing curing time. This is because the reaction (hydration reaction) between additives, cement, and the water filled the voids within the concrete and increased its density. When a comparison was made of all mixes cured under steam and dry oven conditions, we found that mix 1, with a low w/b ratio and fly ash content, possessed superior water absorption when cured in dry conditions for all three curing times, 7, 14, and 28 days. However, the specimens cured under steam conditions possessed superior water absorption for all mixes. This indicated that increasing the w/b ratio along with increasing the binder and the percentage of added silica fume, with a constant fly ash percentage did not improve the properties of concrete cured under hot and dry conditions. Water absorption ranged from 1.94 % to 5.53 % in the oven cured samples, while the water absorption of the steam cured samples ranged from 0.913 % to 3.10 %.

The minimum water absorption range value was noted as 1.94 % for the mix 1 sample cured under dry oven conditions which had a lower w/b ratio and 0 % added silica fume. This value increased with increasing w/b ratio and silica content due to the sensitivity of silica to the drying and evaporation of water. However, good regression was observed in terms of a reduction in water absorption over time due to a reduction in the porosity and pore connectivity. This was in turn due to the pozzolanic reaction leading to an improvement in concrete durability and microstructure.

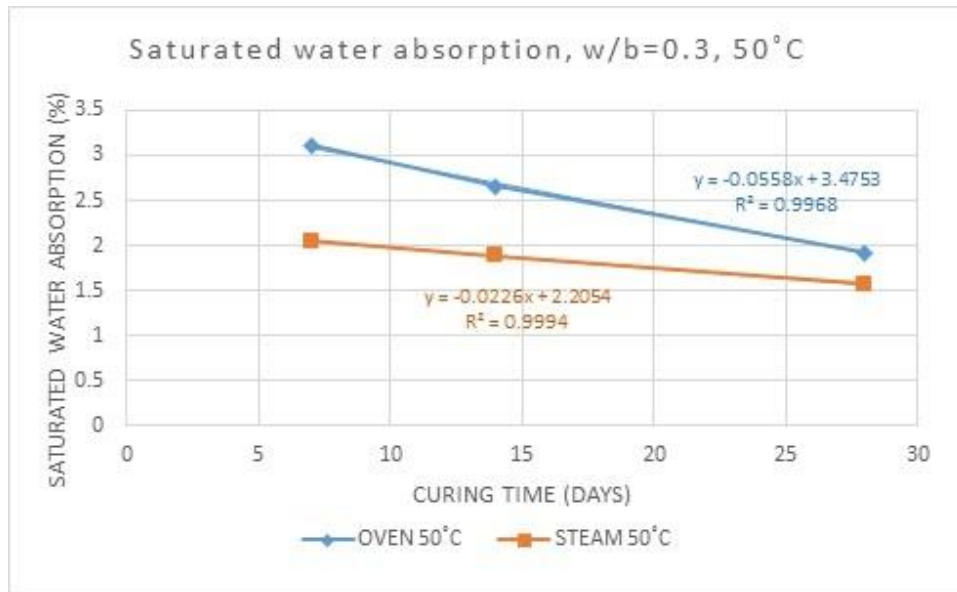


Figure 15. Mix 1 Saturated water absorption % with respect to curing time under varying conditions.

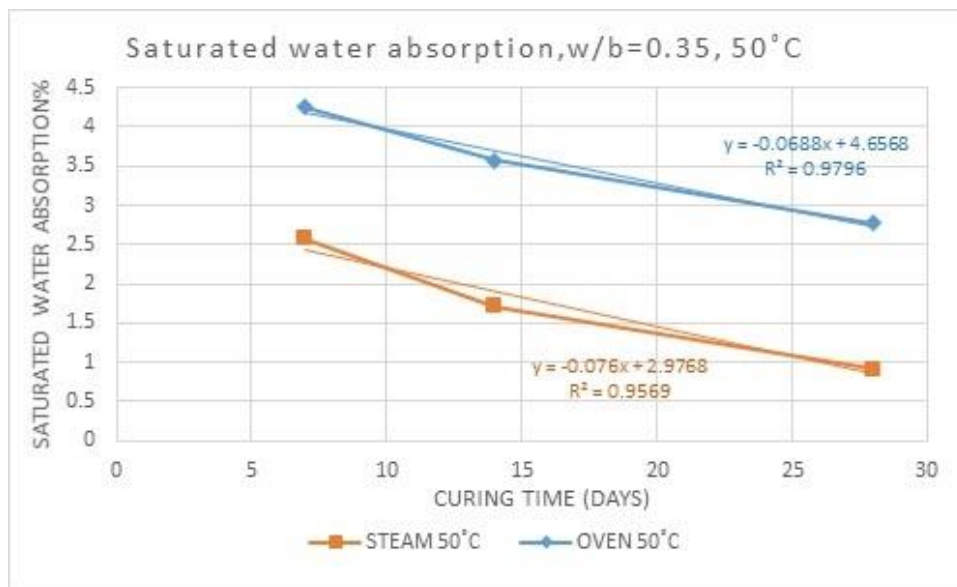


Figure 16. Mix 2 Saturated water absorption % with respect to curing time under varying conditions.

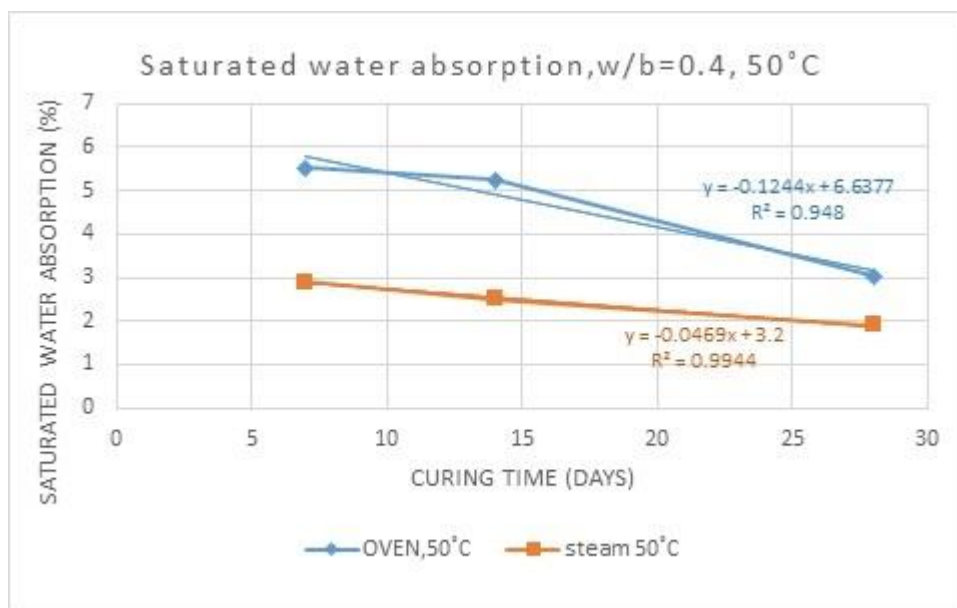


Figure 17. Mix 3 Saturated water absorption % with respect to curing time under varying conditions

3.5. Chloride permeability test

It is important to fully understand the influence that permeability has on concrete durability. Permeability also affects the ability of deleterious ions and salts to permeate into the concrete. Industry awareness of the effect of permeability on the durability of concrete exposed to “water containing salt” or “chemically-rich water” is increasing. The chloride permeability test was performed in accordance with ASTM C 1202 (Table 7) [30]. After the cure for 28 days, the concrete samples were cut in two halves of 50 mm each, and the samples were then dried. The chloride ions entering the concrete were measured in the two 50 mm disc samples exposed to an electrical field of 60 V applied for 6 hours using stainless steel electrodes placed between the two cells. One of the sample halves was in contact with a 3% NaCl solution, and the other halves were in contact with a 0.3% NaOH solution. The current was recorded every 30 minutes for six hours. The experiment was performed after the 28-day cure time was complete. Figures 18, 19, and 20 show the electric flux and the chloride permeability under different conditions[31]. We observed that many ambient conditions had an effect on concrete permeability. It was shown that the blends which contained active silica and fly ash were superior to the blends that contained fly ash under standard curing and steam curing conditions. However, under dry curing conditions, the mixture which contained fly ash was superior to the other mixtures under the same conditions. This was because active silica is more sensitive in dry conditions, and ash decreases the heat of hydration. The presence of pozzolan (active silica and fly ash) had a very significant effect on the permeability of the concrete, which showed significant reductions in the charge passed [17]. Additionally, it was shown that all mixes cured under all conditions fell in the low permeability range according to ASTM C 1202 (Table 7), except for mix 2 cured under dry conditions, which fell in the medium permeability range.

Figure 21 shows the good regression between compressive strength and load (Coulomb electric flux/c). It can be seen that an increasing compressive strength led to a decrease in permeability and improved durability. These results show that good permeability and density can be obtained by increasing the silica fume ratio from 0 to 10%. However, it was observed that concrete containing silica fume was more sensitive to dry conditions. The rapid chloride-ion test also showed that the interconnectivity of the pore system decreased with the reduction of the w/b ratio. The dry curing condition was found to be the most effective at increasing the permeability, particularly when combined with increasing silica content. These results can be seen to indicate that concrete containing silica fume is more sensitive to hot and dry conditions.

Table 7.ID Charge Passed (coulombs) Chloride Ion Penetrability in accordance with ASTM C1202 [30].

ID Charge	COULOMB ELECTRIC FLUX/C
High >	4000
Moderate	2000–4000
Low	1000–2000
Very Low	100–1000

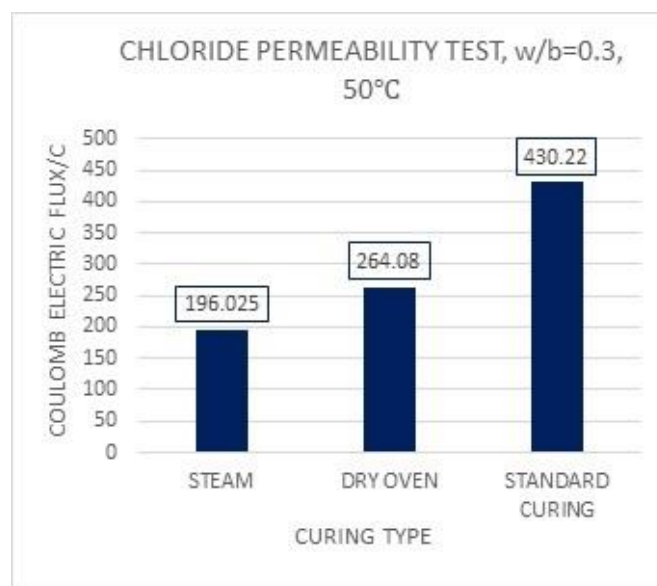


Figure 18. Chloride Permeability test for concrete specimens prepared and cured under different conditions.

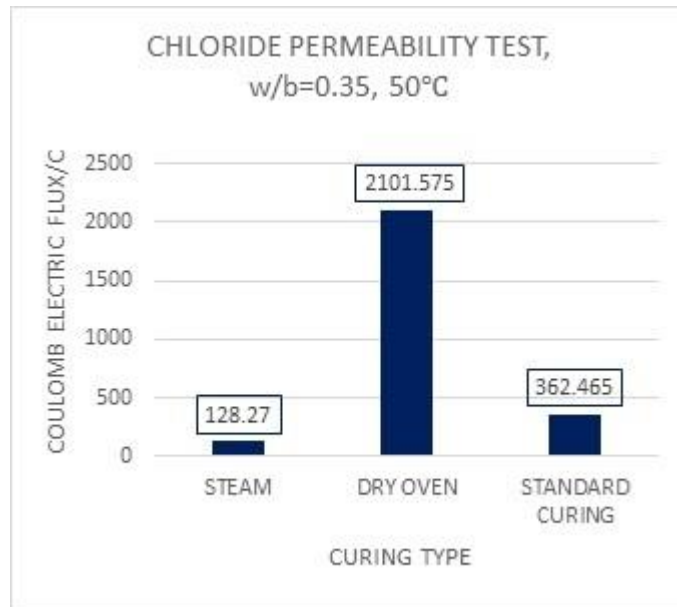


Figure 19. Chloride permeability test for concrete specimens prepared and cured under different conditions.

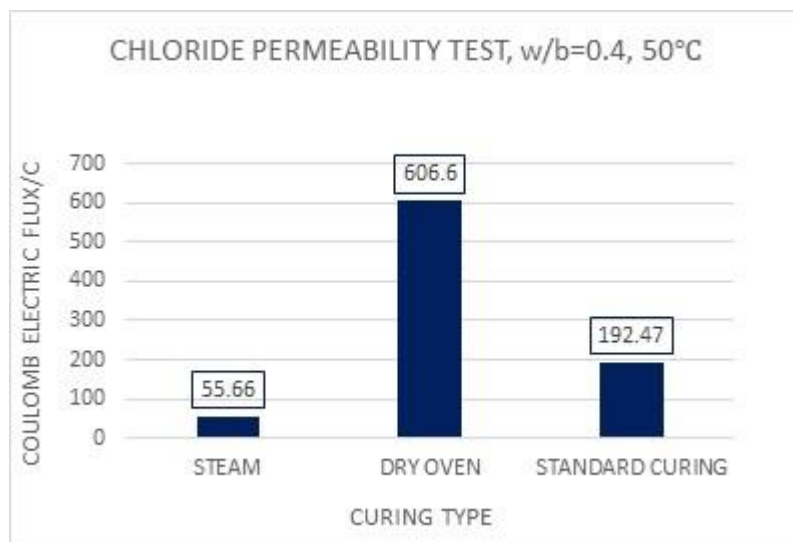


Figure 20. Chloride permeability test for concrete specimens prepared and cured under different conditions.

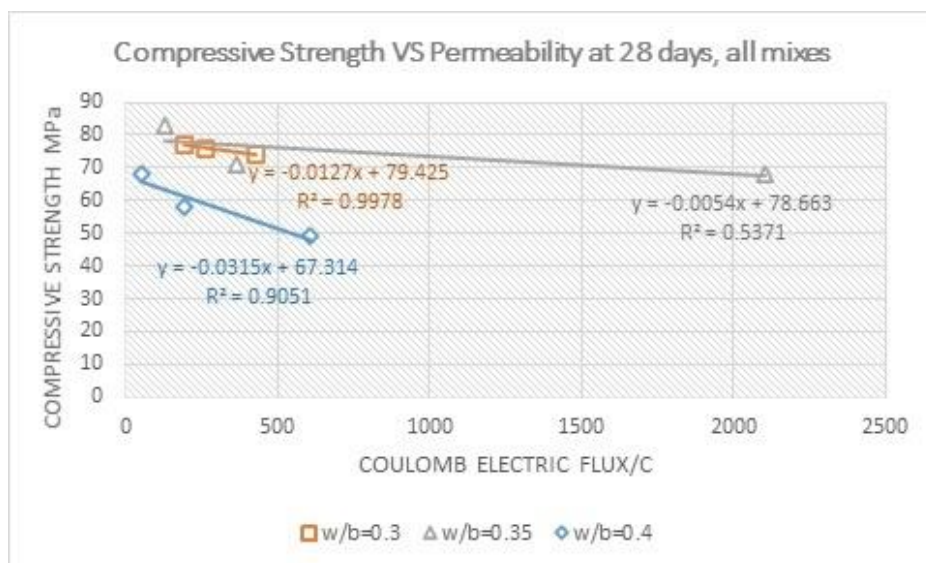


Figure 21. The relationship between the Permeability Chloride test and the Compressive Strength of concrete specimens prepared and cured under different conditions for all mixes.

3.6. Microstructure of concrete

Concrete has a varied microstructure, which differs based on the concrete components, i.e. the cement paste, the pore structure, and the bond between the cement paste and the aggregates (ITZ). In order to improve the mechanical strength and durability of the concrete, these components must be improved. The microstructure of concrete can be improved by adding pozzolanic materials, which enhance the chemical composition and hydration reactions of concrete. The pozzolanic material reaction increases the generation of calcium silicate hydrate (C-S-H) compounds, which is an important product of cement hydration that produces stronger, denser, and more durable concrete over its service life [32]. Pozzolanic additives (such as active silica and fly ash) played a role in micro-filters and resulted in a decrease in the number of pores [17, 33]. The partial replacement of the cement with active silica and ash resulted in a decrease in the number of pores in the ITZ. Additionally, a reduction in the amount of calcium hydrate (CH) crystals and ettringite was observed along with a denser C-S-H gel [34]. As was mentioned, the ITZ was the weakest zone, but became stronger and less porous with the incorporation of mineral additives (e.g. active silica and fly ash) thus improving the microstructure of the concrete. This led to reduced porosity and interconnectivity, lower permeability, and improved durability.

3.7. SEM and EDX analysis

To investigate the effects of environmental conditions (steam, dry oven, and standard cure) on the ITZ, the fracture morphology of concrete cured for 28 days was observed using SEM. The analyzed concrete mixtures consisted of Portland cement, active silica, and fly ash. The specimens were exposed to three types of cure, as mentioned above. The samples of broken concrete were then analyzed using SEM and X-ray microanalysis using Energy-dispersive X-ray spectroscopy (EDX). Microscopic observations were carried out on the topography of the surfaces of the specimens which had been exposed to different curing conditions. The results of the SEM and EDX analysis of the mixtures cured under different conditions are shown in Figures 22, 23, and 24. It is evident in all figures that each mixture possessed a different microstructure and morphology. The specimens treated under standard and steam condition exhibit more homogeneous morphology than the specimens cured under dry conditions, which possessed a smooth surface without visible cracks, as shown in Figures 22-24. The elemental composition as determined using EDX included oxygen (O), calcium (Ca), silicon (Si), carbon (C), potassium (K), magnesium (Mg), aluminum (Al), iron (Fe), and a small amount of sodium (Na) as shown in Table 8 and Figures 22–24.

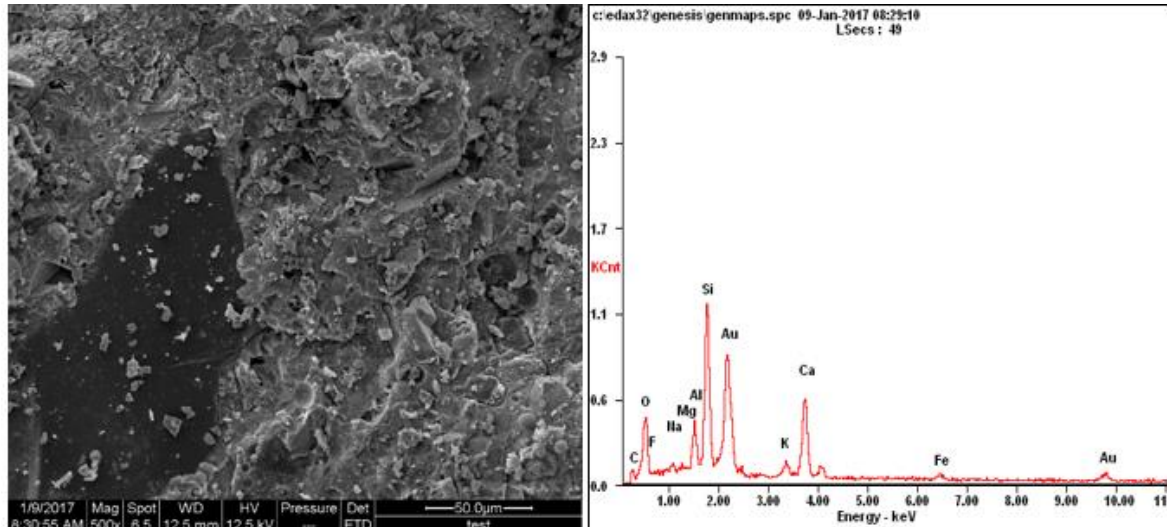
Additionally, the shapes of most of the particles were irregular, dispersed, and uniformly distributed in the gaps between the sand particles with occasional overlapping structures on the crystal surfaces. Figure 22. shows the SEM and EDX images for all the mixtures cured under dry conditions at 50 °C. During the hydration process after curing for 28 days, we observed the deposition of CH and C-S-H on the surface, and the continuation of this process caused the concrete porosity to be reduced. However, micro-cracking was observed on the surface in and near the ITZ. Additionally, CH sediment was noted at the ITZ, which caused a decrease in the micro hardness after being cured for 28 days and increased the permeability of specimens cured under dry conditions at 50 °C. This had a direct effect on compressive strength, flexural strength, permeability, and micro hardness after being cured for 28 days. Figure 23 and Figure 24 show SEM and EDX images for all mixtures cured under standard and steam conditions at 50 °C, respectively. They show more of a homogeneous morphology than specimens cured under dry conditions, and to some extent the specimens possessed a smooth surface with no visible cracks.

Table 8 shows the various elemental percentages, such as O, C, Si, and Ca along with small quantities of Na and Mg which were also detected. Although the presence of calcium and silicate is important evidence for the cement hydration processes, only low Ca/Si and Ca/(Si +Al) ratios were observed. If the Ca/Si ratio is low, this indicates that the concrete is dense. Portland cement composites usually possess a Ca/Si ratio of approximately 1.5. Silica fume and fly ashes are helpful for producing concrete that possesses lower porosity and higher density based on the refinement in pore size due to the pozzolanic reaction [35, 36].

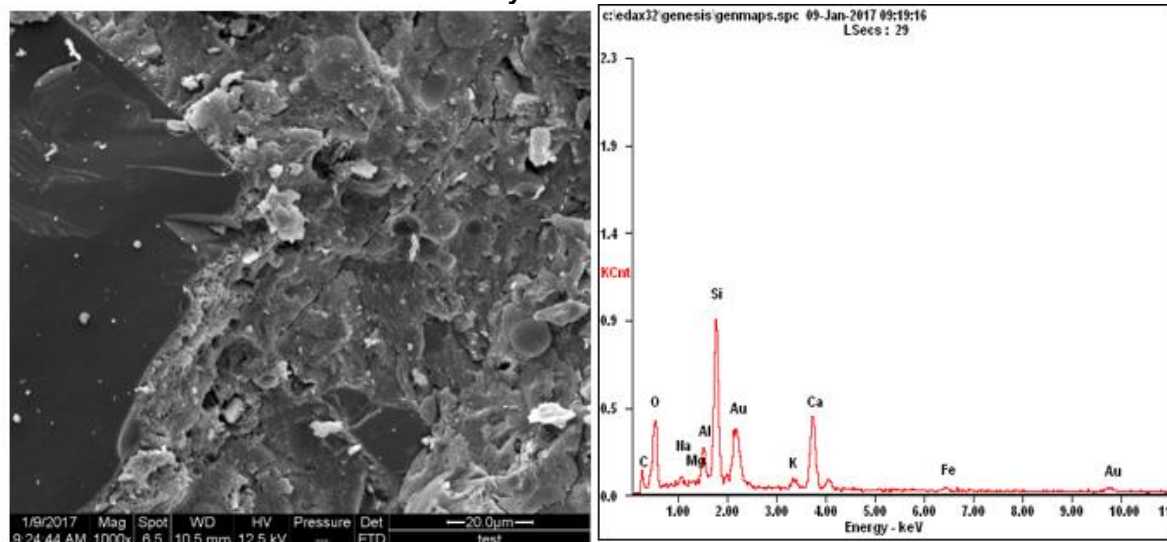
We noted that all mixtures cured under different conditions had a Ca/Si ratio of less than 1.5. This means that concrete is dense, which can also be observed from the result of the permeability. All mixtures cured under all conditions were in the low permeability range according to the ASTM C 1202 (Table 7) [30], except for mix 2, cured under dry conditions, which was in the medium permeability range. Figure 21 shows the relationship between the compressive strength and permeability (Coulomb/C flow), where an increase in the compressive force reduced permeability and improved durability. We noted that the ITZ was well structured, resulting in increased compressive strength and reduced permeability. The results of the EDX confirmed the test results obtained from the samples cured under all conditions. Figures 22–24, where SEM and EDX images are shown for mixtures cured under dry, standard, and vapor conditions. HSC can be produced which exhibits good properties when additional cement materials such as silica and fly ash are used to form a homogeneous concrete with a smooth surface. This can produce concrete with low permeable and high durability.

Table 8. The elemental percentages for all mixes under different conditions.

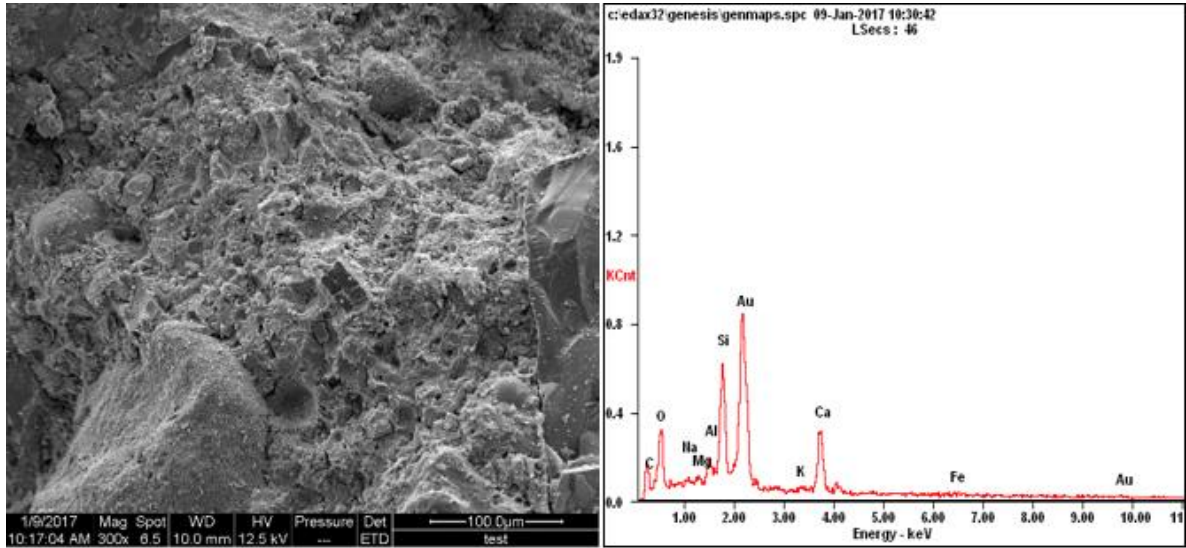
w/b ratio	w/b=0.3			w/b=0.35			w/b=0.4		
Curing type									
	Steam	Water	Oven	Steam	Water	Oven	Steam	Water	Oven
Elements %									
CK	0	0	0	6.13	0	19.72	6.86	0	26.48
OK	31.01	32.15	24.16	24.92	40.08	21.47	26.25	37.38	30.1
MgK	3.90	0.29	0.63	0.92	0.99	1.39	0.23	1.26	0.31
AlK	9.51	14.05	24.64	2.27	20.11	11.42	0	2.91	2.06
SiK	21.47	37.72	37.87	26.23	34.68	28.48	61.25	29.75	17.04
KK	2.54	1.29	2.95	1.99	2.64	1.69	0.76	1.16	1.23
CaK	13.93	4.65	3.14	32.77	1.5	7.39	1.51	27.53	19.17
TiK	0.33	0.36	1.51	2	0	1.68	1.5	0	0
FeK	16.87	2.88	3.94	2.76	0	6.76	1.65	0	2.78
Ca/Si	0.649	0.123	0.083	1.249	0.043	0.259	0.025	0.925	1.125
Ca/(Si+Al)	0.45	0.09	0.050	1.15	0.027	0.185	0.025	0.843	1.003



Dry oven w/b=0.3

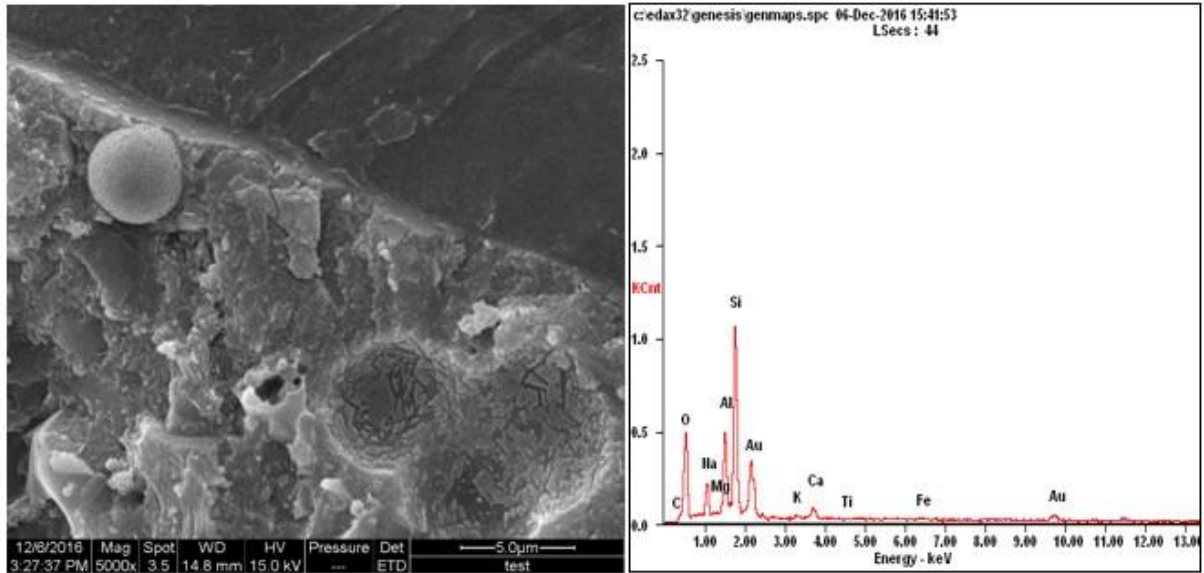


Dry oven w/b=0.35

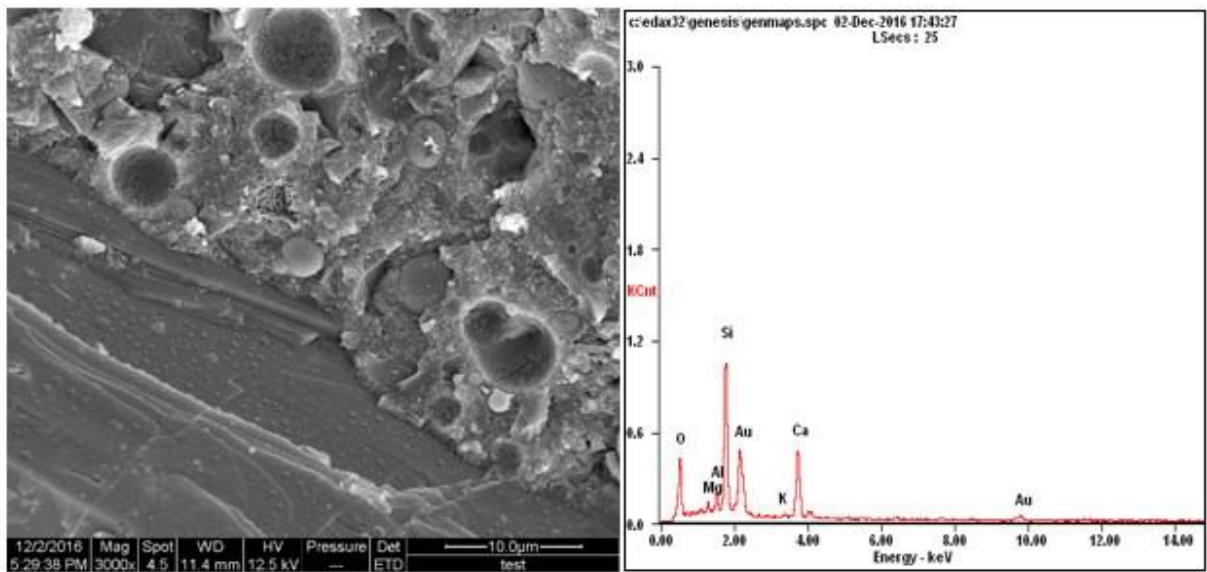


Dry oven w/b=0.4

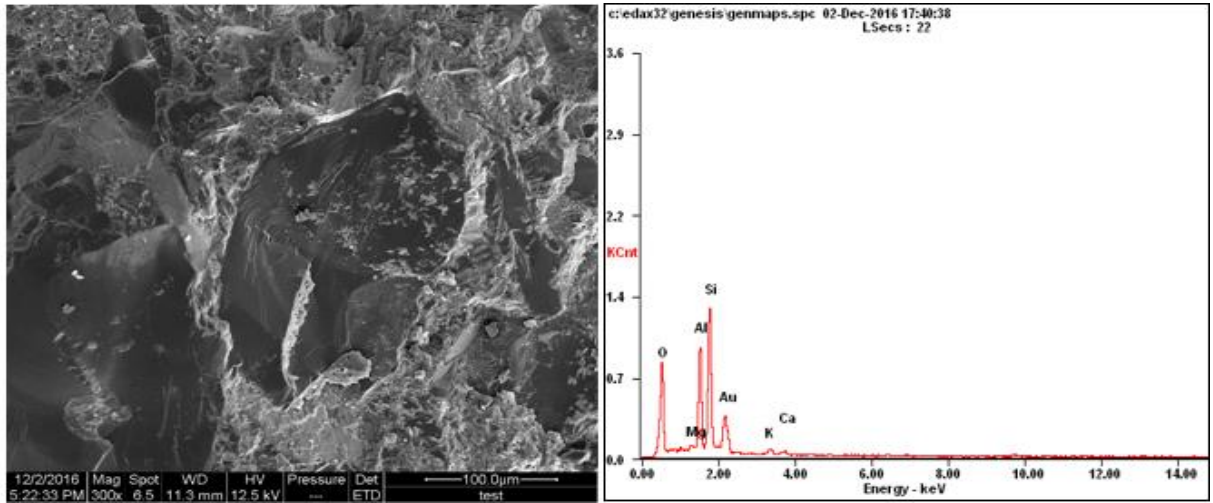
Figure 22. Microstructure evolution for specimens cured under dry oven conditions at 50 °C for all mixes.



Standard curing w/b=0.3

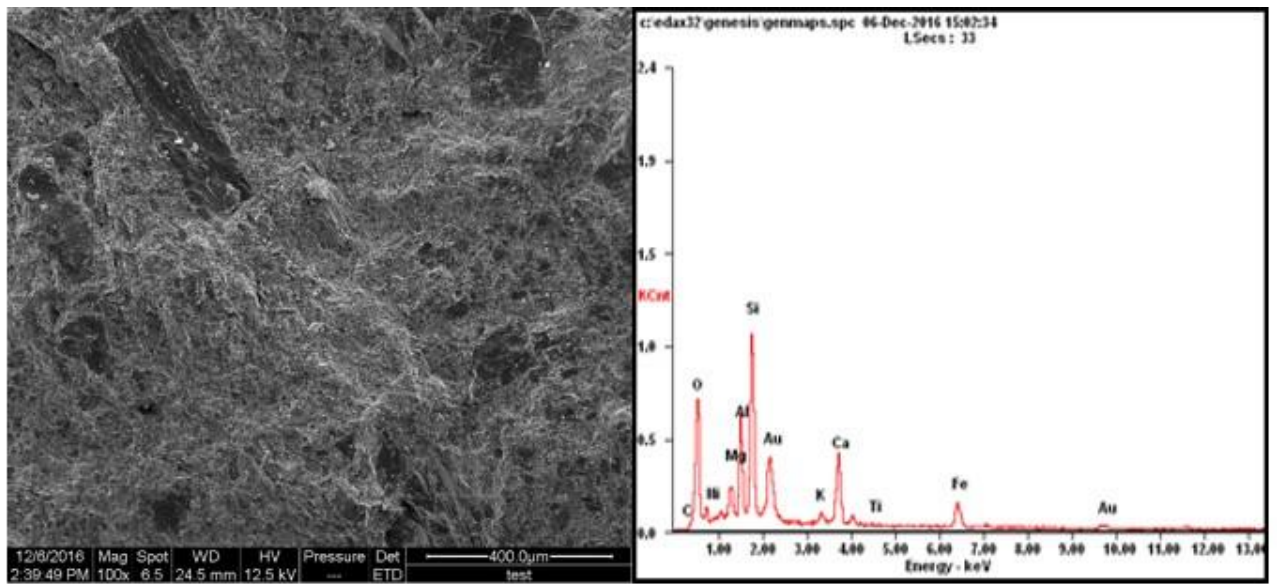


Standard curing w/b=0.35

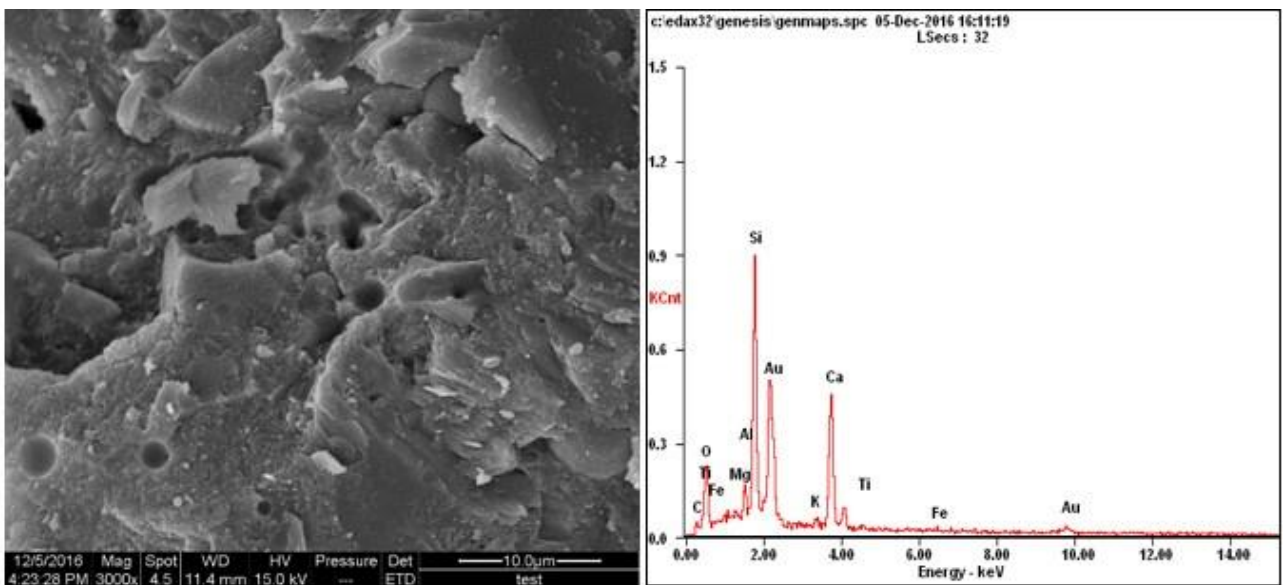


Standard curing w/b=0.4

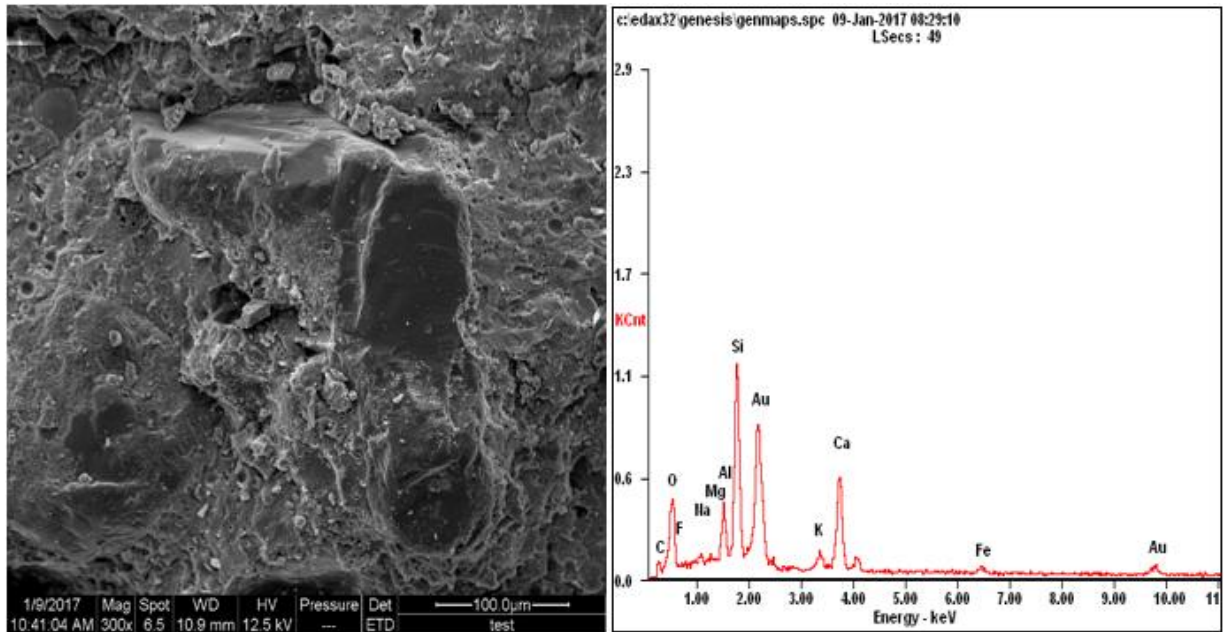
Figure 23. Microstructure evolution of specimens cured under standard conditions for all mixes.



Steam curing w/b=0.3



Steam curing w/b=0.35



Steam curing w/b=0.4

Figure 24. Microstructure evolution for specimens cured under steam conditions at 50 °C for all mixes.

4. Conclusions

From this study, the following could be observed:

1. The effects of the curing process on concrete properties, such as strength, were significantly influenced by exposure to severe conditions. This indicated that more careful and effective treatment practices and mechanisms are required when concrete is exposed to hot, dry environments, such as in the Gulf region (Middle Eastern) climate.
2. The results obtained in this study have shown that silica fume and fly ash are potential additives that are useful for enhancing the properties of concrete cured under different conditions (i.e. in hot and dry environments). Owing to their chemical composition, they contribute to the pozzolanic reactions and enhance the concrete's durability.
3. Pozzolanic materials, such as silica fume and fly ash, used in this study provide a good solution to the problem of durability reduction in harsh environments due to fluctuations in strength and permeability. The XRD results indicated the involvement of pozzolans in the microstructure and the formation of stable, favorable compounds.
4. The three mixtures passed the ASTM C 1202 acceptance criterion for all ambient curing conditions, which is evidence of the effectiveness of added silica fume and fly ash.
5. From the data mentioned above, it could be summarized that the microstructure of HSC was more homogenous, which is a result of the physical and chemical effects of the associated substances (silica fume and fly ash), as well as the decrease in the w/b ratio. Additionally, it could be observed from the above results that adding SMC (individually or in combination) improved and enhanced the strength and durability of concrete in harsh environments.
6. A good regression in terms of a reduction in water absorption with increased curing time was observed. This was due to a reduction in the porosity and pore interconnectivity due to the pozzolanic reaction which led to improvements in the concrete's durability and microstructure.
7. The results of the SEM and EDX analysis showed that the specimens cured under steam and standard conditions displayed a more homogeneous morphology, and to some extent possessed a smoother surface with no visible cracks compared with the specimens cured under hot and dry conditions. Additionally, low ratios of (Ca/Si) and Ca/(Si +Al) were observed. These ratios indicated that the concrete was denser and more durable.

In addition, the results of the SEM and EDX analysis confirmed the test results regarding compressive strength, permeability, and the micro-hardness of the ITZ.

5. Acknowledgements

The authors would like to thank the Hei Longjian province Natural Science Fund for providing support for this study.

References

1. Mehta, P.K. Durability--critical issues for the future. *Concrete international*. 1997. 19. Pp. 27–33.
2. Russell, D., Basheer, P.M., Rankin, G.B., Long, A.E. Effect of relative humidity and air permeability on prediction of the rate of carbonation of concrete. *Proceedings of the Institution of Civil Engineers-Structures and Buildings*. 2001. 146. Pp. 319–326.
3. Roy, D., Arjunan, P., Silsbee, M. Effect of silica fume, metakaolin, and low-calcium fly ash on chemical resistance of concrete. *Cement and Concrete Research*. 2001. 31. Pp. 1809–1813.
4. Merida, A., Kharchi, F. Pozzolan concrete durability on sulphate attack. *Procedia Engineering*. 2015. 114. Pp. 832–837.
5. Du, H., Du, S., Liu, X. Durability performances of concrete with nano-silica. *Construction and Building Materials*. 2014. 73. Pp. 705–712.
6. Hassan, A.A., Lachemi, M., Hossain, K.M. Effect of metakaolin and silica fume on the durability of self-consolidating concrete. *Cement and concrete composites*. 2012. 34. Pp. 801–807.
7. Khan, M.I., Siddique, R. Utilization of silica fume in concrete: Review of durability properties. *Resources, Conservation and Recycling*. 2011. 57. Pp. 30–35.
8. Borosnyói, A. Long term durability performance and mechanical properties of high performance concretes with combined use of supplementary cementing materials. *Construction and Building Materials*. 2016. 112. Pp. 307–324.
9. Cyr, M., Trinh, M., Husson, B., Casaux-Ginestet, G. Effect of cement type on metakaolin efficiency. *Cement and Concrete Research*. 2014. 64. Pp. 63–72.
10. Wu, X., Jiang, W., Roy, D.M. Early activation and properties of slag cement. *Cement and Concrete Research*. 1990. 20. Pp. 961–974.
11. Li, Z., Ding, Z. Property improvement of portland cement by incorporating with metakaolin and slag. *Cement and Concrete Research*. 2003. 33. Pp. 579–584.
12. Li, C., Sun, H., Li, L. A review: The comparison between alkali-activated slag (si+ ca) and metakaolin (si+ al) cements. *Cement and Concrete Research*. 2010. 40. Pp. 1341–1349.
13. Wang, X.-Y. Effect of fly ash on properties evolution of cement based materials. *Construction and Building Materials*. 2014. 69. Pp. 32–40.
14. Wong, H., Razak, H.A. Efficiency of calcined kaolin and silica fume as cement replacement material for strength performance. *Cement and Concrete Research*. 2005. 35. Pp. 696–702.
15. Hilal, A.A. Microstructure of concrete. High performance concrete technology and applications, InTech. 2016. Pp. 3–24.
16. Bentz, D.P., Garboczi, E.J. Simulation studies of the effects of mineral admixtures on the cement paste-aggregate interfacial zone (sp-105). *Materials Journal*. 1991. 88. Pp. 518–529.
17. Setina, J., Gabrenea, A., Juhneva, I. Effect of pozzolanic additives on structure and chemical durability of concrete. *Procedia Engineering*. 2013. 57. Pp. 1005–1012.
18. Atiş, C., Özcan, F., Kilic, A., Karahan, O., Bilim, C., Severcan, M. Influence of dry and wet curing conditions on compressive strength of silica fume concrete. *Building and environment*. 2005. 40. Pp. 1678–1683.
19. Ramezani-pour, A., Malhotra, V. Effect of curing on the compressive strength, resistance to chloride-ion penetration and porosity of concretes incorporating slag, fly ash or silica fume. *Cement and concrete composites*. 1995. 17. Pp. 125–133.
20. Shetty, M. *Concrete technology theory & practice*. S. CHAND & Company. Ram Nagar. New Delhi, 2005. Pp 420–453.
21. Standard, C.C. *Common portland cement (gb175-2007)*. Chinese Standard Publishing. Beijing, 2007.
22. The National Design Code. *Technical Guidelines for Construction of Highway Cement Concrete Pavements (JTG/T F30-2014)*.
23. ASTM C1611 / C1611M-14 (2014) Standard test method for slump flow of self-consolidating concrete. ASTM International, W.C., PA. <https://www.astm.org/Standards/C1611.htm>. Accessed 12 May 2018.
24. ACI 305 (2014) ACI 305:1–14. *Guide to hot weather concreting*. American Concrete Institute, F.h., MI, USA.
25. Bushlaibi, A. Effects of environment and curing methods on the compressive strength of silica fume high-strength concrete. *Advances in cement research*. 2004. 16. Pp. 17–22.
26. Stutzman, P., Clifton, J. *Microstructural features of some low water/solids, csf mortars cured at different temperatures*. Nister 4790. US Department of Commerce Springfield. Virginia, 1992.
27. Shi, C., Wu, Y., Riefler, C., Wang, H. Characteristics and pozzolanic reactivity of glass powders. *Cement and Concrete Research*. 2005. 35. Pp. 987–993.
28. Hooton, R.D. Canadian use of ground granulated blast-furnace slag as a supplementary cementing material for enhanced performance of concrete. *Canadian Journal of Civil Engineering*. 2000. 27. Pp. 754–760.
29. Igarashi, S., Bentur, A., Mindess, S. Microhardness testing of cementitious materials. *Advanced Cement Based Materials*. 1996. 4. Pp. 48–57.
30. ASTM, C. 1202: Standard test method for electrical indication of concrete's ability to resist chloride ion penetration. *Annual Book of ASTM Standards*. 2012. 4. Pp. 7.
31. Wedatalla, A.M., Jia, Y., Ahmed, A.A. Curing effects on high-strength concrete properties. *Advances in Civil Engineering* 2019.. doi.org/10.1155/2019/1683292
32. Sahmaran, M., Kasap, O., Duru, K., Yaman, I. Effects of mix composition and water–cement ratio on the sulfate resistance of blended cements. *Cement and Concrete composites*. 2007. 29. Pp. 159–167.
33. Mardani-Aghabaglou, A., Sezer, G.İ., Ramyar, K. Comparison of fly ash, silica fume and metakaolin from mechanical properties and durability performance of mortar mixtures view point. *Construction and Building Materials*. 2014. 70. Pp. 17–25.
34. Büyükoztürk, O., Lau, D. *High performance concrete: Fundamentals and application*. Department of Civil and Environmental Engineering. Massachusetts Institute of Technology. Cambridge, 2004.
35. Gleize, P., Müller, A., Roman, H.R. Microstructural investigation of a silica fume–cement–lime mortar. *Cement and Concrete composites*. 2003. 25. Pp. 171–175.
36. Gallucci, E., Zhang, X., Scrivener, K. Effect of temperature on the microstructure of calcium silicate hydrate (csh). *Cement and Concrete Research*. 2013. 53. Pp. 185–195.

Contacts:

Afaf Wedatalla, ff_osman@yahoo.com

Jia Yanmin, jiayanmin@nefu.edu.cn



ПОЛИТЕХ
Санкт-Петербургский
политехнический университет
Петра Великого

Инженерно-строительный институт
Центр дополнительных профессиональных программ

195251, г. Санкт-Петербург, Политехническая ул., 29,
тел/факс: 552-94-60, www.stroikursi.spbstu.ru,
stroikursi@mail.ru

Приглашает специалистов проектных и строительных организаций,
не имеющих базового профильного высшего образования
на курсы профессиональной переподготовки (от 500 часов)
по направлению «Строительство» по программам:

П-01 «Промышленное и гражданское строительство»

Программа включает учебные разделы:

- Основы строительного дела
- Инженерное оборудование зданий и сооружений
- Технология и контроль качества строительства
- Основы проектирования зданий и сооружений
- Автоматизация проектных работ с использованием AutoCAD
- Автоматизация сметного дела в строительстве
- Управление строительной организацией
- Управление инвестиционно-строительными проектами. Выполнение функций технического заказчика

П-02 «Экономика и управление в строительстве»

Программа включает учебные разделы:

- Основы строительного дела
- Инженерное оборудование зданий и сооружений
- Технология и контроль качества строительства
- Управление инвестиционно-строительными проектами. Выполнение функций технического заказчика и генерального подрядчика
- Управление строительной организацией
- Экономика и ценообразование в строительстве
- Управление строительной организацией
- Организация, управление и планирование в строительстве
- Автоматизация сметного дела в строительстве

П-03 «Инженерные системы зданий и сооружений»

Программа включает учебные разделы:

- Основы механики жидкости и газа
- Инженерное оборудование зданий и сооружений
- Проектирование, монтаж и эксплуатация систем вентиляции и кондиционирования
- Проектирование, монтаж и эксплуатация систем отопления и теплоснабжения
- Проектирование, монтаж и эксплуатация систем водоснабжения и водоотведения
- Автоматизация проектных работ с использованием AutoCAD
- Электроснабжение и электрооборудование объектов

П-04 «Проектирование и конструирование зданий и сооружений»

Программа включает учебные разделы:

- Основы сопротивления материалов и механики стержневых систем
- Проектирование и расчет оснований и фундаментов зданий и сооружений
- Проектирование и расчет железобетонных конструкций
- Проектирование и расчет металлических конструкций
- Проектирование зданий и сооружений с использованием AutoCAD
- Расчет строительных конструкций с использованием SCAD Office

П-05 «Контроль качества строительства»

Программа включает учебные разделы:

- Основы строительного дела
- Инженерное оборудование зданий и сооружений
- Технология и контроль качества строительства
- Проектирование и расчет железобетонных конструкций
- Проектирование и расчет металлических конструкций
- Обследование строительных конструкций зданий и сооружений
- Выполнение функций технического заказчика и генерального подрядчика

По окончании курса слушателю выдается диплом о профессиональной переподготовке
установленного образца, дающий право на ведение профессиональной деятельности

